

N68-13046  
NASA CR 91361

NATIONAL AERONAUTICS AND SPACE ADMINISTRATION

*Technical Report 32-1246*  
*Surveyor V Mission Report*  
*Part II: Science Results*

*Prepared by:*

*The Surveyor Investigator Teams, Scientific Evaluation Advisory Team, and  
Working Groups*

**CASE FILE  
COPY**

**JET PROPULSION LABORATORY  
CALIFORNIA INSTITUTE OF TECHNOLOGY  
PASADENA, CALIFORNIA**

**November 1, 1967**



NATIONAL AERONAUTICS AND SPACE ADMINISTRATION

*Technical Report 32-1246*

*Surveyor V Mission Report  
Part II: Science Results*

*Prepared by:*

*The Surveyor Investigator Teams, Scientific Evaluation Advisory Team, and  
Working Groups*

JET PROPULSION LABORATORY  
CALIFORNIA INSTITUTE OF TECHNOLOGY  
PASADENA, CALIFORNIA

November 1, 1967

**TECHNICAL REPORT 32-1246**

Copyright © 1967  
Jet Propulsion Laboratory  
California Institute of Technology  
Prepared Under Contract No. NAS 7-100  
National Aeronautics & Space Administration



## Preface

This three-part document constitutes the Project Mission Report on *Surveyor V*, the fifth in a series of unmanned lunar soft-landing missions.

Part I of this Technical Report consists of a technical description and an evaluation of engineering results of the systems used in the *Surveyor V* mission. Part II presents the scientific data derived from the mission, and the scientific analyses conducted by the *Surveyor* Scientific Evaluation Advisory Team, the *Surveyor* Investigator Teams, and the associated Working Groups. Part III consists of selected pictures from *Surveyor V* and appropriate explanatory material.

Results given in this report are based on data evaluation prior to October 26, 1967. It is expected that future evaluation and analysis of the *Surveyor V* data will provide additional scientific results.



## Contents

<b>I. Introduction</b> . . . . .	1
<i>L. D. Jaffe and R. H. Steinbacher</i>	
References . . . . .	3
<b>II. Principal Science Results From Surveyor V</b> . . . . .	5
<i>L. D. Jaffe, S. A. Batterson, W. E. Brown, Jr., E. M. Christensen, S. E. Dwornik, D. E. Gault, J. W. Lucas, R. H. Norton, R. F. Scott, E. M. Shoemaker, G. H. Sutton, and A. L. Turkevich</i>	
<b>III. Television Observations From Surveyor V</b> . . . . .	7
<i>E. M. Shoemaker, R. M. Batson, H. E. Holt, E. C. Morris, J. J. Rennison, and E. A. Whitaker</i>	
A. Landing Site . . . . .	7
B. Landing Site Topography . . . . .	9
C. Morphology and Distribution of Craters . . . . .	14
D. Thickness of Lunar Regolith . . . . .	19
E. Surficial Debris . . . . .	19
F. Size-Frequency Distribution of Fragmental Debris . . . . .	34
G. Photometric Observations . . . . .	36
H. Interpretation of Geologic Observations . . . . .	41
References . . . . .	42
<b>IV. Lunar Surface Mechanical Properties</b> . . . . .	43
<i>E. M. Christensen, S. A. Batterson, H. E. Benson, R. Choate, R. E. Hutton, L. D. Jaffe, R. H. Jones, H. Y. Ko, F. N. Schmidt, R. F. Scott, R. L. Spencer, and G. H. Sutton</i>	
A. Spacecraft Landing . . . . .	43
1. Description . . . . .	43
2. Television Observations of Spacecraft/Soil Interactions . . . . .	45
B. Dynamic Simulations . . . . .	58
C. Soil Characteristics: Spacecraft Slide . . . . .	59
D. Lunar Soil Erosion Test . . . . .	60
1. Erosion Phenomena . . . . .	60
2. Test Explanation . . . . .	61
3. Observed Effects . . . . .	61
4. Simulations and Analysis . . . . .	76
5. Implications of Movement of Alpha-Scattering Instrument by Vernier Engine Firing . . . . .	85
E. Conclusions and Summary . . . . .	87
References . . . . .	88

## Contents (contd)

<b>V. Lunar Surface Temperatures and Thermal Characteristics . . . . .</b>	<b>89</b>
<i>J. W. Lucas, R. R. Garipay, W. A. Hagemeyer, J. M. Saari, J. Smith, and G. Vitkus</i>	
A. Albedo, Lunar Surface Temperatures, and Thermophysical Properties of Landing Site, as Determined by Telescope . . . . .	89
B. Spacecraft View of Lunar Surface . . . . .	93
1. Spacecraft Description . . . . .	93
2. Lunation . . . . .	107
3. Eclipse . . . . .	111
C. Summary . . . . .	111
1. Lunation Data . . . . .	111
2. Eclipse Data . . . . .	112
References . . . . .	113
<b>VI. Astronomy . . . . .</b>	<b>115</b>
<i>R. H. Norton, J. E. Gunn, W. C. Livingston, G. A. Newkirk, and H. Zirin</i>	
<b>VII. Chemical Analysis of the Moon at the Surveyor V Landing Site:</b>	
<b>Preliminary Results . . . . .</b>	<b>119</b>
<i>A. L. Turkevich, E. J. Franzgrote, and J. H. Patterson</i>	
A. Instrument Description . . . . .	120
1. Sensor Head . . . . .	120
2. Digital Electronics . . . . .	122
3. Electronic Auxiliary . . . . .	123
4. Deployment Mechanism/Standard Sample . . . . .	123
5. Characteristics of Alpha-Scattering Instrument Flown on Surveyor V . . . .	124
B. Experiment Control . . . . .	124
1. Alpha-Scattering Analysis and Command . . . . .	124
2. Alpha-Scattering Sequence of Operations . . . . .	125
C. Mission Description . . . . .	126
1. Pre-Launch Operations at Cape Kennedy . . . . .	126
2. Transit Operation . . . . .	127
3. Lunar Landing . . . . .	127
4. Post-Landing Operations . . . . .	127
D. Results . . . . .	132
1. Standard Sample Measurements . . . . .	132
2. Lunar Background Measurements . . . . .	139

## Contents (contd)

3. Lunar Sample Measurements . . . . .	141
E. Discussion . . . . .	146
References . . . . .	148
<b>VIII. Lunar Surface Electromagnetic Properties: Magnet Experiment . . . . .</b>	<b>151</b>
<i>J. Negus de Wys</i>	
A. Purpose of Magnet Assembly . . . . .	151
B. Magnet Assembly Description . . . . .	151
C. Landing and Vernier Rocket Engine Firing . . . . .	157
D. Laboratory Studies . . . . .	164
1. Shadow Progression Studies . . . . .	164
2. Impact Tests in Rock Types . . . . .	164
3. Impact Tests in Basalt With Additions of Iron . . . . .	164
4. Vacuum Studies . . . . .	164
5. Landing Simulation Studies . . . . .	164
E. Discussion . . . . .	173
F. Problems . . . . .	174
G. Conclusions . . . . .	175
<b>IX. Lunar Theory and Processes . . . . .</b>	<b>177</b>
<i>D. E. Gault, J. B. Adams, R. J. Collins, J. Green, G. P. Kuiper, H. Masursky, J. A. O'Keefe, R. A. Phinney, and E. M. Shoemaker</i>	
A. Discussion of Chemical Analysis . . . . .	177
References . . . . .	179
<b>Appendix A. Study of Contamination of Surveyor V Landing Site by     Main Retro Exhaust . . . . .</b>	<b>181</b>
<i>A. L. Turkevich, E. J. Franzgrote, and J. H. Patterson</i>	
<b>Appendix B. Surveyor Science Teams . . . . .</b>	<b>183</b>



## I. Introduction

L. D. Jaffe and R. H. Steinbacher

*Surveyor V* was launched from Cape Kennedy, Florida, at 07:57:01 GMT on September 8, 1967. An *Atlas/Centaur* launch vehicle placed the *Surveyor* into a parking orbit and, at 08:16:27 GMT, injected it into a trajectory intersecting the moon. The spacecraft mass at injection was 1006 kg; after final touchdown, 303 kg.

On September 8 and 9, several midcourse maneuvers were performed. The spacecraft landed in the southwest portion of Mare Tranquillitatis at 00:46:44.28 GMT on September 11, 1967. Based on inflight radio tracking data, the preliminary position was determined to be 23.19°E latitude, 1.50°N longitude; the preliminary position based on post-landing tracking data, to October 25, is 23.18°E latitude, 1.41°N longitude, with a local radius of 1736.9 km.<sup>1</sup>

The spacecraft landed with a vertical velocity of about 4.2 m/sec and a horizontal velocity less than 0.5 m/sec on the southern slope of a crater about  $9 \times 12$  m in horizontal extent and up to 1.3 m deep. One leg touched just outside the crater; the other two legs touched lower down

and within the crater about 0.2 sec later. *Surveyor* then slid a short distance downslope, causing the footpads visible to the television camera to dig trenches in the lunar soil; one of these trenches is about 1 m long and 3 to 10 cm deep. The *Surveyor* came to rest at an angle of about 19.5 deg from the local vertical.

The *Surveyor V* configuration (Fig. I-1) is generally similar to that of *Surveyor I* (Refs. I-1 and I-2), but *Surveyor V* carries an alpha-particle backscattering instrument to analyze the chemical composition of the lunar surface. This instrument irradiates the lunar surface with alpha particles from curium-242 sources and measures the spectra of alpha particles scattered back. It also provides spectral data on protons produced by  $(\alpha, p)$  reactions with the atoms of the lunar surface. These spectra are interpretable in terms of the kind and quantity of elements present in the surface. Physically, the instrument consists of a sensor head, a cube about 15 cm on a side, which is lowered to the surface by a nylon cord some time after the landing; and an alpha-scattering electronics compartment, located on the spaceframe. The instrument has been fully described by Turkevich, et al. (Refs. I-3 and I-4).

<sup>1</sup>R. W. Graves, unpublished work.

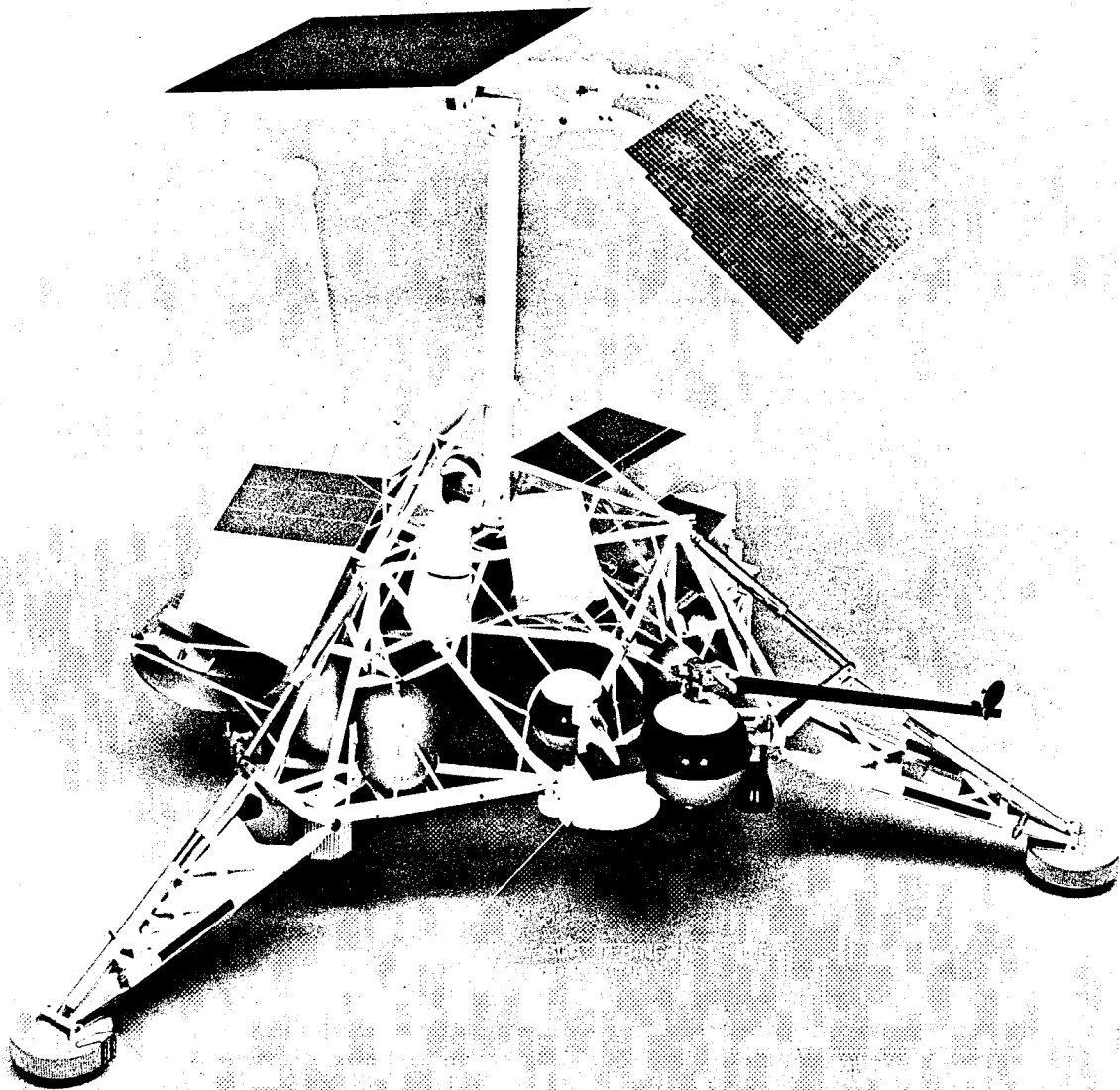


**Fig. I-1. Model of Surveyor V spacecraft in landed configuration.**



In addition, a bar magnet and a nonmagnetic control bar were attached to one of the footpads to indicate the presence of lunar material with a high magnetic susceptibility. Two convex auxiliary mirrors, located low on the spaceframe, permitted better viewing of the lunar surface below the alpha-scattering instrument, a vernier engine, and a crushable landing block.

*Surveyor V* accumulated 104 hr of alpha-scattering data and took 19,054 television pictures from touchdown September 11 to sunset on the second lunar day, October 23, 1967. Of these pictures, 18,006 were taken between September 11 and shortly after first sunset on September 24. They included views of the interior of the crater in which the spacecraft landed and the rather level mare surface surrounding the crater, star and planet sightings for attitude reference, as well as a sequence of solar corona pictures and earthshine pictures after local sunset on the spacecraft. The alpha-scattering instrument accumulated about 82 hr of data the first lunar day, giving the first direct information on the chemical composition of the moon. Views of the magnet assembly after touchdown, before and after the vernier engine firing, also provided good data. To provide information on the effects of engine exhaust upon the lunar surface material, the liquid-propellant vernier rocket engines were fired for 0.55 sec at 05:38 GMT on September 13. Measurements were made of the local radar reflectivity during the spacecraft landing maneuver, of mechanical properties of the lunar surface material from the interaction of the space-

craft with the surface at touchdown and during the vernier engine firing test, and of the radial velocity of the landing site relative to earth as a function of time by post-landing communication doppler shift. Surface temperature data were obtained during the first lunar day and after sunset until September 29.

Spacecraft transmission was resumed for a second lunar day on October 15. An additional 1048 television pictures and 22 hr of alpha-scattering data accumulation were obtained up to the next sunset on October 23. Surface temperature measurements were made during the second lunar day, including the period of total eclipse of the sun by the earth on October 18, and into the second lunar night which began on October 24.

Section II of this document, prepared by the *Surveyor V* Scientific Evaluation Advisory Team, summarizes the principal science results of the *Surveyor V* mission as of October 26. More detailed information may be found in the subsequent sections, which were prepared by the *Surveyor V* Investigators and Working Groups. These sections have been written independently of one another; some differences in interpretation may exist among them.

Individual pictures taken by *Surveyor* are best identified by the day of the year and GMT at which they were taken. September 11, 1967, was Day 254; October 23 was Day 296. Mosaics are best identified by catalog numbers.

## References

- I-1. *Surveyor* Scientific Evaluation Advisory Team, "Surveyor I: Preliminary Results," *Science*, Vol. 152, p. 1737, 1966.
- I-2. Jaffe, L. D., "Lunar Surface Exploration by *Surveyor* Spacecraft: Introduction," *J. Geophys. Res.*, Vol. 72, p. 773, 1967.
- I-3. Turkevich, A. L., Knolle, K., Emmert, R. A., Anderson, W. A., Patterson, J. H., and Franzgrote, E., "Instrument for Lunar Surface Chemical Analysis," *Rev. Sci. Instruments*, Vol. 37, p. 1681, 1966.
- I-4. Turkevich, A. L., Knolle, K., Franzgrote, E., and Patterson, J. H., "Chemical Analysis Experiment for the *Surveyor* Lunar Mission," *J. Geophys. Res.*, Vol. 72, p. 831, 1967.



## II. Principal Science Results From Surveyor V

*L. D. Jaffe, S. A. Batterson, W. E. Brown, Jr., E. M. Christensen, S. E. Dwornik,  
D. E. Gault, J. W. Lucas, R. H. Norton, R. F. Scott,  
E. M. Shoemaker, G. H. Sutton, and A. L. Turkevich*

The area of southwestern Mare Tranquillitatis in which *Surveyor V* landed appears generally similar to the sites in Oceanus Procellarum observed by *Surveyors I* and *III*. All three areas are fairly level, dark maria with rather similar distributions of craters and rocks. A surface layer of weakly cohesive fine particles, aggregates, and rocks is present in both Mare Tranquillitatis and Oceanus Procellarum. Differences between the surface layers in these maria are relatively small.

*Surveyor V* was the first lunar soft-landing spacecraft to obtain information about the chemical nature of the lunar surface. This was achieved through two experiments: one obtained the gross chemical composition by an alpha-particle backscattering instrument, and the other obtained some magnetic characteristics of the surface material with a bar magnet.

The three most abundant elements found by *Surveyor V* at the mare landing site are the same as the most prevalent on the surface of the earth: in decreasing abundance, they are oxygen, silicon, and aluminum. The relative amounts of the chemical elements are similar to those of a silicate rock of a basaltic type.

Lunar surface material of high magnetic susceptibility adhered to the magnet. The quantity of magnetic material observed on the magnet is comparable to that expected if the magnet came in contact with pulverized basalt with 10 to 12% magnetite and not more than 1% admixed metallic iron. Particle size of material attracted by the magnet was less than 1 mm.

*Surveyor V* landed in a dimple-shaped, 9- × 12-m rimless crater, which is the largest member of a small chain of rimless craters; a parallel row of very small craters also occurs within the large crater. The long axis of the large crater and the crater chain are approximately parallel with the dominant linear features in the highlands west of Mare Tranquillitatis and with many other elongate craters and crater pairs in nearby parts of the mare. On the basis of its shape and the alignment of small associated craters, the crater in which *Surveyor V* landed may have been formed by drainage of surficial fragmental debris into a northwest-trending fissure.

Observations of blocky-rimmed craters, relatively nearby, indicate that the local thickness of the layer of fragmental debris with low cohesion is not more than 5 m.

The walls of the *Surveyor V* crater provide exposures of the upper meter of this debris layer. Different types of fragments are revealed in the pictures of the debris dislodged from these walls during the spacecraft landing and in the pictures of the undisturbed parts of the walls. The types of fragments include: (1) bright, angular objects, which are inferred to be pieces of dense rocky material; (2) dark, rounded objects, which are probably aggregates of very fine-grained particles; and (3) dark, lumpy objects, which appear to be aggregates of aggregates. The aggregate character of some of the loose, ejected fragments is well demonstrated by the presence of bright, angular chips set in a dark, fine-grained matrix. At depths greater than about 10 cm, most of the debris layer appears to be composed of slightly shock-compressed aggregates, ranging from a few millimeters up to 3 cm in diameter, set in a matrix of less-coherent, finer particles. Rocky chips and fragments larger than a millimeter are dispersed as a subordinate constituent of the debris.

The estimated normal albedo (normal luminance factor) of the undisturbed parts of the lunar surface near *Surveyor V* is  $7.9 \pm 1.0\%$ , somewhat lower than that observed at the *Surveyor III* landing site. Debris ejected on the lunar surface in front of the footpads has a normal albedo of  $7.5 \pm 1.0$ , which is only about one-twentieth lower than the albedo of the undisturbed surface, but is similar to the albedo of the material disturbed by the footpads at the *Surveyor III* landing site.

New photometric evidence obtained from the *Surveyor V* pictures shows that the bright, angular fragments are denser or at least less porous than the dark, fine-grained surficial material and dark aggregates. The surfaces of the bright, angular fragments have a photometric function more like that of a lambertian scatterer than like that of the fine-grained lunar material.

A spacecraft vernier engine firing against the lunar surface produced observable erosion resulting from two mechanisms: the removal of particles by exhaust gases blowing along the surface, and explosive blowout of entrapped gas and soil from directly beneath the nozzle immediately following engine shutdown. Analyses of the surface disturbance indicate a material permeability of between  $1 \times 10^{-8} \text{ cm}^2$  and  $7 \times 10^{-8} \text{ cm}^2$ , which is comparable to the permeability of terrestrial silts.

As in *Surveyors I* and *III*, the landing produced interactions with the surface. Various analyses of phenomena associated with the landing and with the firing of the vernier rocket engines have provided these additional estimates of surface properties:

Static bearing strength:

For upper few millimeters:  $< 10^4 \text{ dynes/cm}^2$ .

Averaged over upper few centimeters:

$\sim 3 \times 10^5 \text{ dynes/cm}^2$ .

Angle of internal friction: consistent with *Surveyor III* results (37 deg).

Pressure developed by the soil against the footpad in resisting the slide during landing was about  $7 \times 10^4 \text{ dynes/cm}^2$ , which agrees with results obtained from the Soil Mechanics Surface Sampler Experiment on *Surveyor III*. The estimate of permeability indicates that most of the particles are in the 2- to 60- $\mu$  size range; this value agrees with results from photographic observations of the disturbed areas, the match of *Surveyor V* footpad trenches to those produced experimentally in pulverized basalts, and analyses of *Surveyor III* footpad imprints. Clods observed in the disturbed areas appear to be similar to those observed in previous missions, indicating a similar cohesion. In general, the soil at this site appears similar, but somewhat weaker than at the other *Surveyor* landing sites.

The lunar day temperatures derived from *Surveyor V* observations are in fair agreement with predictions based on telescopic observations. The temperatures of the lunar surface after sunset and during total eclipse suggest that the surface material has an effective thermal inertia of approximately 500 (cgs units), in good agreement with *Surveyor III* eclipse data. This differs from a value of approximately 1000 obtained from data derived on earth.

The evidence that the lunar surface material at the *Surveyor V* landing site is basaltic in composition, and the fact that this *Surveyor V* site appears to be typical of the mare areas, suggests that differentiation has occurred in the moon, probably owing to internal sources of heat. The results are consistent with the hypothesis that the mare basins are filled with extensive basaltic volcanic flows. If such flows have occurred, some of the processes and products of lunar magmatic activity are apparently similar to those of the earth.

*Surveyor V* provided the first measurements of the brightness of the solar corona at distances of 10 to 30 solar radii from the center of the sun. Since the brightness is produced by scattering from particulate matter between the earth and the sun, it should prove possible to derive density measurements of particulate matter at distances out to one-third the radius of Mercury's orbit. A good determination of the density distribution with height above the ecliptic plane may be made.

### III. Television Observations From Surveyor V

E. M. Shoemaker, R. M. Batson, H. E. Holt, E. C. Morris,  
J. J. Rennilson, and E. A. Whitaker

*Surveyor V* landed on the lunar surface at 00:46:44 GMT on Day 254 (September 11), 35 hr after local sunrise on the moon. Between the time of landing and lunar sunset, 13 days later, it transmitted more than 18,000 high-quality television pictures of the lunar surface and parts of the spacecraft. The *Surveyor V* camera was operated extensively from the Goldstone, California, and Canberra, Australia, Tracking Stations of the Deep Space Network; some pictures were also received at the Madrid, Spain, Tracking Station.

The *Surveyor V* television camera is similar to the cameras flown on *Surveyors I* and *III* (Ref. III-1). The *Surveyor V* camera, however, is more sensitive than the *Surveyor III* camera. The total range of response of the *Surveyor V* camera, like that of the *Surveyor I* and *III* cameras, is about 1,000,000 to 1, which is achieved by the combined use of various filters, apertures, and exposure times. Three color filters (red, green, and blue), carefully matched to the spectral response of the camera, were carried on *Surveyor V*. The match of the camera-filter spectral response function to the standard CIE color-matching functions was as good as was achieved on the *Surveyor III* camera.

After landing, the mirror and optical parts of the *Surveyor V* camera were clean and free of dust and dirt particles. This resulted in the highest-quality *Surveyor* pictures yet received.

#### A. Landing Site

The landing site of the spacecraft, as determined from inflight tracking data, is at  $1.50^{\circ}\text{N}$  latitude and  $23.19^{\circ}\text{E}$  longitude. On the basis of post-landing tracking data, the landing site is at  $1.41^{\circ}\text{N}$  latitude and  $23.18^{\circ}\text{E}$  longitude. The  $3\sigma$  uncertainty ellipse for the first solution has a semi-major axis of 6.9 km and a semi-minor axis of 2.7 km (Fig. III-1). This site is in the southwestern part of Mare Tranquillitatis, about 70 km north of the southern boundary of the mare and a little over 80 km east of the crater Sabine (Fig. III-2). It is near the periphery of a complex system of mare ridges, but no known mare ridges occur within 19 km of the most probable position of the landing site. The region is crossed by faint rays associated with the major crater Theophilus, 350 km to the south, and the landing site may be within one of the Theophilus rays.

The highlands to the west of Mare Tranquillitatis are characterized by prominent ridges trending northwest

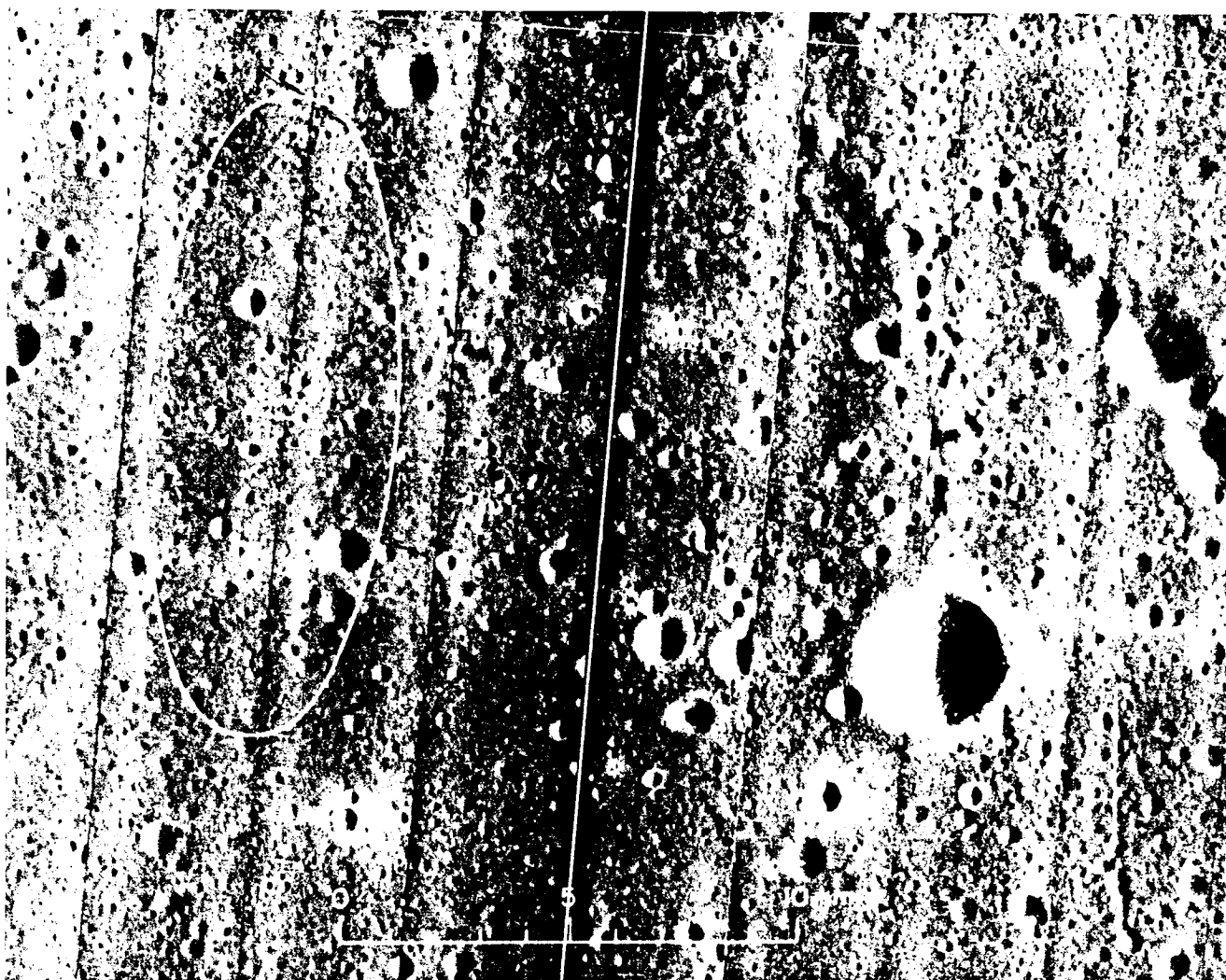


Fig. III-1. *Lunar Orbiter V* medium-resolution photograph (M-74) of an area in the southern part of Mare Tranquillitatis. Cross shows solution from inflight tracking data for the location of Surveyor V, and ellipse shows  $3\sigma$  limit of error of this location. Large crater on the right side of the photograph is Sabine D. The crater in which Surveyor V landed is too small to be resolved in this photograph.

(Fig. III-2); these ridges are part of the system of Imbrian sculpture (Refs. III-2 and III-3). Subordinate linear structures in the highlands, such as the Ariadaeus Rille, trend about  $N70^\circ W$ . High-resolution photographs of the immediate vicinity of the landing site taken by *Lunar Orbiter V* (H-78) reveal many craters about 10 m across and smaller, which are aligned in a northwest direction. Typically, these small craters occur in pairs, and the line between their centers trends northwest; a few individual craters are markedly elongate in this same direction. This alignment follows the dominant trend on this part of the mare of the lunar patterned ground, which consists of

gentle ridges and troughs of very low amplitude. Both the aligned craters and the lunar patterned ground probably reflect a subsurface system of fissures and joints related to the Imbrian sculpture.

An unsuccessful attempt was made to locate the Surveyor V landing site on *Lunar Orbiter V* high-resolution frame H-78. The coordinates of the landing site obtained from the tracking data were plotted on ACIC Lunar Chart AIC 600 and transferred to the *Lunar Orbiter* photograph; the resolution of this photograph is about 2.5 m. The chances were remote of identifying the

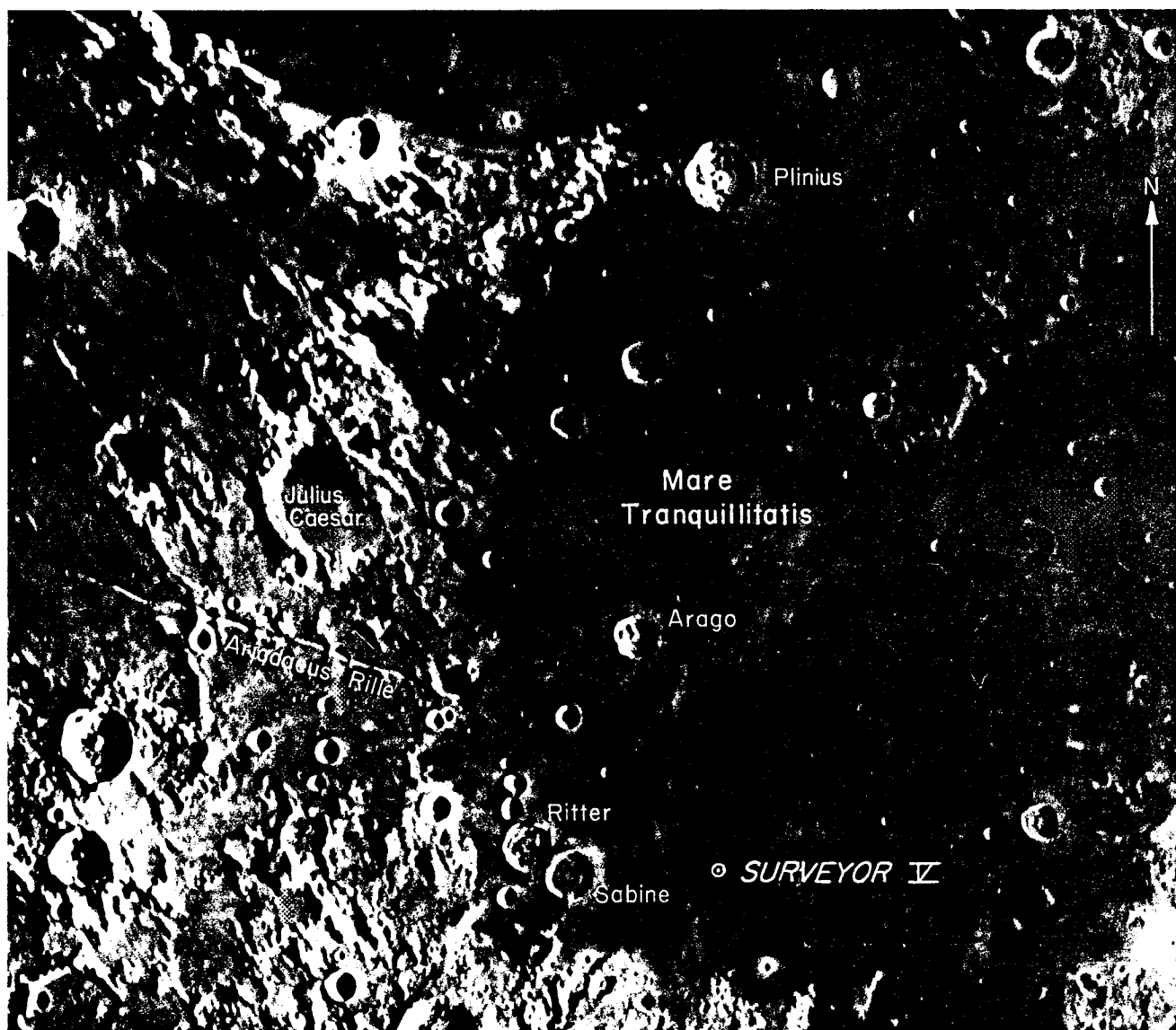


Fig. III-2. Earth-based telescopic photograph of Mare Tranquillitatis and the highlands to the west. Prominent northwest-trending ridges and valleys in the highlands are part of Imbrian sculpture.

*Surveyor V* crater by its size and shape alone. It is hoped that the study of the distant features shown in narrow-angle photographs of the horizon, taken near sunset, will lead ultimately to the identification of the crater in which *Surveyor V* landed.

### B. Landing Site Topography

Data obtained from the television pictures have been used to prepare preliminary topographic maps of small

areas on the lunar surface surrounding *Surveyor V*. The positions of points on the lunar surface, relative to the television camera, were obtained from angular position measurements derived from potentiometers on the elevation and azimuth axes of the camera mirror, and from range measurements based on the solution for points of best focus in pictures taken at many different focus settings. This method of topographic mapping is essentially new; we refer to the technique as *focus ranging*. The technique utilizes pictures taken at eight to ten different focus

settings at each camera elevation position along a given azimuth. Small areas in best focus in each picture are located on a mosaic of pictures taken at specific focus settings; the azimuth and elevation of the centers of each small area in best focus are determined by graphical measurement. The location of a point on the lunar surface with respect to the intersection of the camera-mirror rotation axes is computed from azimuth, elevation, and calibrated focus distance. Focus-ranging surveys of the *Surveyor V* landing site were taken at each available camera elevation position along camera azimuth lines 18 deg apart. The elevation angles are separated by 4.96-deg increments. Partial focus-ranging surveys also were taken along several intermediate azimuths.

More than 4000 focus-ranging pictures were taken during the first lunar day, from which more than 500 control points were computed for compilation of the preliminary topographic maps (Figs. III-3 and III-4). These maps show that the *Surveyor V* spacecraft is located on the southwest wall of a crater, 9 m wide, about 12 m long, and more than a meter deep. Footpads 2 and 3 of the spacecraft came to rest near the foot of the crater wall, and footpad 1 rests near the rim of the crater. For convenience of reference, we will call this crater the *Surveyor V* crater.

The orientation of the spacecraft and of the camera has been determined from television camera observations of stars and planets and of the lunar horizon, and also from the angular settings of the solar panel sun sensor and positional tuning of the spacecraft's planar array antenna. The stars Sirius, Arcturus, Agena, and Capella and the planets Venus and Jupiter were observed. Preliminary reduction of these observations showed that the spacecraft was tilted 19.7 deg at an azimuth of N17°E. Observations of the lunar horizon, on the other hand, indicate that the spacecraft was tilted 19.4 deg at an azimuth of N13°E. The amount of tilt of the spacecraft, at the time of these observations, is known within a few tenths of a degree, but the present solution for the azimuth of tilt has a probable error of several degrees. The camera 0-deg azimuth was found from the stellar and planetary observations to be oriented approximately N24.7°E; this solution is accurate to within a degree. Near the end of the first lunar day, the shock absorbers on legs 2 and 3 compressed, and the spacecraft was tilted about 3 deg more to the northeast. The final attitude of the spacecraft and camera at the end of the first lunar day is not accurately known.

Because the camera is inclined toward the floor and far wall of the *Surveyor V* crater, more than 80% of the field of view below the horizon is occupied by parts of the lunar surface that are not more than 6 m from the camera. The rim or edge of the crater, as seen from the camera, lies about 8 to 19 deg below the horizon and follows a sinusoidal curve approximately parallel with the horizon in the panoramic mosaics prepared from the pictures (Fig. III-5). Under high sun illumination, the edge of the crater can be observed as a region of abrupt change in the apparent eccentricity of very small craters, which reflects the change in surface slope. A rather abrupt change in the observable texture of the surface and in average photographic density or tone also occurs at the edge of the crater (Fig. III-6). At very low angles of solar illumination, the edge of the crater is easily distinguished as the upper edge of the shadow filling the crater.

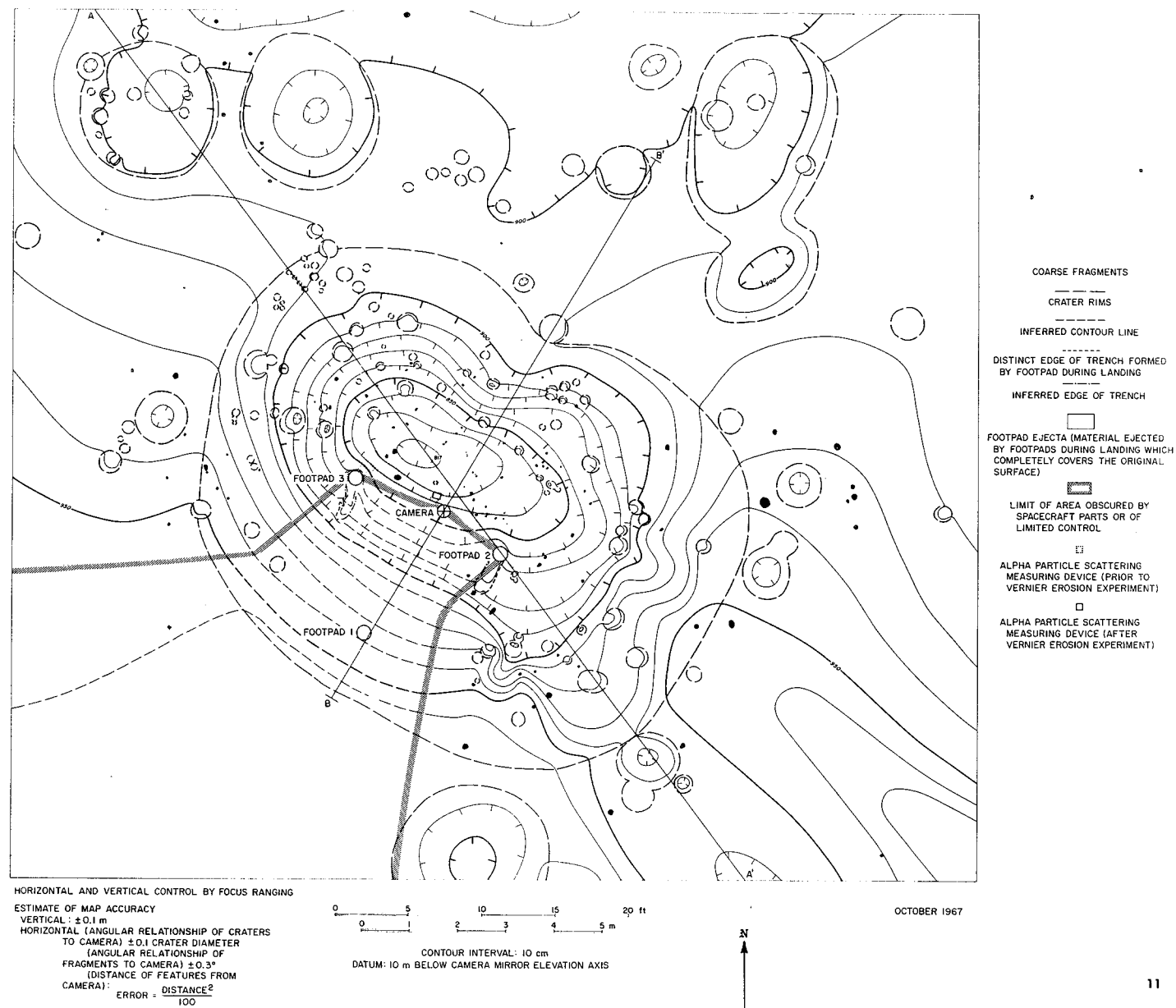
As revealed by Figs. III-3 and III-4, the *Surveyor V* crater is elongate in the northwest direction. It is, in fact, the largest local member of a chain of small craters trending northwest, and it appears to be a compound crater consisting of two partially merged, smaller craters or components separated by a subdued northeast-trending septum or low ridge. Thus, the *Surveyor V* crater appears to be a member of the family of elongated craters and crater pairs observed on the *Lunar Orbiter V* high-resolution photographs in the vicinity of the *Surveyor V* landing site.

The floor of the southeast component of the *Surveyor V* crater is about 20 cm higher than that of the northwest component, but the rim of the compound crater is also 20 to 30 cm higher on the southeast than on the northwest. The camera elevation axis rises almost 80 cm above the north rim of the crater, but only about 30 cm above the south rim.

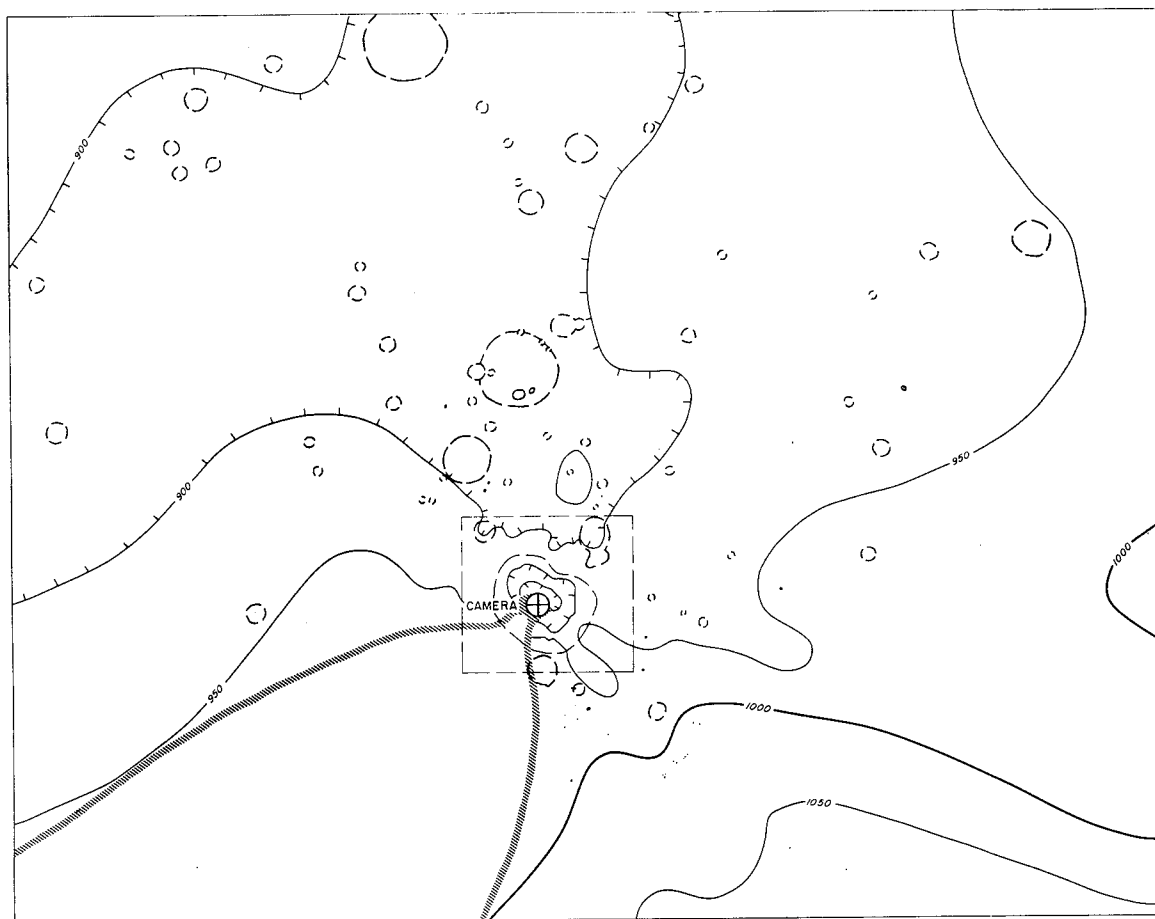
Beyond the rim of the *Surveyor V* crater, the lunar surface is visible out to distances of about a kilometer to the north and west. The horizon to the east and south is closer. In one sector south of the spacecraft, the horizon is only about 100 m distant, where it is occupied by the raised rim of a nearby crater. The horizon lies slightly above the horizontal line of sight in all directions, and is 0.4 deg high on the average. These data suggest the landing site is within, and on the southeast flank of, a very broad, shallow depression on the order of 1 km in width and about 10 m or a few tens of meters deep.



Fig. III-3. Large-scale topographic map of Surveyor V landing site (topography by R. M. Batson, R. Jordan, and K. B. Larson).







HORIZONTAL AND VERTICAL CONTROL BY FOCUS RANGING  
 ESTIMATE OF MAP ACCURACY  
 VERTICAL  $\pm 0.5$  m  
 HORIZONTAL (ANGULAR RELATIONSHIP OF CRATERS  
 TO CAMERA)  $\pm 0.5$  CRATER DIAMETER  
 (ANGULAR RELATIONSHIP OF  
 FRAGMENTS TO CAMERA)  $\pm 0.3^\circ$   
 (DISTANCE OF FEATURES FROM  
 CAMERA): ERROR  $= \frac{\text{DISTANCE}^2}{100}$

0 50 100 150 200 ft  
 0 10 20 30 40 50 m

CONTOUR INTERVAL: 50 cm  
 DATUM: 10 m BELOW CAMERA MIRROR ELEVATION AXIS

OCTOBER 1967

Fig. III-4. Small-scale topographic map of Surveyor V landing site (topography by R. M. Batson, R. Jordan, and K. B. Larson).



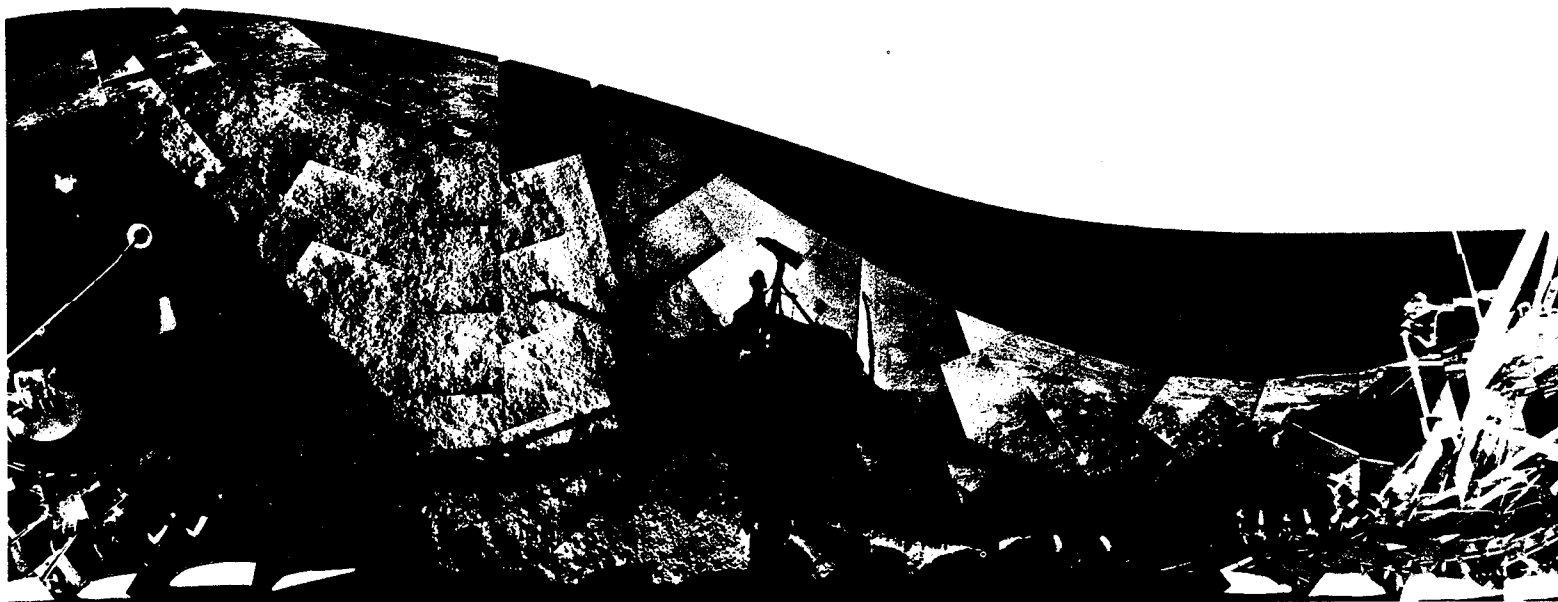


Fig. III-5. Mosaic of wide-angle pictures from Surveyor V taken the day before lunar sunset. The horizon follows a sinusoidal curve because the camera is tilted. The shadow of the west wall of the Surveyor V crater partially fills the crater at the left. Rounded edge of the crater follows the horizon, but lies approximately one-half the width of one wide-angle picture below it (Day 266, 11:20:24 to 11:47:54 GMT).



**Fig. III-6. Mosaic of narrow-angle pictures from *Surveyor V* showing the northwest wall of the *Surveyor V* crater, and the far field beyond the rim of the crater extending to the horizon. Differences in texture of the crater wall and the far field are due to differences in the distance from the camera and inclination of the surfaces (Day 275, 15:12:50 to 16:11:20 GMT).**

### **C. Morphology and Distribution of Craters**

In profile (Fig. III-7), the *Surveyor V* crater is dimple-shaped; it lacks a raised rim, and the slope of the crater wall increases gradually toward the center of the crater. It has a distinct, small, concave floor, however, about 2.4 m wide. Both in plan view and in profile, the *Surveyor V* crater resembles other craters, observed in *Ranger* pic-

tures and *Lunar Orbiter* photographs, which are inferred to have been formed by drainage of surficial debris into subsurface fissures (Refs. III-4 to III-6). We infer that the *Surveyor V* crater has been formed by drainage of surficial fragmental debris into a fissure that passes beneath the center of the crater and extends for some distance both northwest and southwest beneath the crater chain.

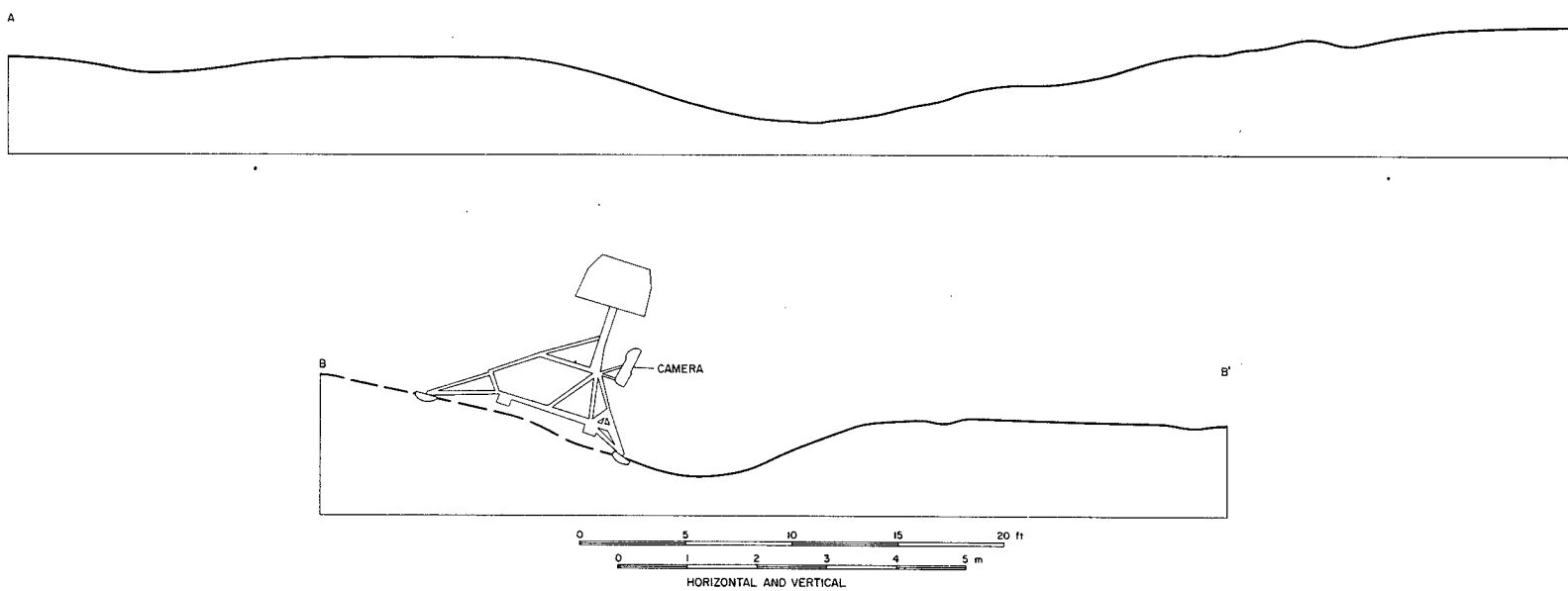


Fig. III-7. Longitudinal and transverse profiles of the Surveyor V crater (see Figs. III-3 and III-4).

Along the northwest wall of the *Surveyor V* crater is a chain of small craters ranging in diameter from 20 to 40 cm (Figs. III-3 and III-8). The trend of this chain is nearly parallel with the long axis of the *Surveyor V* crater. This group of small craters probably has been formed by recent renewed drainage into the underlying fissure or into a parallel fissure. Other small craters are scattered over the walls and floor of the *Surveyor V* crater; many have low raised rims. Most of these craters probably were formed by impact.

The lunar surface beyond the rim of the *Surveyor V* crater is pockmarked with hundreds of craters visible

from the vantage point of the *Surveyor V* camera. They range in diameter from a few tens of centimeters to more than 20 m. About 10 m northwest of the *Surveyor V* camera is another rimless crater about 4 m in diameter (Fig. III-9). This crater has probably been formed by drainage of debris into a subsurface fissure, like the *Surveyor V* crater, and is probably localized over the same fissure or a parallel one. Many other craters observable in the middle distance are of similar rimless form and may have been formed by drainage of surficial debris.

The size-frequency distribution of small craters ranging from 6 cm to 2 m in diameter, which occur within

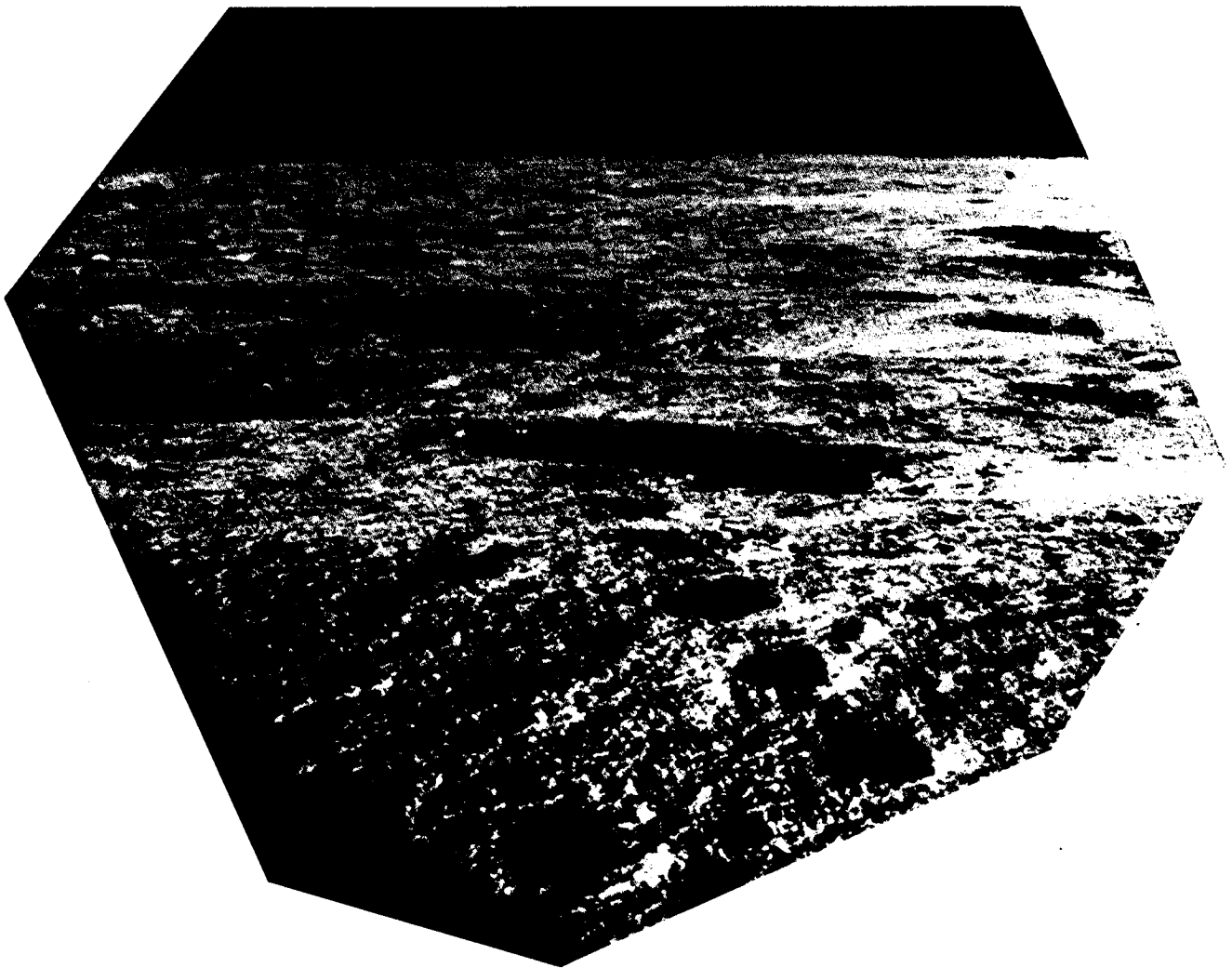


Fig. III-8. Wide-angle picture of the northwest wall of the *Surveyor V* crater. Chain of small craters 20 to 40 cm in diameter extends from the center to the bottom of the picture (Day 266, 11:26:28 GMT).





**Fig. III-9.** Wide-angle picture of the far field and horizon northwest of *Surveyor V*. The dark area along the bottom of the picture is part of the wall of the *Surveyor V* crater in shadow. A crater 4 m in diameter lies between the rim of the *Surveyor V* crater and the horizon. This crater, which is devoid of a raised rim, probably is part of a system of craters aligned in a northwest direction and parallel with one of the major lineation directions in Mare Tranquillitatis (Day 266, 11:27:18 GMT).

the *Surveyor V* crater and in the near field out to 10 m from the spacecraft (Fig. III-10), was determined from *Surveyor V* pictures taken early in the lunar day and just before sunset. In addition, the size-frequency distribution of craters ranging from 4 to 256 m in diameter was determined from *Lunar Orbiter V* photograph H-78 for an area of 1-km radius within the  $3\sigma$  *Surveyor V* landing ellipse. There were 107 craters measured from the *Surveyor V* pictures; 1196 craters were measured from the *Lunar Orbiter* photographs.

A comparison of the cumulative size-frequency distribution of small craters measured from the *Surveyor V* pictures with size-frequency distribution of craters determined for the *Surveyor I* and *III* sites (Fig. III-11) shows fewer small craters at the *Surveyor V* site. This observational difference is due primarily to the incompleteness of

the observational data for the *Surveyor V* site. The low oblique view (from the television camera) of the lunar surface outside the *Surveyor V* crater and unfavorable illumination of parts of the *Surveyor V* crater during the lunar day made recognition of the small craters difficult. The cumulative frequency of craters in the 4- to 256-m-diameter range, determined from the *Lunar Orbiter V* photograph, is somewhat below the average for the lunar plains. This observed low frequency near the *Surveyor V* site is due, in part, to incompleteness of the data near the 4-m end of the diameter range measured; but the number of craters from about 50 to 250 m in diameter is actually somewhat below average in the area examined. The overall cumulative size-frequency distribution of craters at the *Surveyor V* landing site probably approaches the general frequency distribution for craters on the mare surfaces determined from *Ranger VII*, *VIII*, and *IX* pictures (Fig. III-11).

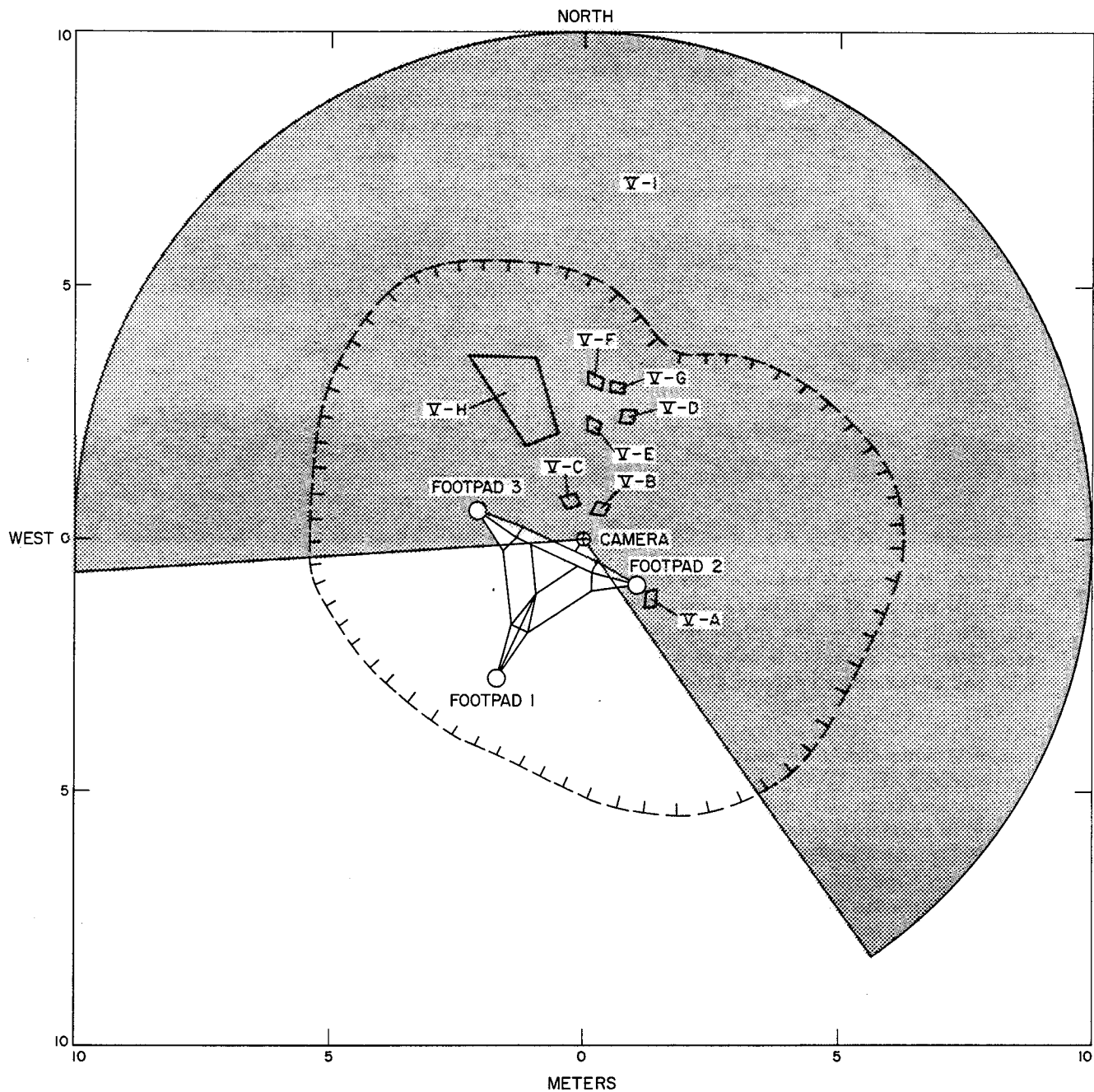


Fig. III-10. Location of areas used in determination of size-frequency distribution of craters (area V-1) and fragments (areas V-A to V-H) at the Surveyor V landing site. Rim of the Surveyor V crater is indicated by broken line; stippled pattern indicates area V-1 used in the determination of size-frequency distribution of craters.

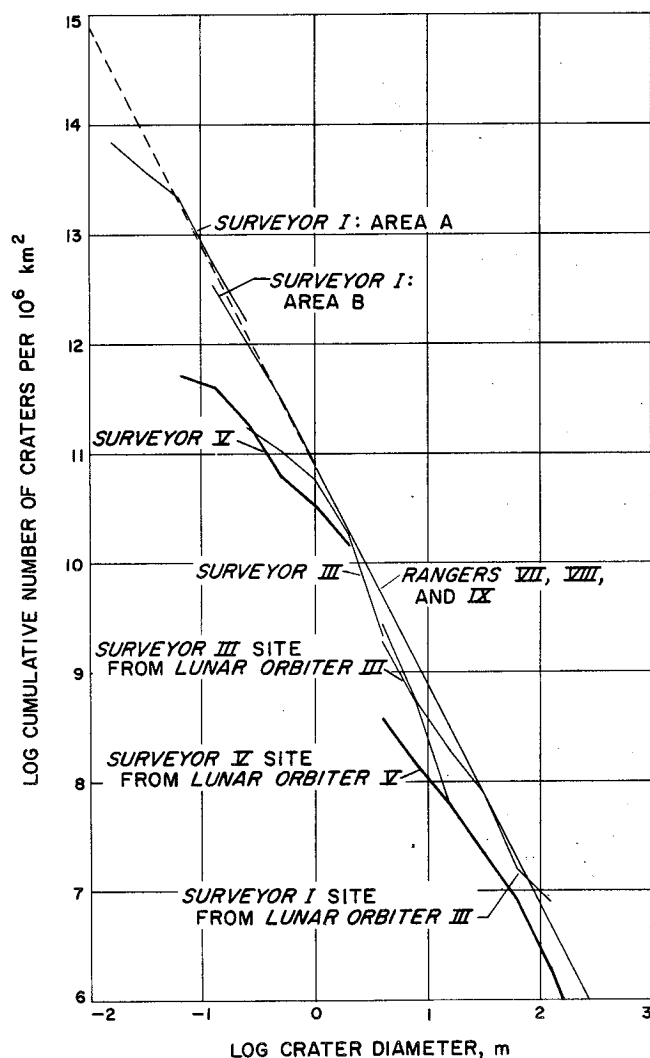


Fig. III-11. Size-frequency distribution of small craters at the Surveyor V landing site compared with the size-frequency distribution of craters estimated for the Surveyor I and III landing sites, and the mean size-frequency distribution of small craters on the lunar plains determined from Ranger VII, VIII, and IX pictures.

#### D. Thickness of Lunar Regolith

A few craters in the middle distance have distinct, raised blocky rims. One crater, about 200 m to the north of the spacecraft (Fig. III-12), is about 15 m in diameter; another crater, about 100 m to the south (Fig. III-13), is about 20 m in diameter. A strewn field of blocks surrounds each of these craters; the strewn field associated

with the crater to the south extends almost to the spacecraft. If the blocky-rimmed craters have depth-to-diameter ratios between 1:3 and 1:4, ratios characteristic of small primary lunar craters, the presence of blocks on their rims indicates that the depth to coarse blocky or coherent material is locally not greater than about 5 m. The scarcity of blocky ejecta around most small craters, however, indicates that at least the upper few meters of material consist predominantly of fine-grained debris with little or no cohesion (Refs. III-6 to III-8).

#### E. Surficial Debris

An unusually detailed view of the surficial debris layer or lunar regolith is provided by the closeup pictures of the walls and floor of the Surveyor V crater. The spacecraft initially touched down on the upper part of the south wall of the crater; footpad 1 touched first outside of the crater, and footpads 2 and 3 part way down the crater wall. As the spacecraft rebounded, it slid down the crater wall and came to rest with footpads 2 and 3 close to the edge of the concave crater floor. A 1-m-long trench dug by footpad 2 in sliding downward is shown in Fig. III-14. It is about 10 cm deep at the upper end and partly filled with loose debris. A good exposure of the fragmental material that lines the Surveyor V crater wall can be seen for about 60 cm along the wall of this trench.

Loose debris was ejected in front of each footpad as the spacecraft slid down the crater wall; this debris formed distinct low piles that extended onto the crater floor in front of footpads 2 and 3 (Fig. III-3). In addition, a considerable amount of loose material cascaded down the slope ahead of footpad 1 and is visible on the floor of the crater directly beneath the camera.

Many individual fragments rolled a short distance, leaving tracks on the original surface (Fig. III-15). Some of these tracks, which are a millimeter to a few millimeters deep, were formed by fragments no more than 2 cm across. On the assumption that the density of the fragments does not exceed 3 g/cm<sup>3</sup>, the development of the tracks shows that the bearing strength of the uppermost few millimeters of the fine-grained debris on the lunar surface is less than 10<sup>4</sup> dynes/cm<sup>2</sup>, for surface areas of about 1 cm<sup>2</sup>. This fragile, uppermost layer was disturbed not only by fragments set in motion during landing of the spacecraft, but also by the scouring effect of the gases exhausted from the vernier engines, when they were turned on to conduct an erosion experiment. At distances more than a meter from the vernier engines, the surface has a marked swept appearance with many low parallel grooves

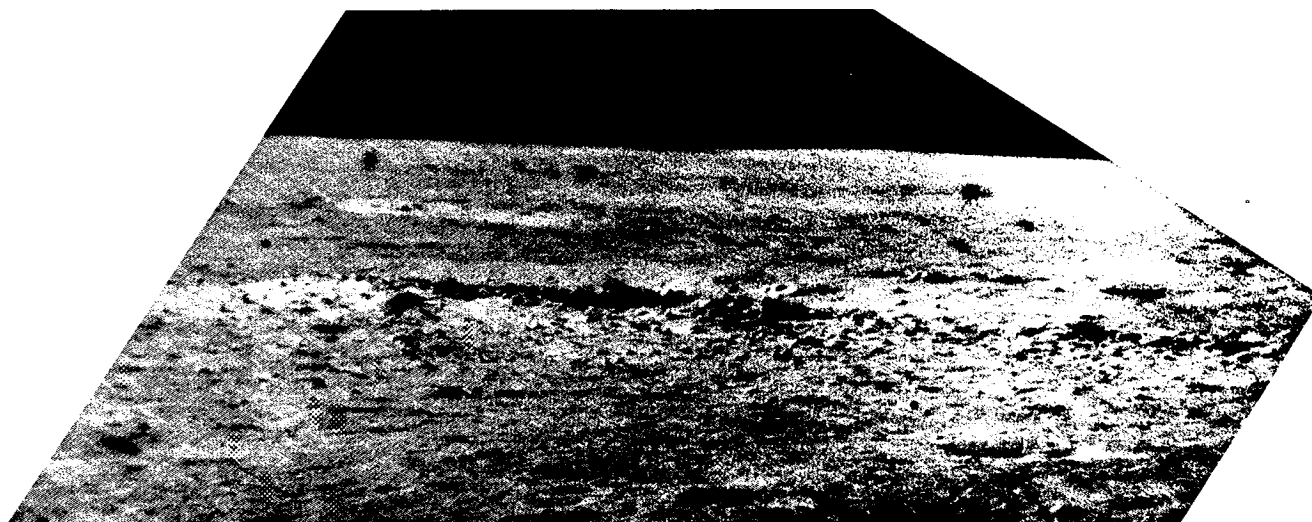


Fig. III-12. Narrow-angle picture showing blocky-rim crater about 15 m in diameter, approximately 200 m north of Surveyor V (Day 265, 15:30:48 GMT).

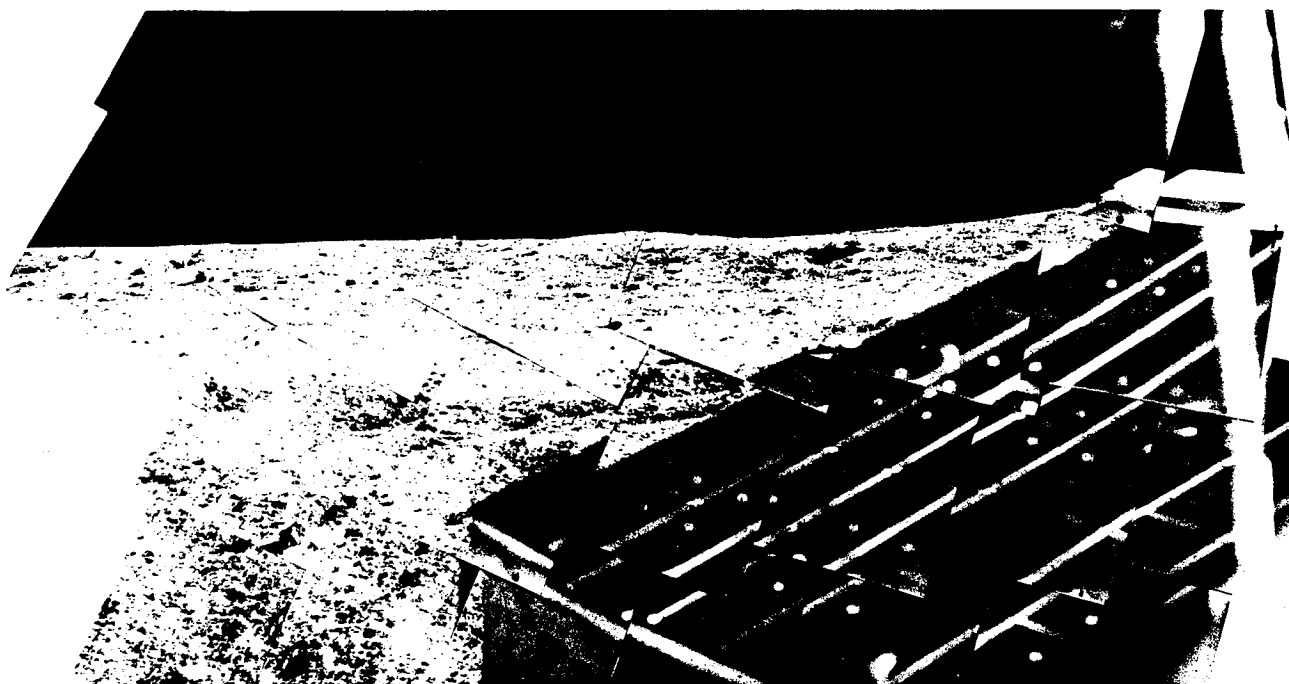


Fig. III-13. Mosaic of narrow-angle pictures from Surveyor V taken on the second day before lunar sunset. The low rim of a nearby crater 20 m in diameter forms a slight bump on the horizon. A strewn field of blocky debris adjacent to the crater lies in the far field just below the horizon. Rim of the Surveyor V crater lies midway between the horizon and bottom of the mosaic. Dark object at right is part of the spacecraft (Day 265, 11:16:31 to 11:21:44 GMT).

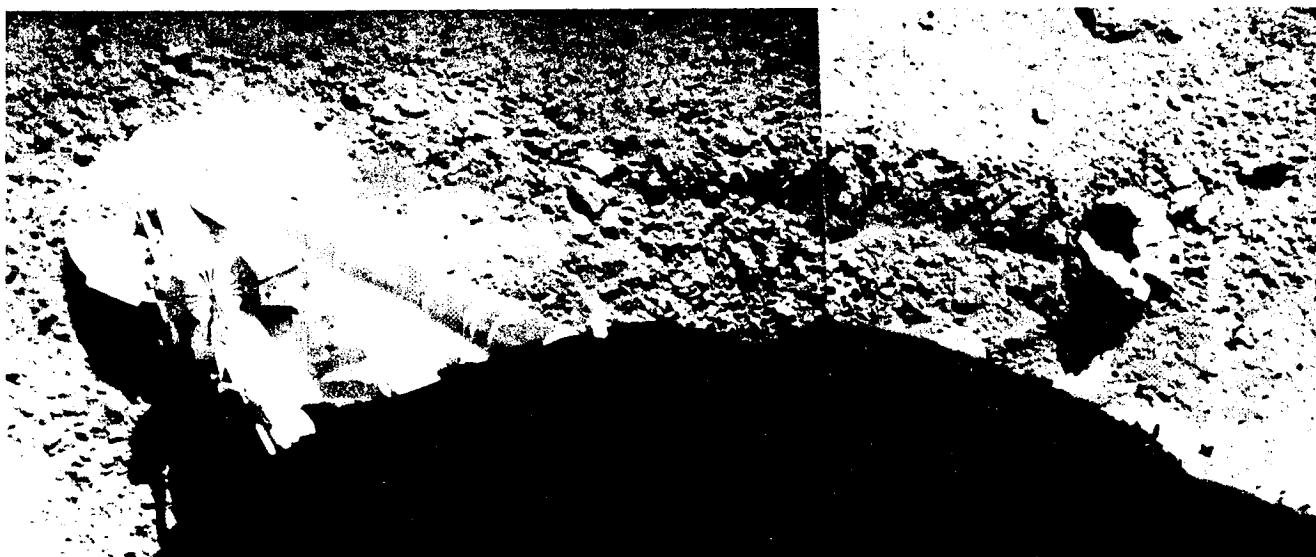


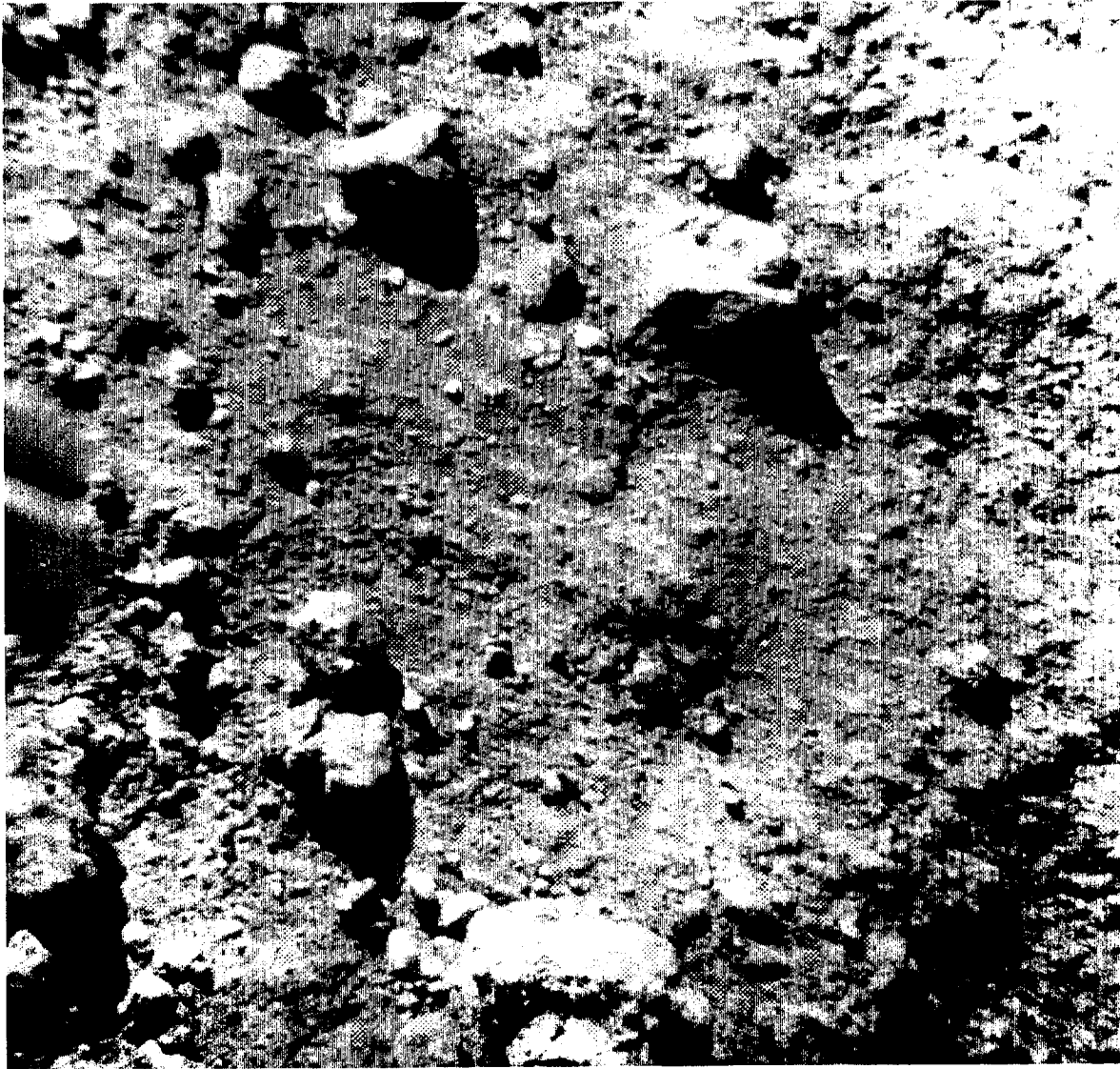
Fig. III-14. Mosaic of two wide-angle pictures showing footpad 2 and the trench it dug when the spacecraft slid down the inner slope of the crater. The trench is about 1 m long and 3 to 10 cm deep (Day 258, 03:24:59 and 03:40:28 GMT).



Fig. III-15. Wide-angle picture of the lunar surface just below the television camera showing tracks made by lunar fragments set in motion downslope during landing of the spacecraft on the moon. White bar and dark area at the bottom of the picture are parts of the camera (Day 254, 23:52:53 GMT).

(Fig. III-16). These grooves probably were formed primarily by the sliding and rolling of loose fragments ranging in size from a few millimeters to a few centimeters across (Fig. III-17a and b). Many loose fragments ejected during the landing of the spacecraft were moved again during the firing of the vernier engines.

Many types of fragments are revealed in the pictures of the debris dislodged by the spacecraft and also in pictures of the undisturbed surface. In the debris in front of footpad 2 (Fig. III-18) are: (1) bright, angular fragments, which are inferred to be pieces of dense rocky material; (2) dark, rounded objects, which are probably aggregates of very fine-grained particles; and (3) dark, lumpy objects, which appear to be aggregates of aggregates. The aggregate character of some of the loose, ejected fragments is well demonstrated by the presence of bright, angular chips set in a dark, fine-grained matrix (Fig. III-19a and b). The surface texture of one fragment several centimeters across, originally lying on the southeast wall of the crater (Fig. III-19c), suggests that it too is composed in part of resolvable pieces and chips, each a few millimeters across. Its surface is marked by numerous small, angular protuberances and indentations. Similar, but slightly more rounded, protuberances 1 to 3 mm across were observed on a dark, rounded object exposed in the wall of the trench dug by footpad 2 (Fig. III-19d).



**Fig. III-16. Area V-C: a small area on the floor of the Surveyor V crater strewn with fragments scattered by the spacecraft as it landed. Part of the surface has a swept appearance produced by the rolling and sliding of particles set in motion by the exhaust from one of the vernier engines. Smallest fragments resolved are about 1 mm across, and the largest fragments are about 3 cm across (Day 264, 12:22:43).**

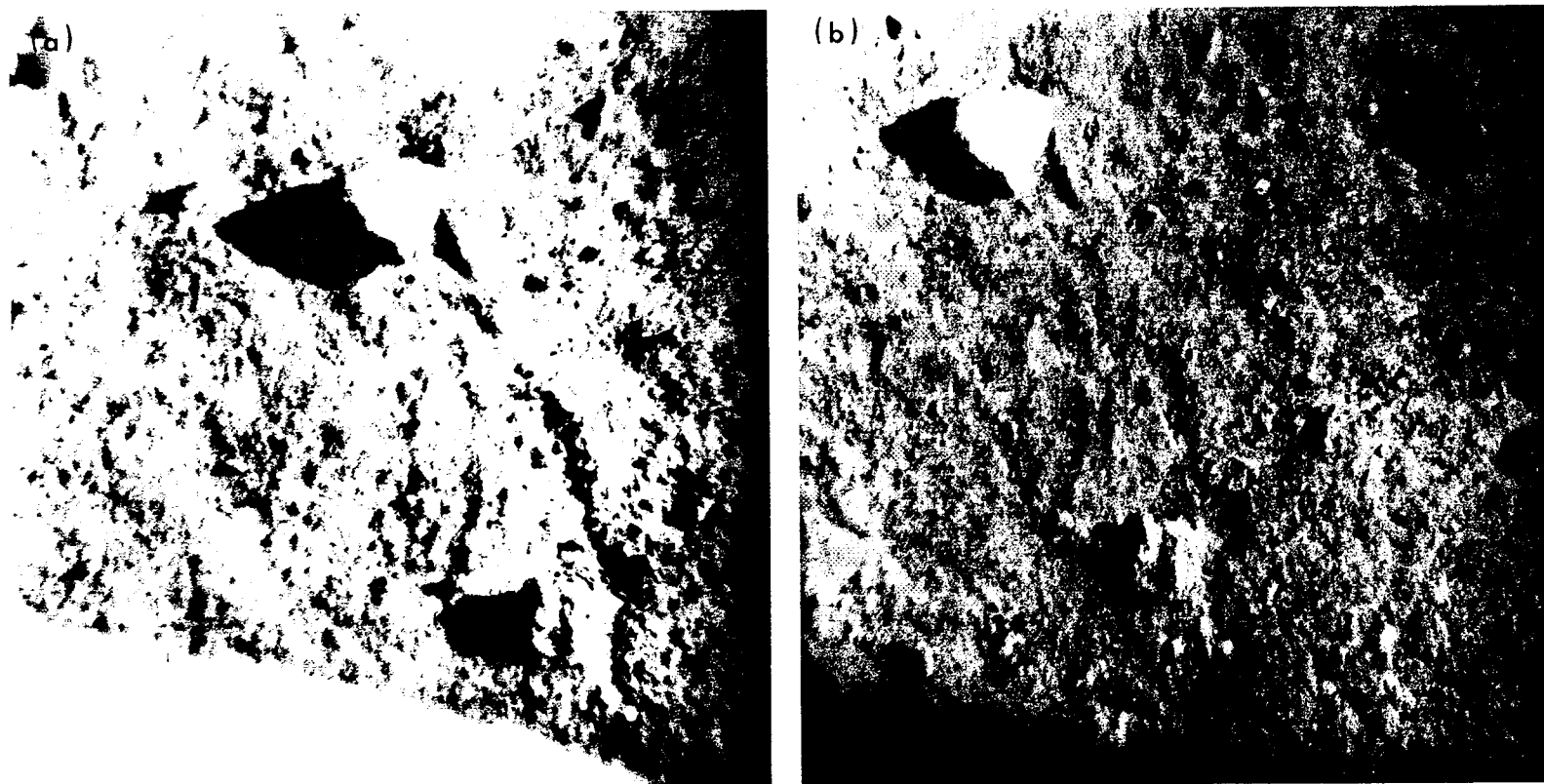
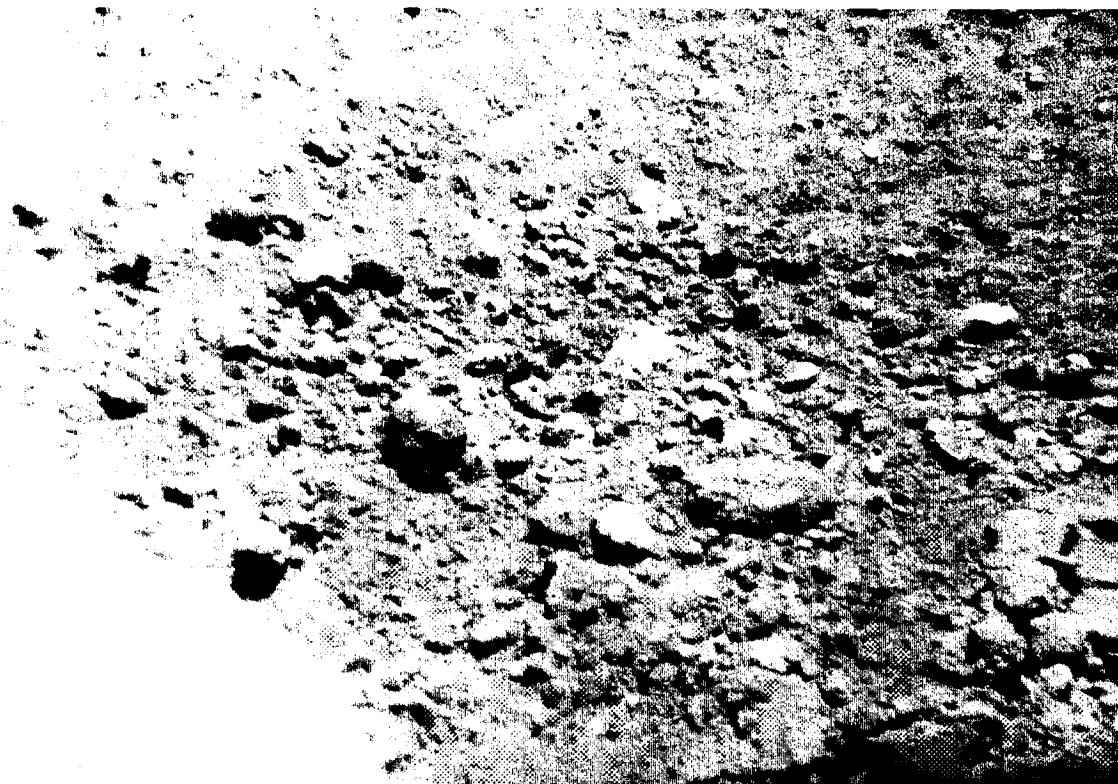


Fig. III-17. A small area on the lunar surface about 2 m from the spacecraft, in which loose fragments moved during the firing of the vernier engines. (a) Picture taken approximately 24 hr before firing of the vernier engines. A fragment approximately 3 cm wide was disturbed by Surveyor V during landing and rolled and bounced across the lunar surface, leaving a track which can be seen near the center of the picture (Day 255, 06:07:26 GMT). (b) Picture of the same area approximately 24 hr after firing of the vernier engines. A comparison with (a) shows that, while some of the larger fragments and lumps have not moved, most of the finer fragments have shifted positions (Day 257, 08:21:19 GMT).



**Fig. III-18. Area V-A: an area used to determine size-frequency distribution of fragmental material thrown onto the lunar surface in front of footpad 2 during landing. Most of the fragments are aggregates of fine particles. The bright fragments probably are pieces of coherent rock. Some dark, lumpy objects may be aggregates of aggregates. Smallest fragments resolved in this picture are about 1 mm across, and the largest fragments are about 3 cm across (Day 258, 08:40:04 GMT).**



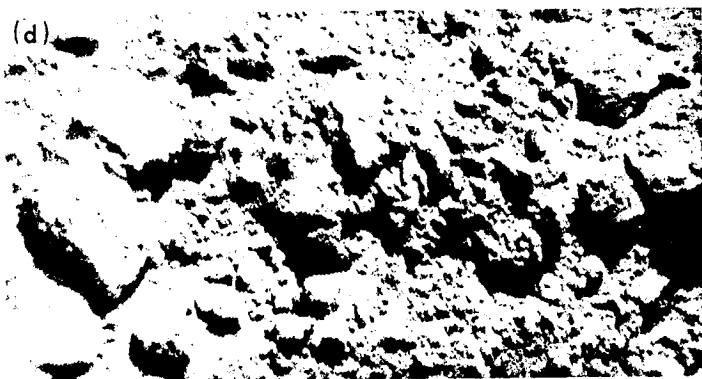
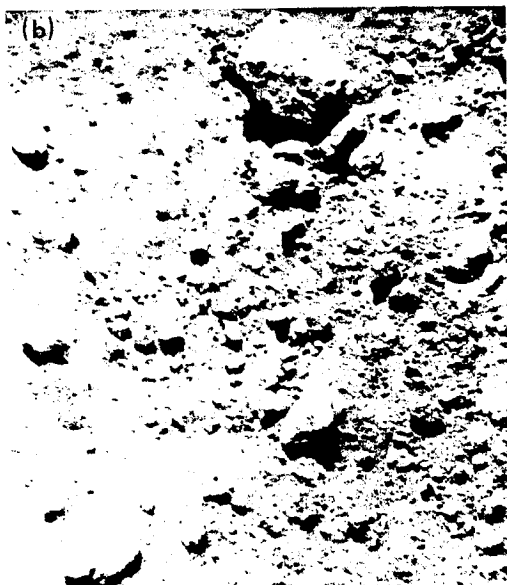
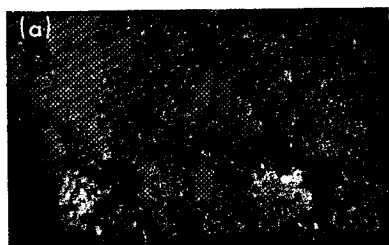


Fig. III-19. Narrow-angle pictures showing various types of aggregate fragments observed in the Surveyor V crater. (a) Two fragments, each about 2 cm across, ejected during landing. Bright spots with angular outlines on these fragments are probably tiny, bright rock fragments embedded in a very dark, fine-grained matrix (Day 264, 11:47:56 GMT). (b) Fragments ejected from trench made by footpad 2 during landing. Angular fragment at top of picture, which is about 4 cm long, has bright and light gray spots, which may represent rocky chips and compacted aggregates of fine-grained particles. The whole fragment appears to be a complex aggregate composed of rock chips and smaller aggregates (Day 258, 01:41:27 GMT). (c) Fragment 10 cm across lying on southeast wall of Surveyor V crater. Surface of fragment exhibits numerous small, angular protuberances and indentations, which suggests it is a conglomerate or breccia composed of resolvable pieces and chips (Day 258, 08:33:13 GMT). (d) Wall of trench dug by footpad 2 during lunar landing. Largest, dark rounded object to left has rounded protuberances 1 to 3 mm across, each of which may be an aggregate of fine particles. The entire object appears to be an aggregate of smaller aggregates (Day 258, 08:39:28 GMT).

Material exposed in this trench is closely similar to the rubble or debris exposed in many of the small craters (a few tens of centimeters across) that dot the walls and floor of the *Surveyor V* crater (Fig. III-20). Most of the debris appears to consist of clods or aggregates of fine particles; however, some appear to be complex aggregates or individual, bright, angular pieces of rocky material.

New photometric evidence obtained from the *Surveyor V* pictures shows that the bright, angular fragments are denser or at least less porous than the dark, fine-grained surface material and dark aggregates. Figure III-21 illustrates a bright, angular fragment, about 12 cm across and 2 m from the camera, under two different angles of solar illumination. The shadow of one of the omnidirectional antennas on the spacecraft passed over this fragment during the lunar day, and we have referred to it as the "omni rock." In Fig. III-21a, this object is seen as it appeared in the late lunar morning at a small phase angle (angle between the vector from the object to the camera,

and the vector from the object to the sun). At this phase angle, most parts of the surface of the fragment are slightly brighter than the surrounding fine-grained debris. Some parts of the fragment, however, are covered with material that has nearly the same brightness as the nearby fine-grained debris. These covered parts of the fragment are depressions that appear to be partly filled with dark, very fine-grained material. In Fig. III-21b, the fragment is shown as it appeared in the late lunar afternoon at a large phase angle. Here the exposed surfaces of the fragment are much brighter than the surrounding fine-grained debris and much brighter than the fine-grained material in the depressions on its surface. The difference in contrast in the two pictures is due to differences in the photometric function of the fine-grained debris and the photometric function of the surface of the angular fragment. Much more light is scattered from the surface of the angular fragment at large phase angles than from the dark, fine-grained material, whereas the luminance of the angular fragment and the fine-grained debris is more



**Fig. III-20.** Narrow-angle picture showing fragments in small crater on the north wall of the *Surveyor V* crater. The small crater is lined with fragments similar to those exposed in the trench dug by footpad 2 during landing. Most of the fragments are aggregates of fine particles; complex aggregates and individual, bright, rocky chips also appear to be present (Day 264, 12:12:24 GMT).



Fig. III-21. Two narrow-angle pictures showing an angular fragment 12 cm across lying 2 m from the television camera on the floor of the Surveyor V crater. (a) Picture taken in late lunar morning. Exposed parts of fragment are slightly brighter than surrounding surface debris. Parts of the fragment covered with fine-grained debris appear as slightly darker patches (Day 257, 02:47:27 GMT). (b) Picture taken in late lunar afternoon. The exposed parts of the fragment are conspicuously brighter than the surrounding fine-grained debris on the lunar surface and also brighter than the small patches of debris lying in depressions on the upper surface of the fragment (Day 264, 04:22:25 GMT).

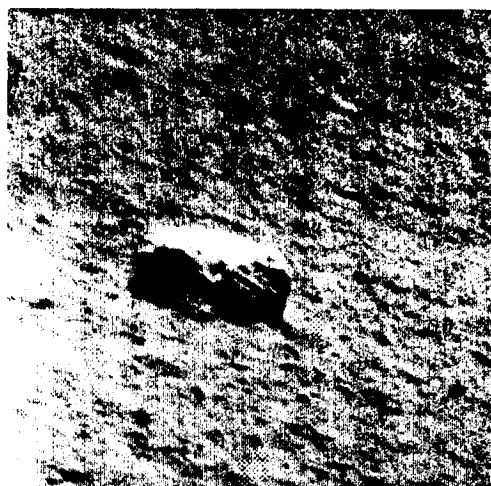


**Fig. III-22. Angular block 11 cm in diameter on the east rim of the Surveyor V crater. The nearly level, upper surface of this block is much brighter at large phase angles than the surrounding fine-grained debris (Day 258, 08:44:16 GMT).**



**Fig. III-23. Rounded, broken fragment lying in the trench dug by footpad 2. This fragment appears to have rolled into the upper end of the trench soon after it was formed. It is conspicuously bright at large phase angles compared with the surrounding dark clods and rubble (Day 258, 08:30:02 GMT).**

nearly equal at small phase angles. This indicates that the surface of the fragment is more like a lambertian scattering surface than is the dark, fine-grained surface material. It is, therefore, less porous or less rough at a scale below the resolution of the television pictures.

Many other bright, angular objects in the field of view around *Surveyor V* show photometric properties similar to that observed for the "omni rock." The top of an angular block, about 11 cm across and 6 m from the camera, is seen to be much brighter at large phase angles than the nearly parallel surface of the fine-grained debris surrounding the block (Fig. III-22). A bright, rounded object, which rolled into the head of the trench formed by footpad 2 (Fig. III-23), was also conspicuously bright at large phase angles compared with the surrounding dark clods and rubble. This object may have been partly broken by the impact of footpad 2 before rolling into the trench and, if so, some of the surfaces observed may have been freshly formed. It may be inferred that all bright objects, which exhibit a photometric function more like that of a lambertian surface than like most other parts of the lunar surface, are relatively dense, coherent material. Probably they are either rocks or compacted aggregates of fine particles whose mechanical properties are similar to those of rocks. Some such compacted aggregates may have been formed by shock compression during impact cratering.

The blocks on the raised rims of some of the larger craters in the middle distance are too numerous for all of them to have been formed by shock compaction of weakly coherent, fine-grained fragmental material. Impact experiments in weakly coherent, target materials show that the amount of rocky material produced by shock compression is a small fraction of the total debris ejected from the impact craters, and the rocky pieces so formed are small compared with blocks ejected from craters of comparable size formed in targets of coherent rock.<sup>1</sup> It is highly probable that the blocky fragments in the strewn fields around the raised-rim craters north and south of

the spacecraft are derived from a rocky substratum that underlies the surface debris layer.

Blocks in the strewn field south of the spacecraft are close enough to be observed in some detail in the narrow-angle, high-resolution *Surveyor V* pictures (Fig. III-24a and b). They are angular to subrounded, and generally do not exceed 25 to 50 cm in maximum observable dimension. At low phase angles, they appear slightly brighter than the surrounding fine-grained debris on the lunar surface (Fig. III-24b), and some of them are distinctly mottled with irregular, bright spots 1 to 2 cm across. In this respect, these fragments resemble a mottled angular-to-subrounded block 50 cm across that was observed near *Surveyor I*, over 1000 km to the west of the *Surveyor V* landing site (Ref. III-1). This widespread distribution of mottled rocks suggests they may be an important lithologic component of the maria.

*Surveyor V* pictures show two fragments of unique appearance that may once have been melted or partially melted by shock. One fragment, on the wall of the *Surveyor V* crater just above the trench formed by footpad 2, is about 3 cm long and irregular to knobby in shape. A picture of it taken in the late lunar morning (Fig. III-25) suggests that its upper surface is partly specular. Various parts of the fragment are either much brighter or much darker than the surrounding fine-grained debris.

The other fragment is about 1 cm long and was deposited on the floor of the *Surveyor V* crater during the firing of the vernier engines. This fragment is exceedingly ragged in outline and appears to be pierced by holes, as indicated by gaps in the shadow it casts (Fig. III-26). It is probably a natural object blown out of the crater wall by the vernier engine exhaust, but there is a possibility that it is simply an artifact created by the interaction of the rocket fuel or oxidizer or the exhaust with the lunar surface material. Both this object and the partly specular fragment may be comparable to shock-formed glasses and impactites shown in Fig. III-27. Specular surfaces and irregular shapes are common characteristics of impactites, and we suggest that these two unusual lunar fragments may be impactites.

<sup>1</sup>H. J. Moore, personal communication, based on observations of missile impact craters at the White Sands Missile Range, New Mexico.

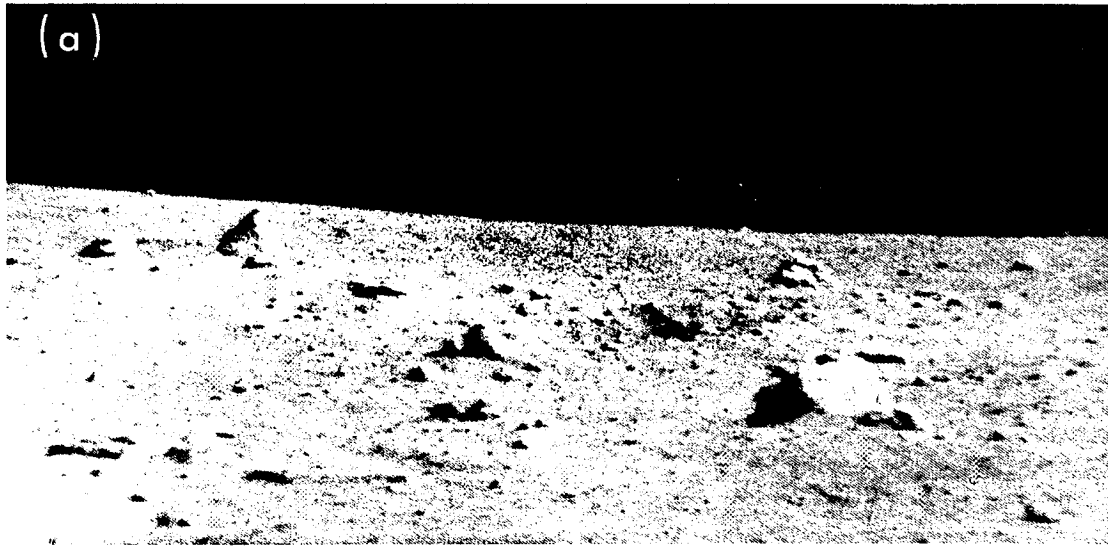


**Fig. III-24. Fragments in a strewn field of blocks south of the spacecraft. (a) Subrounded fragments lying 18 to 30 m from Surveyor V television camera. Largest fragment, which casts a small shadow, is 30 to 40 cm across. These are some of the largest fragments in the field of view around Surveyor V (Day 263, 07:38:46 GMT). (b) Mottled, subrounded fragments, largest of which is about 20 cm across, lying 5 to 6 m from Surveyor V television camera. These fragments exhibit bright spots 1 to 2 cm across, similar to those on one of the large rocks observed at the Surveyor I landing site (Day 264, 11:37:01 GMT).**

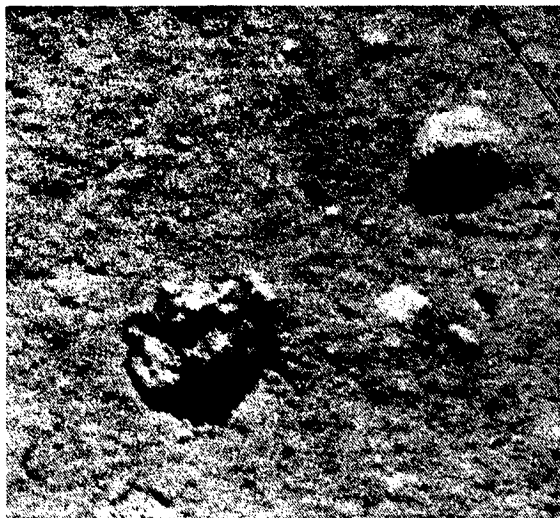


**Fig. III-25. Small, irregular fragment, about 3 cm across, close to spacecraft. Various parts of fragment are either much brighter or much darker than surrounding fine-grained debris, which suggests that this fragment is partly glassy. It resembles impactites from Meteor Crater, Arizona, and shock-melted ejecta from nuclear craters (see Fig. III-27; Day 258, 08:30:15 GMT).**

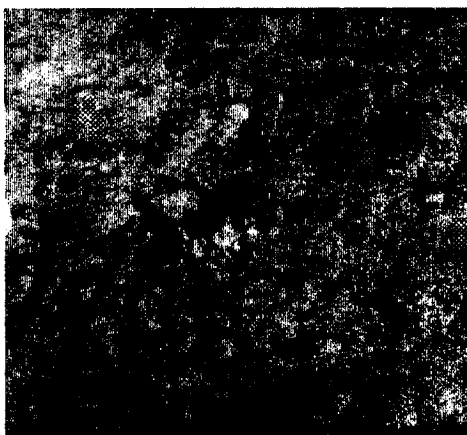


**Fig. III-26. Strange, ragged object on floor of Surveyor V crater; this object is about 1 cm across and apparently has holes through it. It arrived in its present position during or after firing of the spacecraft's three vernier engines. This object may be an impactite or it may be an artifact produced during engine firing (Day 257, 02:49:06 GMT).**

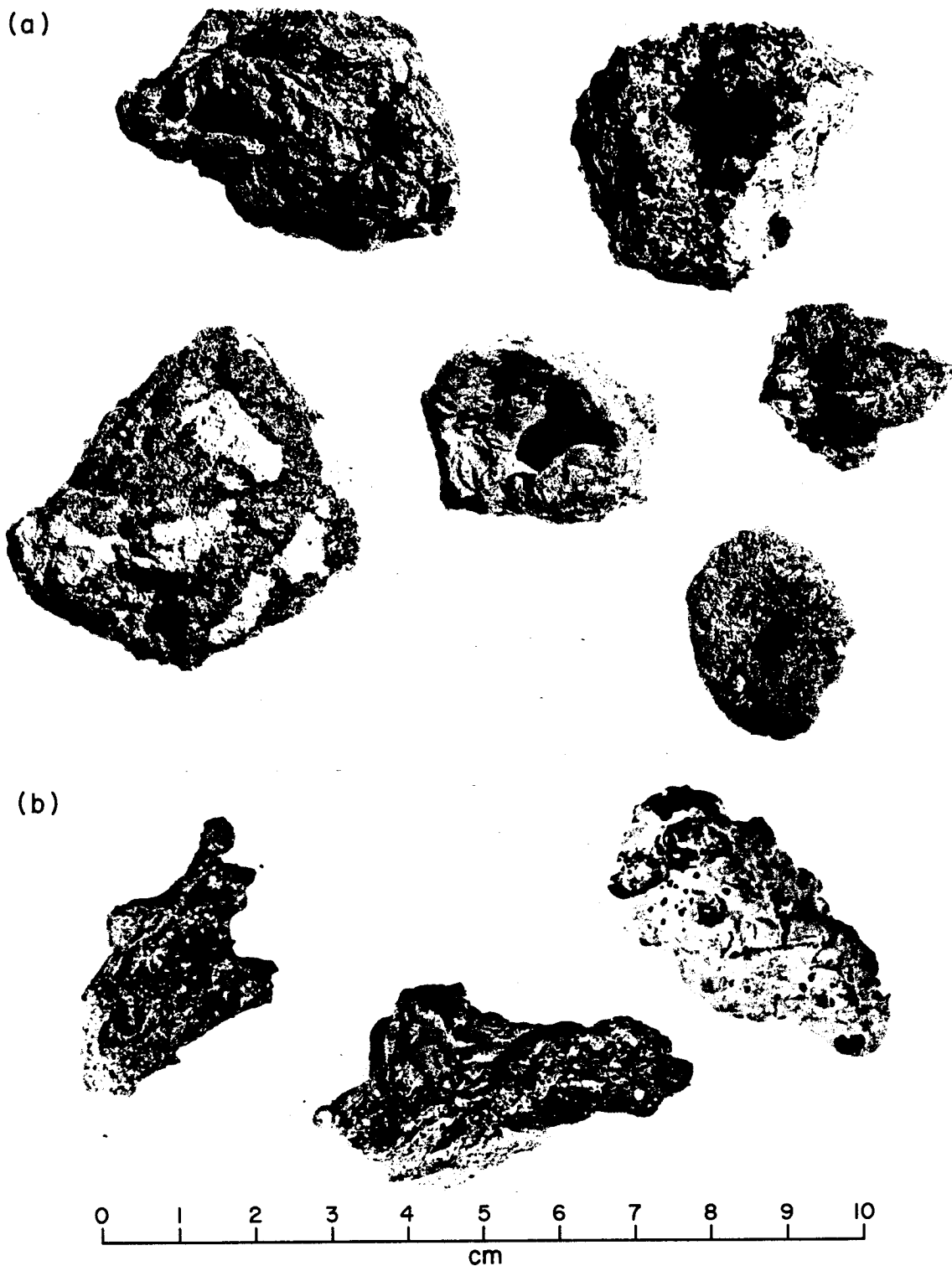
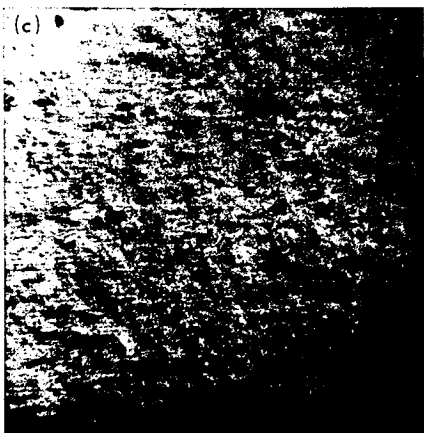
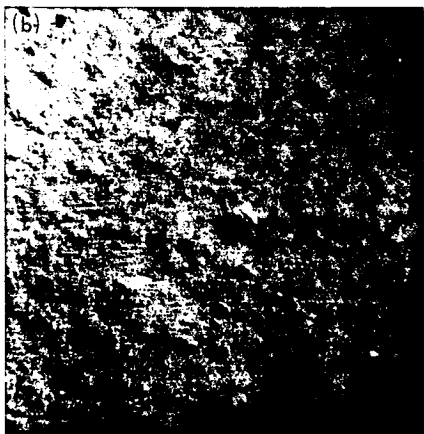
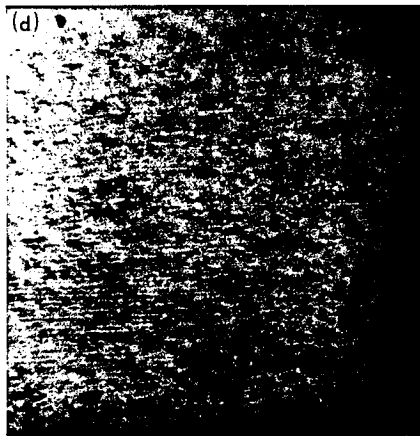


Fig. III-27. Terrestrial impactites and shock-melted ejecta. (a) Impactites from Meteor Crater, Arizona, formed from shock-melted Kaibab dolomite. (b) Shock-melted ejecta from the small nuclear crater, Teapot ESS, at the Nevada Test Site of the U.S. Atomic Energy Commission. These specimens are largely glass, derived from melted alluvium.





**Fig. III-28. Areas on the lunar surface near Surveyor V in which size-frequency distribution of fragments was measured. The location of these areas is shown in Fig. III-10. (a) Area V-B: on the floor of the Surveyor V crater. Smallest fragments resolved are about 1 mm across, and the largest fragments are about 4 to 5 cm across (Day 265, 12:15:52 GMT). (b) Area V-D: on the wall of the Surveyor V crater approximately 2.5 m from the spacecraft. Smallest fragments resolved are about 2 mm; the largest fragment is about 3 cm across (Day 257, 07:08:23 GMT). (c) Area V-E: on the wall of the Surveyor V crater about 2.4 m from the spacecraft. Smallest fragments resolved are about 1 mm, and the largest fragments are about 6 to 8 mm (Day 257, 07:08:44 GMT). (d) Area V-F: on the wall of the Surveyor V crater about 3 m from the spacecraft. Smallest fragments resolved are about 1 mm, and the largest fragments are about 1 cm (Day 257, 07:10:20 GMT). (e) Area V-G: on the wall of the Surveyor V crater about 3 m from the spacecraft. Smallest fragments resolved are about 2 mm, and the largest fragments are about 1 cm across (Day 264, 12:14:09 GMT). (f) Mosaic of narrow-angle pictures showing area V-H on the wall of the Surveyor V crater approximately 2 to 4 m from the spacecraft. Smallest fragments resolved are about 4 mm across, and the largest fragment is about 10 cm across (Day 257, 07:18:30 to 07:21:58 GMT).**

## F. Size-Frequency Distribution of Fragmental Debris

The size-frequency distribution of the fragmental debris was studied in eight sample areas (Fig. III-10) close to the spacecraft. One sample area (area V-A in Fig. III-10, and Fig. III-18), near footpad 2, is entirely in the loose material ejected in front of the footpad, and two sample areas (area V-B in Fig. III-10, Fig. III-28a, and area V-C

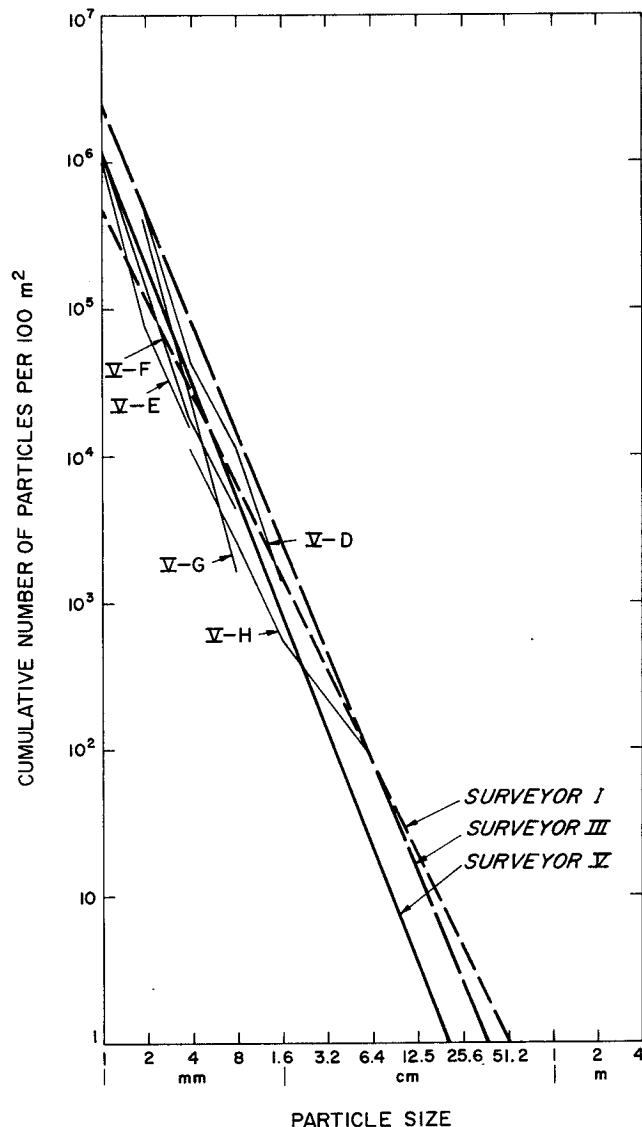


Fig. III-29. Size-frequency distribution of fragments on the undisturbed surface around Surveyor V (solid line) compared with the average size-frequency distribution of fragments at the Surveyor I and III landing sites (dashed lines).

in Fig. III-16) are on the floor of the Surveyor V crater between footpads 2 and 3. The other sample areas are on the undisturbed northeast and northwest walls of the crater (Fig. III-10 and Fig. III-28b through f). A total

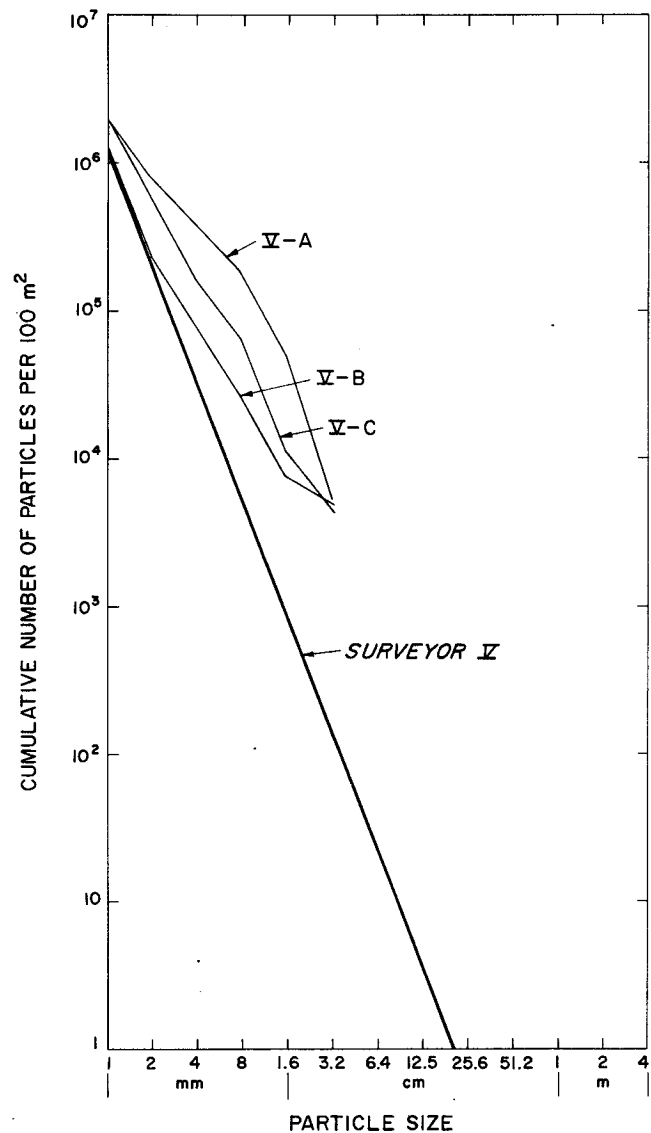


Fig. III-30. Size-frequency distribution of fragments in material disturbed by Surveyor V during landing (areas V-A to V-C) compared with the average size-frequency distribution of fragments on the undisturbed surface (heavy solid line). Area V-A is located in the ejecta around footpad 2. Areas V-B and V-C contain material which was kicked up by the footpads during landing, and which has cascaded down the wall of the Surveyor V crater and onto the floor of the crater near the spacecraft.

of 4602 fragments was counted, ranging in size from 1 mm to 6.4 cm.

The cumulative size-frequency distribution of fragments on the undisturbed surface, normalized to an area 100 m<sup>2</sup> for each of the sample areas, may be compared with the average size-frequency distribution of fragmental debris on undisturbed parts of the lunar surface at the *Surveyor I* and *III* landing sites (Fig. III-29). The size-frequency distribution of the fragmental material on the undisturbed walls of the *Surveyor V* crater is similar to that observed at the *Surveyor I* and *III* sites. Most of the size-frequency distribution curves for the debris on the wall of the *Surveyor V* crater have a slightly steeper slope, however, than the curves obtained for fragmental debris at the *Surveyor I* and *Surveyor III* sites (Refs. III-9 and III-10). Thus, there are fewer fragments larger than 6 cm per unit area around the *Surveyor V*

crater. This paucity of coarse fragments may be the result of two related factors:

- (1) A greater thickness of the fragmental debris layer at the *Surveyor V* landing site, compared with the *Surveyor I* and *III* landing sites.
- (2) A greater distance from *Surveyor V* to the nearest raised-rim craters with associated strewn fields of coarse blocks.

The size-frequency distribution of the lumpy, fragmental material kicked out on the surface by the footpads during landing is clearly much coarser than the particles observed on the undisturbed surface (Fig. III-30), as was the case at the *Surveyor I* landing site (Ref. III-1). The areas studied on the floor of the crater between footpads 2 and 3 (areas V-B and V-C in Fig. III-31) contain fragmental material not quite as coarse as the disturbed material around footpad 2 (area V-A in Fig. III-31). The ejected

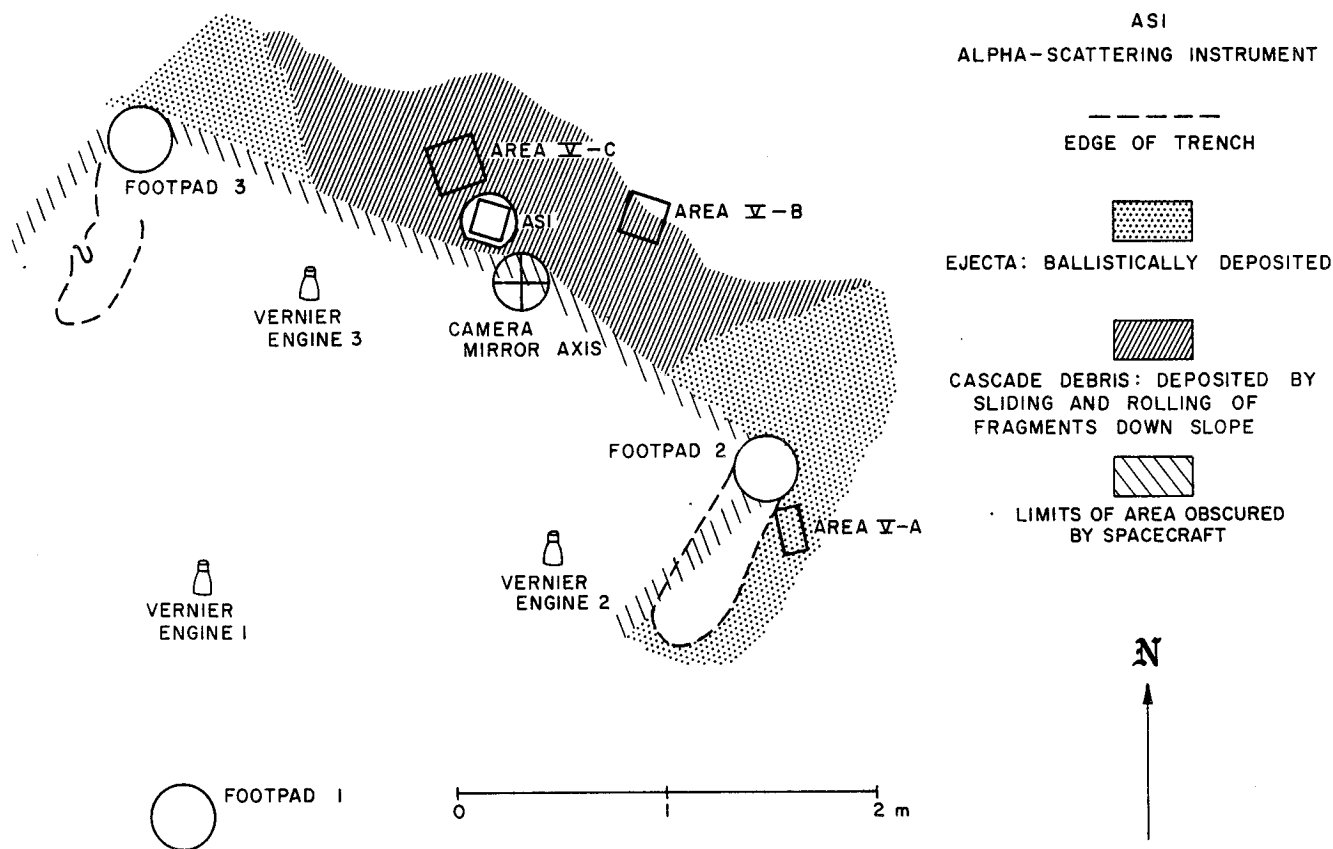


Fig. III-31. Location of areas V-A, V-B, and V-C within the material disturbed by *Surveyor V* during landing. The size-frequency distribution of the particles within these areas (Fig. III-30) was obtained from pictures taken after the firing of the vernier engines 53 hr after landing. Many of the smaller particles were moved a second time during the firing of the engines.

material around the footpads and on the floor of the crater is interpreted to consist primarily of clods or aggregates of fine-grained material. Most of the clods are irregular to rounded in shape, and their albedo is similar to, or slightly lower than, the surrounding undisturbed surface material. The material between footpads 2 and 3 was probably ejected by footpad 1 and has cascaded down the wall of the crater and out onto the floor. The finer particles have been strewn downslope, and the larger particles have tended to roll to the base of the slope and accumulate there. The difference in the size-frequency distribution of areas V-A, V-B, and V-C is interpreted to be due to a sorting effect as the material kicked out by footpad 1 cascaded downslope.

A study of the fragmental material in the *Surveyor V* crater has shown that many of the fragments, up to a few centimeters grain size, are aggregates of finer particles. Almost certainly, many of the small fragments and grains counted on the wall of the crater in the study of the size-frequency distribution of fragments are aggregates. This probably accounts for the large number of particles in the size range of a few millimeters observed on the wall and for the steepness of size-frequency distribution curves. Many aggregates probably were also included in the counts of small particles at the landing site of *Surveyor III*, but we believe that most of the small particles counted at the *Surveyor I* landing site are individual rocky chips. Care was taken in the study of the fragmental debris at the *Surveyor I* landing site to count only bright, angular objects. Nearly all the fragments larger than a few centimeters, which were counted at all three *Surveyor* landing sites, are believed to consist of fairly dense, rocky material.

## G. Photometric Observations

Preliminary photometric measurements have been made of the undisturbed lunar surface, disturbed material, and parts of the trench formed by footpad 2 during landing.

Reduction of 16 photometric measurements of the undisturbed lunar surface near the spacecraft indicates that the photometric function of this site is similar to that observed at the *Surveyor I* and *III* landing sites. The estimated normal albedo (normal luminance factor) of undisturbed parts of the lunar surface near the spacecraft is  $7.9 \pm 1.0\%$ . Telescopic photometric measurements of the normal albedo of an area several kilometers in diameter around the landing site<sup>2</sup> averaged about 9.4%. Apparently,

*Surveyor V* landed in a dark spot or patch within a relatively bright area. This bright area is part of the ray system of Theophilus, and the dark patch may simply be a gap in the ray.

The debris kicked out on the floor of the *Surveyor V* crater in front of the footpads has a photometric function similar to that of the undisturbed material, but is slightly darker (Fig. III-32). The normal albedo of this material is estimated to be  $7.5 \pm 1.0\%$ , about one-twentieth lower than that of the undisturbed surface. Dark, rubbly material exposed in the wall of the footpad 2 trench also has a normal albedo about one-twentieth lower than the undisturbed surface. Although the contrast in albedo between the ejected debris and the undisturbed surface is less than that observed at the *Surveyor I* and *III* sites (Refs. III-9 and III-10), the albedo of the dark, ejected material is nearly the same at the *Surveyor III* and *V* sites (Ref. III-10).

Parts of the floor and walls of the trench formed by footpad 2 have been smoothed by the pressure and sliding of the footpad (Fig. III-14). As observed in the footpad imprints at the *Surveyor III* landing site (Ref. III-10), these smoothed surfaces are brighter than the undisturbed parts of the lunar surface at certain phase angles. This effect is a result of the difference in photometric function between the rough, undisturbed surface and the smoothed surface. The smoothed floor of the trench is about 10% brighter than the undisturbed lunar surface in the mid-lunar morning, and a small part of this smoothed surface is about 20% brighter.

Both photometric targets on the spacecraft were illuminated during the middle of the lunar day (Days 257 through 263), which permitted a comparison to be made of photometric measurements of each chart. Luminance measurements of the photometric target on the spacecraft leg were consistently lower than measurements made of the omni-photometric target. The preflight calibration data indicated that the light-transfer characteristic determined from observation of each photometric target was nearly identical. We concluded, therefore, that the photometric properties of the photometric target on the spacecraft leg have changed between the time of preflight calibrations and the photometric observations on the moon.

The gray steps 5, 6, 7, 11, 12, and 13 of the photometric target on the spacecraft leg (Fig. III-33) showed an increase in reflectance from preflight calibration ranging

<sup>2</sup>H. A. Pohn and R. L. Wildey, personal communication.

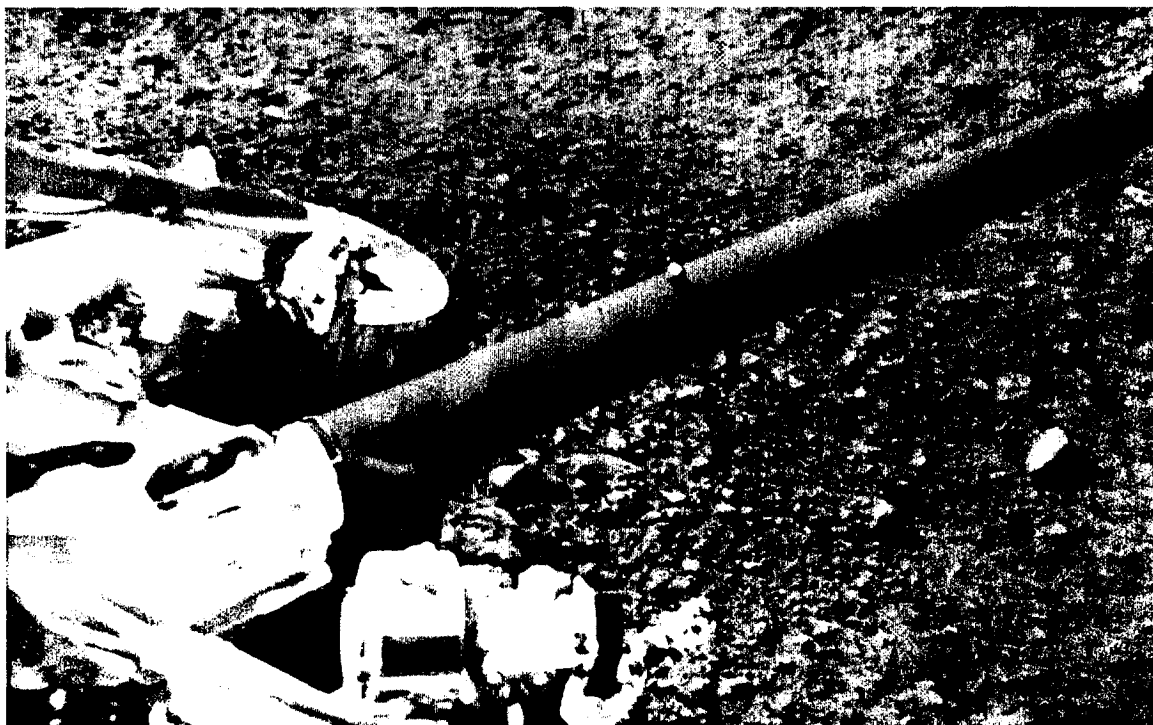


**Fig. III-32. Footpad 3 of Surveyor V spacecraft. Black, tubular object extending through the center of picture is the omnidirectional antenna boom. Dark, lumpy material extending to the right of the footpad is disturbed lunar surface material ejected in front of the footpad during landing (Day 263, 06:52:37 GMT).**

from 1.5 to 4.8%. The gray steps 8, 9, and 10 had a decrease in reflectance from preflight calibration varying from 11 to 18%. This change in gray step reflectance can be attributed to a very light coating of material having a normal albedo (normal radiance factor) between  $8 \pm 3\%$ . It is hoped that the error in this estimate can be reduced by more accurate measurements based on magnetic-tape records of the video signal.

The material coating the photometric target is too fine-grained to be resolved by the camera, indicating a grain size smaller than 0.3 mm. We believe this material consists of lunar particles because its normal albedo (normal radiance factor) is about the same as that of the undisturbed lunar surface material (about 8%). The target surface is rough in texture and inclined at 45 deg to the

lunar vertical, which would permit fine-grained material to adhere easily to the target.

The leg 2 photometric target was probably contaminated during landing by deposition of fine lunar material sprayed up by footpad 2 as it dug a trench while the spacecraft slid down the inner slope of the *Surveyor V* crater (Fig. III-34). Also, the firing of the vernier engines scattered some lunar material over the spacecraft, as indicated by material deposited on top of the compartments (Fig. III-35). It cannot be determined which event was more significant in coating the photometric target with lunar surface material, since the target was first observed under solar illumination nearly 22 hr after the vernier engine firing experiment.

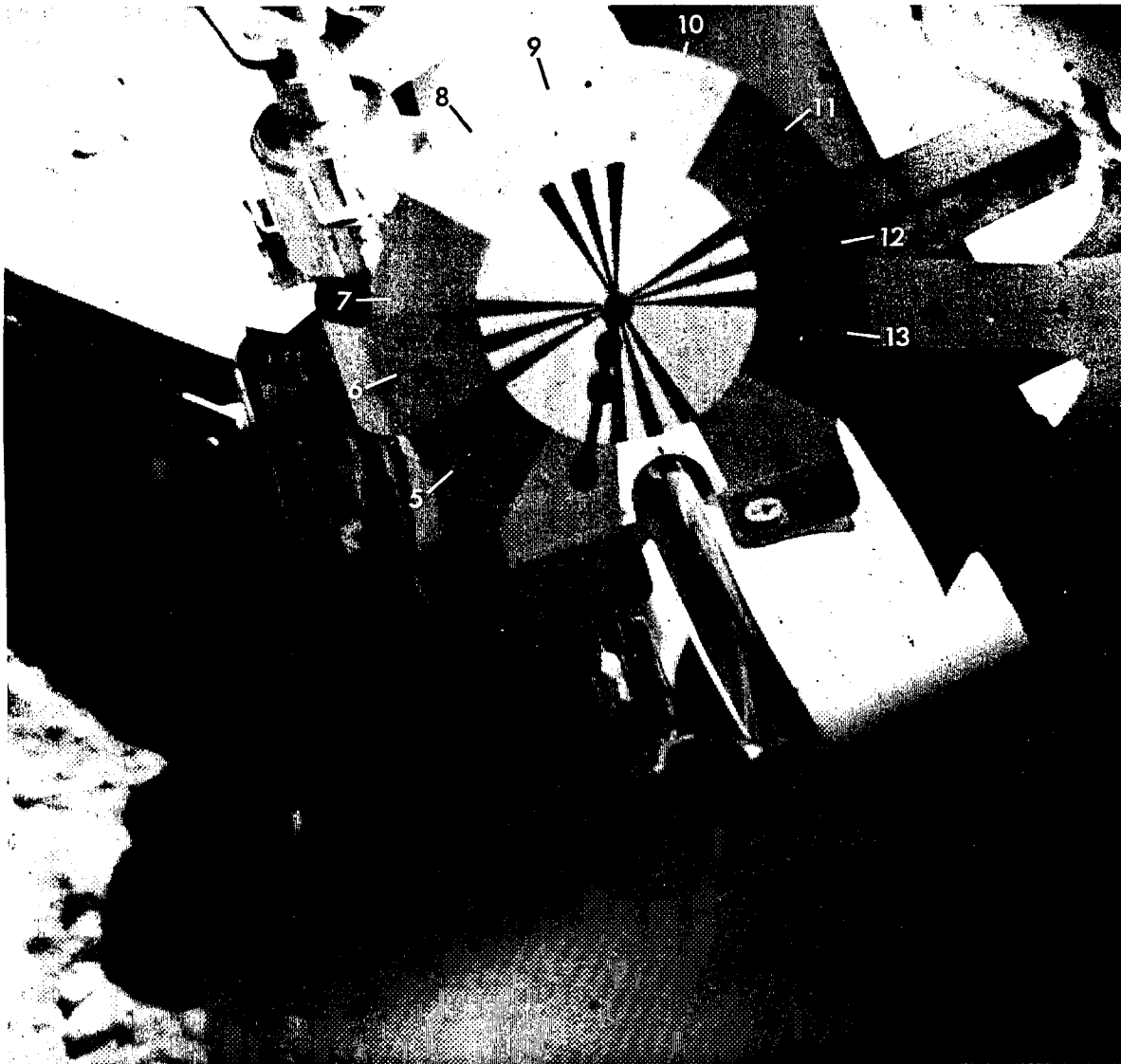


**Fig. III-33. Picture of the photometric target mounted on leg 2. The gray steps are indicated by numbers. A small pin protrudes from the center of the target, parallel to the camera line of sight, and casts a shadow downward across the target. The scattered, small dark spots across the photometric target are caused by dust within the camera's optical system and do not represent lunar material (Day 259, 04:36:25 GMT).**

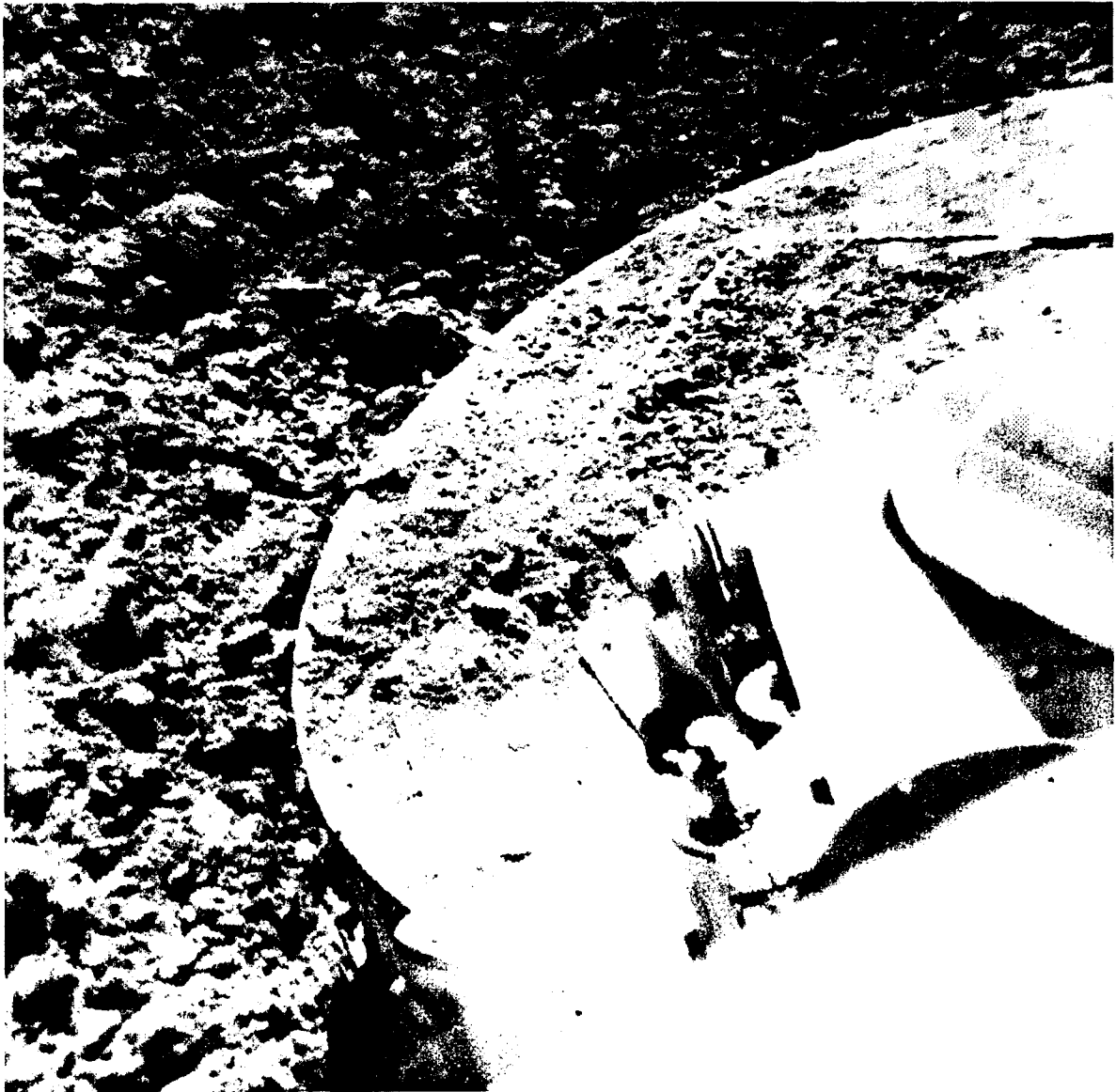


Fig. III-34. Narrow-angle picture of footpad 2. Lunar surface material was deposited on top of the footpad after landing as the spacecraft slid down the inside slope of the Surveyor V crater and dug a trench about 1 m long (Day 256, 06:22:49 GMT).



**Fig. III-35. Narrow-angle picture of part of the top of compartment B of the Surveyor V spacecraft showing small clod of lunar surface material, dislodged by the exhaust from the vernier engines during an erosion experiment 53 hr after landing. This material has impacted the top of the compartment and broken into very fine grains (Day 258, 04:31:24 GMT).**



## H. Interpretation of Geologic Observations

Several lines of evidence support the interpretation that the *Surveyor V* crater was formed by drainage of surficial fragmental debris into a subsurface fissure. The absence of a raised rim and the dimple shape of this crater suggest that it was not formed by impact, since experimental impact craters in this size range have raised rims and generally have profiles that are concave upward. The elongated shape and compound character of the *Surveyor V* crater, and the fact that it is a member of a chain of small craters, suggest that it has been localized by a linear subsurface structure. This suggestion is strengthened by the facts that the *Surveyor V* crater and the crater chain are aligned parallel with the major linear features of this region of the moon, and that there is a large number of similarly aligned, small craters and crater pairs in the vicinity.

The shapes of small craters in the vicinity of *Surveyor V* and the interaction of the spacecraft footpads with the lunar surface show that the near-surface material is composed of relatively fine-grained debris with very low cohesion. The mechanical properties of this debris are similar to the properties inferred for the lunar surface material at the *Surveyor I* and *III* landing sites (Refs. III-11 to III-13). The cohesion of the debris is sufficiently low that, if a cavity or fissure were opened beneath the debris, it would tend to flow or drain into the cavity, particularly if agitated by impact events or shaken by moonquakes.

As indicated by the size of the smallest craters with coarse, blocky rims in the area around *Surveyor V*, the thickness of the fragmental debris that might flow is several meters. Thus, it would be possible for a crater the size of the *Surveyor V* crater to be formed by the drainage mechanism. It is probably significant that the characteristic dimension of the aligned crater pairs and elongated craters in the vicinity of *Surveyor V* is about 10 m. If all of these craters have been formed by drainage, it suggests the thickness of the debris that flows is about 3 m, a result consistent with the evidence derived from craters with blocky rims. The small, concave floor of the *Surveyor V* crater probably was formed after most of the drainage had ceased. Small craters on the moon tend to fill up fairly rapidly with ballistically deposited debris produced by meteoritic bombardment.

The walls of the *Surveyor V* crater provide a natural exposure of material that originally lay at depths of as much as a meter beneath the surface of the debris layer. Much of this material appears to consist of clods or aggregates of fine particles. Many clods appear to be complex objects composed of smaller aggregate units and, in some cases, angular chips of rock. Observable differences in the photometric properties of various clods suggest that they vary in porosity or have been compacted to various degrees. Both the aggregates and complex aggregates probably have been formed by shock compression of finer fragmental material in the course of repetitive impact cratering.

A clearer picture of the subsurface structure of the lunar surface debris layer, or regolith, has thus emerged from our study of the *Surveyor V* television pictures. At depths below about 10 cm, the regolith is probably composed mainly of shock-compressed aggregates ranging from a few millimeters to 3 cm in diameter, set in a matrix of less coherent, finer particles. Rocky chips and fragments larger than a millimeter are dispersed as a subordinate constituent of the debris. Most fragments larger than 3 cm, however, are rocky material. Both the fragmentation and aggregation of the material in the debris are probably the direct results of prolonged meteoritic bombardment of the lunar surface.

It is important to recognize the complicated history of the lunar surface debris in evaluating the chemical analysis provided by the alpha-scattering instrument on *Surveyor V* (see Section VII of this Technical Report). The instrument was lowered from the spacecraft and came to rest on loose debris that had been kicked out on the wall of the *Surveyor V* crater during landing. This debris is composed mostly of aggregates of fine particles; the particles of which the aggregates are composed probably have been derived from a wide region on the lunar surface and transported ballistically to the site of the *Surveyor V* crater. The analysis does not, therefore, represent a single rock, but a mixture of rock particles, possibly of diverse origin. Most particles probably have not been transported more than a few kilometers, however, so that the analysis represents, for the most part, a mixture of rock particles derived from a small area on Mare Tranquillitatis.

## References

- III-1. Rennilson, J. J., et al., "Lunar Surface Topography," *Surveyor I Mission Report. Part II: Scientific Data and Results*, Technical Report 32-1023, pp. 1-44, Jet Propulsion Laboratory, Pasadena, Calif., September 10, 1966.
- III-2. Morris, E. C., and Wilhelms, D. E., Geologic Map of the Julius Caesar Quadrangle of the Moon, U.S. Geological Survey Misc. Geol. Inv. Map I-510, 1967.
- III-3. Wilhelms, D. E., and Morris, E. C., "Geology of the Julius Caesar and Mare Vaporum Quadrangles," *Astrogeologic Studies Annual Progress Report, July 1, 1965, to July 1, 1966. Part A: U.S. Geological Survey Open-File Report*, pp. 51-62, 1966.
- III-4. Kuiper, G. P., "Interpretation of Ranger VII Records," *Ranger VII. Part II: Experimenters' Analyses and Interpretations*, pp. 9-73, Technical Report 32-700, Jet Propulsion Laboratory, Pasadena, Calif., February 10, 1965.
- III-5. Urey, H. C., "Observations on the Ranger VII Pictures," *Ranger VII. Part II: Experimenters' Analyses and Interpretations*, Technical Report 32-700, pp. 135-148, Jet Propulsion Laboratory, Pasadena, Calif., February 10, 1965.
- III-6. Shoemaker, E. M., "Progress in the Analysis of the Fine Structure and Geology of the Lunar Surface From the Ranger VIII and IX Photographs," *Rangers VIII and IX. Part II: Experimenters' Analyses and Interpretations*, Technical Report 32-800, pp. 249-338, Jet Propulsion Laboratory, Pasadena, Calif., March 15, 1966.
- III-7. Moore, H. J., "Cohesion of Material on the Lunar Surface," *Rangers VIII and IX. Part II: Experimenters' Analyses and Interpretations*, Technical Report 32-800, pp. 263-270, Jet Propulsion Laboratory, Pasadena, Calif., March 15, 1966.
- III-8. Gault, D. E., et al., "Luna 9 Photograph; Evidence for a Fragmental Layer," *Science*, Vol. 153, No. 3739, pp. 985-988, August 26, 1966.
- III-9. Shoemaker, E. M., et al., "Surveyor I: Preliminary Results," *Science*, Vol. 152, No. 3730, pp. 1737-1750, June 24, 1966.
- III-10. Shoemaker, E. M., et al., "Television Observations From Surveyor III," *Surveyor III: a Preliminary Report*, Special Publication 146, pp. 9-60, National Aeronautics and Space Administration, Washington, D.C., 1967.
- III-11. Christensen, E. M., et al., "Lunar Surface Mechanical Properties," *Surveyor I Mission Report. Part II: Scientific Data and Results*, Technical Report 32-1023, pp. 69-84, Jet Propulsion Laboratory, Pasadena, Calif., September 10, 1966.
- III-12. Scott, R. F., Roberson, F. I., and Clary, M. C., "Soil Mechanics Surface Sampler: Lunar Surface Tests and Results," *Surveyor III: A Preliminary Report*, Special Publication 146, pp. 61-93, National Aeronautics and Space Administration, Washington, D.C., 1967.
- III-13. Christensen, E. M., et al., "Lunar Surface Mechanical Properties," *Surveyor III: A Preliminary Report*, Special Publication 146, pp. 94-120, National Aeronautics and Space Administration, Washington, D.C., 1967.

## IV. Lunar Surface Mechanical Properties

E. M. Christensen, S. A. Batterson, H. E. Benson, R. Choate, R. E. Hutton,  
L. D. Jaffe, R. H. Jones, H. Y. Ko, F. N. Schmidt, R. F. Scott,  
R. L. Spencer, and G. H. Sutton<sup>1</sup>

Information on mechanical properties<sup>2</sup> of the lunar surface was derived from data and observations associated with the *Surveyor V* lunar-landing mission. It is based primarily on studies of pictures showing the disturbances caused by the landing, and a comparison of pictures taken before and after firing of the vernier engines. Analyses and laboratory simulations have been conducted to assist in the interpretation of results.

*Surveyor V* landed on a sloping crater wall and slid downslope, with the footpads forming trenches, before reaching its final position. The vernier rocket engines were fired to test the effects of rocket engine exhaust upon the lunar surface. Studies of the landing, especially of the trenches formed during the slide and the effects created by the vernier engine firing, provided significant, additional knowledge of the lunar surface mechanical properties.

### A. Spacecraft Landing

#### 1. Description

The basic configuration and landing mechanism for *Surveyor V* were essentially the same as for *Surveyors I*

<sup>1</sup>In the brief time available to prepare this report, prior to the next *Surveyor* mission, it was impossible to obtain the concurrence of all the authors.

<sup>2</sup>In this section, centimeter-gram units are used. To convert to foot-pound units, the following factors apply: 1 m = 3.28 ft; 1 cm = 0.394 in.; 1 N (newton) = 10<sup>3</sup> dynes = 0.225 lb; 1 N/cm<sup>2</sup> = 1.45 lb/in.<sup>2</sup>.

and *III* (see Section I, Fig. I-1). During landing impact, the three landing legs rotate upward against the resistance of the shock absorbers. Following the initial impact, the shock absorbers re-extend, returning the legs to their pre-touchdown positions. Additional capability for energy dissipation is provided by crushable footpads and crushable honeycomb blocks mounted on the underside of the space-frame, inboard of each leg.

The actual landing of *Surveyor V* can be reconstructed quite accurately from various telemetry signals in connection with available landing-dynamic simulations. Pertinent telemetry data are:

- (1) Digital indications of spacecraft altitude; three orthogonal velocities; three orthogonal, angular positions; one accelerometer reading; and three vernier engine thrust commands.
- (2) Analog signals monitoring three strain-gage bridges, one on each landing leg shock absorber, indicating its axial loading.
- (3) Post-landing television camera coverage of footpads, crushable blocks, and areas on the lunar surface in which these spacecraft members contacted the surface and came to rest.
- (4) Post-landing attitude determinations based on the position of the planar array antenna, horizon sightings, and star sightings.

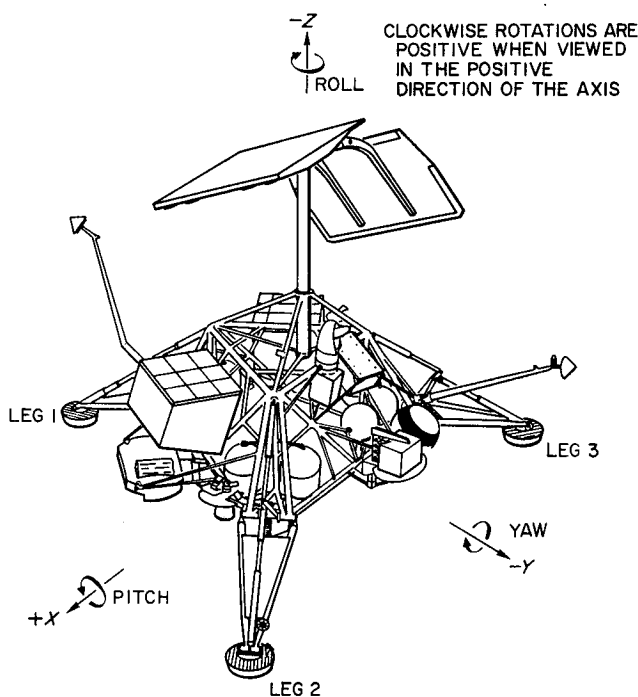


Fig. IV-1. Surveyor spacecraft configuration and coordinate system.

An evaluation of the data indicates the following sequence of events during final descent and landing. At an altitude of  $4.8 \pm 0.7$  m, all three vernier engines were cut off, resulting in a free-fall period, during which the spacecraft vertical velocity increased to  $4.2 \pm 0.4$  m/sec at the time leg 1, the first to contact, encountered the lunar surface. Slight angular motions were induced at cutoff of the vernier engines, increasing immediately before initial touchdown to a pitch of 0.7 deg/sec, a yaw of 0.5 deg/sec, and a roll of 0.4 deg/sec. (Pitch, yaw, and roll are rotations about the X, Y, and Z axes, respectively (Fig. IV-1). After leg 1 contact, a sudden negative pitch motion with a velocity in excess of 13 deg/sec occurred (range of pitch gyro was exceeded). Little angular motion in yaw and roll occurred until legs 2 and 3 contacted the ground almost simultaneously: leg 2, 190 msec and leg 3, 197 msec after leg 1 impact. A slideout period of approximately 1.7 sec followed, during which the spacecraft rolled approximately +5.9 deg with less than a +1-deg change in yaw.

Figure IV-2 shows the time histories of the axial forces in the landing-gear shock absorbers from prior to surface contact until after the spacecraft reached its final position. For each leg, the initial high loading, caused by the first impact, lasted approximately 0.2 to 0.25 sec. This was followed by a near-zero force period lasting approximately

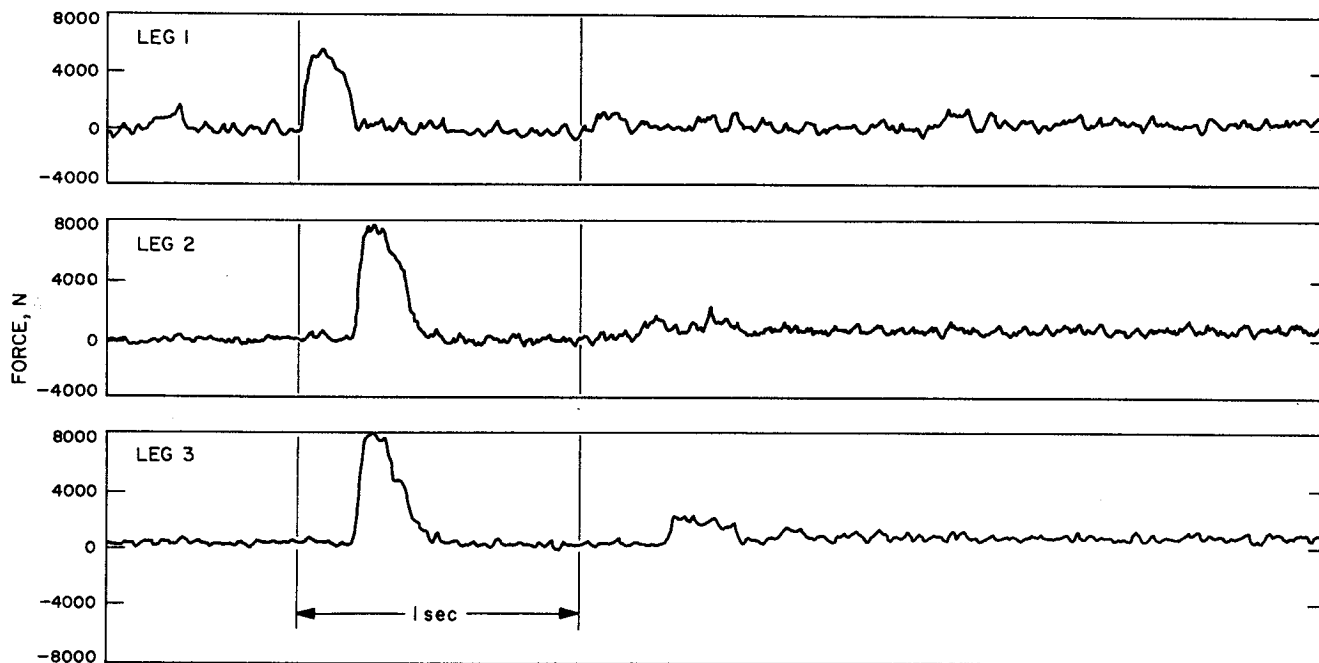


Fig. IV-2. Strain-gage telemetry data showing shock-absorber axial load histories during landing of Surveyor V.

0.6 to 0.8 sec, indicating a rebound of the spacecraft due to the landing-gear spring forces. Finally, a second low-energy impact was registered, followed by a poorly defined, low-amplitude oscillation. Similar oscillations, observed during the *Surveyor I* and *III* touchdowns, were related to the combined elastic properties of the spacecraft and the lunar surface (Refs. IV-1 and IV-2). Following the oscillations, the strain gages indicated a small loading, corresponding to the static loading of the shock absorbers, due to the 480-N lunar weight of the spacecraft. Table IV-1 gives the maximum force levels experienced by each shock absorber, and the impact times of each footpad.

The relative timing of the initial footpad impacts indicates that the spacecraft rotated approximately 17 deg between the footpad 1 impact and the footpad 2 and 3 impacts. The final angle between the roll axis and lunar vertical is about 19.5 deg. The final position of the space-

craft, following the slide (see Section III, Fig. III-7), suggests that the initial contact of footpad 1 occurred on the level, or gently sloping, surface just outside of the crater. Also, differences in final penetration of the footpads, a pre-touchdown 2.5-deg, off-vertical attitude of the spacecraft, or a combination of these factors could account for this angular deviation.

## 2. Television Observations of Spacecraft/Soil Interactions

*Surveyor V* landed on the inner slope of a 9- × 12-m crater. Following initial touchdown, it slid downslope creating clearly visible surface disturbances. The distance that footpad 2 slid was  $81 \pm 2$  cm, as indicated by an almost-straight trench shown in wide-angle pictures in Fig. IV-3. The trench, including footpad (diameter 30 cm), is 1.1 m long. The trench depth is estimated to be from 8 to 10 cm at the uphill end and from 3 to 6 cm at the downhill end. As shown in Fig. IV-3, the rim of the trench has crumbled, partially filling the trench and obscuring visibility of the bottom. The axis of the trench, i.e., the direction of the footpad motion, is estimated to have been parallel to the spacecraft Y axis within 2 deg (Fig. IV-1).

The composite images in Fig. IV-4 indicate the range of the spacecraft movement during the landing phase of *Surveyor V*. The two images represent the probable spacecraft position at the time of the first landing impact and the final position of the spacecraft.

**Table IV-1. Maximum shock-absorber forces and footpad impact times**

Leg assembly	Maximum shock-absorber force, N	Time of impact after initial contact, sec
1	$5620 \pm 350$	0
2	$7280 \pm 350$	0.190
3	$7300 \pm 350$	0.197

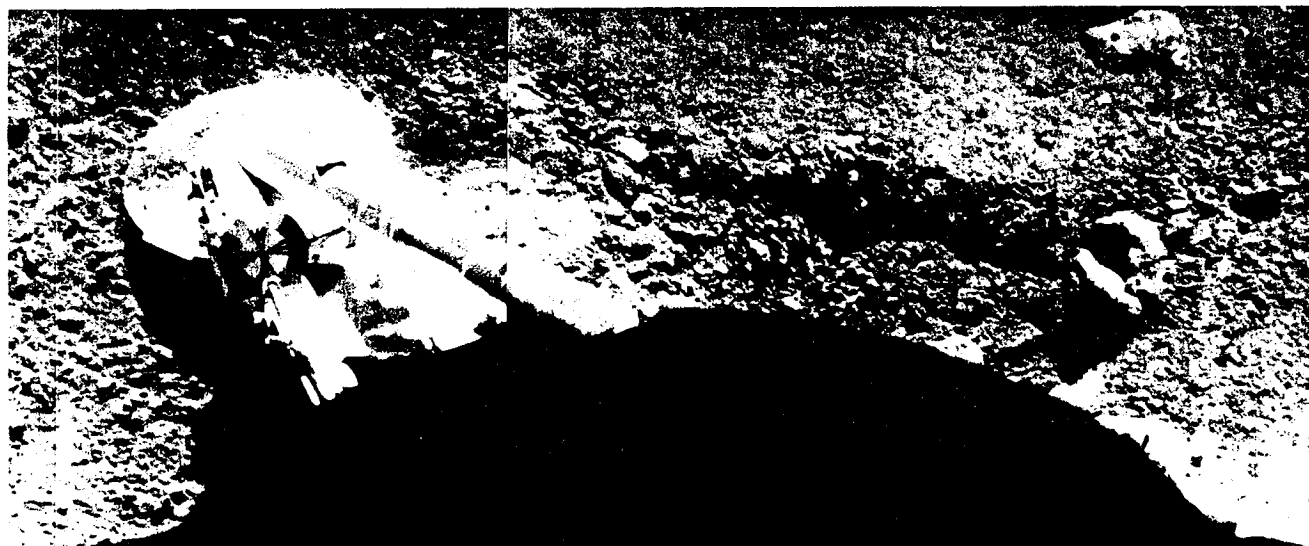


**Fig. IV-3. Wide-angle mosaic of footpad 2 and the trench formed during landing of *Surveyor V*. The depression formed during the first impact of footpad 2 can be seen at the right-hand end of the trench (Day 257, between 04:00 and 06:00 GMT; Catalog 5-MP-19).**

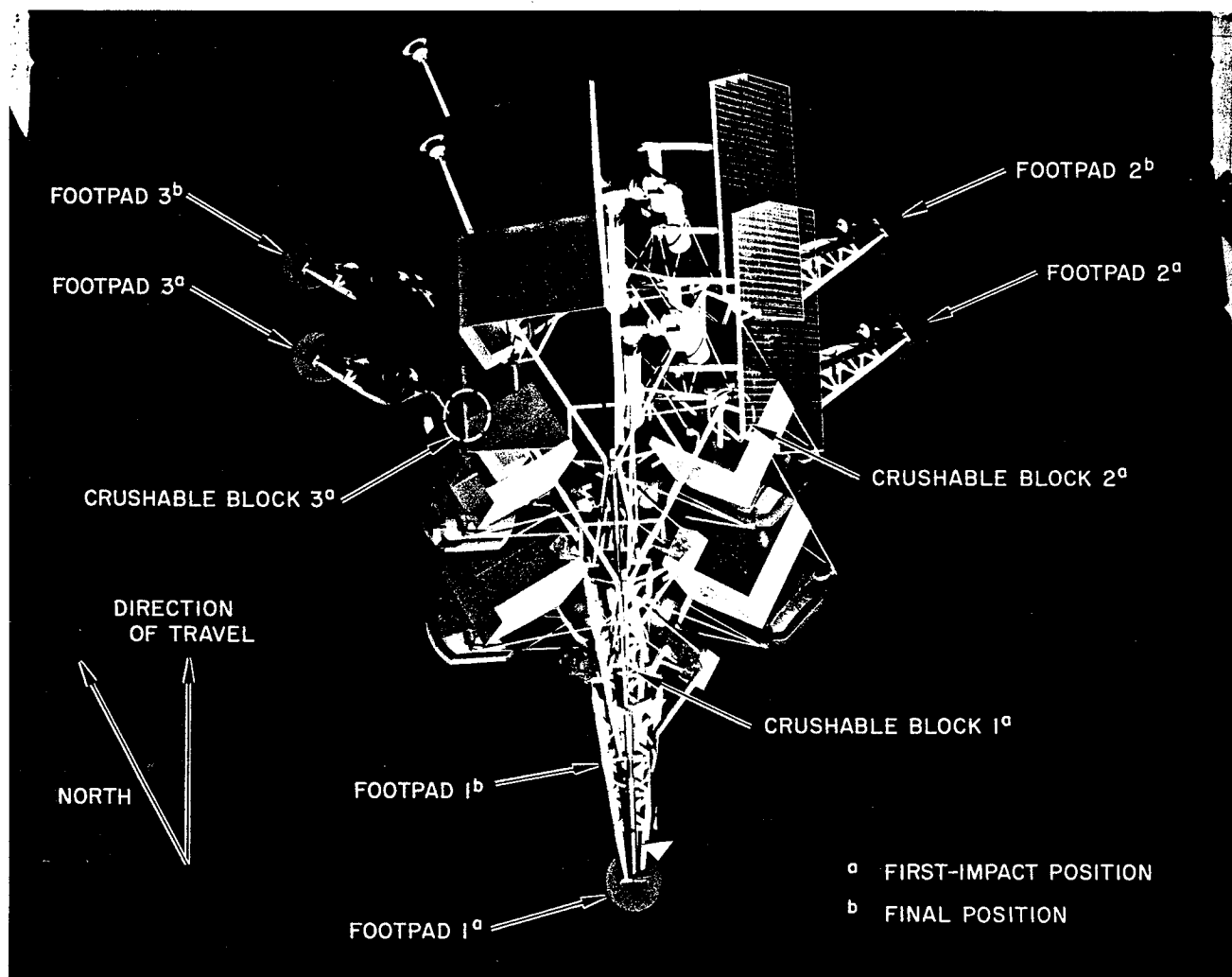


Fig. IV-4. Spacecraft motion during landing. (a) Probable spacecraft position at time of first landing impact. (b) Final position after the spacecraft had come to rest.

The depression caused by the first impact of footpad 2 can be seen at the right-hand end of the trench (Fig. IV-3); this feature can be seen more clearly in Fig. IV-5. A footpad penetration of 12 cm is estimated to have occurred here. The fragment in the center of the trench at the right-hand end is estimated to be 7 cm long and 5 cm high. The fragment visible to the right of the initial imprint is estimated to be approximately 12 cm in diameter. These fragments were used in determining the trench depth. Clear evidence of footpad-scraping action can be seen along the trench wall near the footpad (Fig. IV-6). The smooth appearance of this area indicates that the material consists primarily of very small-sized particles.

At impact, footpad 2, after possibly grazing the 12-cm-diameter fragment, penetrated the soil and ejected material for a distance up to 80 cm (Fig. IV-7). One fragment (apparently a soil clump), 6 cm long, remained intact after being thrown a minimum distance of 30 cm. In the subsequent downslope motion, footpad 2 displaced soil in the manner of a snowplow. The outer rim of the footpad

tipped downward as soil piled up in front of the footpad and was pushed and thrown forward and sideward. The ejected material beside the trench extends outward for approximately 30 cm; ejected material beyond footpad 2 extends for 75 cm along the direction of the spacecraft motion. Coarser fragments of this ejected material are shown in Fig. IV-8.

The movement of footpad 3 also caused some trenching during the landing and subsequent sliding motion. The visibility of this area to the television camera is partially obscured, but it appears that footpad 3 moved approximately the same distance as footpad 2. A part of the footpad 3 trench disturbance can be seen through the landing leg structure in Fig. IV-9. The pattern of large clumps and fine soil visible above and to the right of the footpad indicates the extent of material ejected by footpad 3. The material ejected from the surface by the *Surveyor V* footpads exhibits less contrast with the undisturbed surface than did the soil ejected by *Surveyors I* and *III*.

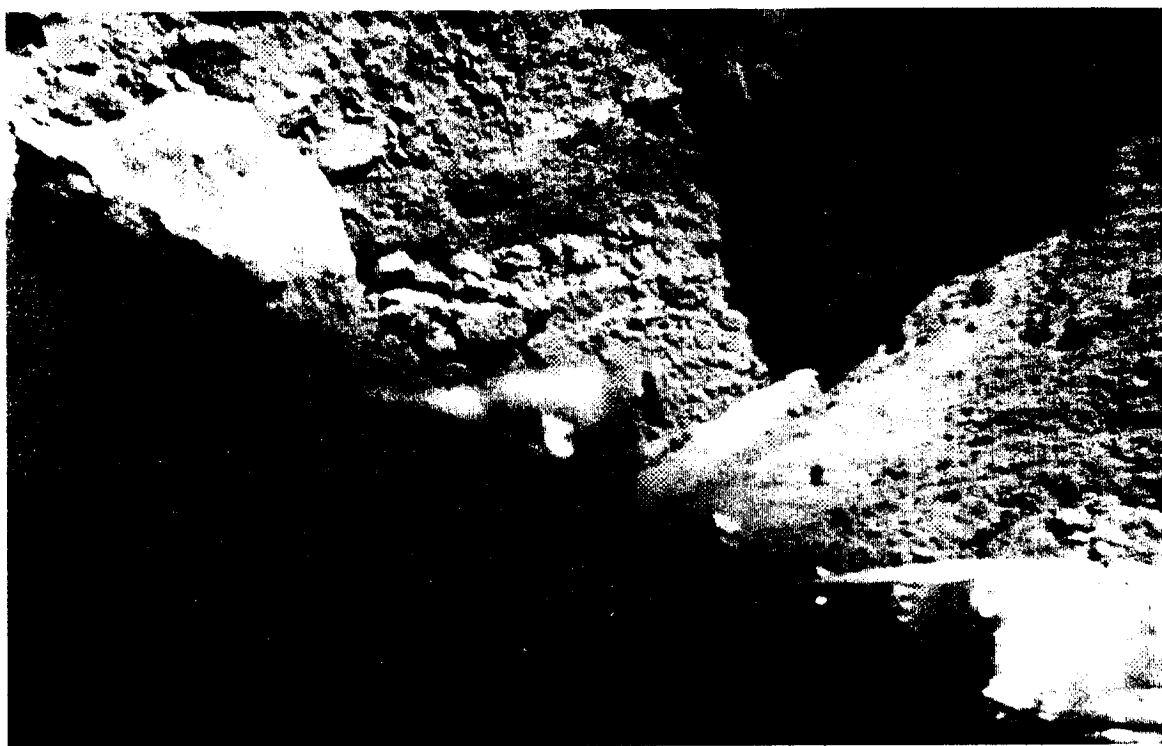


Fig. IV-5. Narrow-angle picture of the depression formed by the first landing impact of footpad 2 (Day 258, 08:29:44 GMT).



**Fig. IV-6. Narrow-angle picture showing detailed view of a part of the trench wall formed by the scraping action of footpad 2 (Day 257, 04:42:06 GMT).**



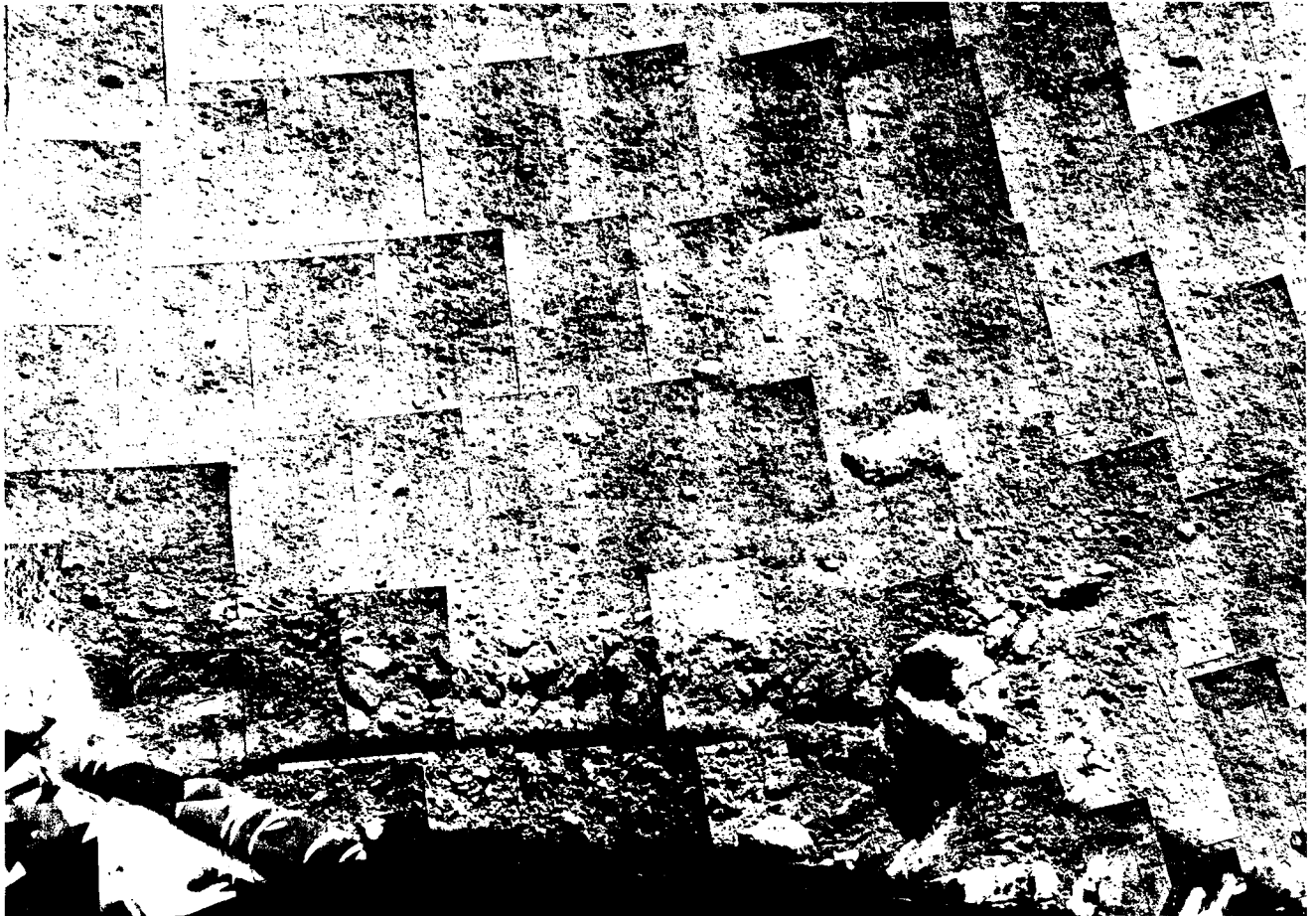


Fig. IV-7. Narrow-angle mosaic showing the trench formed by footpad 2 during the spacecraft landing (Day 258, about 08:00 GMT; Catalog 5-MP-34).

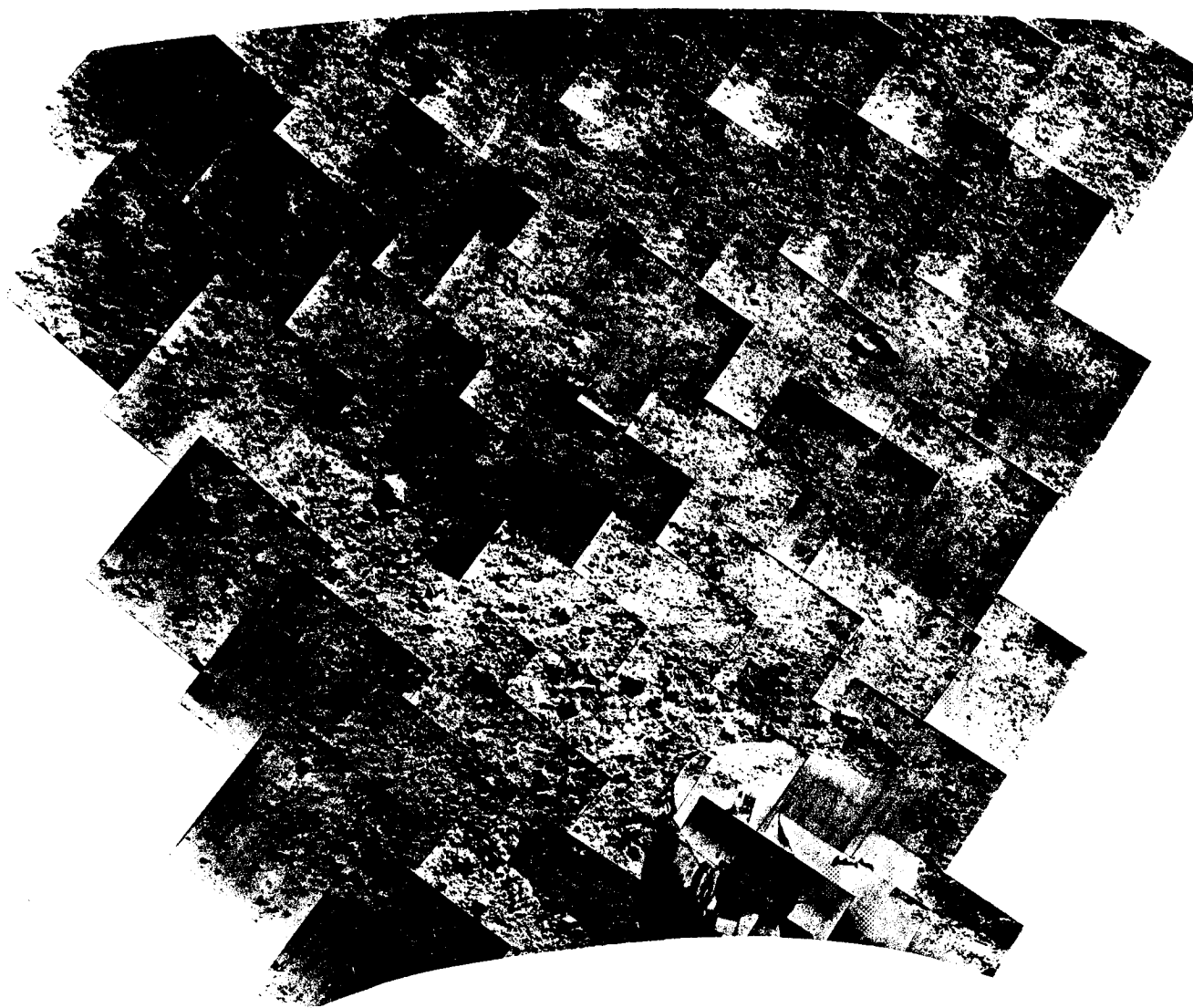


Fig. IV-8. Narrow-angle mosaic of footpad 2 and some of the lunar material ejected during the landing and the formation of the trench (Day 255, about 10:11 GMT; Catalog 5-MP-26).

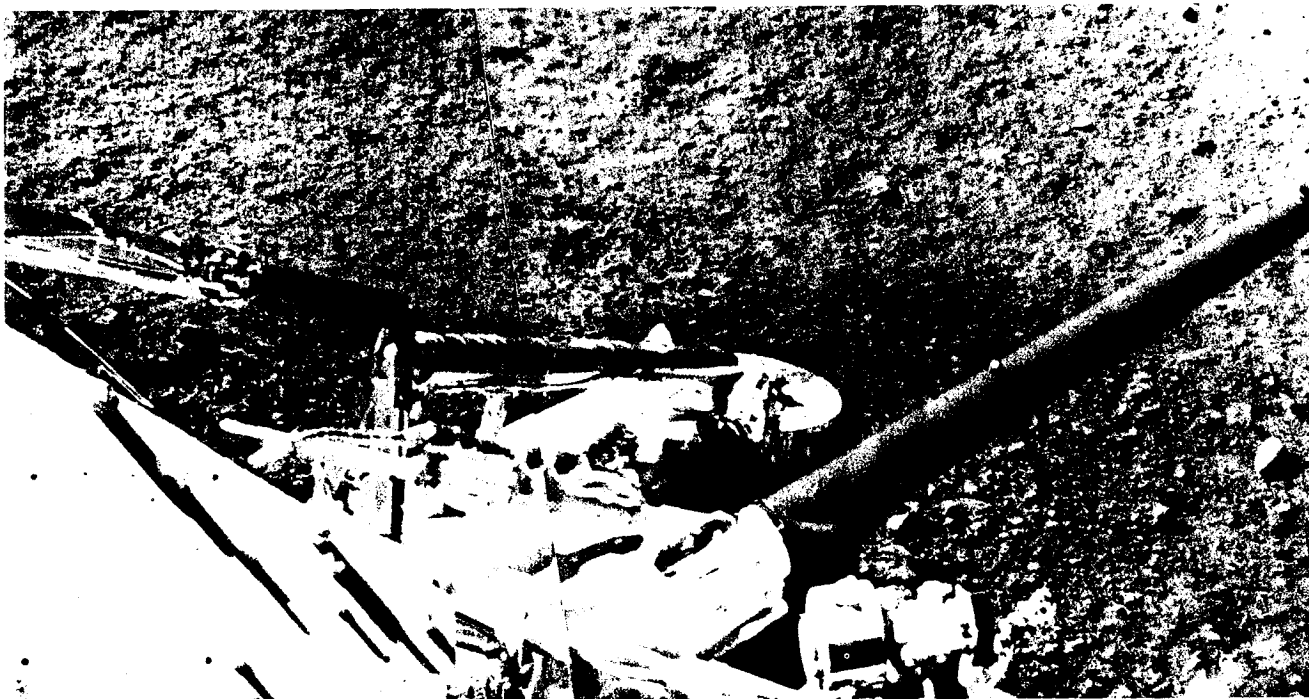
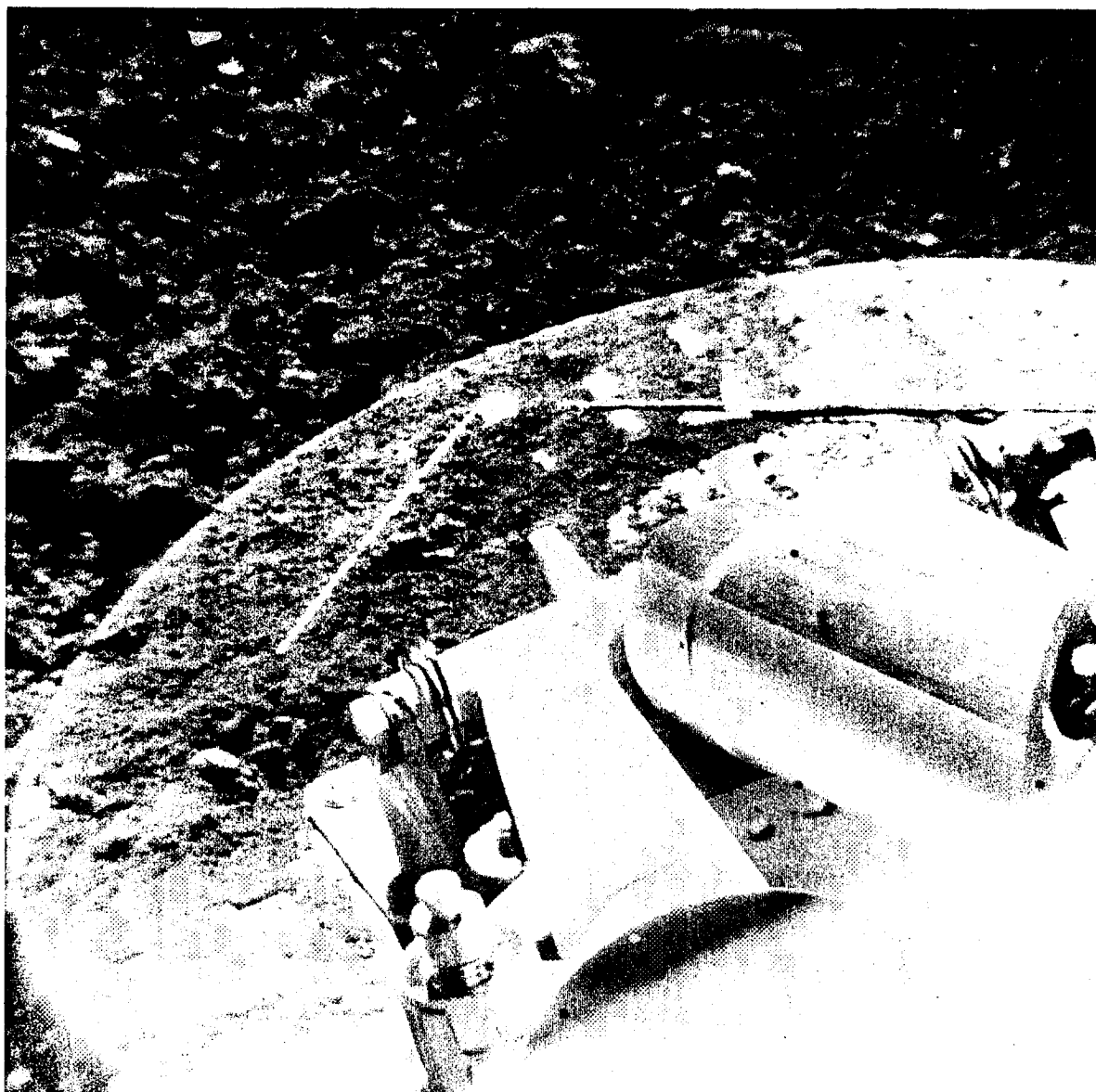


Fig. IV-9. Wide-angle mosaic of spacecraft landing leg 3 and footpad 3. A portion of the trench formed by footpad 3 during the landing can be seen through the leg structure. The throwout pattern of lunar material ejected during the landing is visible above and to the right of the footpad (Day 263, about 06:50 GMT; Catalog 5-MP-33).

Both footpads 2 and 3 were tipped downward by the trenching, and lunar material was deposited on top of the footpads (Figs. IV-10 and IV-11). No visible soil was deposited on the footpad tops of *Surveyors I* or *III* during landing. To improve the capability of detecting material on the footpads, the tops of footpads 2 and 3 (*Surveyor V*) had been painted with a low-reflectivity gray with several narrow, white stripes. A pre-launch view of footpad 2 in which the paint pattern can be seen is shown in Section VIII, Fig. VIII-1. Portions of the white stripes are visible in post-landing pictures of the footpads (Figs. IV-10 and IV-11). Figures IV-12 and IV-13 show footpad 3 tilted, with its inboard rim raised free of the surface. The raised ridge of the footpad impression in the lunar soil can be seen just above the antenna boom in Fig. IV-12. In Fig. IV-13, the conical surface of the footpad appears undamaged; i.e., no crushing occurred. Footpads 2 and 3 are tilted to an angle of approximately 16 deg, relative to the plane of the three footpads. This is based on a study of the elliptical shape of the footpad image and the position of the tilted footpad, relative to the leg structure. This is the maximum tilt possible, since at this angle the footpad top plates contact the leg struts.

There is evidence that the crushable blocks contacted the lunar surface during the landing. Figure IV-14 is a narrow-angle view of crushable block 3 in which a small rock or clod appears to be wedged between the block and its thermal shield. In a picture taken later, at a low sun angle, this fragment is no longer visible, but a deposit of soil particles can be seen adhering to the bottom edge of the block (Fig. IV-15). No clear evidence of crushable block imprints was obtained. However, the probable locations where crushable block imprints might exist are in areas obscured or shaded by the spacecraft.

The appearance of the lunar surface material at the *Surveyor V* landing site is similar to that in the vicinity of the *Surveyor I* and *III* landing sites (Refs. IV-1 and IV-2). The soil is granular, slightly cohesive, and generally fine-grained. Some lighter appearing, or more reflective, fragments are seen and presumably are rocks. Darker appearing fragments are presumed to be soil aggregates of both natural origin and those produced by the spacecraft landing.



**Fig. IV-10. Narrow-angle picture of top of footpad 2 showing lunar material that collected on the footpad during landing (Day 255, 05:45:22 GMT).**

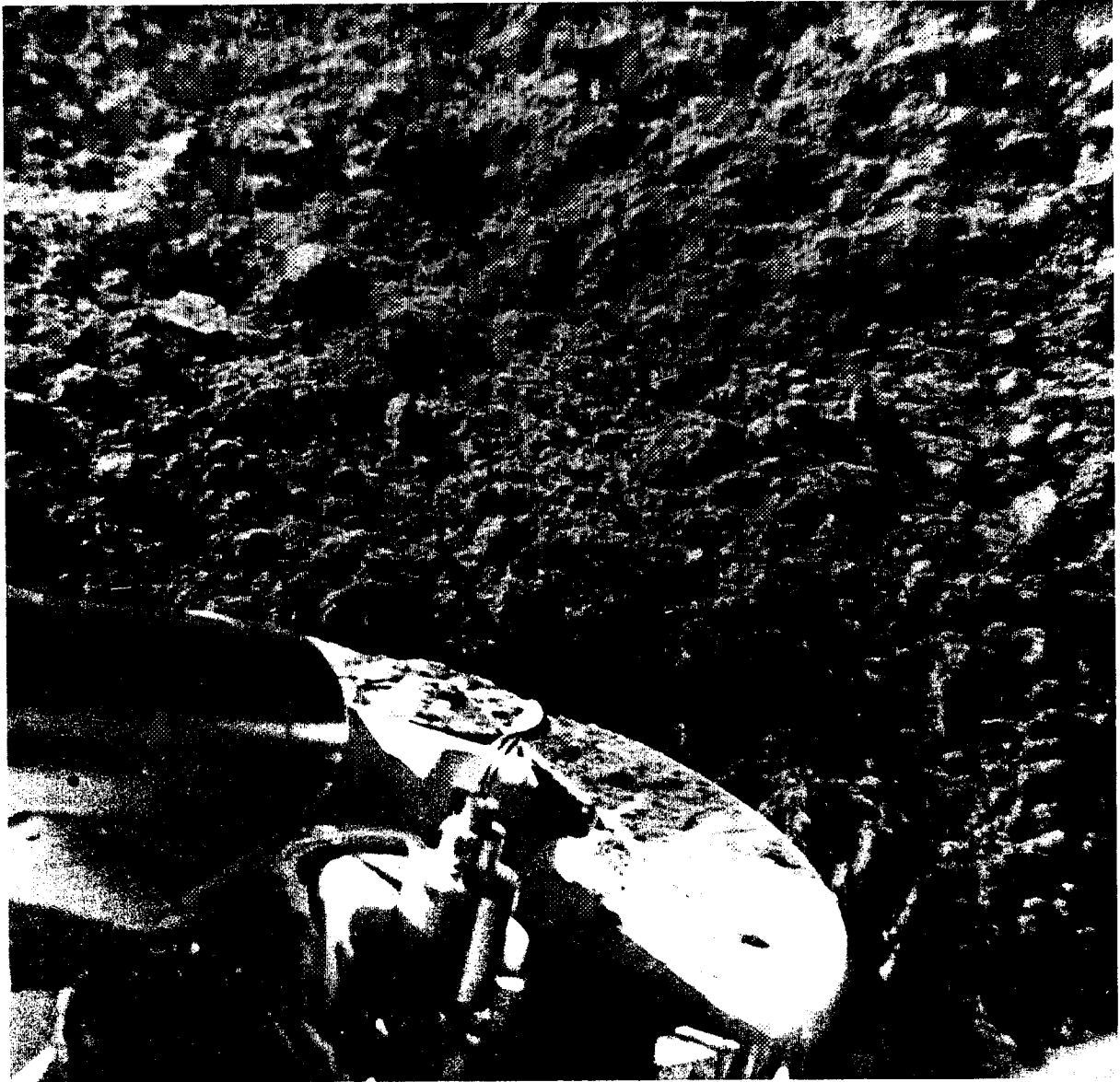


Fig. IV-11. Narrow-angle picture of top of footpad 3, showing the lunar material on the footpad (Day 265, 13:48:13 GMT).



**Fig. IV-12. Wide-angle picture of footpad 3. The footpad imprint in the lunar material can be seen above the antenna boom. The footpad remained tilted after the landing phase. Ghost image of the helium tanks was caused by incomplete erasure of previous image on vidicon (Day 254, 23:50:28 GMT).**



Fig. IV-13. Narrow-angle picture of the inboard section of footpad 3. The tilted footpad and the footpad imprint can be seen (Day 255, 02:09:40 GMT).



**Fig. IV-14. Narrow-angle view taken through the auxiliary mirrors showing the bottom of crushable block 3. A small rock or clod, seen wedged between the block and the thermal shield, was probably picked up during the first landing impact (Day 263, 11:47:23 GMT).**



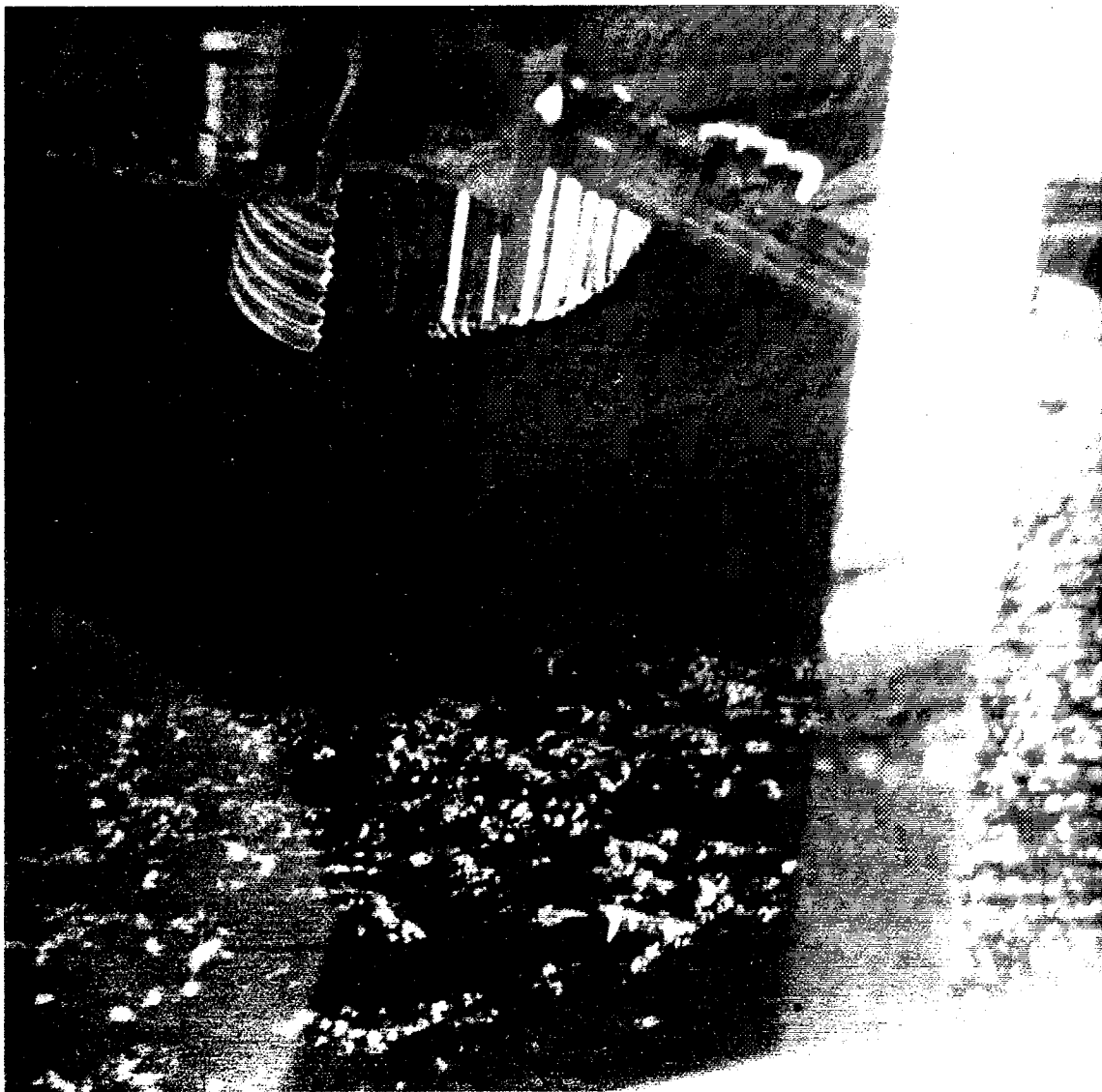


Fig. IV-15. Narrow-angle view of crushable block 3 taken through the auxiliary mirrors under low sun illumination. Lunar material can be seen adhering to the bottom of the block. The material probably was picked up during the first landing impact (Day 266, 06:02:50 GMT).

## B. Dynamic Simulations

Computer simulation studies of landings, using several analytical soil models, are being performed to estimate the mechanical properties of a surface material that will yield penetrations and shock-absorber axial loads similar to those obtained during the *Surveyor V* landings. The compressible soil model used in the simulations performed so far is described below (Refs. IV-3 and IV-4). The best correlation obtained to this date is shown in Fig. IV-16, which compares the shock-absorber force histories for a simulated landing on a lunar surface with a 2.7-N/cm<sup>2</sup> static bearing strength, with the histories from *Surveyor V*. The impact velocities used are 3.7 m/sec vertical and 0.3 m/sec horizontal, the initial estimates of touchdown velocities. The slope of the landing surface was assumed to be 17 deg, with the spacecraft in a horizontal position at the moment of footpad 1 impact; penetrations by footpads 1, 2, and 3, obtained in this simulation, are 6, 12, and 12 cm, respectively. Because of limited visibility, it is not possible to estimate the initial penetrations of footpads 1 and 3 of *Surveyor V*. The analytical simulation indicates that crushable blocks 2 and 3 each penetrated about 8 cm and that crushable block 1 did not touch the surface.

The soil model used in this analysis is completely compressible; the forces developed on the footpad are expressed by

$$F = p_0 A (1 + cs) + \frac{\rho_1 \rho_2}{\rho_2 - \rho_1} A s^2$$

where

$F$  = total force on footpad

$p_0$  = static bearing pressure of surface

$A$  = effective footpad area

$c$  = frictional constant

$s$  = depth of penetration

$\rho_1$  = original density of soil

$\rho_2$  = density of soil compressed by footpad

Figure IV-17 is an illustration of the soil model being penetrated by a footpad. The surface material, initially of density,  $\rho_1$ , is compressed at pressure,  $p_0$ , to a density,  $\rho_2$ , under the penetration of a footpad. Forces resisting penetration are the static bearing pressure that is assumed constant with depth, friction that increases linearly with penetration, and soil inertia. For the above soil model the assumed relationships between the density of the soil,

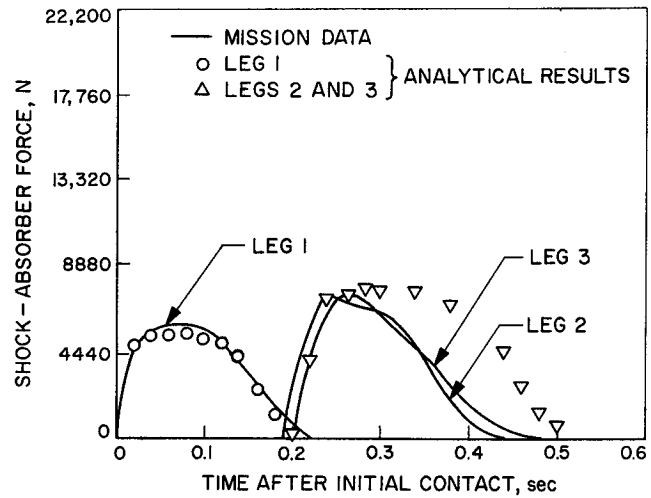


Fig. IV-16. A comparison of *Surveyor V* landing data with analytically obtained shock-absorber force/time histories.

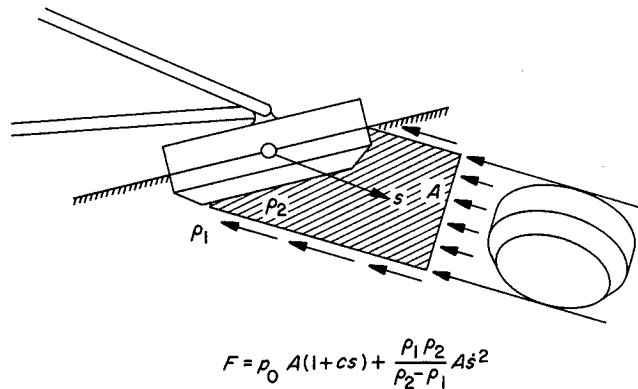


Fig. IV-17. Soft surface model for the landing dynamics analysis.

density of the soil compressed by a footpad, and static bearing pressure are shown in Fig. IV-18. As indicated, for a 2.7-N/cm<sup>2</sup> bearing-strength surface, the density of the undisturbed material would be 1.1 g/cm<sup>3</sup>. By use of other hypothetical relationships between static bearing pressure, initial density, and the final density, the numerical values presumably will result in better correlations between the analyses and the strain-gage data. The 1.1-g/cm<sup>3</sup> density of the soil is lower than some estimates derived from previous *Surveyor* landings, and may be changed as the agreement between simulation and actual landing is improved in subsequent solutions. It should be pointed out that data

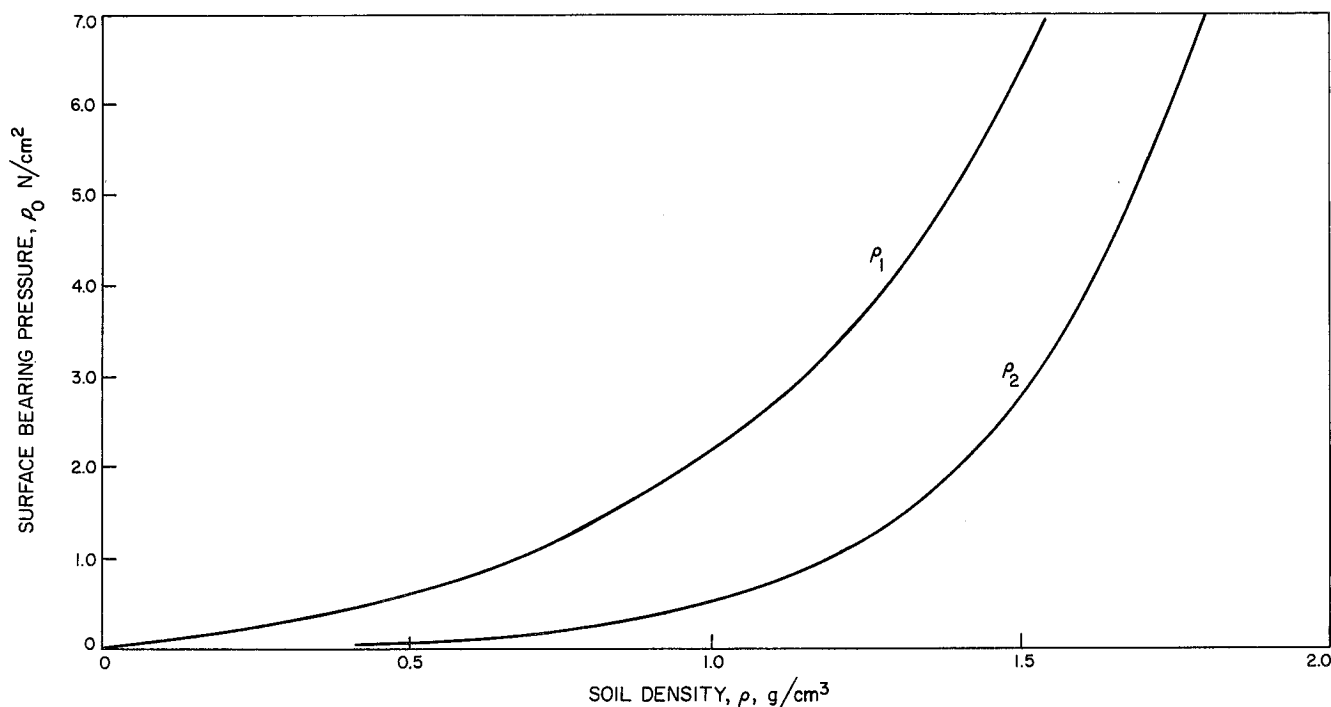


Fig. IV-18. Assumed relationship between surface bearing pressure and the soil density at the surface.

in Ref. IV-2 indicate that the lunar surface material has little compressibility. Dynamic analyses using incompressible soil models have not yet been performed for *Surveyor V*.

Another difference between the results of the *Surveyor V* landing analysis and those made for the previous missions is in the value obtained for the static bearing pressure of the surface. For the *Surveyor V* analysis with the above soil model, static bearing pressures  $< 3.4$  N/cm<sup>2</sup> have resulted in the best agreement with flight data. Simulations of the earlier missions, using the same soil model, showed good correlation with landing data for static bearing pressures of 3.4 N/cm<sup>2</sup> (Refs. IV-3 and IV-4). However, the downslope landing of *Surveyor V* produced a horizontal loading on the soil with a possible deformational mode which would result in greater footpad penetration. Furthermore, good correlation of shock-absorber forces has been obtained, assuming a rigid-surface landing simulation for *Surveyors I* and *III*; however, it has not yet been attained for *Surveyor V*. A rigid surface was defined as one with a bearing strength exceeding 6.9 N/cm<sup>2</sup>, since the footpad crushable material fails for higher loads.

These preliminary results suggest that the lunar surface material at the *Surveyor V* landing site is somewhat weaker than the material at the previous landing sites.

### C. Soil Characteristics: Spacecraft Slide

The distance that the spacecraft slid is a function of the drag forces between the three footpads and the lunar surface, and the initial spacecraft velocity parallel to the landing surface. This velocity is approximately 1.2 m/sec assuming zero horizontal velocity at footpad 1 touchdown, 4.2-m/sec vertical landing velocity, and a 17-deg ground slope. Since a velocity of 0.9 to 1.2 m/sec is consistent with both the time and distance associated with the spacecraft sliding, it is estimated that any horizontal spacecraft veloc-

The following effort was an attempt to obtain some bounding numbers for the lunar surface characteristics. Since the spacecraft is at rest on a 20-deg slope<sup>3</sup>, a minimum value of  $\mu_{min} = \tan 20 \text{ deg} = 0.36$  is obtained for both the internal angle of friction of the soil and the external coefficient of friction between the footpads and the soil. Because the spacecraft came to rest at about the same angle, the minimum effective coefficient of friction (braking) between the footpads and the surface has the same value. Since the footpads have penetrated the surface, the total static tangential force,  $F$ , is probably a more meaningful number. This is  $F = Mg \sin 20 \text{ deg} = 164$  N, where  $M$  is the landed mass of the spacecraft and  $g$  the lunar gravity.

<sup>3</sup>This value is based on preliminary data and was used as the basis for these calculations.

During landing, the spacecraft slid to a stop along the sloping surface. The time,  $t_f$ , from initial touchdown of footpads 2 and 3 to stopping is known to be about  $t_f = 1.7$  sec from the telemetry data.

Assuming a constant stopping force  $\bar{F}_x$  and pure linear motion of the spacecraft parallel to the slope, the following equation is derived from the equation of motion:

$$\bar{F}_x = M \left( g \sin \theta + \frac{2\dot{x}_f}{t_f^2} \right) = 330 \text{ N}$$

where  $g$  and  $\theta$  are lunar gravity and angle of the slope (20 deg), respectively, and  $x$  is the spacecraft motion along the slope. The terms  $x_f$  and  $t_f$  indicate final distance and final time, respectively.  $F_x$  is about twice the static tangential force. (This force is below the resolution of the shock-absorber strain gages.) The initial downslope velocity  $\dot{x}_0$  is

$$\dot{x}_0 = \frac{2x_f}{t_f} = 1.0 \text{ m/sec}$$

This is somewhat lower than the value of  $\dot{x}_0 = 1.4$  m/sec resulting from the downslope component of the vertical landing speed (4.2 m/sec), thus indicating that the assumption of a constant stopping force is not valid, or possibly indicating there was a small amount of horizontal velocity, about 0.4 m/sec upslope, at the time of landing.

An effective coefficient of friction can be estimated from

$$\mu_{eff} = \frac{\bar{F}_x}{F_n} = \frac{\bar{F}_x}{Mg} \cos \theta = 0.73$$

However, this number is of limited value because there were obvious significant variations in the trenching and in the normal force of the footpads against the lunar surface, as indicated by the strain gages and trench depths. Perhaps a more meaningful number is the average stopping pressure,  $\bar{P}_x$ , supplied by the soil against the footpads

$$\bar{P}_x = \frac{\bar{F}_x}{A_x}$$

Estimating an average depth of penetration of 5 cm,  $A_x \approx 375 \text{ cm}^2$  (three footpads);  $\bar{P}_x \approx 0.9 \text{ N/cm}^2$ . This value for  $\bar{P}_x$  is consistent with the stalling pressure observed during the *Surveyor III* lunar trenching operations using the soil mechanics surface sampler (Ref. IV-2).

## D. Lunar Soil Erosion Test

The lunar soil erosion test was performed to determine the characteristics and amount of lunar soil erosion caused by the interaction of the spacecraft vernier rocket engine exhaust gases and the lunar surface. The results will be used to estimate the amount of soil erosion during a landing of the *Apollo Lunar Module* (LM), and to estimate such lunar surface properties as permeability, cohesion, and particle size.

### 1. Erosion Phenomena

Soil erosion caused by rocket engine exhaust gas impingement is of three basic types, which usually occur in combination, although one mode may predominate:

- (1) *Viscous erosion* (Ref. IV-5): erosion by entrainment of soil particles as the gas flows over the surface.
- (2) *Gas diffusion erosion* (Ref. IV-6): movement of the soil caused by the upward flow of gas through the pores of the soil during and after the firing.
- (3) *Explosive cratering* (Ref. IV-7): rapid cratering caused by the exhaust gas pressure on a normal surface exceeding the bearing capacity of the lunar surface.

In the lunar environment, where full expansion of the exhaust plume occurs during the vernier engine firing, the third process is considered unlikely to occur for the firing of the LM descent engine or the *Surveyor* vernier engines at their respective thrust levels and nozzle heights above the lunar surface.

**a. Viscous erosion.** When a soil is subjected to rocket engine exhaust in a direction normal to the soil surface, erosion may occur, depending on the forces transmitted to the soil by the gases and the properties of the soil. The gas that flows radially along the surface may dislodge soil particles from the surface and entrain them. The erosion characteristics of a bed of particles under vacuum conditions ( $10^{-4}$  torr) were investigated by Land and Clark (Ref. IV-8) for various particle sizes and nozzle heights. Their results showed that, for the nozzle heights where erosion occurred, erosion was more rapid in soils with coarser particles (within limits) than in fine-grained soils, and that the maximum crater depth was not necessarily directly below the nozzle. Often the resulting crater was in the shape of the lower half of a toroid. Observations show, and theory predicts, that the soil particles leave the surface in a fairly flat trajectory when the surface erosion is small. As the erosion depth increases, the trajectory angle between the particle and the surface increases.

**b. Gas diffusion erosion.** The erosion of a soil surface by the diffusion of exhaust gases was investigated by Scott and Ko (Ref. IV-6) to explain the effects of *Surveyor* vernier engine firing tests against earth soils under vacuum (Refs. IV-9 through IV-11). During a firing, exhaust gases flow into and through the porous soil exiting upward at some radial distance and possibly lifting soil from the surface. For soil removal to occur during this period, the engine must be fired for a time sufficient to achieve a significant upward flow of gases at a distance from the central higher pressurized region. If a crater forms during this period of firing, then it would have the shape of a half of a toroid. Upon sudden removal of the surface pressure at engine shutdown, some of the gas diffused into the soil during firing will flow to the surface and may produce an eruption. Such a disturbance would occur in the high-pressure region directly under the engine.

Whether the diffusion process has reached a steady state depends on the porosity and the permeability of the soil medium. The extent of the potentially unstable (erodable) portions of the soil also depends on these parameters. The depth of erosion is largely influenced by the cohesion of the soil, but not the extent of horizontal erosion. Therefore, it is possible to estimate the permeability and cohesion of the lunar soil.

## 2. Test Explanation

Because the lunar surface loadings developed by exhaust gases from the LM descent engine during landing and by a *Surveyor* vernier engine firing at low thrust on the moon are similar, it was possible to simulate, in the lunar environment, the soil erosion effects to be experienced during a LM landing.

To simulate the viscous erosion anticipated by LM, a firing time of about 5 sec would have been required for the *Surveyor* engines at their minimum thrust level. This takes into consideration the pressure profiles exerted on the soil by the exhaust gases from the *Surveyor* engines located a fixed distance above the lunar surface and from the LM engine during a nominal descent to the lunar surface, i.e., from a negligible value at a 25-ft altitude to the maximum value at engine cutoff, 10 sec later.

The simulation of the gas diffusion eruption phenomenon would require a *Surveyor* engine firing time equivalent to 1/100 of the surface loading time during the LM descent, or approximately 0.1 sec. This time ratio is based on the theory (Ref. IV-6) that, for equivalent loading levels, times should be scaled as the square of the ratio of the nozzle exit radii.

It was apparent, therefore, that both erosion effects would not be simulated with a single vernier engine firing. Indications of the viscous erosion effects were available from the *Surveyor III* second landing event. During that event, an erosion trench over 1 m long and possibly 2 to 5 cm deep, was caused by the continuous firing of the vernier engines during the 2-sec interval in which the engine passed above the trench (Ref. IV-2). However, diffused gas eruption was minimized because the spacecraft lifted off the moon without a sudden engine shutdown. Therefore, it was decided that the lunar soil erosion test on *Surveyor V* should be devoted, within spacecraft constraints, to obtaining the best simulation of engine shutdown effects.

To ensure predictable performance (temperatures were higher than normal engine starting temperatures) and to permit a complete engine performance telemetry cycle, a firing time of 0.55 sec was considered the minimum that should be performed. By using the minimum firing time, it was felt that the viscous erosion effects would be minimized while the gas diffusion effects would be maximized; thus, the results of the experiment could better be analyzed to give meaningful conclusions. The selection of a short firing time and a minimum thrust level also reduced possible hazards to the spacecraft such as tipping over, thermal degradation, and degraded mirror optical properties.

## 3. Observed Effects

At 05:38 GMT on Day 256, approximately 53 hr after landing, the *Surveyor V* liquid-propellant vernier engines were fired at a low thrust level for  $0.55 \pm 0.05$  sec. Engines 1 and 3 fired at a  $120 \pm 22$  N thrust level, and vernier engine 2 fired at a  $76 \pm 18$  N thrust level. These thrust levels were determined by strain gages on the engine support structures during vernier firing (see *Surveyor V* Mission Report, Part I). During the firing, the spacecraft remained stationary except for the motion of the alpha-scattering instrument sensor head. Observations of the effects of the vernier engine firing were made by comparing television pictures obtained before and after the firing. Pictures of the lunar surface directly below the engines and in the near vicinity of the engines, as well as pictures of various spacecraft components, were used to establish the soil erosion effects. The location and relationship of the *Surveyor V* vernier engines and television camera to other spacecraft components that appear in the pictures are shown in Figs. IV-19 and IV-20. Areas where erosion effects were detected are shown in Fig. IV-20. The erosion caused by vernier engine 3 provided the primary erosion experimental data. The area under vernier engine 1 was partially visible.

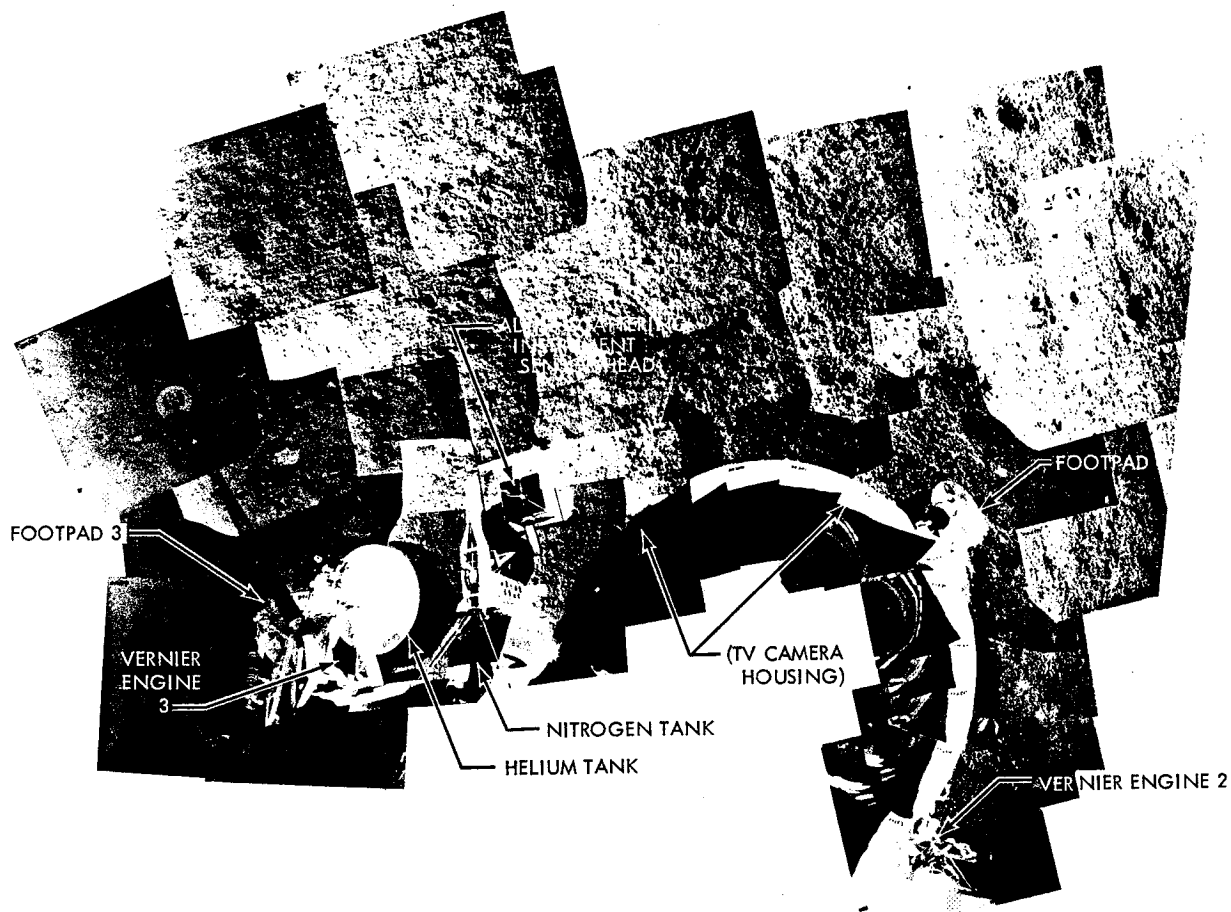
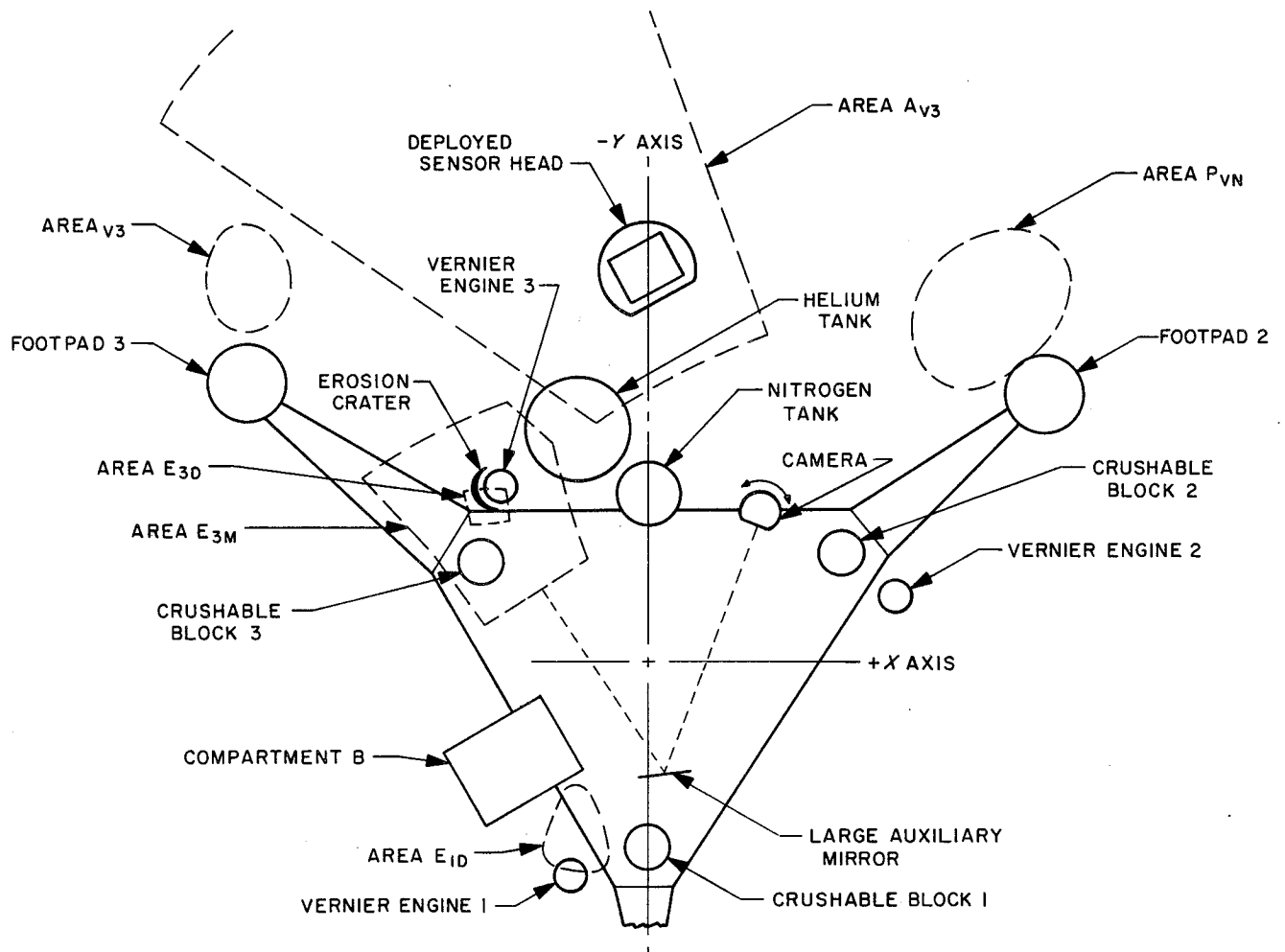


Fig. IV-19. Panoramic view as seen by the television camera. The view includes legs 2 and 3 (Day 254; Catalog 5-MP-9).



**Fig. IV-20. Drawing showing the relationship of the spacecraft to lunar surface areas affected by the vernier engine firing.**

*a. The lunar surface below vernier engines 1 and 3.*

Changes in the lunar surface caused by erosion beneath vernier engine 3 can be seen in the series of pictures in Figs. IV-21 and IV-22, which are the areas  $E_{3M}$  and  $E_{3D}$ , as illustrated in Fig. IV-20. ( $E_{3M}$  and  $E_{3D}$  are the areas under engine 3, viewed, respectively, by mirror and directly.) Each series of pictures shows the lunar surface as illuminated at various sun elevations progressing from morning to late afternoon. In the pictures taken 4 hr before and 2 hr after firing (Fig. IV-21b and c, respectively), it is evident that there has been movement of fragments on the surface and a change in surface structure, thereby proving that soil was moved. Since no pictures could be taken during the firing, these are the closest in time (pre- and post-firing) to the firing of the vernier engines. Soil erosion known to have occurred below and adjacent to vernier engine 3 includes:

- (1) Erosion of a layer of soil of indeterminate depth by viscous erosion during the firing from the area seen in the large auxiliary mirror. Evidence for this erosion consists mainly of the observations that most, if not all, soil fragments visible in the mirror pictures have been moved by the firing.
- (2) Formation of a shallow, crescent-shaped crater directly below vernier engine 3. This crater was formed at engine shutdown by eruption of exhaust gases that had diffused into the soil during the engine firing. The crater is 20 cm in diameter and 0.8 to 1.3 cm deep. The crater is best seen when accentuated by shadows occurring in the late afternoon pictures (Figs. IV-21 and IV-22). The open end of the crater points approximately toward the sensor head of the alpha-scattering instrument.

In an early, pre-firing, wide-angle picture of the auxiliary mirror, a slightly darker area that may have been a natural crater can be faintly seen downslope from vernier engine 3 (Fig. IV-23). The location of this darker area is such that it is unlikely that the spacecraft landing created it. This depression is barely evident in post-firing pictures.

Part of the surface below vernier engine 1 was directly viewable with the television camera. However, shadows prevented the return of pictures of the area before the firing. Although the area was free of shadows in the lunar afternoon, as can be seen in Fig. IV-24, the effect of the vernier engine firing on the surface has not been determined. This is attributed to the fact that the amount of surface area actually viewable is small and that there are no pre-firing pictures.

*b. Erosion effects on surrounding areas.*

*Area around alpha-scattering sensor head.* The surface area immediately adjacent to the alpha-scattering instrument shows most clearly the extent and amount of soil disturbance caused by the vernier engine firing. Figs. IV-25 and IV-26 are controlled mosaics (each frame orientation and center is correct) composed of narrow-angle, pre- and post-firing pictures of the area ( $A_{V3}$  in Fig. IV-20). A comparison of Figs. IV-25 and IV-26 indicates that the firing caused a number of changes, including movement of the alpha-scattering instrument sensor head, movements of rock and soil fragments, and alteration to general surface features. In Figs. IV-27 and IV-28, some of the features have been identified to clarify the following discussion. Representative rock and soil fragments that were not moved by the firing have been outlined; i.e., they are identified in both mosaics. Some of these fragments are labeled with the same lower-case letters in both figures, since they are discussed in the text. Fragments that were moved during the firing are marked with an "x"; some are numbered so that they also can be discussed in the text.

None of the fragments that moved can be positively identified in both the pre- and post-firing mosaics. In some cases, this could be due to movement of particles into the area from locations not in the pre-firing mosaic, or in other cases, particles shown in the pre-firing mosaic could have moved out of the area during the firing. It is also possible that some of the same fragments appear, but, because of the movement and their irregular shape, they present different distinguishing features to the camera and, therefore, cannot be identified as the same fragment.

Examination of Figs. IV-25 and IV-26 indicates that in places the basic soil surface has been changed by the firing. Clear evidence of this is shown by noting the track of fragment "h," indicated by the dotted line in Fig. IV-27. This feature, which is about 2 mm in depth, appears in the pre-firing picture; fragment "h," probably ejected during the landing, made the track as it rolled downhill. Because the track is essentially straight for its entire 58-cm length, its direction probably defines the local direction of maximum slope. As can be seen in Fig. IV-28, this track no longer exists, having either been filled in or eroded away by the firing. Another example is the material to the right of the helium tank, which is ejected material deposited during the landing. This material, which is in an area 40 to 60 cm from vernier engine 3, is not visible after the firing. Although the ejecta could have been covered, or swept away by the firing, evidence suggests the latter (see area E in Fig. IV-27, which is adjacent to the helium tank and rock "a"). It can be concluded that some soil around fragment



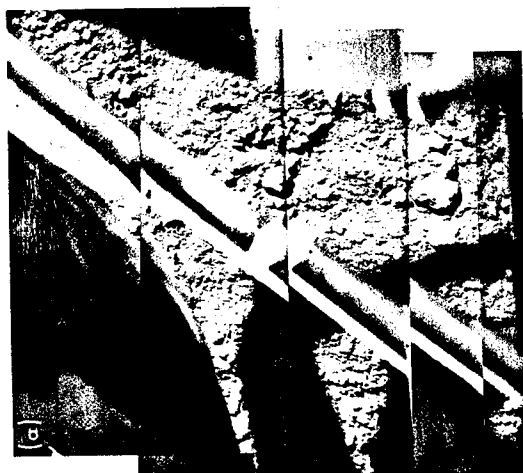






Fig. IV-21. A series of narrow-angle mosaics of the lunar surface beneath vernier engine 3, as seen through the auxiliary mirror. The series included two pre-firing (a and b) and four post-firing pictures. Sun elevation relative to the local surface was 35, 45, 47, 39, 16, and 11 deg (a through f, respectively). Part of the spacecraft frame and one crushable block are visible at the top of the picture.



Fig. IV-22. A series of narrow-angle mosaics of the lunar surface beneath vernier engine 3. The series includes two pre-firing (a and b) and four post-firing pictures. Sun elevation relative to the local surface was 33, 44, 40, 31, 20, and 16 deg (a through f, respectively). Two spacecraft tanks and the electronics box on the bottom bound the pictures. A spacecraft structural member divides the visible lunar surface.



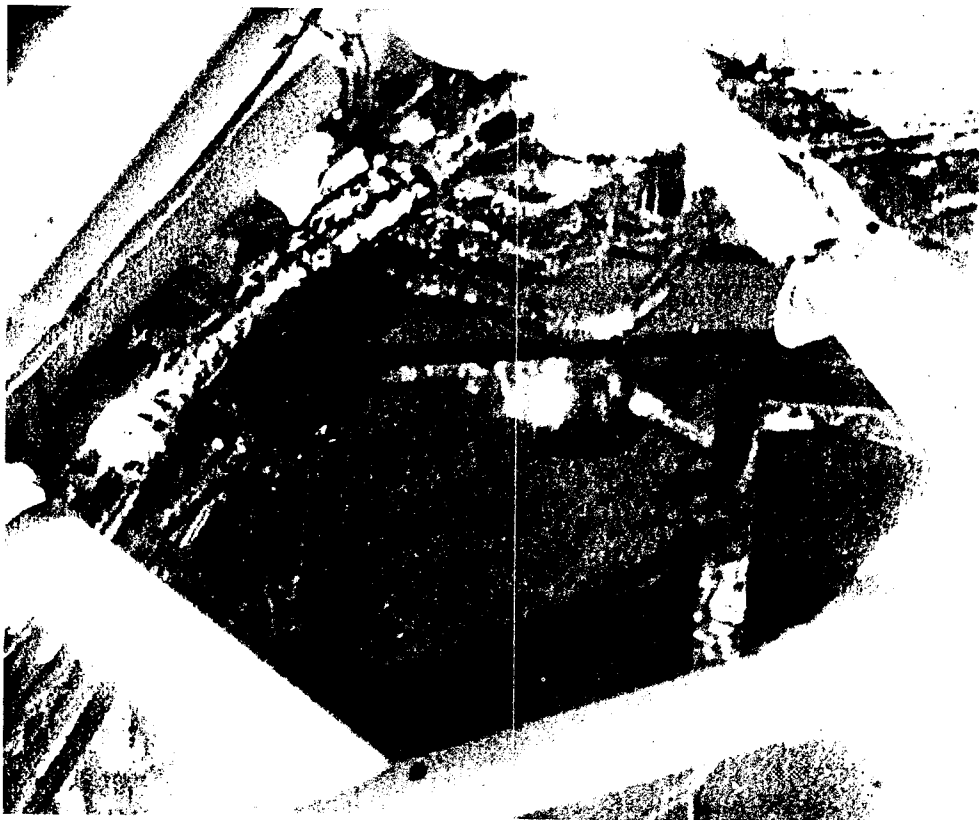


Fig. IV-23. Early pre-firing, wide-angle, digitized picture of large auxiliary mirror. A crater rim (?) is faintly highlighted by the early morning sun in the upper-left corner of the mirror (Day 254, 08:26:08 GMT).



Fig. IV-24. A post-firing view of the only part of the vernier engine 1 imp. the television camera. The rough-textured lunar surface within the small part of an erosion crater. This area was in shadow before the firing (Day 2





act area that can be seen by  
triangular area is probably  
63, 11:47:05 GMT).

Fig. IV-25. Far left: pre-firing mosaic of alpha-scattering  
instrument area (Day 255; Catalog 5-MP-24). →

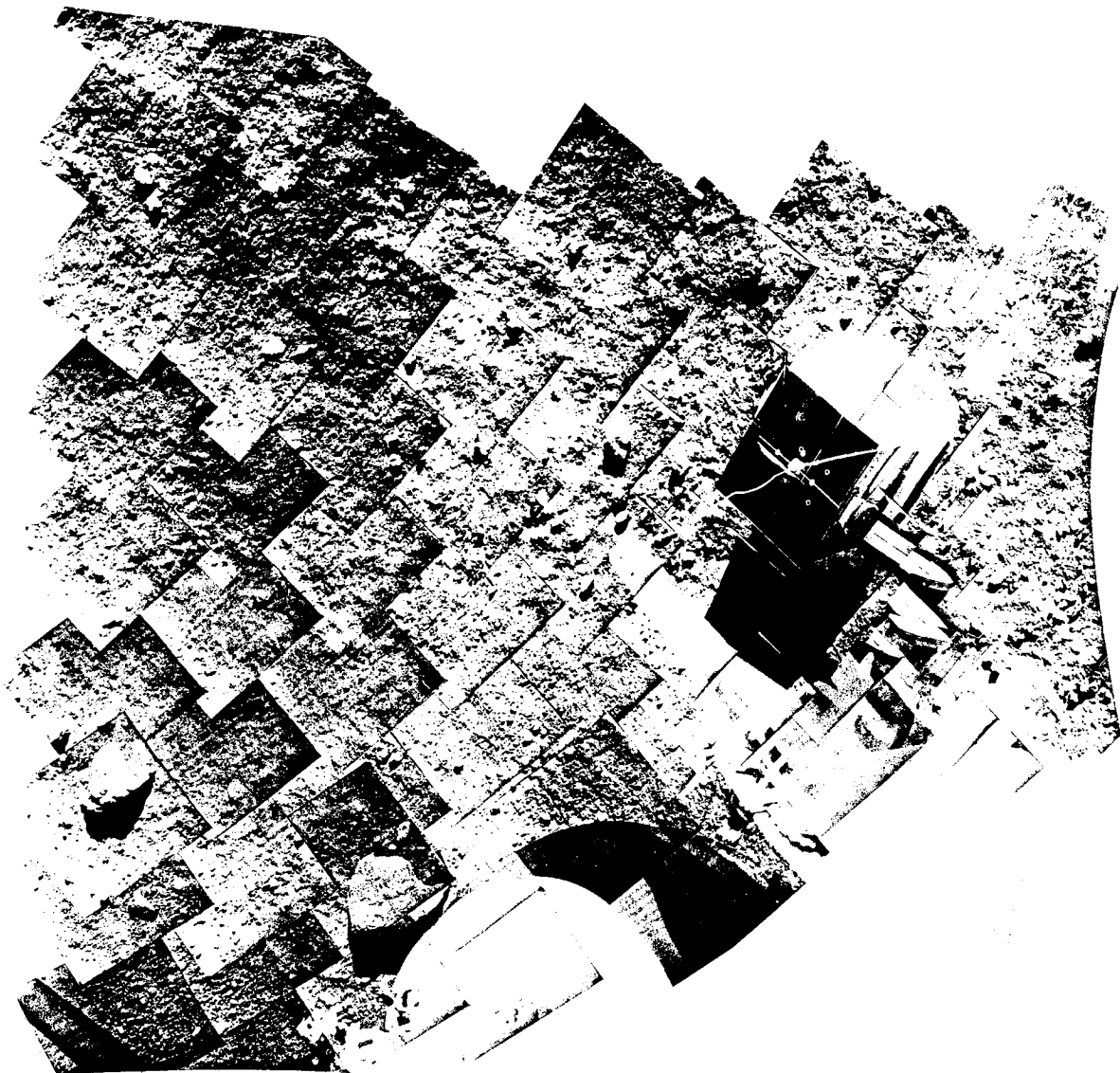
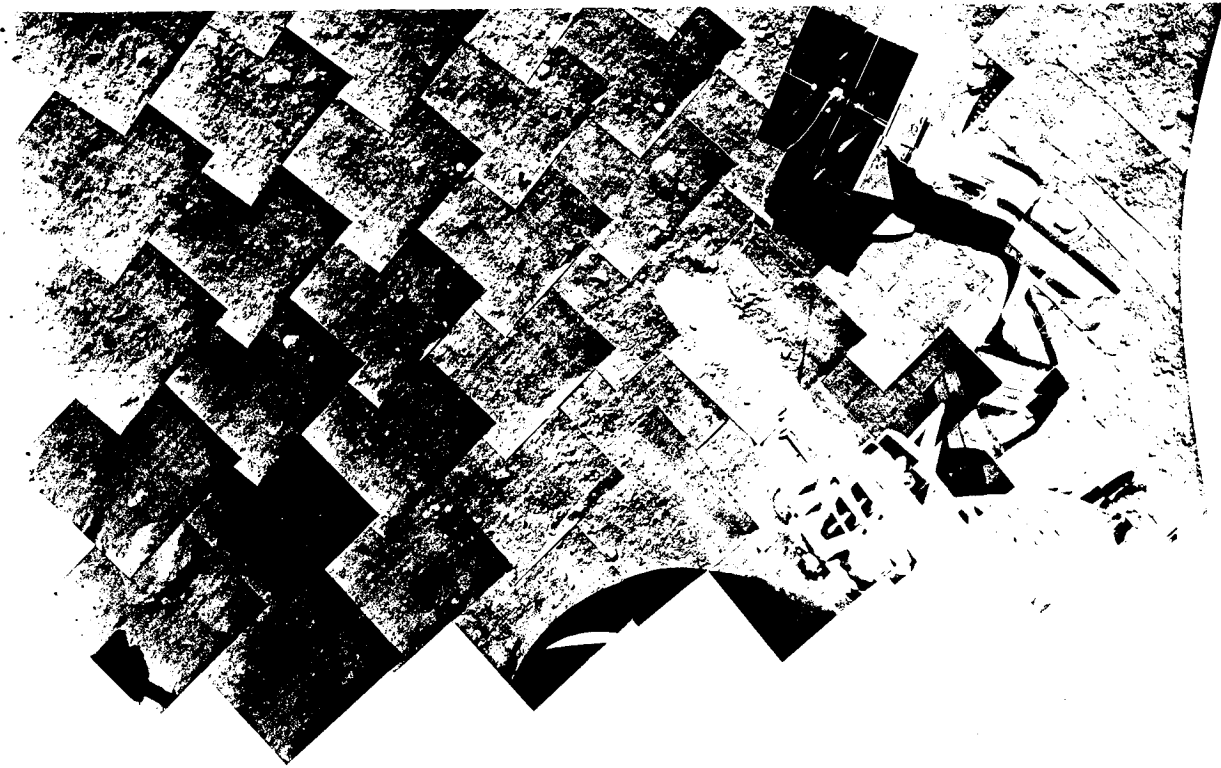
Fig. IV-26. Middle left: post-firing mosaic of alpha-  
scattering instrument area (Day 257; Catalog 5-MP-25). →

Fig. IV-27. Middle right: pre-firing, annotated mosaic of  
alpha-scattering instrument area. Rock and soil frag-  
ments that were not moved by the firing are outlined; →  
fragments that were moved are marked with an "x"  
(Day 255).

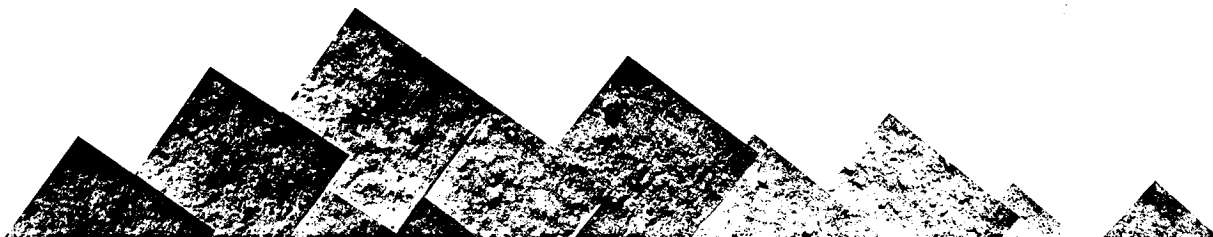
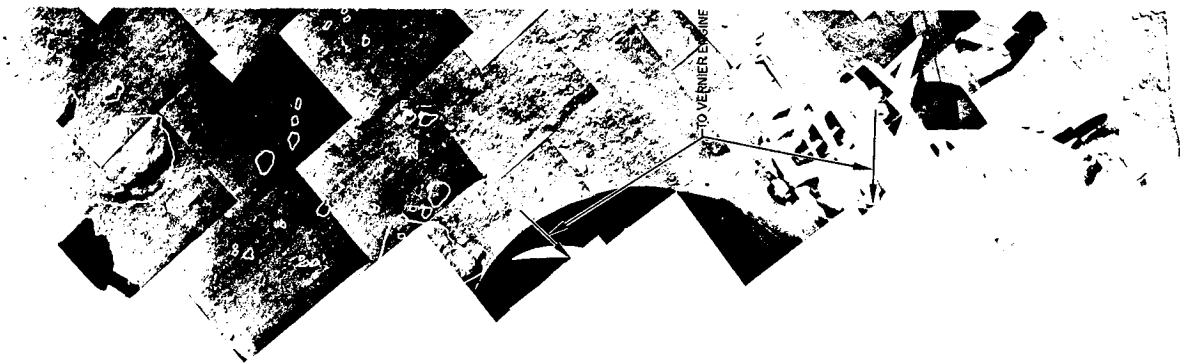
Fig. IV-28. Far right: post-firing, annotated mosaic of  
alpha-scattering instrument area. Annotations are the →  
same as in Fig. IV-27 (Day 257).



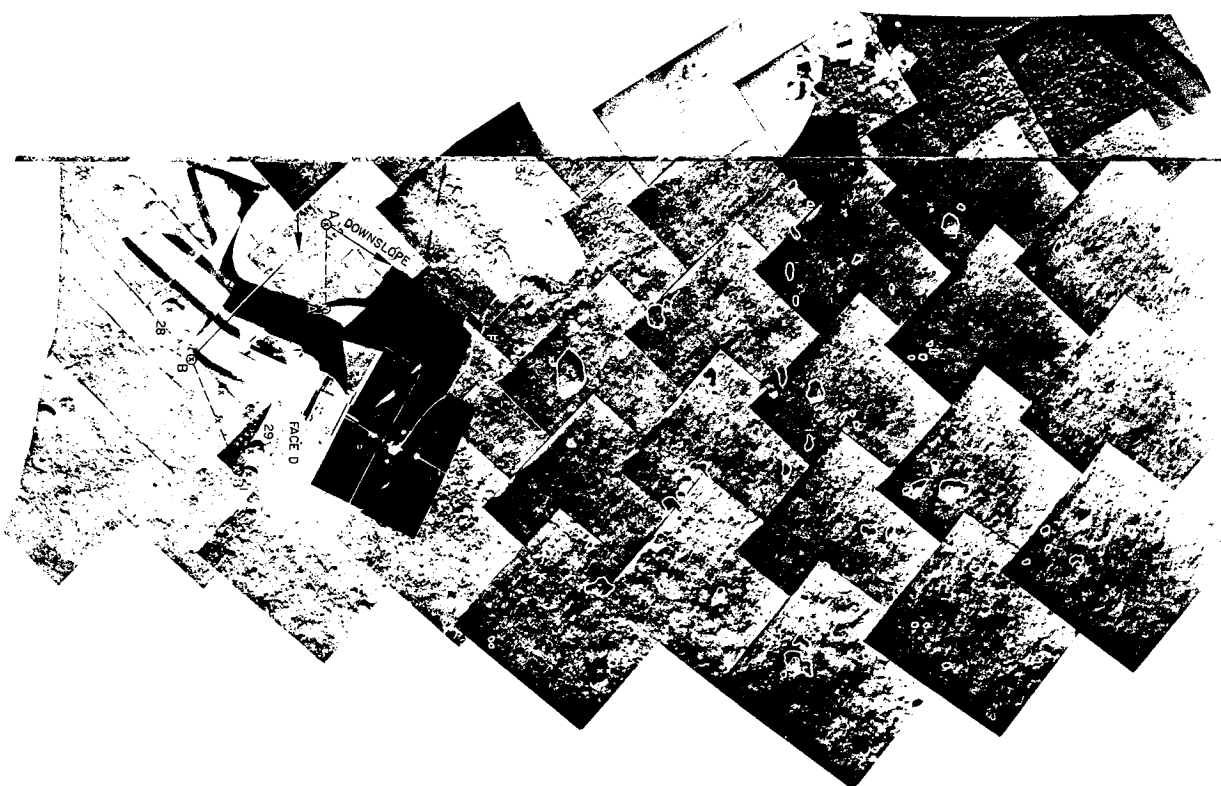






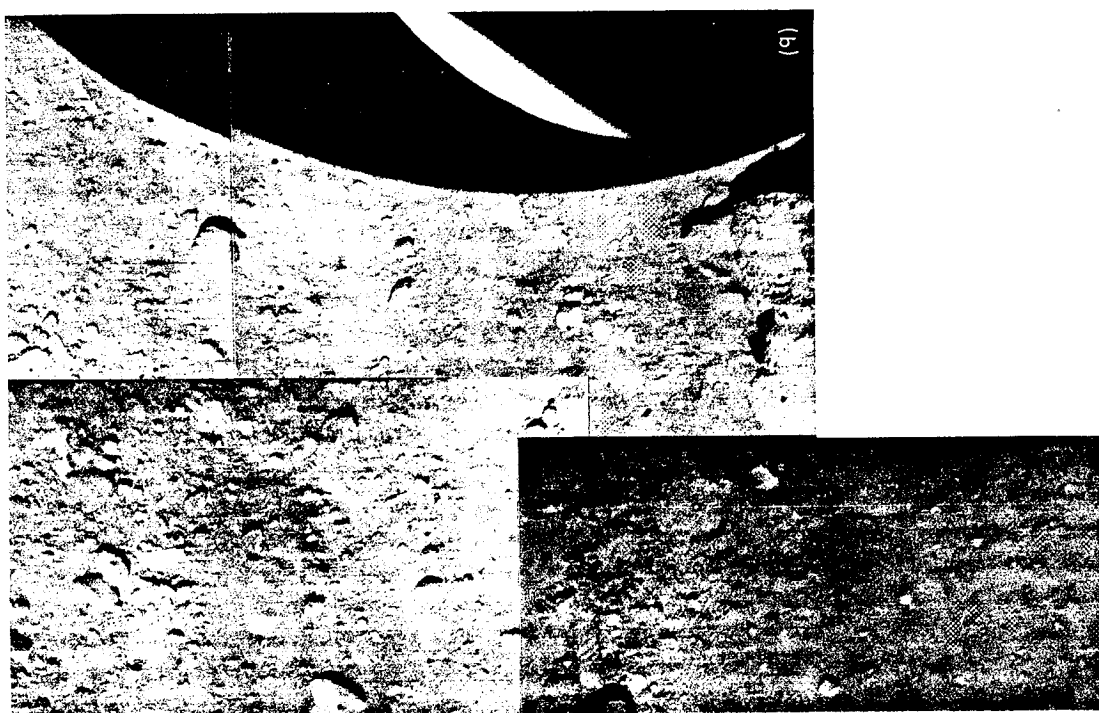
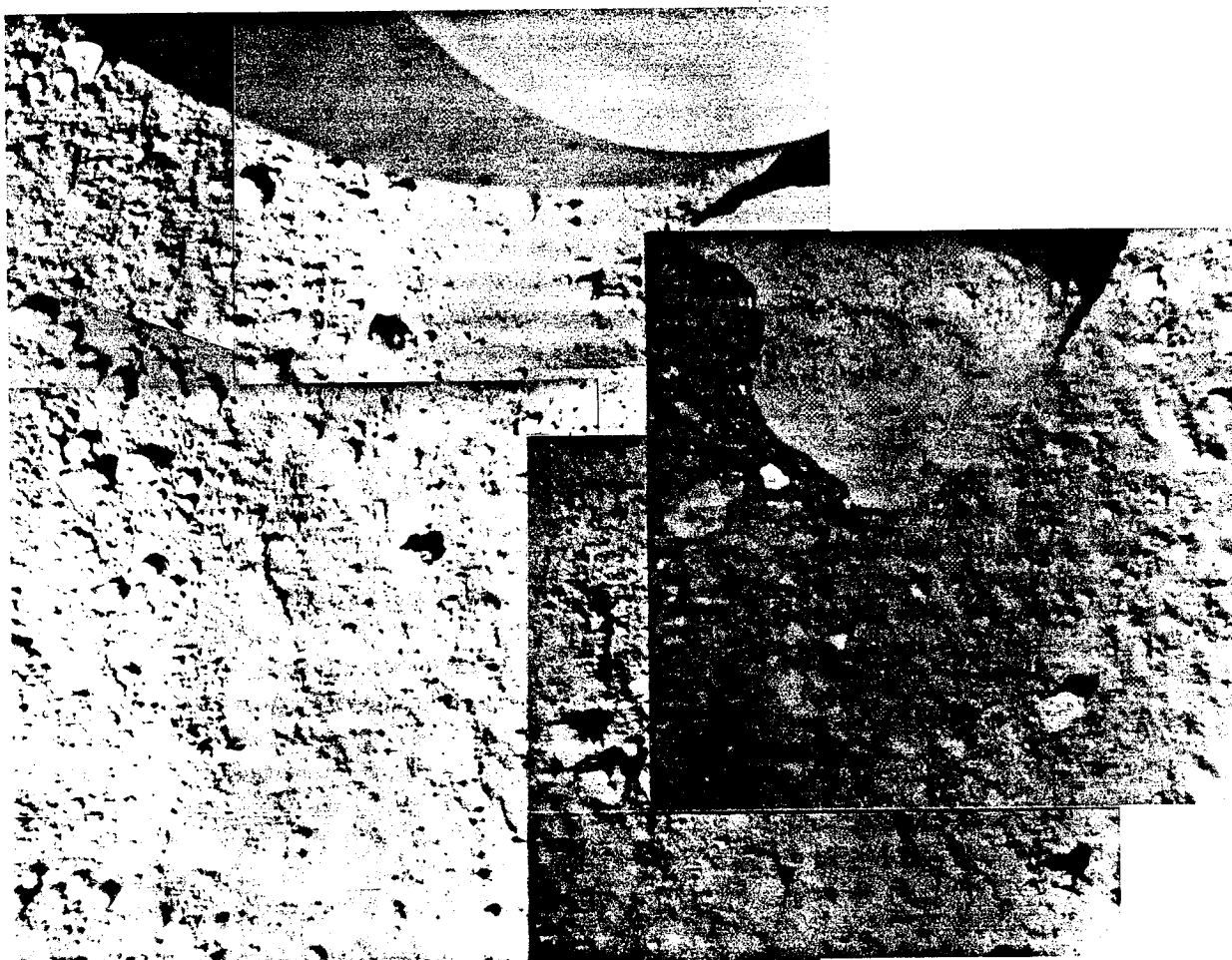






ROCK	AVERAGE DIAMETER, cm
25	4.4
26	3.5
27	3.4
28	1.9
29	2.2
30	2.8









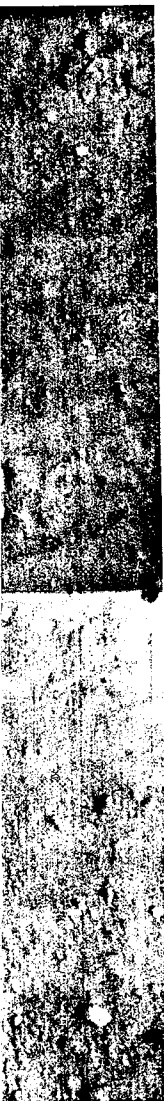


Fig. IV-29. Lunar surface beside the helium tank (see Figs. IV-27 and IV-28). Soil erosion from around rock "a" and the trail left by impact of fragment 26 were caused by the firing. (a) Pre-firing picture; Catalog 5-MP-43. (b) Post-firing picture; Catalog 5-MP-44.



"g" and partly covering rock "a" was definitely swept away because rock "a" is exposed to a somewhat greater depth after the firing (Fig. IV-29). For this area, 40 to 60 cm from vernier engine 3, the estimated depth of deposition, erosion, or soil replacement is 1 cm or more.

Fragments "a" through "f" did not move, and therefore appear in both Figs. IV-27 and IV-28. In general, these are the larger fragments; many, if not most, appear to be partly buried. Fragment "g," probably a small rock, did not move; it is located beside the large rock "a," which may have shielded it from the vernier engine firing.

Studies of the pre-firing mosaic (Fig. IV-27) indicated that the largest fragment in the mosaic displaced during the firing was fragment 1, which had an average diameter of about 2.6 cm and was initially located about 35 cm from vernier engine 3. Table IV-2 lists the average diameters and distances from engine 3 for a number of the larger displaced fragments that appear in this mosaic.

Studies of the post-firing mosaic (Fig. IV-28) indicated that fragment 25, having an average diameter of 4.4 cm, was the largest fragment in the mosaic displaced by the firing. In all probability, because of its size, the pre-firing position of this rock was much closer to the vernier engine, and therefore did not appear in the pre-firing picture. It is interesting to note in Figs. IV-28 and IV-29b that fragment 26, 4.3 cm long, was ejected by the firing and produced a skid mark about 4 to 5 cm long.

Figure IV-30 is a plot of fragment diameter vs pre-firing distance from vernier engine 3. The fragments that moved are indicated by crosses; those that did not move are indi-

cated by circles. The circles plotted in this figure are for fragments that probably were lying on the surface and not partially buried prior to firing. Since fragments 25 and 27 appear only in the post-firing mosaics, their point of origin is unknown. Therefore, only a probable range of distance can be shown for these fragments. This figure indicates a boundary below which a fragment could have been moved by the firing and which depends on the size of the fragment and its distance from the vernier engine.

The alpha-scattering sensor head was displaced by the vernier engine 3 firing. The alpha-scattering instrument's 13-cm-high compartment faces C and D (Fig. IV-28) were oriented at approximately a 45-deg angle in the direction of vernier engine 3. The firing displaced corner A to A', a distance of 9 cm, in a direction approximately 60 deg from downslope. The instrument rotated 15 deg counterclockwise (viewed from above) as corner B moved obliquely to B'. A depression left in the soil by the straight edge of the circular plate in its pre-firing position can be seen in Fig. IV-31a and at the arrow beside corner A in Fig. IV-28.

In Fig. IV-31a (pre-firing), the image of the sensor head circular plate is clearly reflected by the gold-plated front of face D. After the firing (Fig. IV-31b), no reflected image of the plate can be seen. The entire surface of D appears to be nonreflective, with the bottom 3 cm appearing darker than the top 10 cm. This change is probably caused by the adherence of fine lunar material. Erosion debris covers the intersection of face D and the plate. Fragments and soil appear to have landed on and near the plate after the sensor head was stopped when the leading edge of the plate dug into the soil (Figs. IV-31b and IV-26).

**Table IV-2. Diameters and distances from vernier engine 3 centerline, prior to firing, for representative fragments near the alpha-scattering instrument, which have been displaced by the vernier firing**

Fragment	Diameter, cm	Distance from vernier engine 3, cm	Fragment	Diameter, cm	Distance from vernier engine 3, cm
1	2.6	35	13	0.4	125
2	2.1	110	14	0.6	154
3	1.7	75	15	0.8	166
4	2.2	83	16	0.6	184
5	1.8	80	17	1.8	110
6	1.9	82	18	1.3	109
7	1.8	125	19	0.4	168
8	0.9	100	20	0.6	179
9	0.9	91	21	0.6	189
10	1.6	75	22	0.5	175
11	0.8	83	23	0.6	162
12	1.1	115	24	0.6	148

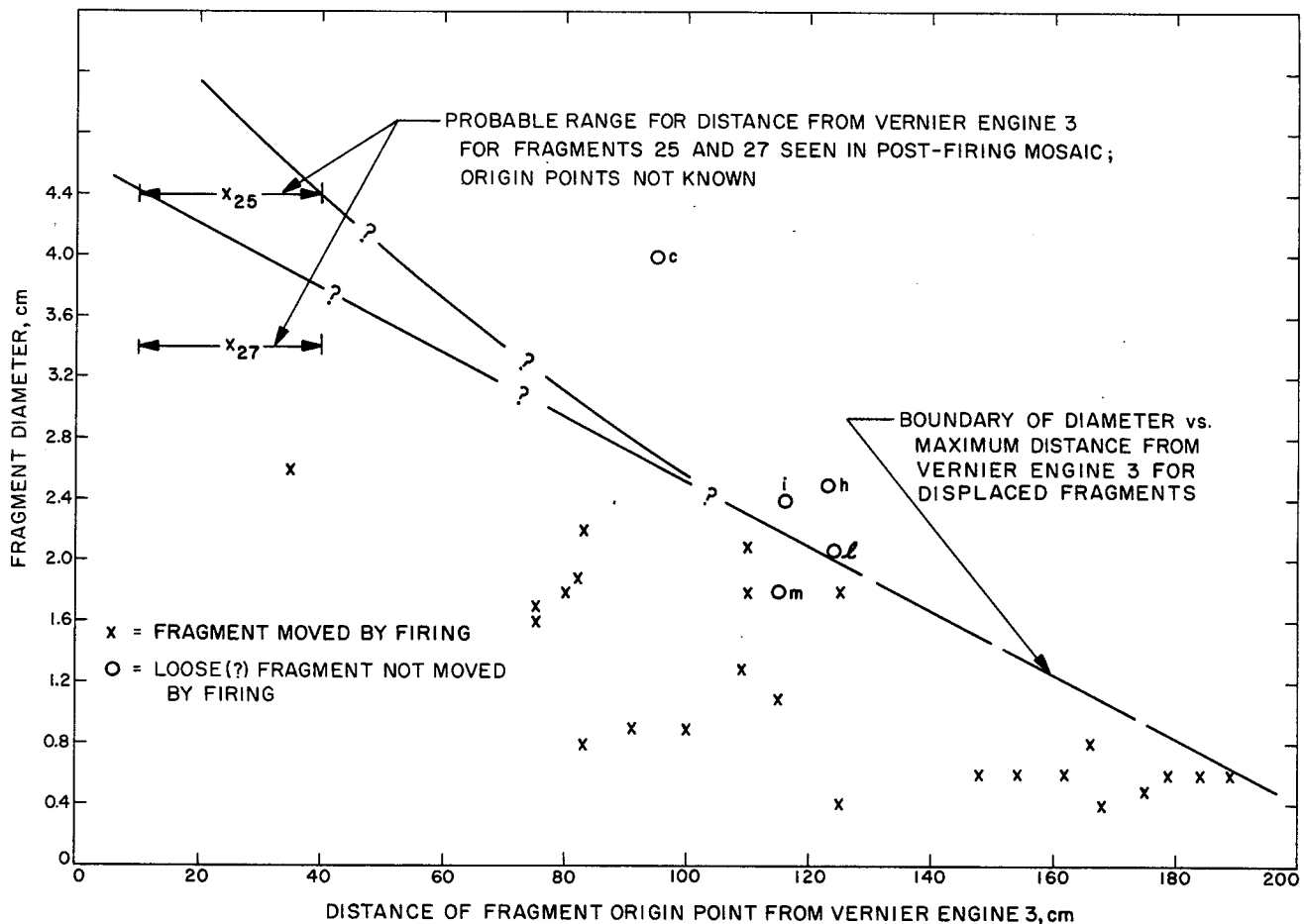


Fig. IV-30. Graph of diameter vs distance for fragments moved by the firing. The dashed line represents the probable maximum sizes for fragments that could be moved by the firing at distances ranging from 10 to 200 cm.

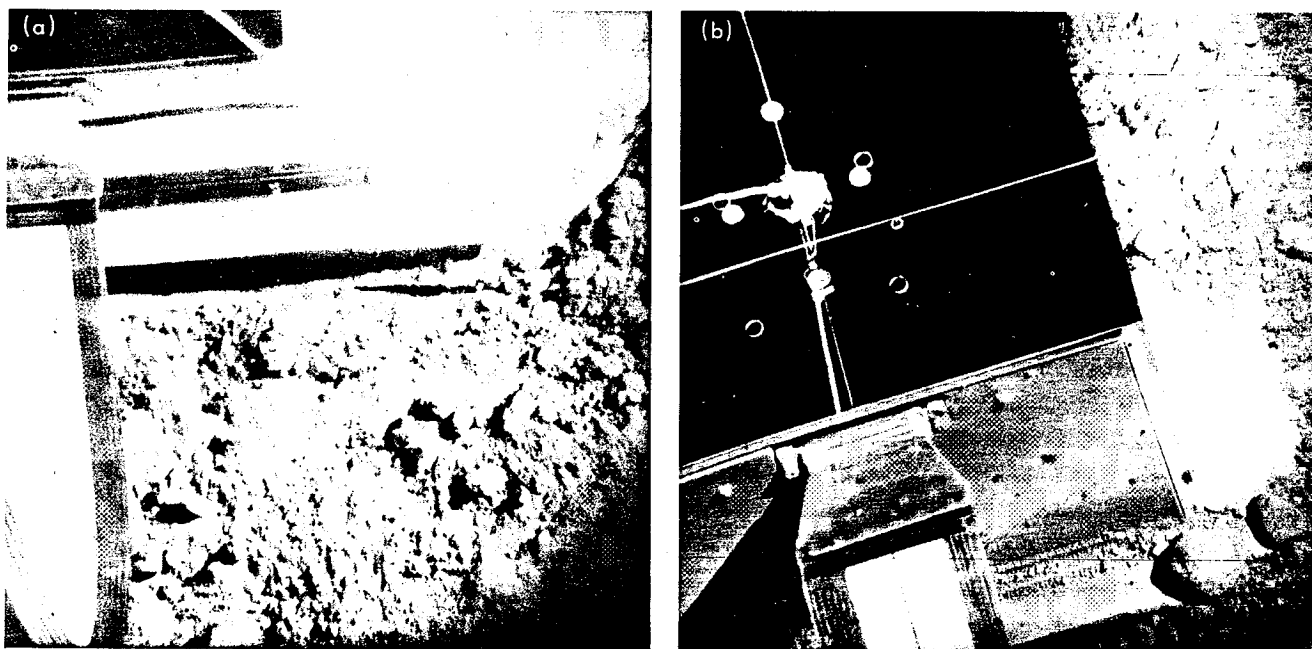


Fig. IV-31. Gold-plated face D (see Figs. IV-27 and IV-28) of the sensor head. (a) Pre-firing picture; face D is highly reflective (Day 255, 05:06:27 GMT). (a) Post-firing picture; face D is nonreflective (Day 257, 07:15:09 GMT).

*Footpad 3 area.* A fragment-by-fragment study of the footpad 3 area in Fig. IV-32 (pre-firing) was made by comparing individual pre- and post-firing pictures using the blink technique (a technique by which two frames are placed in a superimposed position, and the top frame is manually flipped for easy comparison of features). Figures IV-33 and IV-34 are post-firing mosaics of the footpad 3 area. None of the numerous soil fragments outboard of footpad 3 and between the antenna and its shadow in Fig. IV-32 were displaced by the firing. However, this area is at least partly shielded from the direct blast of vernier engine 3 by footpad 3 and its leg. The soil visible below the antenna in Fig. IV-32 is not shielded from vernier engine 3, and many of the fragments here were swept away by the firing. The area is 120 to 130 cm from the engine centerline; the largest fragment displaced was 2.0 cm in diameter.

*Footpad 2 area.* In either the pre- or post-firing mosaics of the footpad 2 area, fragments that can be seen to have moved are entirely limited to the lower-left quarter of the controlled mosaics in Figs. IV-35 and IV-36. Most of the displaced soil is limited to the area in the two frame rows left of footpad 2 in front of the magnet. Soil was blown off the magnet bracket and control bar.

Some of the representative larger fragments in the pre-firing mosaic that have moved are marked with an "x" and

numbered 1-11 in Fig. IV-35. Distances, parallel to the ground, from vernier engines 2 and 3 for these fragments are given in Table IV-3.

Though only a relatively few fragments of 1-cm diameter or larger have been displaced, the fine soil between the larger fragments in the area to the left of footpad 2 was disturbed by the firing. This detail can be seen only in

Table IV-3. Diameters and distances from the centerline of vernier engines 2 and 3, prior to firing, for fragments near footpad 2 which have been moved by the vernier firing

Fragment	Diameter, cm	Distance from vernier engine 2, cm	Distance from vernier engine 3, cm
1	1.6	170	256
2	1.8	105	211
3	1	106	209
4	1	105	205
5	1	104	206
6	1	125	194
7	1	102	186
8	1	144	232
9	1	145	235
10	1	110	216
11	1	115	222

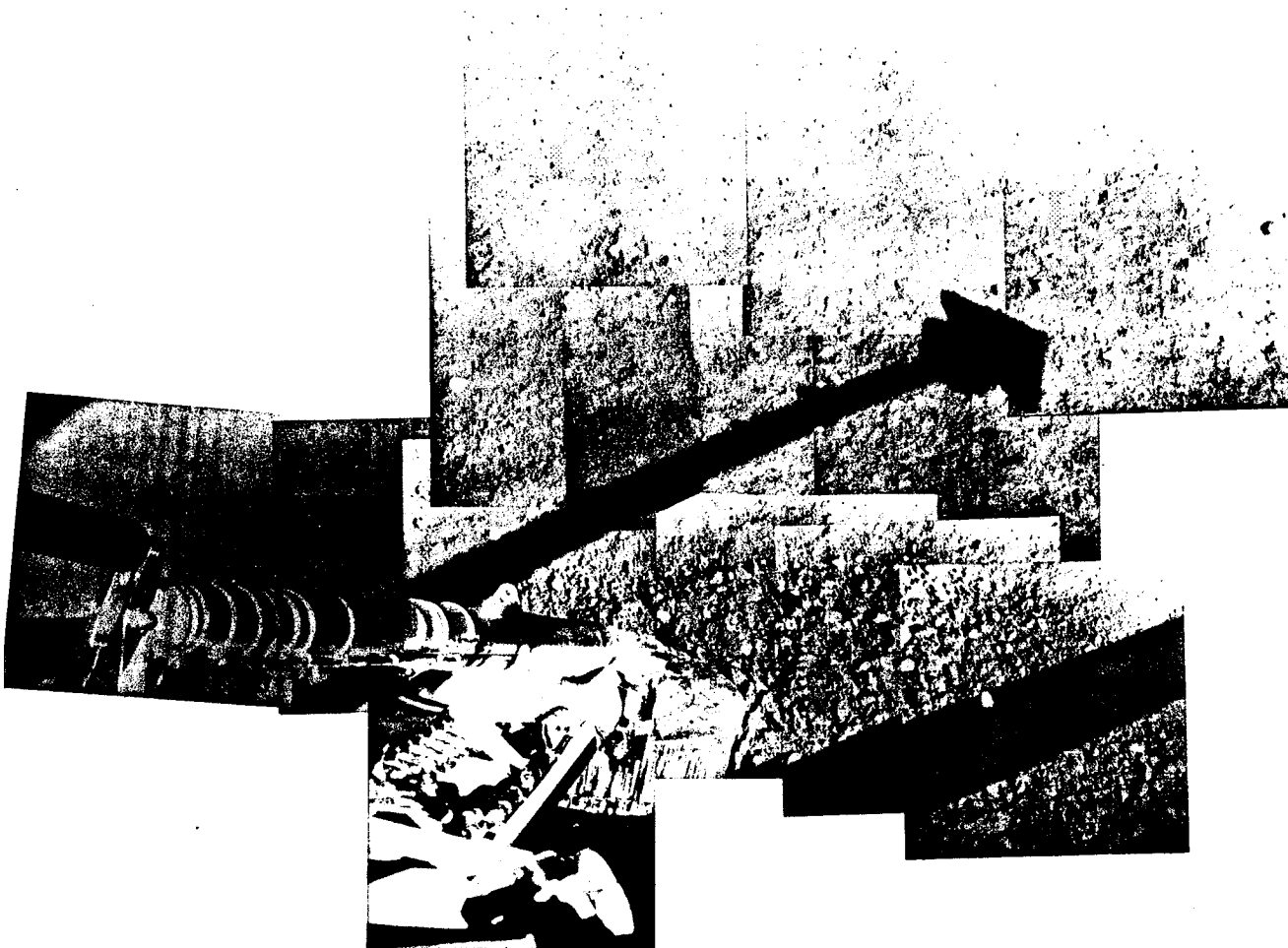


**Fig. IV-32. Pre-firing mosaic of footpad 3 area. Most of the fragments below the antenna in the lower-right corner of the mosaic were swept away by the vernier engine firing (Day 255, Catalog 5-MP-32).**



**Fig. IV-33. Post-firing mosaic of footpad 3 area. The small, light-colored fragments above the leg probably are small rocks rather than soil clumps (Day 258, Catalog 5-MP-29).**



**Fig. IV-34. Post-firing mosaic of footpad 3 area. A portion of the trench dug by footpad 3 during landing can be seen below the shock absorber to the left of the footpad (Day 264; Catalog 5-MP-30).**

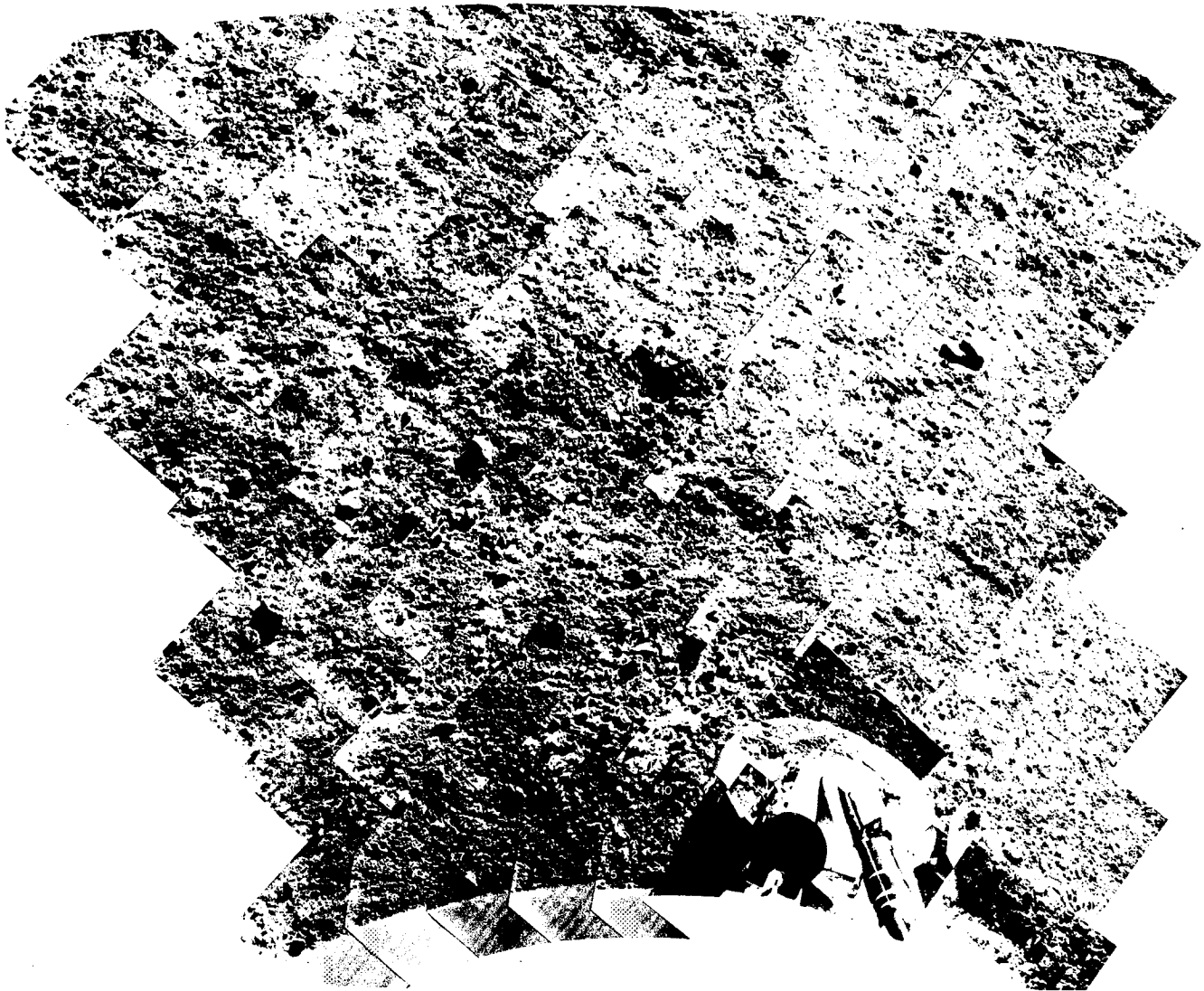
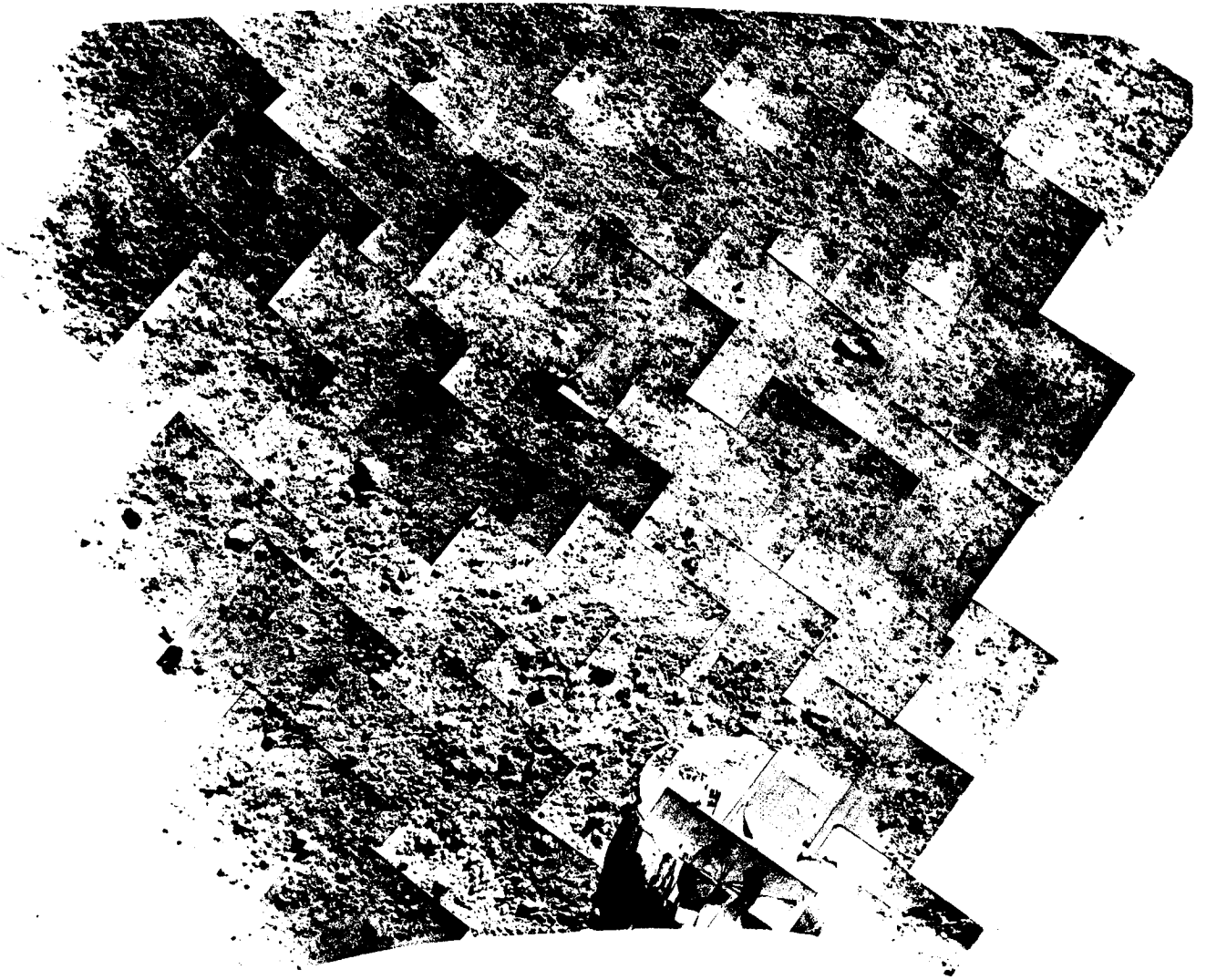


Fig. IV-35. Pre-firing mosaic of footpad 2 area. Representative fragments that were moved by the vernier engine firing are marked with an "x" (Day 255).





**Fig. IV-36. Post-firing mosaic of footpad 2 area. Soil on top of the footpad was little disturbed by the firing (Day 256; Catalog 5-MP-27).**

large prints of individual narrow-angle pictures. The relative influence of engines 2 and 3 in causing this erosion is unknown.

*Footpad 2 trench area.* Only a portion of the trench dug by footpad 2 is visible in narrow-angle pictures taken before vernier engine firing. That portion of the trench for which both pre- and post-firing, narrow-angle pictures are available is shown in the mosaics of Figs. IV-37 and IV-38. Detailed frame-by-frame comparison of these pictures, using the blink technique, shows no visible erosion. None of the loose soil fragments comprising the landing ejecta lying on the trench rim and floor have been moved. In ad-

dition, there has been little, if any, filling or removal of fine soil along the numerous fractures and crevices in the trench wall. Distance along the ground, from the centerline of vernier engine 2 to the top of the trench in Figs. IV-37 and IV-38 ranges from 90 cm at the south end to 115 cm at the north end.

*c. Soil deposits on electronic compartment tops.* A measure of erosion by diffused gas eruption was obtained by comparing pre- and post-firing pictures of the compartment B top (Fig. IV-39). In Fig. IV-39b, clumps of soil, which landed on the compartment top and broke, are visible. Some of the small fragments appear to have rolled

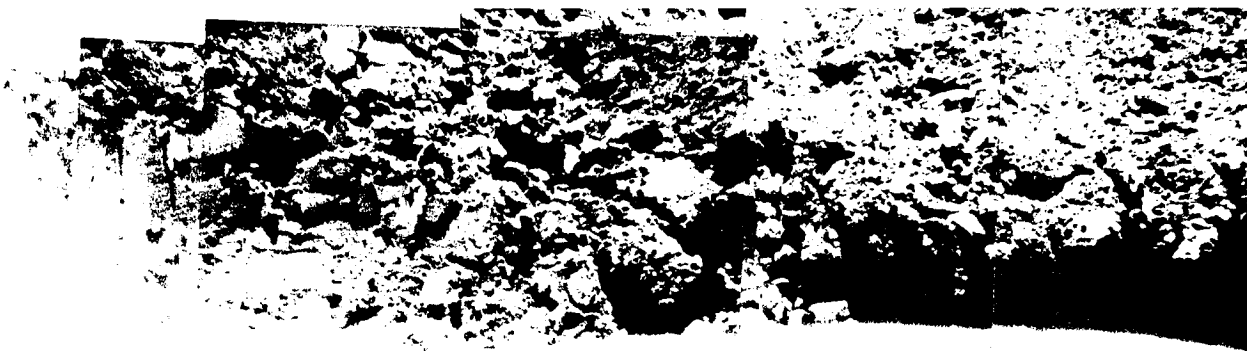


Fig. IV-37. Pre-firing mosaic of part of the trench dug by footpad 2 during landing (Day 256; Catalog 5-MP-36).

downslope or splattered in the plane of the trajectory. The relationship of compartment B to vernier engine 1 is shown in Fig. IV-20; the top of the compartment was 1.1 m above the lunar surface. The particles must have had a near-vertical trajectory in reaching the top of compartment B from the area under vernier engine 1. There were no noticeable changes in spacecraft temperatures, although the thermal characteristics of the electronic compartment top would have been significantly modified even by a thin layer of soil.

#### 4. Simulations and Analysis

*a. Simulations.* In order to perform an analysis of a simulated erosion, the following factors had to be determined.

*Height of the engine 3 nozzle above the lunar surface.* The nozzle height was determined by comparison of pictures obtained before launch and on the lunar surface. Before launch, but after final *Surveyor V* camera alignment, pictures were taken of the region below vernier engine 3 and crushable block 3, as viewed by the auxiliary mirrors. A platform was positioned at various known distances below the spacecraft (equivalent to the spacecraft resting on its footpads with zero penetration; Fig. IV-40). A square grid with lines at 5.1-cm centers was painted on this platform along with circles showing the relative location of the areas below the nozzle and the crushable block; a vertical distance scale, as measured on these pictures at the centerline of the engine nozzle, was thus established. With this scale, the distance from the vernier engine 3 nozzle exit plane to the lunar erosion crater was deter-

mined to be  $37 \pm 1$  cm. The location of the lunar erosion crater under engine 3 was determined by a comparison of lunar pictures (Figs. IV-21 and IV-22) with pictures obtained of a simulated crater by use of a full-size spacecraft.

*Lunar erosion crater dimensions.* By use of the technique described above, the crater diameter was determined to be 20 cm. Estimates of crater depth were determined by shadow studies, conducted with a full-scale spacecraft and a simulated sun, which was adjusted to the correct azimuth and elevation angles relative to the spacecraft. Depressions of various depths were made in simulated soil surfaces. By comparing the crater shadows on the lunar pictures with those obtained in laboratory simulations, the average crater depth was determined to be  $0.8 \pm 0.2$  cm.

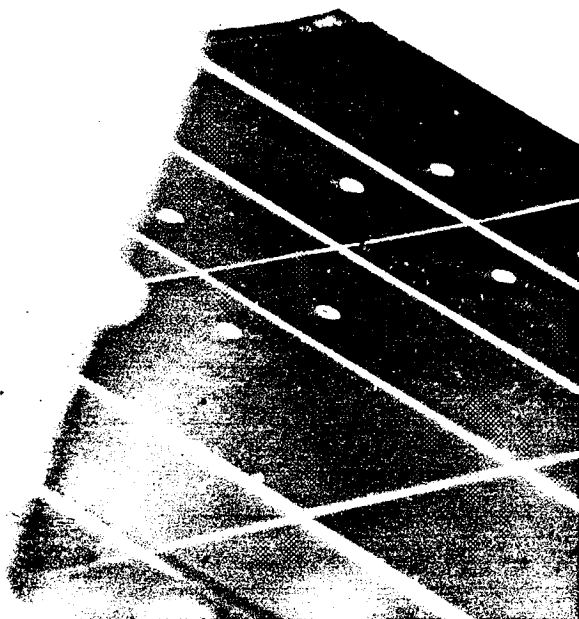
Estimates of the crater dimensions were also made by the use of photogrammetry by the Mapping Science Branch of the Lunar and Earth Science Division of the Manned Spacecraft Center. The results (Fig. IV-41) indicate that the crater had a diameter of 20 cm and a maximum depth of 1.3 cm.

*Slope of the erosion crater relative to the engine nozzle.* The full-scale laboratory spacecraft was oriented such that the simulated sun elevation and azimuth angles were the same as for the *Surveyor V* spacecraft. A horizontal platform was placed below the spacecraft corresponding to the nozzle height of 37 cm. Comparison showed the shadows on this platform, as observed through the television camera system, were in substantial agreement with



**Fig. IV-38. Post-firing mosaic of the same portion of footpad 2 trench seen in the pre-firing mosaic (Fig. IV-37). No disturbance was caused by the firing of vernier engine 2, which was approximately 1 m away (Day 258).**

(a)



(b)



Fig. IV-39. Top of compartment B taken before and after the firing. A lump of material was transported to the compartment top and splattered in a direction away from vernier engine 1. (a) Day 255, 02:29:29 GMT. (b) Day 265, 05:48:58 GMT.

those taken on the lunar surface. The platform was tilted at various angles, and comparisons were made. It was noted that, when the sun angle was such that a good shadow pattern existed below the nozzle, tilting the platform produced only small changes in the shadow pattern. Consequently, precise measurement of the relative surface slope below the nozzle was not possible. Estimate of the slope, relative to the engine nozzle exit plane, is 0 to 10 deg down toward the alpha-scattering sensor head.

**Erosion crater orientation.** The axis of the crescent-shaped erosion crater makes an angle of 30 deg with the  $+X$  axis (measured towards the  $-Y$  axis) of the spacecraft. That is, the points or cusps of the crescent point in the general direction of the sensor head. Because the spacecraft is sitting in a crater only three times its own diameter, the lunar surface beneath the spacecraft should be gently curved relative to the spacecraft  $X$ - $Y$  plane. Therefore, the lunar surface beneath both vernier engines 2 and 3 should slope toward the  $Y$  axis of the spacecraft at approximately the location of the alpha-scattering

instrument. This gentle slope of the lunar surface relative to the spacecraft probably caused differential erosion by each vernier engine. Such differential erosion could account in part for the orientation and crescent shape of the erosion crater.

**b. Viscous erosion.** The viscous erosion studies here and the diffused gas studies in the next part of this section make use of the theoretical flow field along the lunar surface and the associated surface loadings, as determined using Roberts' theory (Ref. IV-5).

Table IV-4 lists the engine parameters used in the calculations, and Figs. IV-42 through IV-44 show the theoretical predictions. Figure IV-42 shows the theoretical surface pressure, gas radial velocity, and the corresponding dynamic pressure [equal to  $(\frac{1}{2})\rho u^2$ , where  $\rho$  is the gas mass density and  $u$  is the gas radial velocity along the surface] associated with this radial velocity over a range of distances measured from a point directly below the engine (the stagnation point) for the *Surveyor V* vernier engine 3.

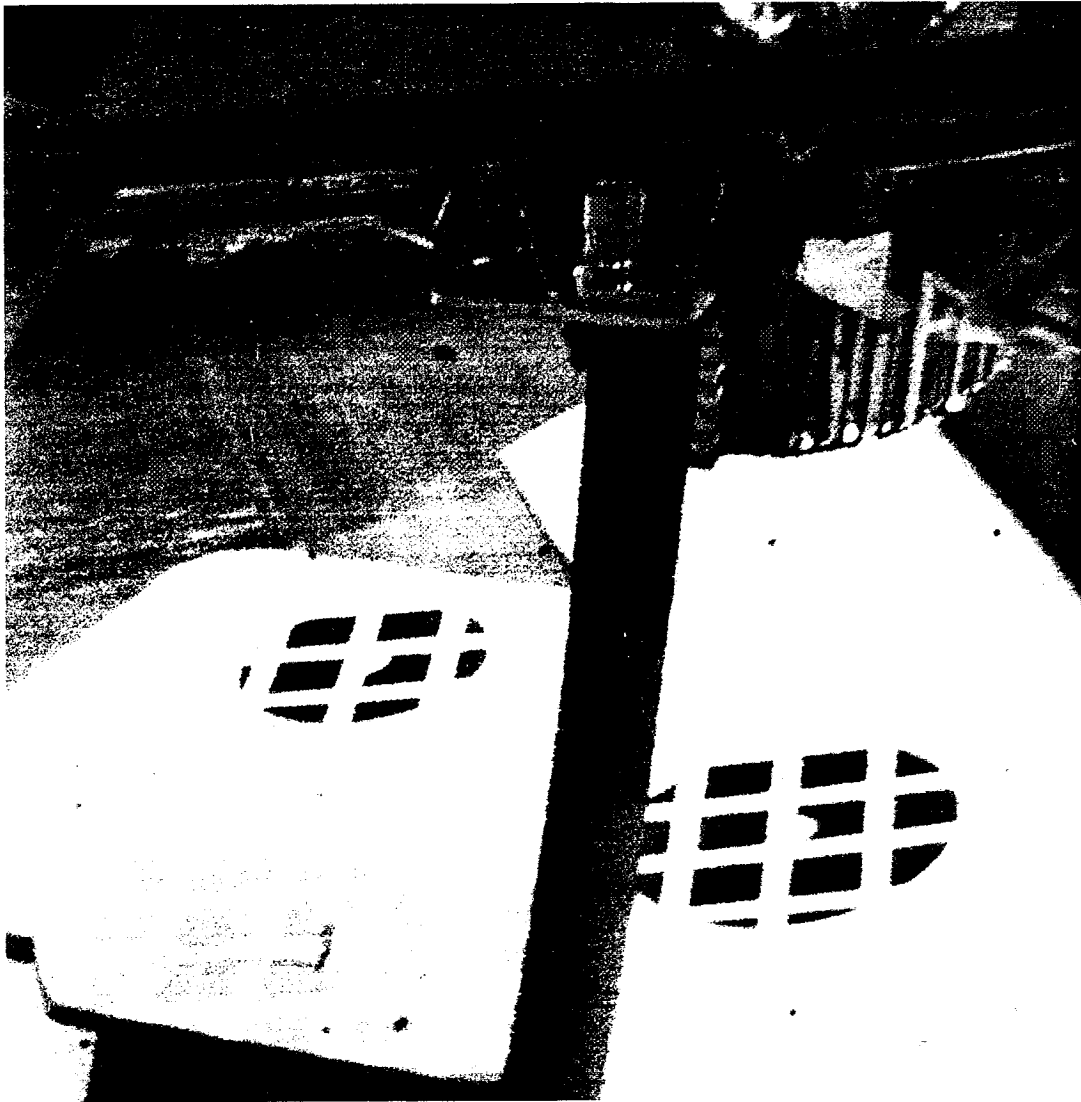
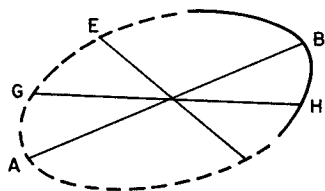
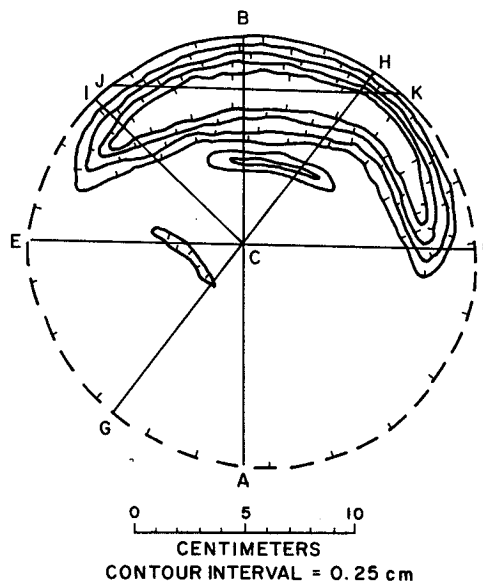


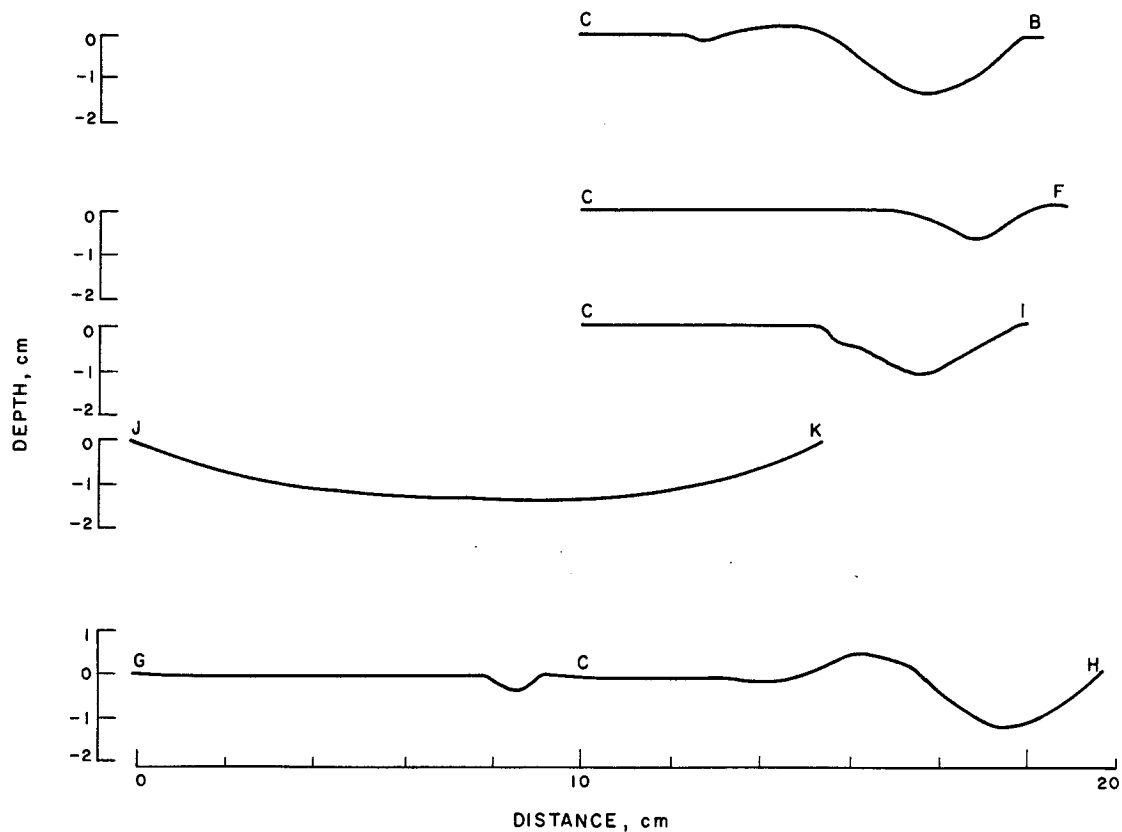
Fig. IV-40. Narrow-angle picture taken by the Surveyor V television camera system prior to launch.



(a) ORIENTATION OF CRATER AS SEEN THROUGH MIRROR BY TV CAMERA



(b) PLAN VIEW OF CRATER



(c) PROFILES ACROSS CRATER

**Table IV-4. Estimated vernier engine 3 data  
(used in calculations)**

Nozzle height .....	39.4 cm (15.5 in.)
Thrust .....	120 N (27 lb)
Chamber pressure .....	46.9 N/cm <sup>2</sup> (68 psia)
Chamber gas temperature .....	2950°K (5300°R)
Chamber gas viscosity .....	$5.6 \times 10^{-4}$ poise ( $1.17 \times 10^{-6}$ lb-sec/ft <sup>2</sup> )
Gas specific heat .....	1.313
Gas constant .....	367 m <sup>2</sup> /sec <sup>2</sup> °K (2190 ft <sup>2</sup> /sec <sup>2</sup> °R)
Nozzle exit radius .....	6.46 cm (0.2121 ft)
Nozzle exit mach number .....	5.2

These data correspond to conditions where the engine is exhausting onto a flat plane parallel with the nozzle exit plane. The figure indicates that surface pressure drops off rapidly with radial distance. Figure IV-44 again shows the dynamic pressure for surfaces tilted 0, 10, and 20 deg from the nozzle exit plane. For example, Fig. IV-44 indicates that, at a radial distance of 76 cm (about the distance from vernier engine 3 to the alpha-scattering instrument experimental package), the theoretical dynamic pressures are about 14, 76, and 210 dynes/cm<sup>2</sup> on surfaces tilted 0, 10, and 20 deg, respectively, relative to the nozzle exit plane.

Roberts' theory (Ref. IV-5) was also used to estimate the theoretical amount of viscous erosion for a range of soil cohesion for four particle sizes, for the engine conditions listed in Table IV-4 and the associated surface loadings shown in Figs. IV-42 through IV-44. The results of these computations are shown in Fig. IV-45. In these calculations, the aerodynamic friction and drag coefficients acting on the soil particles were taken to be 0.3 and 2, respectively. The soil internal friction angle was taken to be 35 deg.

According to Fig. IV-45, a soil composed of 100- $\mu$ -diameter particles and a cohesion of 1430 dynes/cm<sup>2</sup> would erode at a maximum rate of 0.36 cm/sec. Thus, for an engine firing time of 0.55 sec, the maximum erosion depth should be 0.2 cm (0.079 in.). If the soil particle diameter were 10 $\mu$  and had the same cohesion, the resulting erosion rate would be 0.061 cm/sec and, for the 0.55 sec, should produce a maximum erosion depth of 0.024 cm.

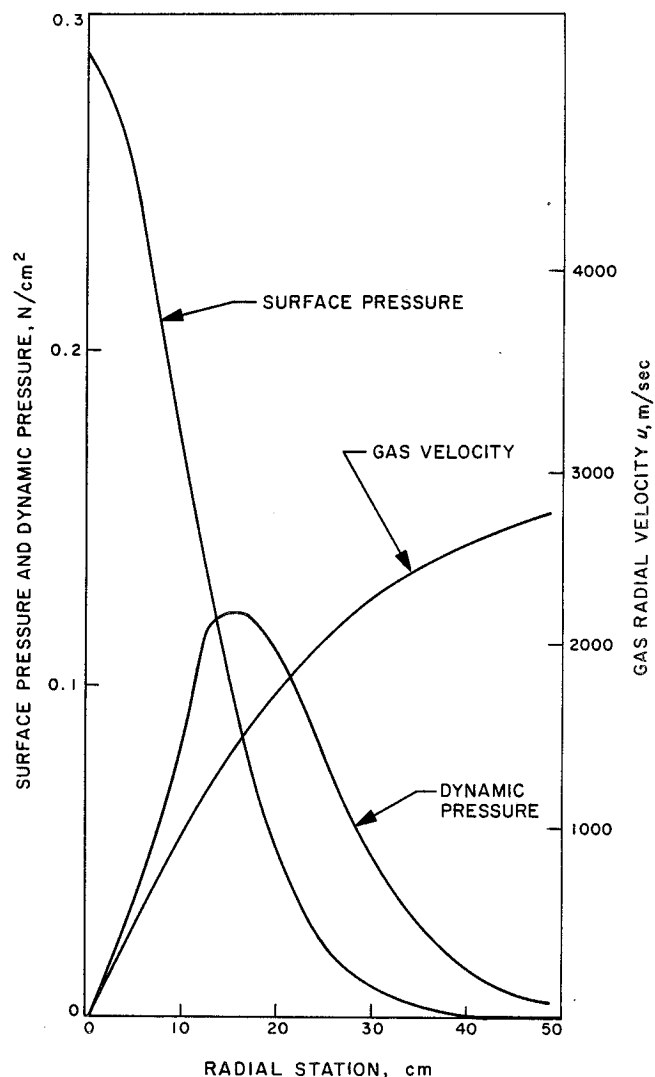


**Fig. IV-42. Theoretical static pressure, dynamic pressure, and exhaust gas radial velocity at the surface of a plane, parallel to the engine nozzle exit plane; engine thrust = 120 N, nozzle height = 39.4 cm.**

Theoretically, then, according to Fig. IV-45, the amount of erosion observed under vernier engine 3 (a depth of about 1 cm) could have occurred by viscous action only on a soil composed of particles larger than 500 $\mu$ . Since

**Fig. IV-41. Plan view and profiles of the crescent-shaped crater produced by the vernier engine 3 firing (taken from a drawing by the Mapping Science Branch, Lunar and Earth Science Division, Manned Spacecraft Center).**

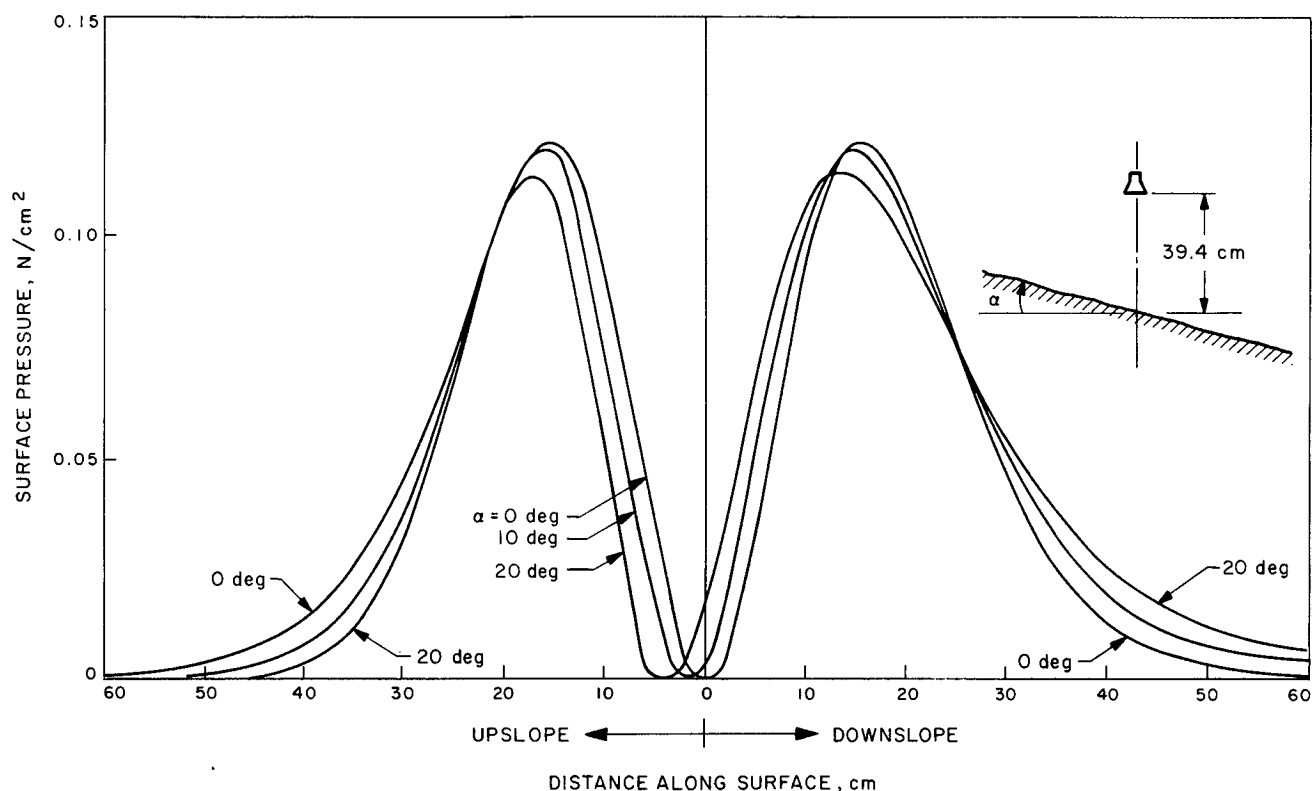


**Fig. IV-43. Theoretical dynamic pressure at the surface of planes tilted 0, 10, and 20 deg to the engine nozzle exit plane; engine thrust = 120 N; nozzle height = 39.4 cm. Dynamic pressure over a 60-cm range from a point directly below the engine.**

estimates of the lunar soil particle size indicate that the major proportion of grains present are smaller than  $500\mu$ , the comparison of theoretical and observed crater depths suggests that viscous erosion was not the major erosion mechanism for the removal of fine-grained material. Additional evidence that such is the case is suggested by a comparison of theoretical and observed crater diameters. The erosion crater was computed according to Roberts' theory for a soil composed of  $600\text{-}\mu$ -diameter particles and with a cohesion of  $960\text{ dynes/cm}^2$  (selected to approximate the observed average erosion rate). The results of these calculations are shown in Fig. IV-46. The figure indicates the crater diameter should have been 66 cm, whereas the observed crater diameter was about 20 cm. Thus, here again, evidence suggests that viscous erosion was not the major erosion in forming the crater.

**c. Gaseous diffusion erosion.** The results presented here were attained by use of the surface pressure obtained from Roberts' theory (Fig. IV-47) for a jet firing normally onto a horizontal surface of a homogenous, isotropic, porous medium. It should be noted that the diffusion

process is essentially independent of the direction of gravity and that the diffusion-caused soil erosion on a slope of 20 deg, calculated from the diffusion theory, is hardly distinguishable from that on a horizontal surface.

Results of diffusion calculations (by use of equations in Ref. IV-6) indicate that a diffusion-caused eruption crater, 32 cm in diameter and 3.5 cm in depth, would have been formed in a completely cohesionless and very permeable soil, (i.e., one in which steady-state gas flow conditions were reached by an 0.5-sec firing) for surface loading conditions corresponding to the *Surveyor V* test. However, for the same test conditions, but in a cohesionless and less permeable soil (requiring 5 sec to reach steady-state gas flow), the eruption crater would have been 18 cm in diameter and 1.5 cm in depth.

Diffusion theory indicates that the diameter of the diffusion-caused erosion crater is almost independent of the cohesion. Thus, by comparing the calculated crater diameter with the actual crater diameter formed during



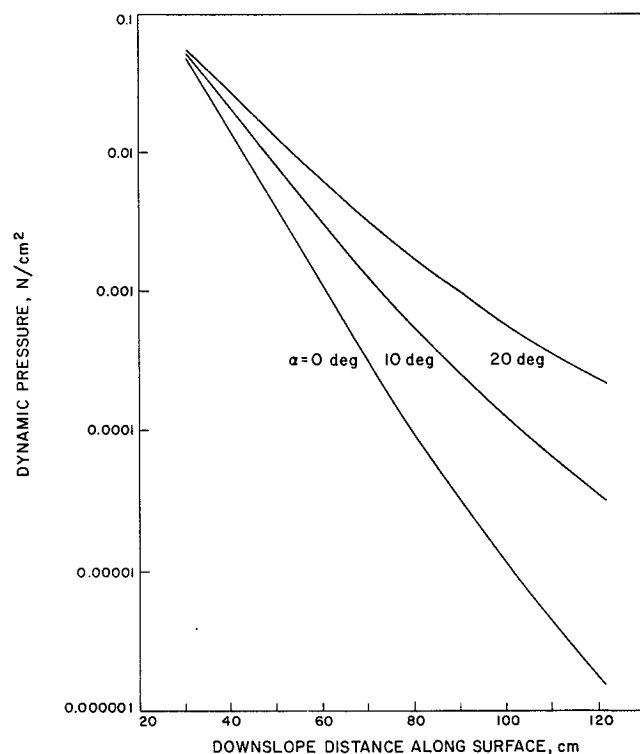


**Fig. IV-44. Theoretical dynamic pressure at the surface of planes tilted 0, 10, and 20 deg to the engine nozzle exit plane; engine thrust = 120 N; nozzle height = 39.4 cm. Dynamic pressure over a 30- to 120-cm range from a point directly below the engine.**

the experiment, it is possible to conclude that the experiment was performed on a relatively impermeable soil. By assuming that the soil porosity is between 0.3 and 0.5, the viscosity of the vernier exhaust gases in the soil is  $1 \times 10^{-4}$  poises and  $3 \times 10^{-4}$  poises (Ref. IV-12), and that an 0.5-sec firing is equivalent to about one-tenth the time required to reach steady-state conditions, the permeability of the soil medium is calculated to be between  $1 \times 10^{-8}$  and  $7 \times 10^{-8}$  cm². For comparison, consider the permeabilities of soils of different uniform grain sizes as measured on earth and shown in Fig. IV-48. This figure shows that the permeability range for the lunar surface material (down to a depth of around 25 cm) fits into the permeability range of silts having grain sizes between 2 and 60  $\mu$ . The lunar material, of course, contains particles larger and possibly some smaller than this range. However, the estimated lunar permeability indicates most of the particles are in the 2 to 60- $\mu$  size range. This estimate is also in agreement with conclusions reached from simulations of footpad imprints from *Surveyor III* (Ref. IV-2).

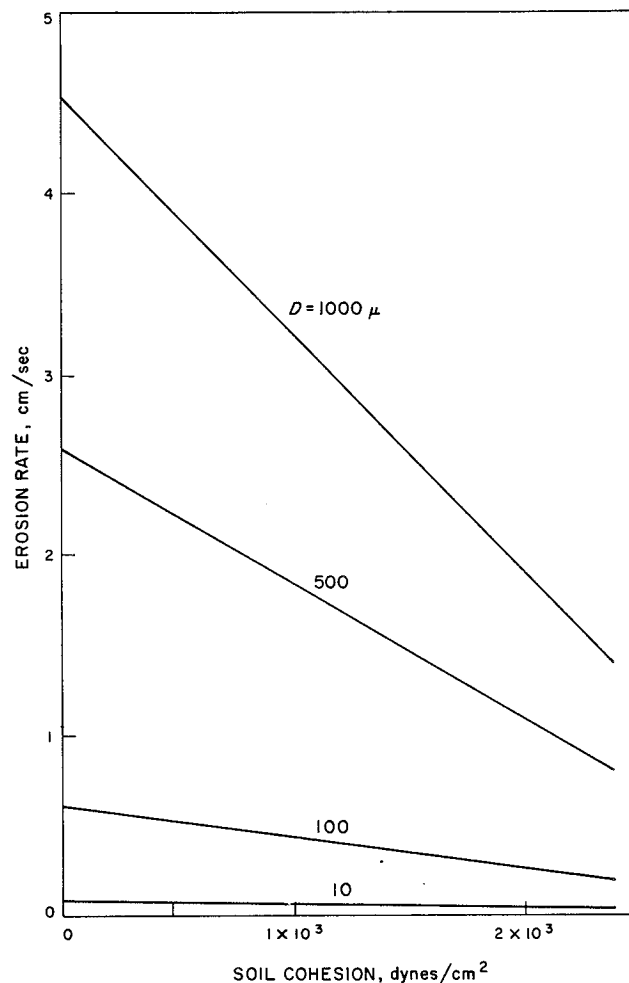


**Fig. IV-45. Theoretical viscous erosion rates as functions of soil cohesion and particle size; engine thrust = 120 N, nozzle height = 39.4 cm.**

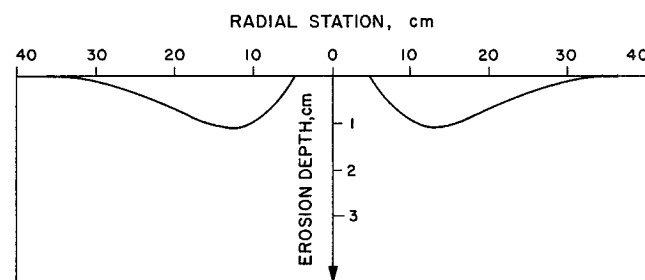


**Fig. IV-46. Theoretical viscous erosion crater profile for an arbitrarily chosen set of soil parameters selected to match the observed erosion depth. The actual lunar soil has smaller particle diameters. These results indicate that the lunar erosion crater was not produced by viscous erosion. Engine thrust = 120 N, nozzle height = 39.4 cm.**

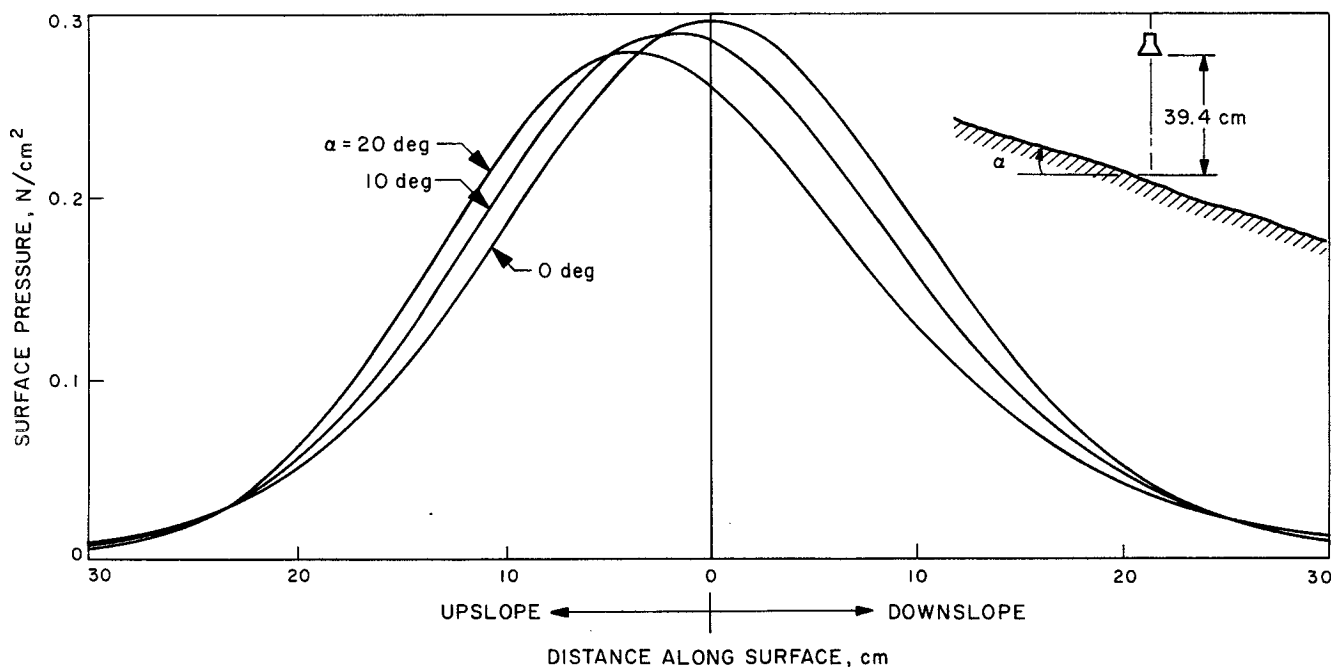


Fig. IV-47. Theoretical static pressure at the surface of planes tilted 0, 10, and 20 deg to the engine nozzle exit plane; engine thrust = 120 N; nozzle height = 39.4 cm.

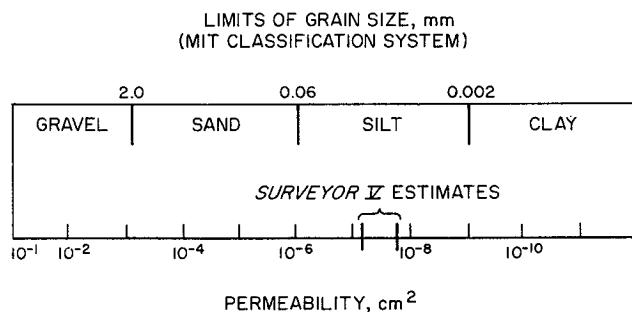


Fig. IV-48. Permeability of earth soils vs grain size and classification (Ref. IV-13).

Diffusion theory indicates that soil cohesion (and permeability) has a strong influence on crater depth, but that the frictional resistance has little influence on crater depth. This is because the soil elements are made potentially unstable and erodible by the upward flow of gases which essentially cancels the gravitational forces between soil grains, resulting in negligible interparticle frictional forces. If the lunar soil has the permeability indicated, then the gases flowing into and through the soil during an 0.5-sec *Surveyor V* firing would not have produced surface ero-

sion. If the firing time had been increased, or the soil permeability were different, so that diffusion erosion did occur before engine shutdown, then the crater from this erosion would have formed at a distance of about 19 to 25 cm from the stagnation point. Since the erosion crater on the moon has only a 10-cm radius, it is concluded that it was formed by diffused-gas eruption. Possibly a dish-shaped depression was first formed due to the shutoff eruption; but, since some of the materials erupted in trajectories nearly normal to the local surface, the downslope portion of the dish could be covered by materials that moved downslope as they fell back onto the surface. In the absence of good, simulated vernier firing tests, it is difficult to calculate the effect of a slight amount of cohesion on influencing the depth of erosion.

*d. Differences of theoretical predictions and experimental findings.* In the preceding sections, comparisons were made of the observed lunar erosion crater under vernier engine 3 with theoretical craters formed by gas viscous forces and diffused gas forces. The theoretical predictions were not in complete agreement with observed results, i.e., the observed crater shape is not what would be predicted by theory. In addition, theory does not predict that soil would be eroded at the large distances observed.

The theories predict an axisymmetric crater, whereas, the observed crater was crescent-shaped. It is surmised that the lunar crater shape could have been caused by one or several of the following factors:

- (1) Flow of gases out of the nozzle may not have been symmetrical.
- (2) Material that blew upward could have settled unevenly because of the surface slope.
- (3) Lunar surface below the nozzle may have been nonhomogeneous, had an irregular shape, and have been tilted relative to the nozzle exit plane.

These theories also would not have predicted the movement of fine soils that occurred as far as a meter from vernier engine 3. However, neither theory makes any attempt to explain the soil motions after the soil particles leave the crater. It is surmised that this erosion of fine soils did occur by a viscous erosion mechanism and/or by the impact of material ejected from under the engine.

Both theories of soil cratering used the axisymmetric surface loading predicted by Roberts' theory when the nozzle exit plane is parallel with the surface. However, tests made on earth indicate that the engine exhaust gases can deviate substantially from perfect symmetry and thereby produce a nonsymmetric surface loading.

Another basic assumption in the theory is that the lunar soil is uniform and the surface is a flat plane. Instead, the lunar surface is an undulating, irregular surface with a top layer that is more porous and less dense than the soil that is centimeters below the top (Ref. IV-2). These conditions would strongly influence both theories.

## 5. Implications of Movement of Alpha-Scattering Instrument by Vernier Engine Firing

Several calculations, based on the observed effects of the vernier engine firing in moving the alpha-scattering instrument, provide information on the resistance of the lunar soil to the motion of the alpha-scattering instrument sensor head.

The alpha-scattering instrument, located at a distance (nearest corner) of 68 cm from vernier engine 3 (the nearest *Surveyor* vernier engine), was moved downslope during the firing so that its distance from the engine became 77 cm. The spacecraft is assumed, for calculation purposes, to be resting on a slope of about 20 deg to the horizontal, dipping downward in a direction parallel to the spacecraft's -Y axis.

*a. Soil resistance from static considerations.* Pressure may be developed both from the engine gas pressure and momentum exchange from soil particles impinging on the alpha-scattering instrument. However, on *Surveyor V*, pressure on the instrument during firing was not great enough to overturn it. Bounds on this pressure,  $p$ , can be calculated from Fig. IV-49. Assume that the pressure is equally distributed over one face of the instrument, having an area of 225 cm<sup>2</sup>. The center of this face is 7.9 cm from the lunar surface, a vertical line through the center of gravity is 11.1 cm from the circular plate edge furthest from this face, and the mass of the alpha-scattering instrument is 2.2 kg. Equating the torques arising from pressure and from weight, the applied force at which the alpha-scattering instrument would start to overturn is  $6.5 \times 10^5$  dynes, and the corresponding pressure on the face is  $2.4 \times 10^3$  dynes/cm<sup>2</sup>. This sets an upper bound for  $p$ . Because the sensor head moved during the firing, it follows that the pressure acting on it was sufficient to overcome the frictional resistance on the base of the apparatus. If it is assumed that there was no adhesion between the alpha-scattering instrument and the lunar surface, which seems reasonable from the pictures taken after the movement (Fig. IV-28), a friction coefficient,  $\mu$ , can be assumed to act between the alpha-scattering instrument and the soil. Referring to Fig. IV-49, a balance of forces parallel to the slope gives a pressure not exceeding  $(1.65\mu - 0.59) \times 10^3$  dynes/cm<sup>2</sup>. This is a lower bound for  $p$ . Since the lower bound must be less than the upper bound, the maximum possible value for the coefficient of friction,  $\mu_{max}$ , is 1.84. As the far side of the circular plate appears to have dug into the lunar surface during the sliding, it is probably more satisfactory to derive, not a value of  $\mu$ , since the resistance was not all frictional, but a soil resisting force, which then would have a maximum value of

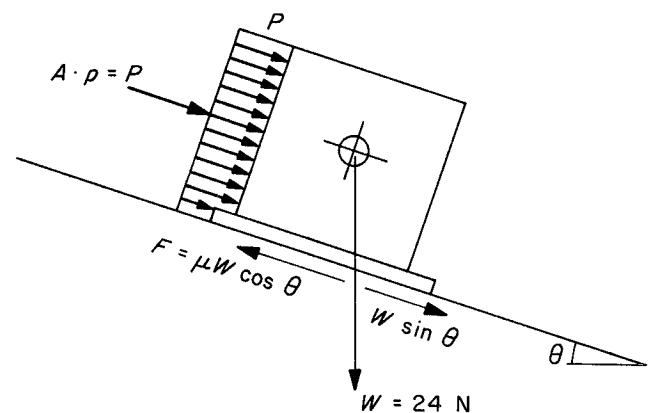


Fig. IV-49. Balance of forces on the alpha-scattering instrument sensor head during the vernier engine firing.

$6.9 \times 10^5$  dynes. This analysis neglects any small forces on the alpha-scattering instrument that may arise from the attached nylon cord and electrical cable.

**b. Soil resistance from dynamic considerations (equation of motion).** The equation of motion for the alpha-scattering instrument during vernier engine firing is established on the basis that the acting force is constant during the period of firing, and that the resisting force has a constant magnitude at all stages during the motion. The equation follows:

$$\ddot{x} = g \sin \theta + \frac{(P - F)}{m} \quad (1)$$

where

$x$  = distance parallel to the surface

$g$  = lunar gravitational constant

$\theta$  = tilt angle

$P$  = force on alpha-scattering instrument from vernier engine firing

$F$  = resisting force of soil

$m$  = mass of sensor head

The initial conditions are  $\dot{x} = 0$ ,  $x = 0$ , taking the  $x$ -coordinate downslope. Integrating twice and substituting for  $t$ , a firing duration of 0.5 sec (which allows a short time for pressure buildup in the vernier engine firing) gives the velocity and displacement reached by the end of vernier fire as

$$\dot{x}_e = \left( g \sin \theta + \frac{P - F}{m} \right) 0.5 \quad (2)$$

$$x_e = \left( g \sin \theta + \frac{P - F}{m} \right) \frac{(0.5)^2}{2} \quad (3)$$

After firing stops, we take a new  $t$  and  $x$  beginning at the end of firing. The equation of motion is now

$$\ddot{x} = g \sin \theta - \frac{F}{m} \quad (4)$$

with initial conditions  $\dot{x} = \dot{x}_e$  and  $x = 0$ . Integration twice gives

$$\dot{x} = \left( g \sin \theta - \frac{F}{m} \right) t + \dot{x}_e \quad (5)$$

$$x = \left( g \sin \theta - \frac{F}{m} \right) \frac{t^2}{2} + \dot{x}_e t \quad (6)$$

The alpha-scattering instrument comes to rest when  $x = 0$ , at time  $t_0$  so that, from Eq. (5)

$$\left( g \sin \theta - \frac{F}{m} \right) t_0 = -\dot{x}_e = -g \sin \theta + \frac{(P - F)}{m} 0.5 \quad (7)$$

Equation (7) then gives a relation among  $P$ ,  $F$ , and  $t_0$ , the time between cessation of firing and the time when the alpha-scattering instrument stops moving. However, the total distance moved by the sensor head is estimated at 11 cm from Figs. IV-27 and IV-28; this can be equated to the sum of the displacements given by Eqs. (3) and (6)

$$g \sin \theta + \frac{P - F}{m} \frac{(0.5)^2}{2} + g \sin \theta - \frac{F}{m} \frac{t_0^2}{2} + \dot{x}_e t_0 = 11 \quad (8)$$

Equation (8) gives a second relation among values of  $P$ ,  $F$ , and  $t_0$ .

Since more observational requirements are met by the solution of Eqs. (7) and (8), they are more restrictive than the general limiting analyses given previously. Consequently, the upper limit of  $P$  can be used in Eqs. (7) and (8) and they determine an upper bound on  $F$  of  $5.2 \times 10^5$  dynes. This corresponds to an upper limit of frictional coefficient of 1.38, if the frictional mechanism is assumed. The lowest value of  $F$  which will satisfy Eqs. (7) and (8) is  $F = 2.2 \times 10^5$  dynes at  $t_0 = 0.6$  sec. The value of  $P$  corresponding to this value of  $F$  is  $1.8 \times 10^5$  dynes. It follows, therefore, that an absolute lower bound on the effective coefficient of friction is  $\mu = 0.59$ , and on the value of pressure represented by  $P$  is  $8.1 \times 10^3$  dynes/cm<sup>2</sup>. Therefore, from this analysis, the following tabulation can be compiled:

Bound	Acting force, $P$ , dynes	Acting pressure, $p$ , dynes/cm <sup>2</sup>	Resisting force, $F$ , dynes	Effective coefficient of friction, $\mu$
Upper	$6.5 \times 10^5$	$2.4 \times 10^3$	$5.2 \times 10^5$	1.38
Lower	$1.8 \times 10^5$	$8.1 \times 10^2$	$2.2 \times 10^5$	0.59

It may be remarked that it does not seem reasonable that the duration of sliding of the alpha-scattering instrument,  $t_0$ , after vernier engine shutdown, could be as long as the 0.6 sec required by the lower-bound case. If it is assumed that the sliding duration would be less than the firing duration, and the observation is made that the far edge of the alpha-scattering instrument is dug into the lunar surface, suggesting some tendency to overturning,

more reasonable values of  $t_0$  such as 0.3 or 0.4 sec might be taken. For these values, solution of Eqs. (7) and (8) gives

Duration of sliding after vernier shut-down, sec	$P$ , dynes	$p$ , dynes/cm <sup>2</sup>	$F$ , dynes	$\mu$
0.3	$4.4 \times 10^5$	$2.0 \times 10^3$	$4.1 \times 10^5$	1.10
0.4	$3.2 \times 10^5$	$1.4 \times 10^3$	$3.1 \times 10^5$	0.84

The angle of internal friction, indicated by the surface sampler tests on *Surveyor III*, was about 37 deg. The tangent of this angle (friction coefficient) is 0.75, so that either of the last two values in the table,  $\mu = 0.84$  or 1.10, would be compatible with the *Surveyor III* results plus some small amount of cohesion. If there were no plowing, the  $\mu$  determined should therefore be a lower bound for the soil coefficient. It is likely, however, that the effect of plowing increases the effective value of  $\mu$ .

**c. Movements of particles by vernier exhaust.** A calculation has been made of the size of soil or rock fragments, at a distance of approximately 80 cm from vernier engine 3, that would be expected to slide downslope under the pressure  $p$ , and with the friction coefficient  $\mu$ , shown previously. This indicates that the pressure was sufficient to cause the motion of the particles noted in Figs. IV-27 and IV-28 and also the motion of appreciably larger particles.

## E. Conclusions and Summary

- (1) During landing, *Surveyor V* slid about 0.8 m down the inner slope of a 9- × 12-m crater. During this sliding, at least two of the footpads dug trenches in the lunar surface material. The initial depth of penetration for one footpad was about 12 cm. Ejecta was thrown 80 cm or more.
- (2) Soil pressure developed in resisting the footpad sliding during the landing was about 0.9 N/cm<sup>2</sup>, which agrees with the stalling pressure during

trenching with the soil mechanics surface sampler on *Surveyor III*.

- (3) Minimum effective coefficient of friction (braking) between the footpads and the surface is 0.36.
- (4) Best agreement obtained for a compressible soil model with the observed *Surveyor V* footpad penetrations and landing leg loads is for a soil static-bearing capability of 2.7 N/cm<sup>2</sup> and a density of 1.1 g/cm<sup>3</sup>. Incompressible soil model analyses have not yet been performed for *Surveyor V*. Preliminary analyses indicate that soil at the *Surveyor V* landing site is weaker than at previous *Surveyor* landing sites.
- (5) Surface material is granular, slightly cohesive, and generally fine-grained, as at the *Surveyor I* and *III* landing sites. However, the differences in reflectivity between disturbed and undisturbed lunar soil is less than at the *Surveyor I* and *III* landing sites.
- (6) During the 0.5-sec vernier engine firing, soil and fragments to undetermined depths were removed by viscous erosion from areas below and adjacent to at least one vernier engine. Soil or rock fragments moved included large fragments up to 4.4 cm in diameter, which were close to the vernier engine, and small fragments up to 0.6 cm in diameter at distances up to 1.9 m. At engine shutdown, exhaust gas which had diffused into the soil erupted, producing a crater 20 cm in diameter and 0.8 to 1.3 cm deep under one engine.
- (7) Permeability of this lunar soil, to a depth of 25 cm or so, is  $1 \times 10^{-8}$  to  $7 \times 10^{-8}$  cm<sup>2</sup>. This corresponds to the permeability of earth silts and indicates most of the lunar particles are in 2- to 60- $\mu$  size range.
- (8) Capability of lunar material to adhere to a smooth vertical surface is indicated by the change of reflectivity of the alpha-scattering sensor head as a result of the vernier engine firing.
- (9) Vernier engine firing did not cause any degradation in the functional capability of the spacecraft.

## References

- IV-1. Christensen, et al., "Lunar Surface Mechanical Properties – *Surveyor I*," *J. Geophys. Res.*, Vol. 72, pp. 801–813, 1967.
- IV-2. Christensen, E. M., et al., "Lunar Surface Mechanical Properties," and Scott, R. F., et al., "Soil Mechanics Surface Sampler," *Surveyor III Mission Report. Part II: Scientific Results*, Technical Report 32-1177, Jet Propulsion Laboratory, Pasadena, Calif., 1967.
- IV-3. *Surveyor I Flight Performance Final Report*, Hughes Aircraft Co. Report SSD 68223R, Vol. 3, October 1966.
- IV-4. *Surveyor III Flight Performance Final Report*, Hughes Aircraft Co. Report SSD 68189-3, August 1967.
- IV-5. Roberts, L., "The Action of a Hypersonic Jet on a Dust Layer," IAS Paper 63-50, Presented at the IAS 31st Annual Meeting, New York, New York, January 21–23, 1963.
- IV-6. Scott, R. F., and Ko. H. Y., "Transient Rocket-Engine Gas Flow in Soil," to appear in *J. AIAA*.
- IV-7. Alexander, J. D., Roberds, W., and Scott, R. F., "Soil Erosion by Landing Rockets," Final Report NASA Contract NAS9-4825, July 1966.
- IV-8. Land, N. S., and Clark, L. V., "Experimental Investigation of Jet Impingement on Surfaces of Fine Particles in a Vacuum Environment," NASA TND-2633, February 1965.
- IV-9. Stocky, J. F., and Breshears, R. R., "Surveyor Vernier Engine/Surface Interaction Experiments," *Flight Projects*, Space Programs Summary 37-47, Vol. I, Jet Propulsion Laboratory, Pasadena, Calif., September 30, 1967 (confidential).
- IV-10. Dodge, C. H., *Space Exploration Programs and Space Sciences*, Space Programs Summary 37-40, Vol. VI, pp. 11–15, Jet Propulsion Laboratory, Pasadena, Calif., July 31, 1966.
- IV-11. Dodge, C. H., *The Lunar Program*, Space Programs Summary 37-43, Vol. I, pp. 7–11, Jet Propulsion Laboratory, Pasadena, Calif., January 31, 1967 (confidential).
- IV-12. Pao, R. H. F., "Fluid Dynamics," C. E. Merrill, Columbus, Ohio, 1967.
- IV-13. Scott, R. F., "Principles of Soil Mechanics," Addison-Wesley, Reading, Mass., 1963.

## Acknowledgment

Thanks are given to Frank Sperling, JPL, for his major contributions to the section on spacecraft landing analysis and dynamic simulations; to Charles Goldsmith, William Peer, Alex Irving, Albert Plescia, and Lloyd Starkes, JPL, for their work on spacecraft shadow predictions and assembly of photographic mosaics; to Robert Breshears, John Stocky, and Charles Dodge, for their vernier engine performance analyses; and to Dave Conaway, Margaret Dove, and John Hinchey, Hughes Aircraft Company, for assisting in the landing dynamic simulations.

## V. Lunar Surface Temperatures and Thermal Characteristics

J. W. Lucas, R. R. Garipay, W. A. Hagemeyer, J. M. Saari,  
J. Smith, and G. Vitkus

Another opportunity to obtain spacecraft thermal performance data on the lunar surface was provided by *Surveyor V*, which landed on Day 254 (September 11, 1967), at 00:46:44 GMT; the sun was approximately 17 deg above the horizon. *Surveyor V* was interrogated during the first lunar day until Day 272 (September 29) at 06:37 GMT or about 115 hr after sunset; interrogation on *Surveyor I* terminated 48 hr after sunset, and on *Surveyor III* 2 hr after sunset. Thus, *Surveyor V* provided the most extended lunar night performance data. On Day 288 (October 15), the spacecraft was reactivated for the second lunar day; on that day, the sun was rising at the landing site and was approximately 75 deg above the local horizon. On Day 291 (October 18), between 07:58 and 12:59 GMT, a lunar eclipse occurred; excellent temperature readings were obtained. Data received to sunset of the second lunar day are presented here; data received until 12:15 GMT on Day 305 (November 1) into the lunar night will be reported at a later date.

Following the *Surveyor I* and *III* analyses (Refs. V-1 and V-2), outboard-face temperatures of compartments A and B were used to derive average brightness temperatures of the lunar surface. Calculated temperatures during the night and during the eclipse were used to estimate the thermal inertia,  $\gamma$ , of the lunar surface material.

### A. Albedo, Lunar Surface Temperatures, and Thermophysical Properties of Landing Site, as Determined by Telescope

The total surface albedo for the landing site was determined to be 7.7%, and was derived by the same method as for the *Surveyor III* landing site (Ref. V-1). The method used to calculate total albedo depends on a telescopic measurement made to a resolution of 10 sec of arc (18 km at the center of the lunar disk). Thus, the local actual albedo of the *Surveyor V* landing site may depart from the predicted value because only a lunar disk of approximately 100-m diameter (with a spacecraft at the center) is of interest.

The lunar surface temperatures during lunation depend upon the lunar surface thermal inertia parameter, defined as

$$\gamma = (k\rho c)^{-1/2}$$

where  $k$  is thermal conductivity,  $\rho$  is density, and  $c$  is specific heat. For a  $\gamma$  of 500, 800, and 1000 (in cgs units), lunar surface brightness temperatures (Fig. V-1) for an equatorial site were computed (Ref. V-3). (Note that only after sunset is it possible to distinguish the thermal inertia parameter of lunar surface material for  $\gamma > 500$ .)

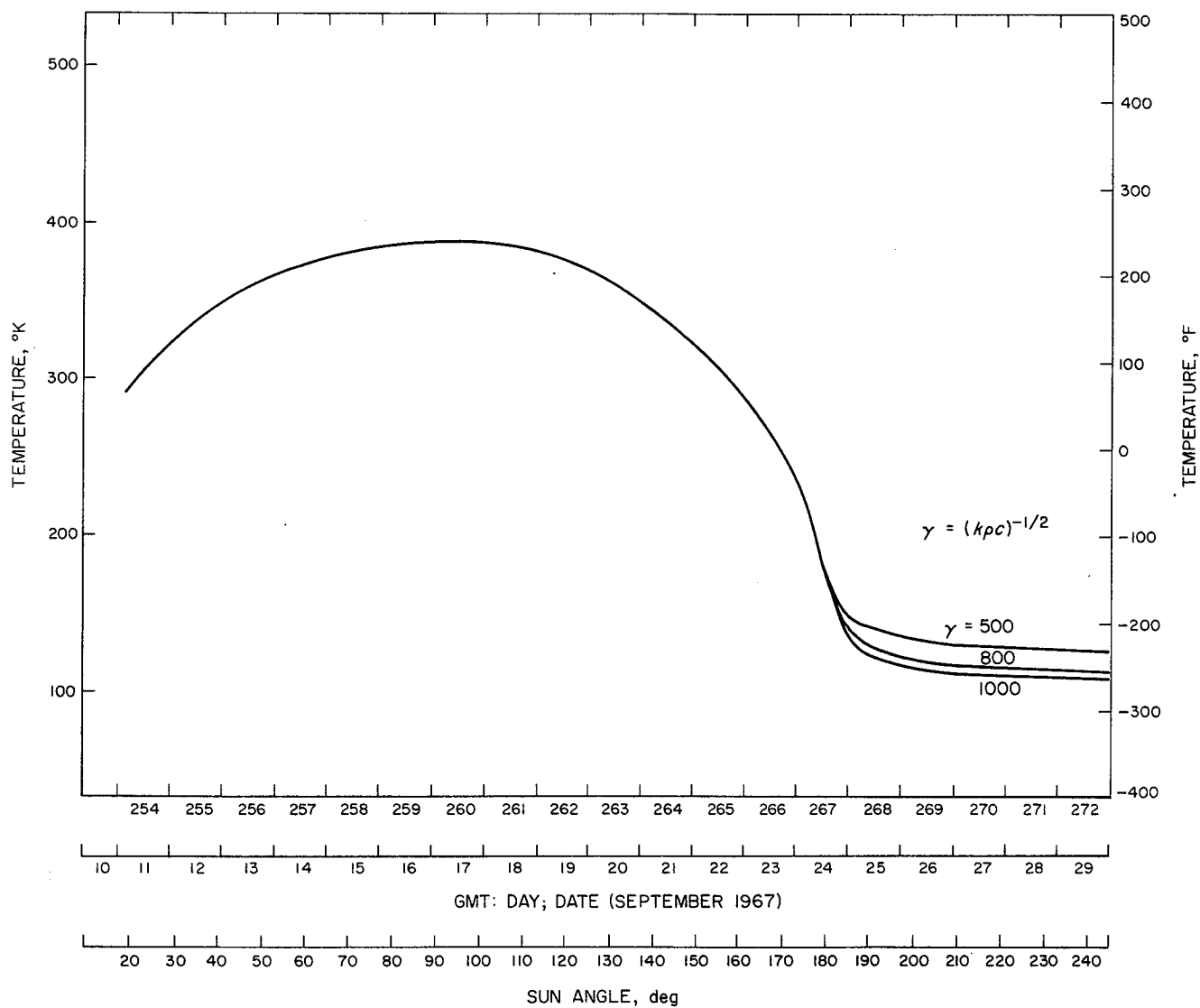
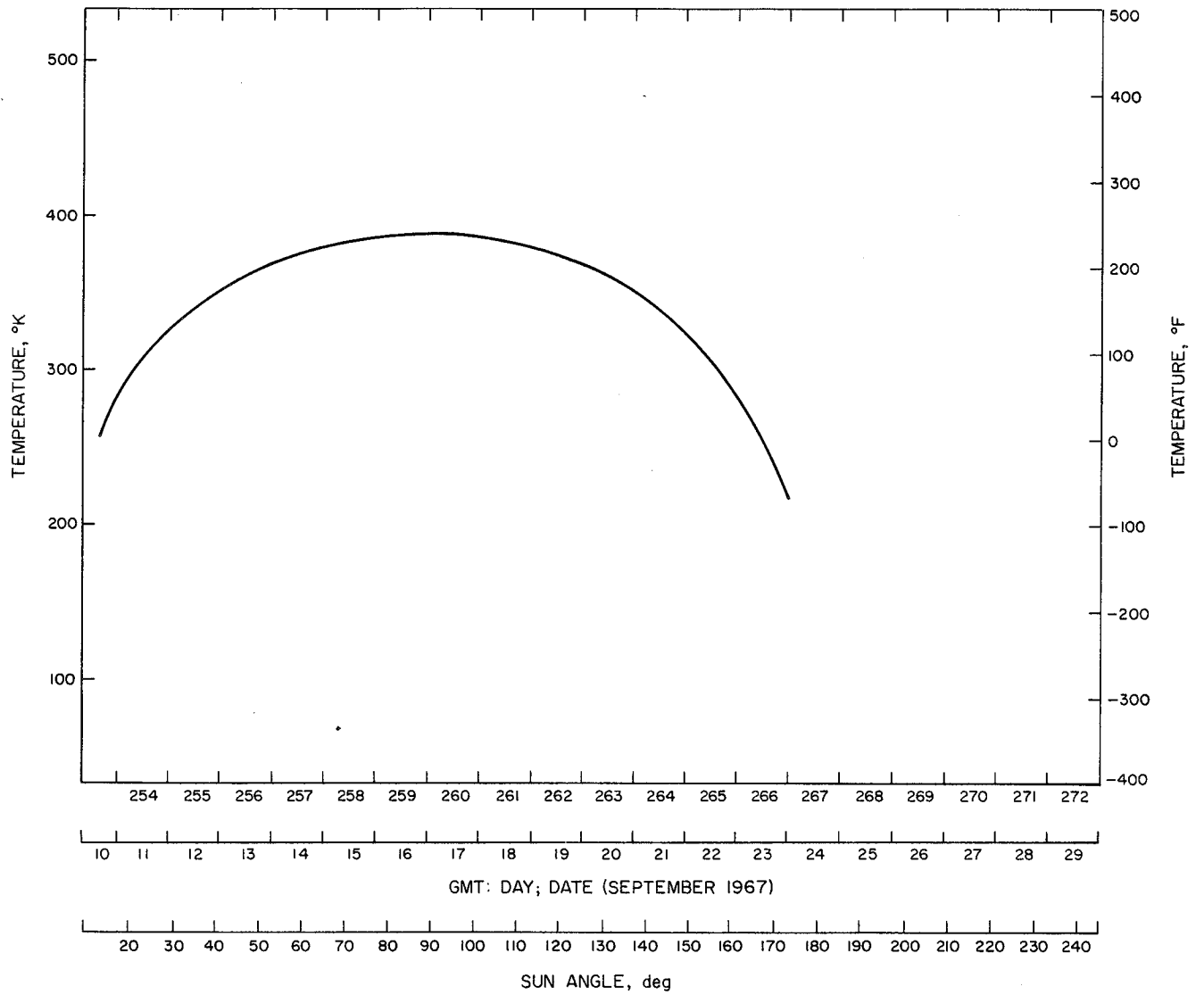


Fig. V-1. Predicted lunar surface brightness temperatures on the lunar equator.





**Fig. V-2. Earth-based lambertian temperatures for Surveyor V landing site, assuming level lunar surface.**

The calculated lambertian temperatures for the *Surveyor V* landing site are shown in Fig. V-2. A total solar albedo of 7.7% and a value of 2 cal/cm<sup>2</sup>-min for solar isolation were used in calculations. The calculated lambertian lunar surface temperatures during the sunlit portion of the lunation are in agreement with those shown in Fig. V-1.

Infrared measurements made during the December 19, 1964, eclipse showed that the lunar surface exhibits a great deal of thermal inhomogeneity (Refs. V-4 and V-5). The isothermal contours of the *Surveyor V* landing site obtained during total eclipse are shown in Fig. V-3. The

region appears to be relatively bland when observed from earth with a resolution of 18 km. It is expected that temperature fluctuations could exist to a scale comparable to that of the *Surveyor V* landing site; thus, it is possible that the thermal characteristics of the site are considerably different than they appear as observed from earth.

Figure V-4 is a predicted eclipse cooling curve for the site, based on measurements obtained by Saari and Shorthill (Refs. V-4 and V-5) during the December 1964 eclipse. The warming portion of the curve represents calculated equilibrium surface temperatures corresponding to the insolation at each time. By using the theoretical

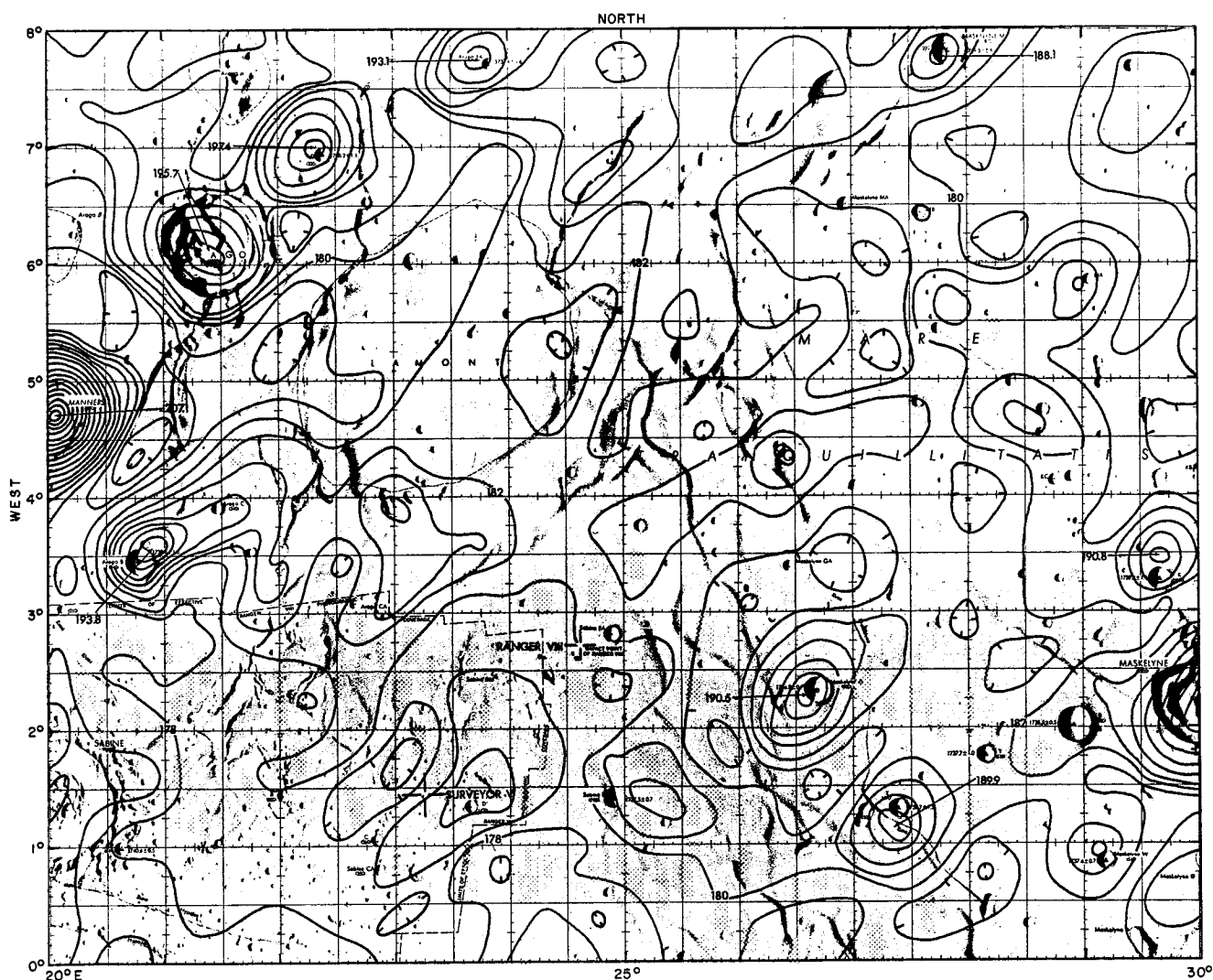
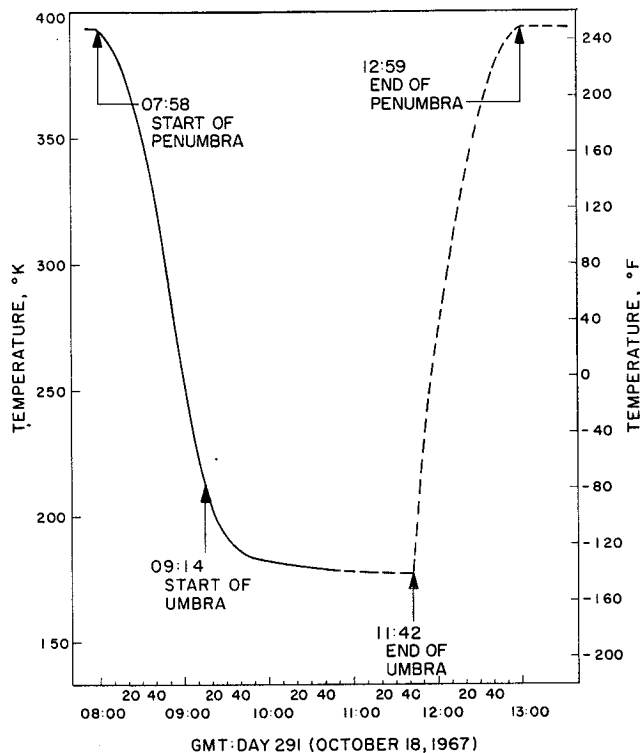


Fig. V-3. Isothermal contours for landing site region, obtained during totality of lunar eclipse of December 19, 1964.



**Fig. V-4. Predicted lunar surface temperatures during eclipse (data from December 19, 1964, eclipse adjusted in time for October 18, 1967, eclipse).**

eclipse cooling curves for a homogeneous model (Ref. V-5), a  $\gamma$  of 1350 is obtained for the lunar surface material.

## B. Spacecraft View of Lunar Surface

*Surveyor V* landed in a small ( $9 \times 12$  m) crater, with leg 1 positioned near the crater rim and legs 2 and 3 downslope on the southwest wall of the crater. (For details of the landing site, see Fig. III-3 of Section III.) At approximately sunset of the first lunar day, the shock absorbers on legs 2 and 3 compressed, placing the spacecraft even more downslope. Figure V-5 shows the assumed orientation of *Surveyor V* with respect to the lunar coordinates after landing, and after sunset of the first lunar day. During the second lunar day, the spacecraft positioned itself to the orientation it had during the first lunar day.

The location of the spacecraft within the crater profile is shown in Fig. V-6. Compartment A primarily views the east side of the crater, the surface above the crater, and space. The overall view factor from compartment A to

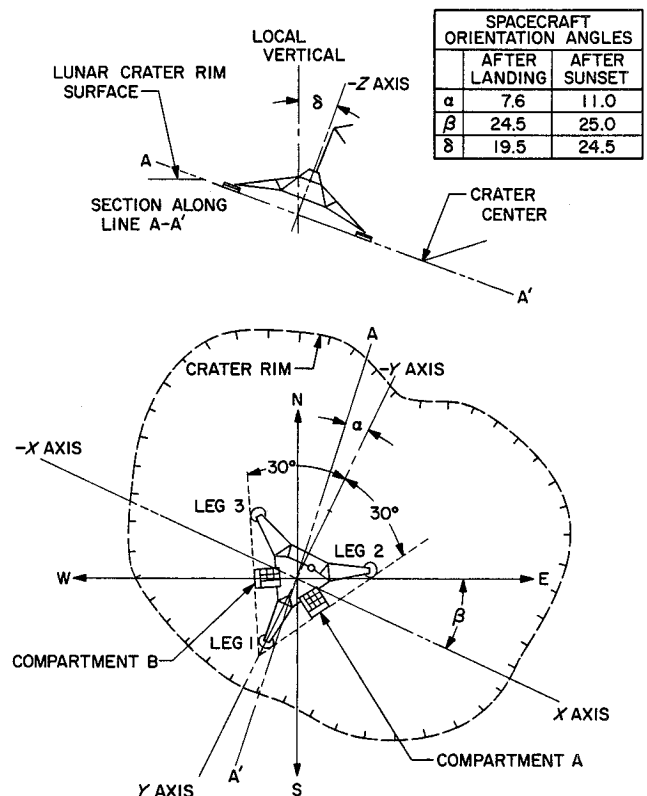


**Fig. V-5. Surveyor V landed orientation.**

the lunar surface is 0.247, of which 0.163 is to the crater wall; the remaining view factor of 0.084 is to the surface above the crater rim. Compartment B views the west side of the crater, the surface above the crater rim, and space. The overall view factor from compartment B to the lunar surface is 0.255; the view factor to the crater wall is 0.153; the view factor above the crater wall is 0.102. Spacecraft positioning after sunset had very little effect on the overall view factor for either compartment.

## C. Spacecraft Raw Data

### 1. Spacecraft Description

*Surveyor V* is similar in structural and thermal designs to *Surveyors I* and *III*. The basic frame (Fig. V-7) is tubular aluminum, which serves as a tetrahedral mounting structure for the electronic gear and propulsion systems. The three spacecraft legs are attached at the three corners of the base. The planar array antenna and solar panel, mounted on a mast approximately 1 m above the structure's apex, cast varying shadow patterns on the spacecraft and on the lunar surface throughout the lunar day.

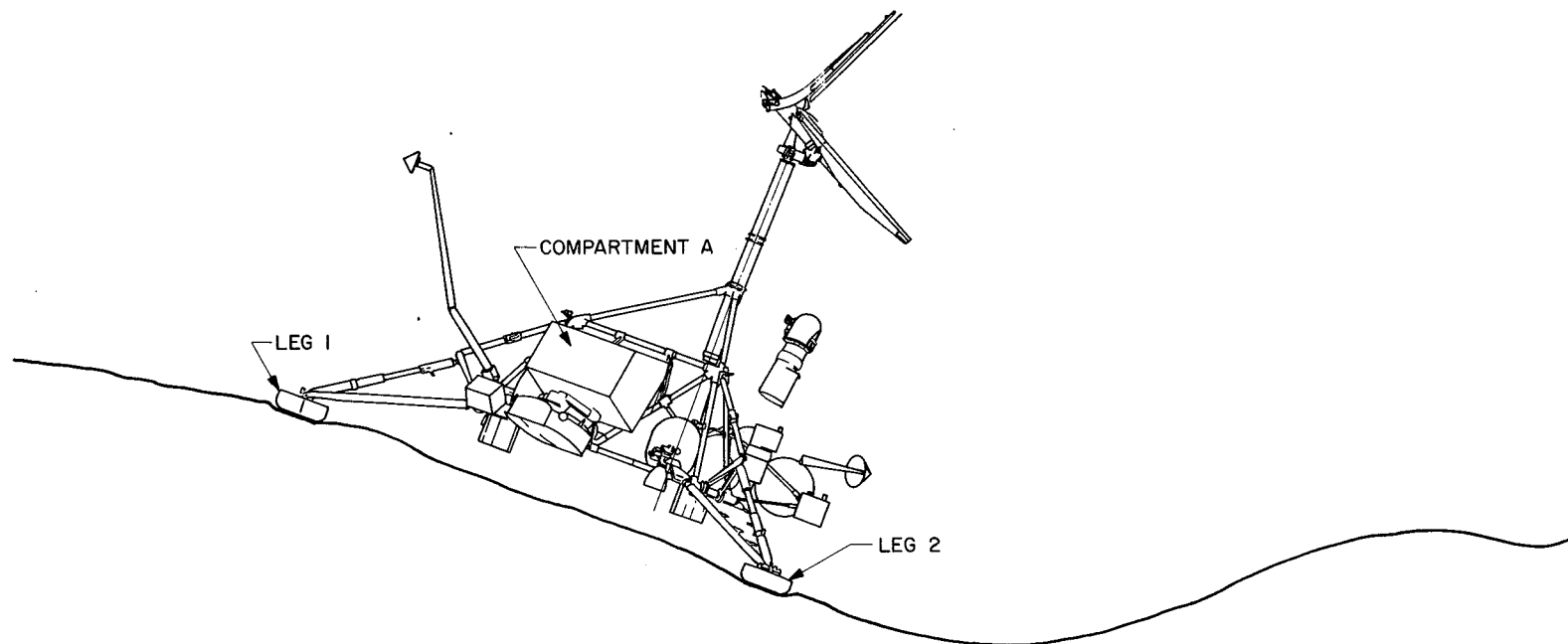


Fig. V-6. Profile of crater in which Surveyor V landed.

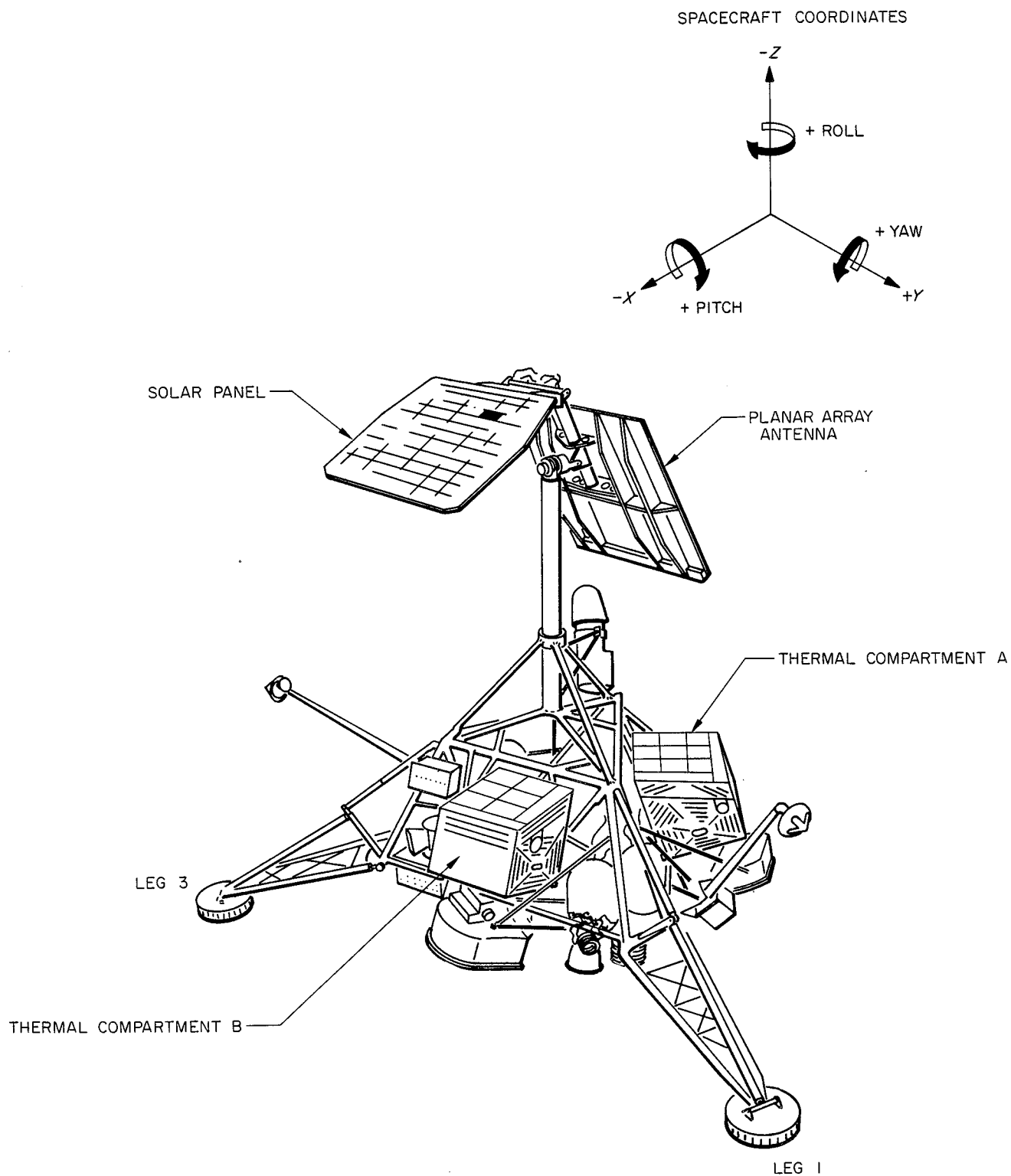


Fig. V-7. Surveyor spacecraft configuration.

Changes in shadow patterns occur as a result of the repositioning of the planar array antenna and solar panel and from the normal (0.5-deg/hr) movement of the sun.

The thermal finish of the structural members is a combination of inorganic white paint, applied to all top and visible side surfaces, and polished aluminum (Ref. V-2); the underside of the surface is polished metal. This thermal finish distribution provides a low-solar-absorptance, white-paint surface in the sun-illuminated areas, with a high-emittance coupling to space in the infrared regions. The polished-aluminum underside isolates the spacecraft from the hot lunar surface.

**a. *Compartment canisters.*** Compartments A and B house spacecraft batteries and electronics. Most of the top surface of each compartment is covered with Vycor glass, second-surface mirrors. These mirrors are part of the bimetallic-actuated thermal switches used to reject heat from temperature-controlled compartments. The outboard faces of the compartments look away from the spacecraft and are made of 0.4-mm-thick aluminum panel. Their purpose is to contain a blanket of superinsulation that surrounds each compartment. A temperature sensor is bonded to the polished-aluminum inner surface of the outboard face (i.e., the surface facing the superinsulation) of each compartment.

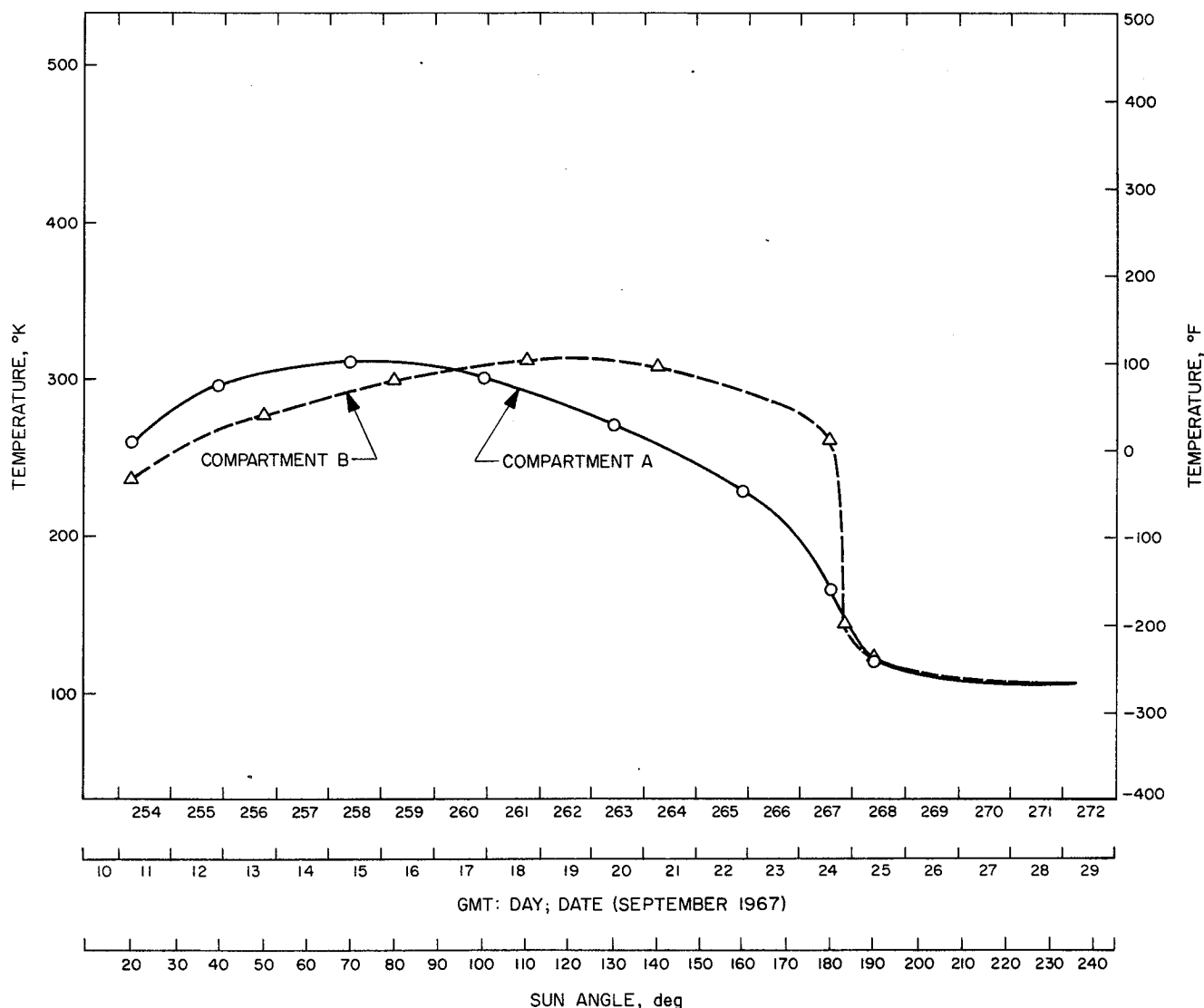


Fig. V-8. Temperatures of outboard faces of compartments A and B during first lunar day.

The outboard faces are insulated from the rest of the compartment and spacecraft structure. They are, therefore, essentially in thermal equilibrium with their environment, which is composed of the lunar surface, space, and solar energy input. The superinsulation isolates the surfaces from the inside of the compartment so that heat input from that boundary is negligible during the lunar day. This assumption is not valid when calculating lunar surface temperatures during a lunar eclipse or during the lunar night.

Parameters needed to compute lunar temperature by the methods described in this report are:

- (1) Angle between normal to compartment outboard face and spacecraft -Z axis.
  - (a) Compartment A:  $69^{\circ}30'$ .
  - (b) Compartment B:  $69^{\circ}58'$ .
- (2) Compartment outboard-face properties before launch.

- (a) Infrared hemispherical emittance:  $\epsilon_H = 0.87 \pm 0.02$ .
- (b) Solar normal absorptance:  $\alpha_s = 0.20 \pm 0.02$ .
- (c) Material: 2024 aluminum, 0.4-mm-thick panel with corrugations, coated with inorganic white paint.

The first and second lunar day outboard-face temperatures of compartments A and B are presented in Figs. V-8 and V-9, respectively. On Day 256 (September 13), at 05:38 GMT, the vernier engines were fired. Note that, after the firing, no irregularities in the temperature data were observed. By superimposing the first-day temperature data over the second-day temperature data (Figs. V-10 and V-11), it is apparent that outboard-face temperatures run higher during the second day, especially when the sun shines on them. It is believed that the temperature increase may be caused by deterioration of the inorganic white paint, causing the solar absorptance to increase.

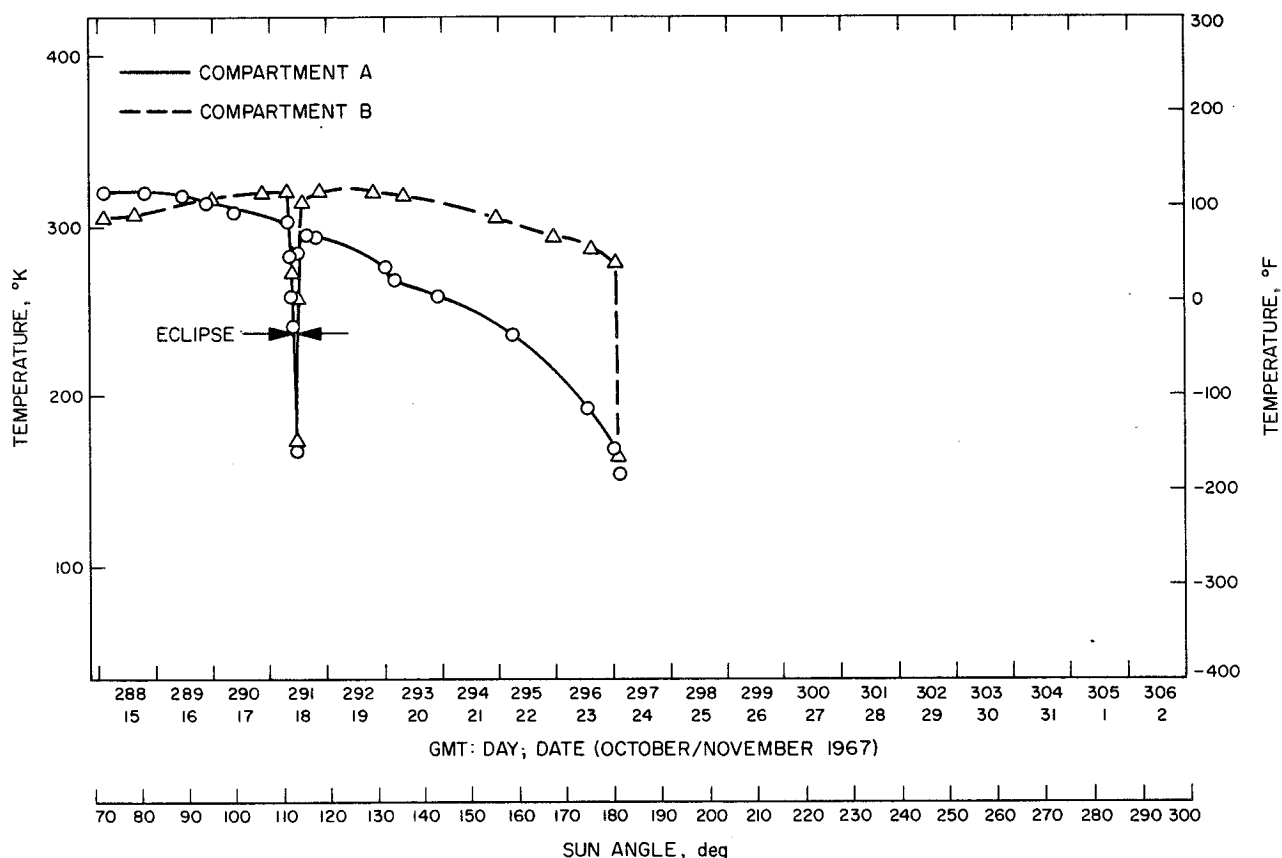


Fig. V-9. Temperatures of outboard faces of compartments A and B during second lunar day.

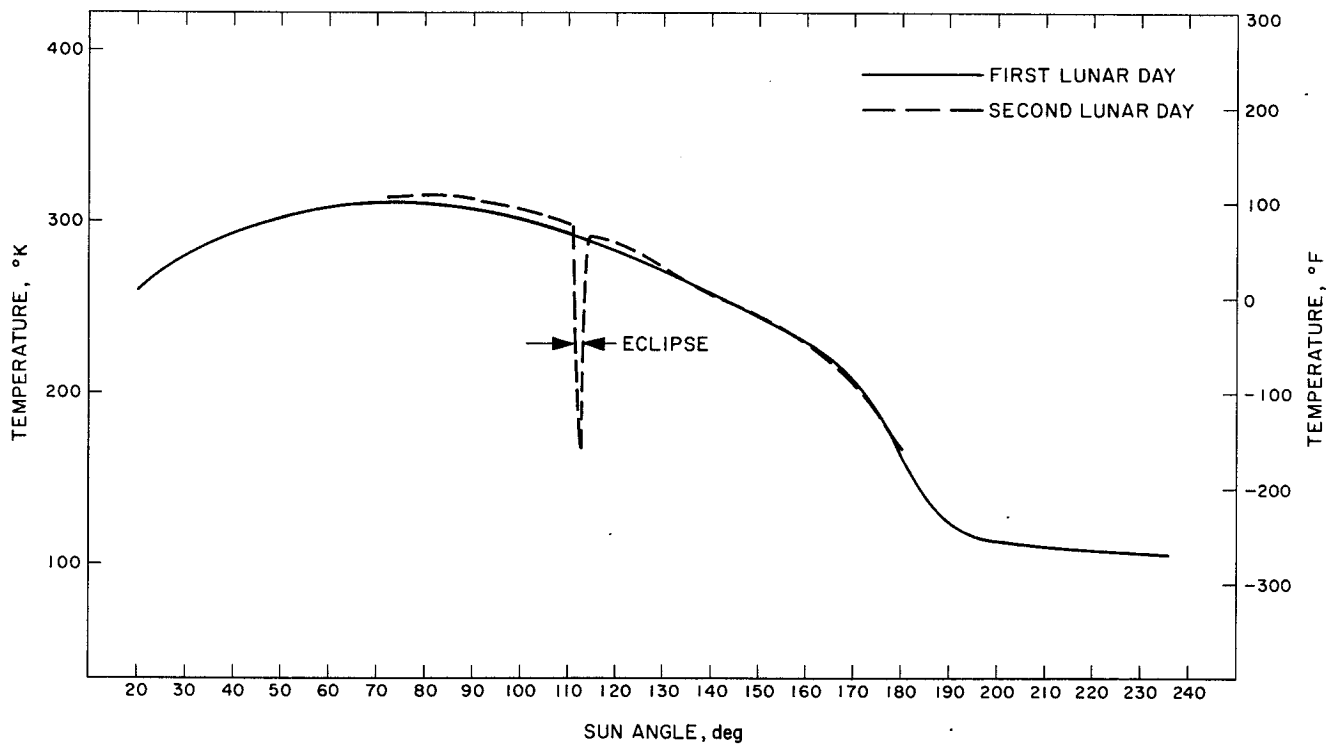


Fig. V-10. Temperatures of outboard face of compartment A during first and second lunar days.



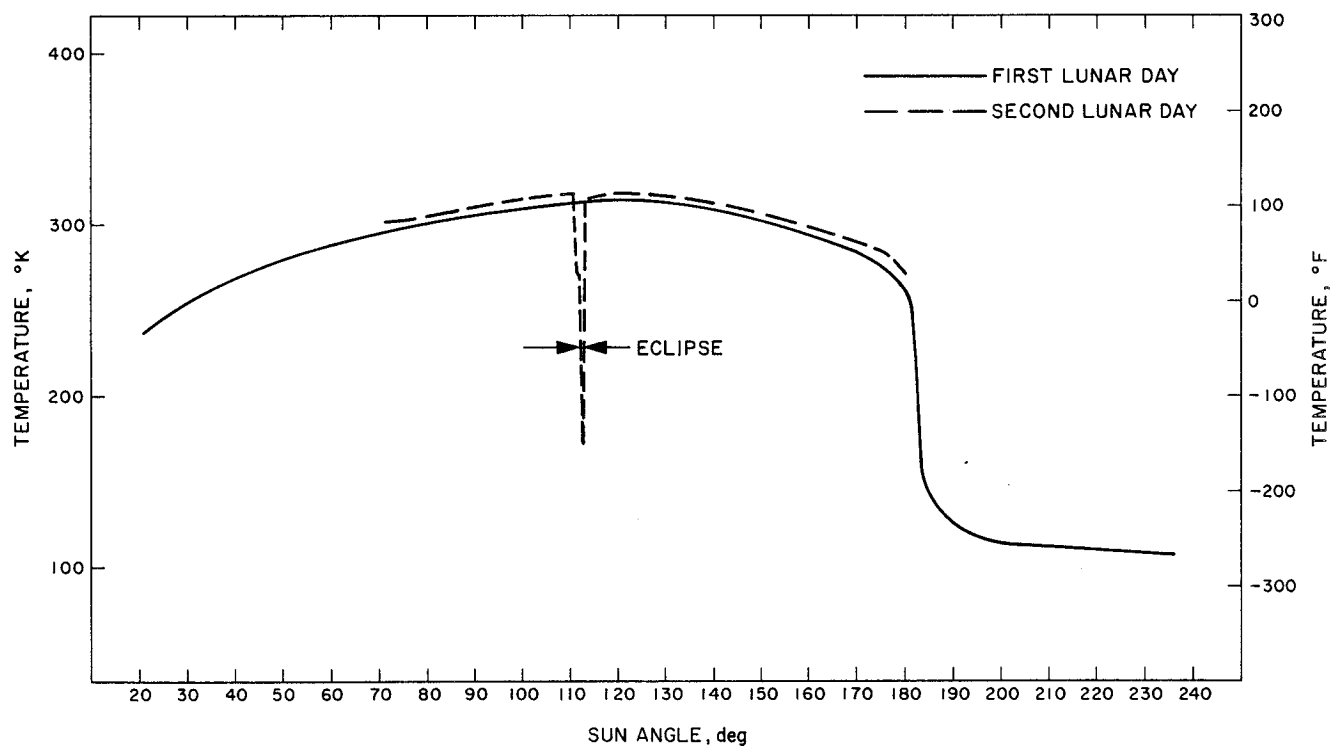
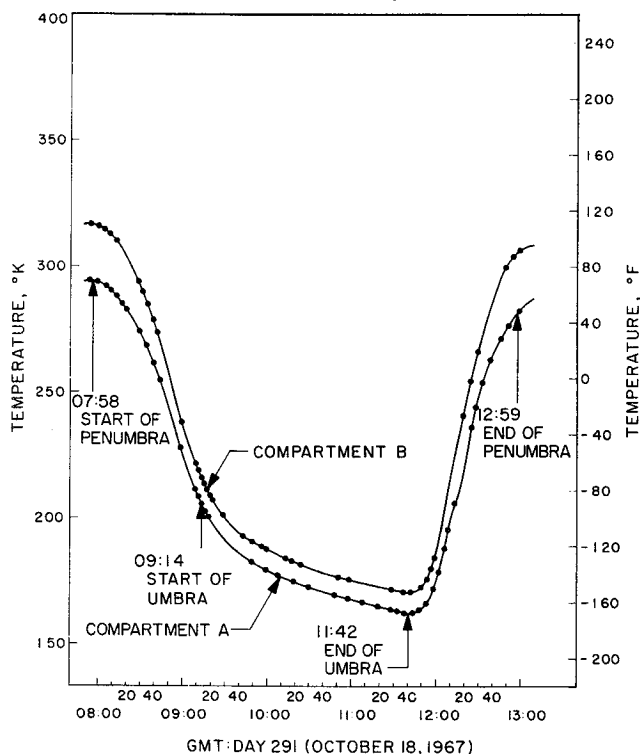


Fig. V-11. Temperatures of outboard face of compartment B during first and second lunar days.

Good temperature data were obtained on the lunar eclipse during the second lunar day (Fig. V-12). The angle between a normal to the compartment outboard faces and the sun vector is presented in Fig. V-13. The extent of shading by either the solar panel or planar array antenna was negligible on the outboard faces of compartments A and B.

**b. Planar array antenna and solar panel.** The planar array antenna and solar panel are relatively low-heat-capacity planar surfaces. Data derived from them may be used to negate some of the uncertainties associated with lunar surface temperatures based on data from the compartment outer faces, especially for calculations during the eclipse and lunar night. Temperature data for the solar panel and planar array antenna during the first lunar day are given in Figs. V-14 and V-15. Figure V-16 shows the solar panel and planar array antenna temperature data during the eclipse. The angles between the normal to the solar panel and the sun vector, and to the spacecraft -Z axis (for the first lunar day) are shown in Fig. V-17. Figure V-18 shows the angles on the first lunar day between the normal to the planar array antenna and the sun vector, and to the spacecraft -Z axis.



**Fig. V-12. Temperatures of outboard faces of compartments A and B during eclipse.**

The parameters needed to compute lunar surface temperatures are:

(1) Solar panel properties.

(a) Surface area.

Front: 0.855 m<sup>2</sup>.

Back: 0.855 m<sup>2</sup>.

(b) Total heat capacity: 0.798 kg-cal/hr °C.

(c) Conductance (front to back): 50.3 kg-cal/hr °C.

(d) Solar normal absorptance.

Front surface:  $0.76 \pm 0.02$ .

Back surface:  $0.30 \pm 0.02$ .

(e) Infrared hemispherical emittance.

Front surface:  $0.80 \pm 0.02$ .

Back surface:  $0.84 \pm 0.02$ .

(f) Angle between normal to solar panel and spacecraft -Z axis.

First lunar night (Day 267): 99.64 deg.

Eclipse (Day 291): 90.0 deg.

(g) Angle between -X axis and projection of normal into X-Y plane (measured toward -Y axis).

First lunar night: 301.0 deg.

Eclipse: 211.2 deg.

(2) Planar array antenna properties.

(a) Surface area.

Front (projected): 0.97 m<sup>2</sup>.

Back (total): 1.40 m<sup>2</sup>.

(b) Total heat capacity: 1.04 kg-cal/hr °C.

(c) Conductance (front to back): 16.8 kg-cal/hr °C.

(d) Solar normal absorptance:  $0.80 \pm 0.02$ .

(e) Infrared hemispherical emittance:  $0.88 \pm 0.02$ .

(f) Angle between normal to planar array antenna and spacecraft -Z axis.

First lunar night: 25.5 deg.

Eclipse: 5.3 deg.

(g) Angle between -X axis and projection of normal into X-Y plane (measured toward -Y axis).

First lunar night: 301.0 deg.

Eclipse: 31.2 deg.

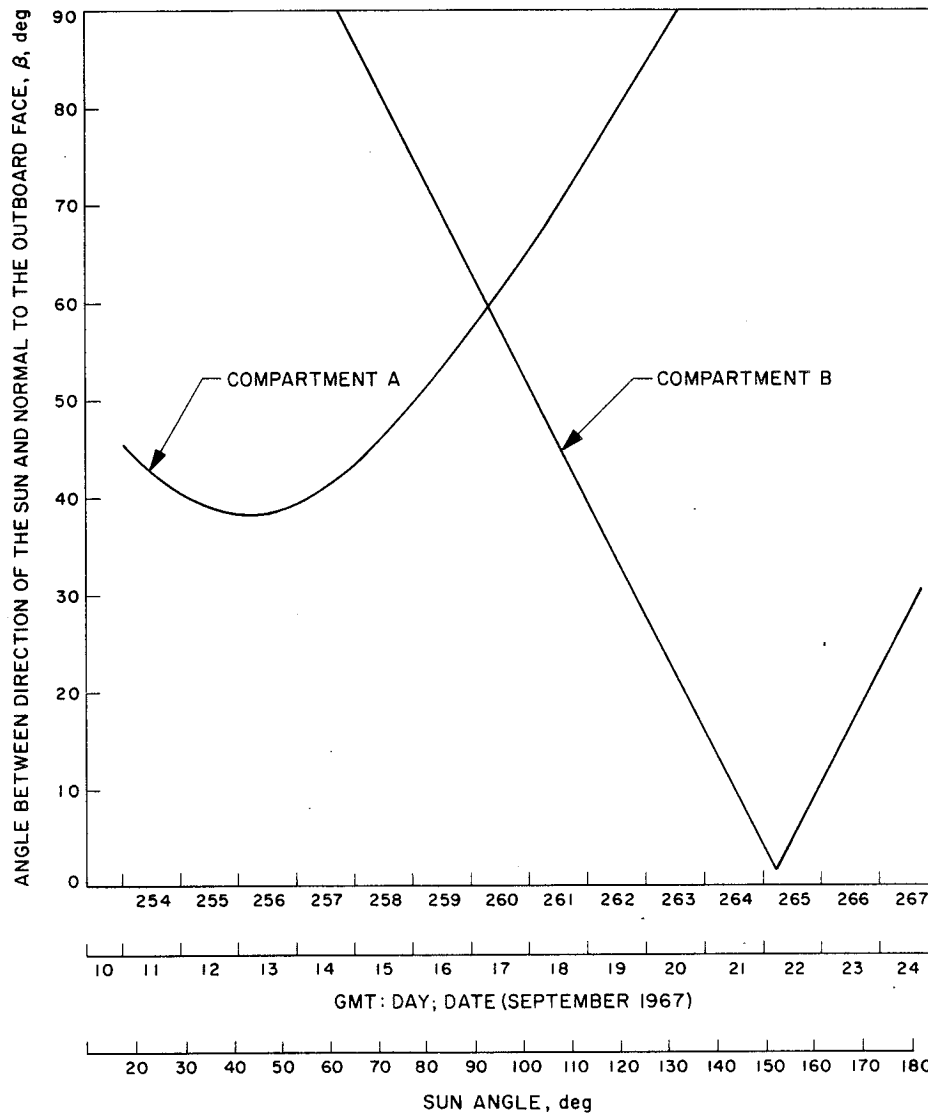
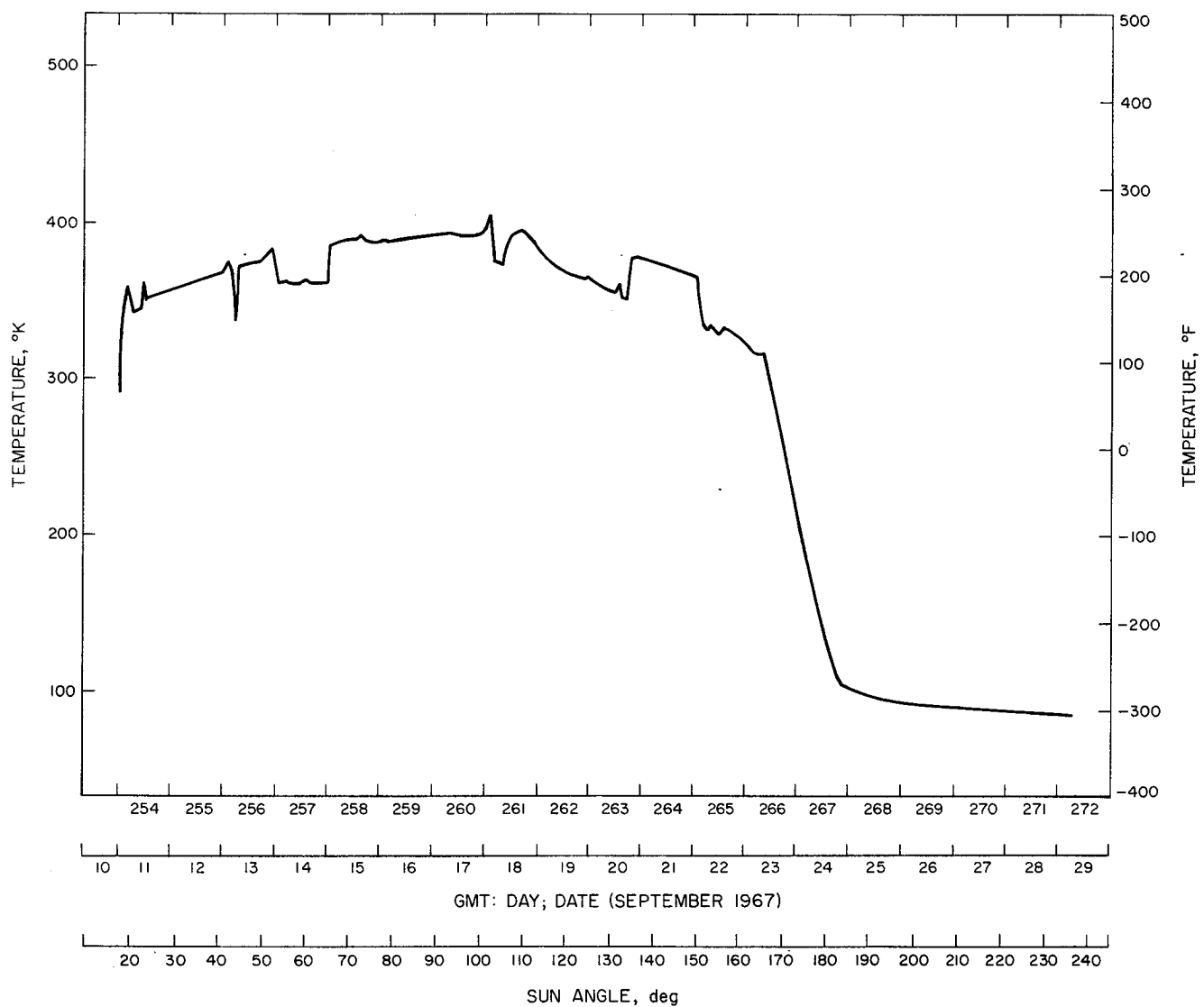
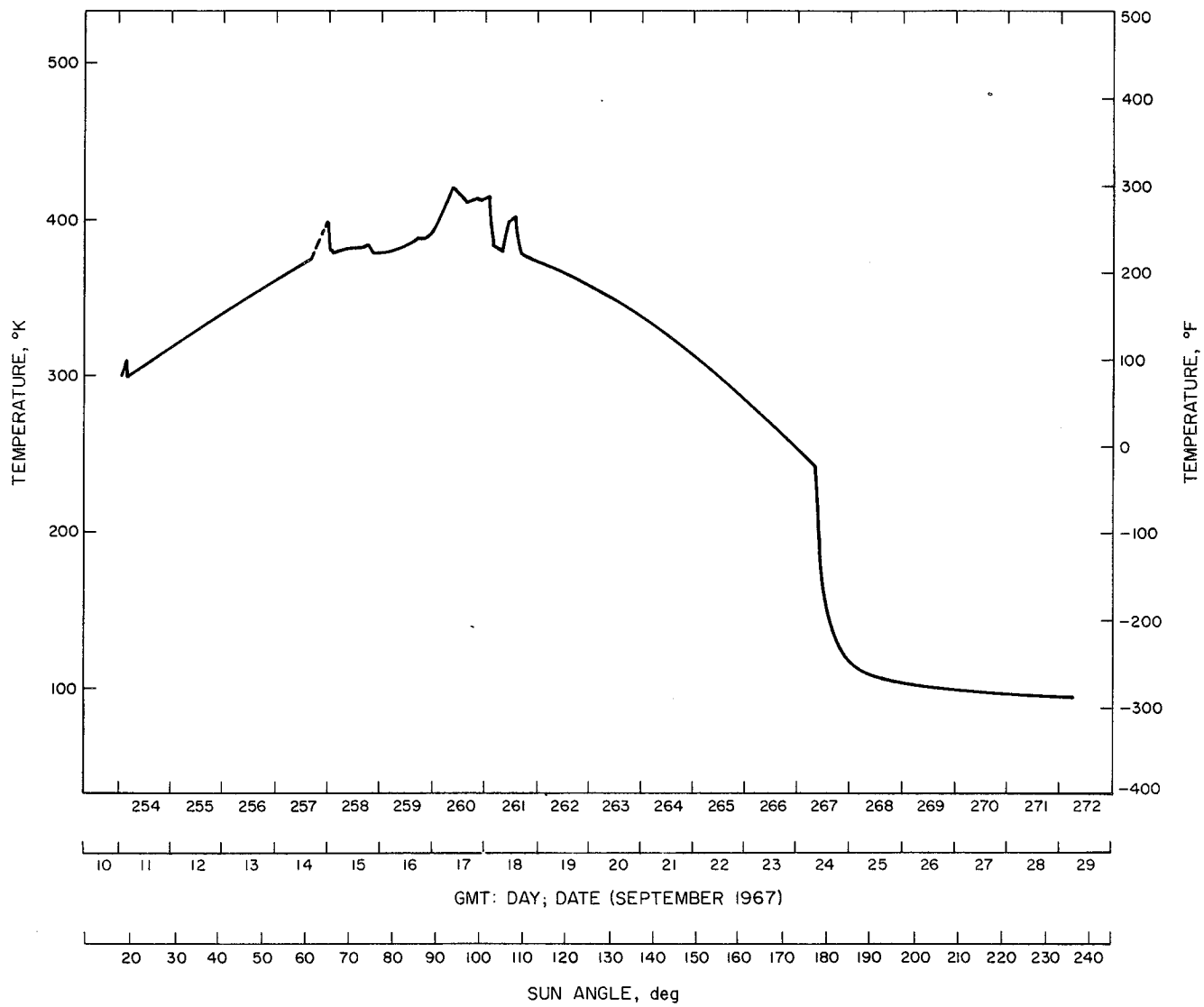


Fig. V-13. Angle between direction of sun and normal to outboard plane of compartments A and B during first lunar day.



**Fig. V-14. Temperature of solar panel during first lunar day.**



**Fig. V-15. Temperature of planar array antenna during first lunar day.**

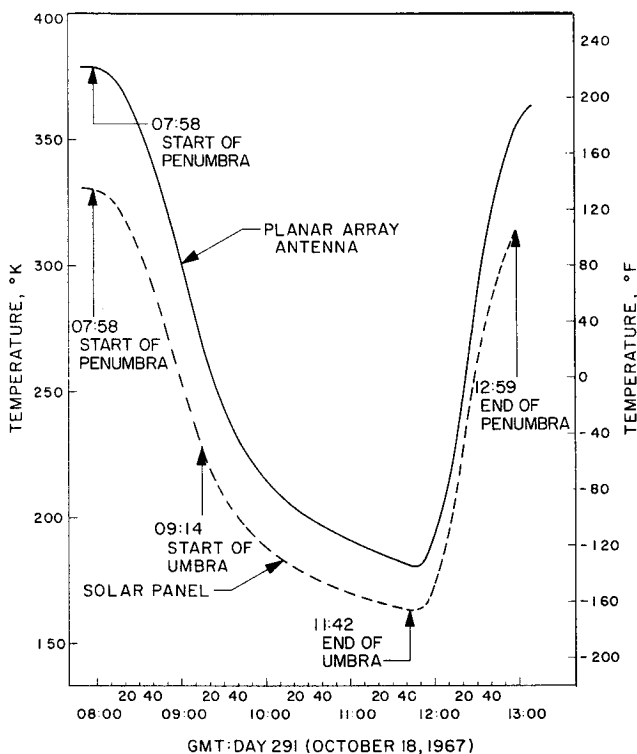


Fig. V-16. Temperatures of solar panel and planar array antenna during eclipse.

**c. Thermal instrumentation.** Platinum resistance temperature sensors provided temperature data of various points in the spacecraft. Each sensor is calibrated individually to  $\pm 1^\circ\text{C}$ ; other nominal-system inaccuracies degrade the system to  $\pm 3^\circ\text{C}$ .

**d. Lambertian lunar surface temperature calculations.** Calculations were performed using the following equation taken from Ref. V-1:

$$\sigma T_2^4 = \frac{\sigma T_1^4}{\epsilon_2 (F_{12} - F_{13})} - \frac{F_{13}}{F_{12} - F_{13}} \sigma T_3^4 - \frac{\alpha_{1s} S}{\epsilon_1 \epsilon_2 (F_{12} - F_{13})} [(F_{12} - F_{13}) \rho_2 \sin \theta + \cos \beta] - \frac{\dot{q}}{\epsilon_1 \epsilon_2 (F_{12} - F_{13})} \quad (1)$$

where

$T_1$  = compartment surface temperature

$T_2$  = lunar surface brightness temperature

$T_3$  = lunar surface brightness temperature in shadow;  
 $T_3^4 < T_2^4$  is assumed

$S$  = solar irradiation constant =  $1375 \text{ W/m}^2$

$F_{12}$  = geometric view factor from 1 to 2

= 0.247 for compartment A

= 0.255 for compartment B

$F_{13}$  = geometric view factor from 1 to 3 (see Table V-1)

$\dot{q}$  = conduction heat flux between inside and outside of compartment wall

=  $3.5 \text{ W/m}^2$

$\sigma$  = Stefan-Boltzmann constant

=  $5.675 \times 10^{-8} \text{ W/m}^2 \text{ } ^\circ\text{K}^4$

$\epsilon_1$  = compartment surface emittance

=  $0.87 \pm 0.02$

$\epsilon_2$  = lunar surface emittance

= 1.0

$\alpha_{1s}$  = compartment surface solar absorptance

=  $0.20 \pm 0.02$

$\beta$  = angle between direction of sun and normal to compartment surface (from Fig. V-13)

$\theta$  = sun angle (between lunar surface and direction of sun)

$\rho_2$  = 0.077 = lunar reflectivity to solar irradiation

Table V-1. View factor,  $F_{13}$ , from compartments A and B to lunar surface in shadow

Sun angle	From compartment A	From compartment B
20	Negligible	0.045
30		0.037
40		0.030
50		0.022
60		0.007
70		0.002
80 to 180	Negligible	Negligible

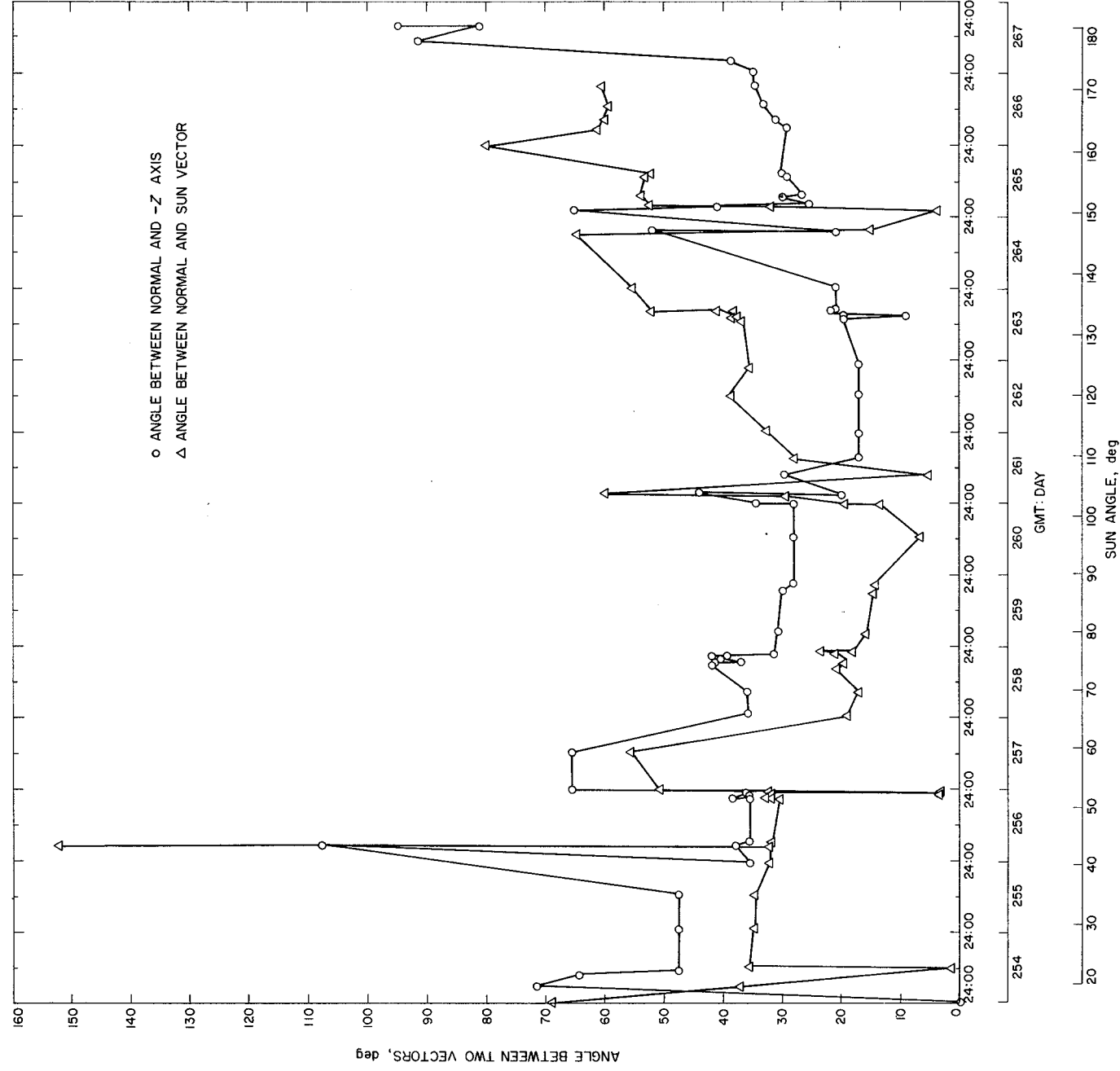


Fig. V-17. Angle that normal to solar panel makes with sun vector and  $-Z$  axis during first lunar day.

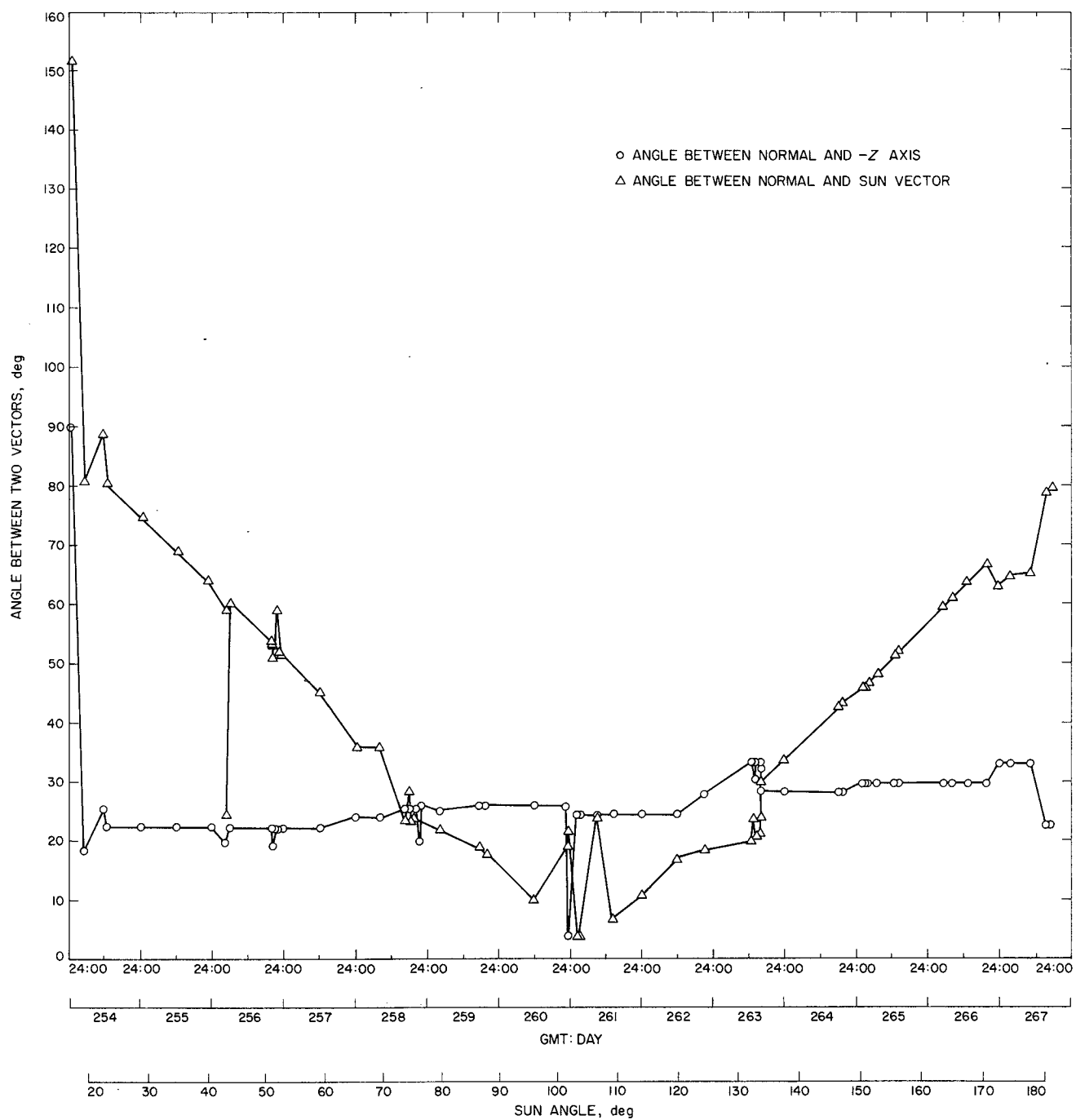


Fig. V-18. Angle that normal to planar array antenna makes with sun vector and  $-Z$  axis during first lunar day.



## 2. Lunation

Figure V-19 represents a first-day average brightness temperature, as calculated from compartment A and B telemetered temperatures using Eq. (1). The crater wall and the surface above the crater rim are at different temperatures for a given sun angle. Since the compartment outboard faces view the crater wall and the surface above, the telemetered temperatures of compartments A and B depend on these two different lunar surface temperatures. Solution of Eq. (1) yields a single lunar surface temperature; thus, this temperature may be considered as an average lunar surface temperature of the crater wall and the

surface above it. The temperature derived from compartment B is higher early in the day than that of compartment A because compartment B views the western part of the crater, which has a higher temperature because of the relatively greater sun elevation. In the afternoon, the reverse is true.

In Figs. V-20 and V-21, lunar surface temperatures indicated by compartments A and B are shown separately. Also shown is the computed curve of lambertian temperature given in Fig. V-2, but shifted 10 deg to the right for compartment A and 15 deg to the left for compartment B

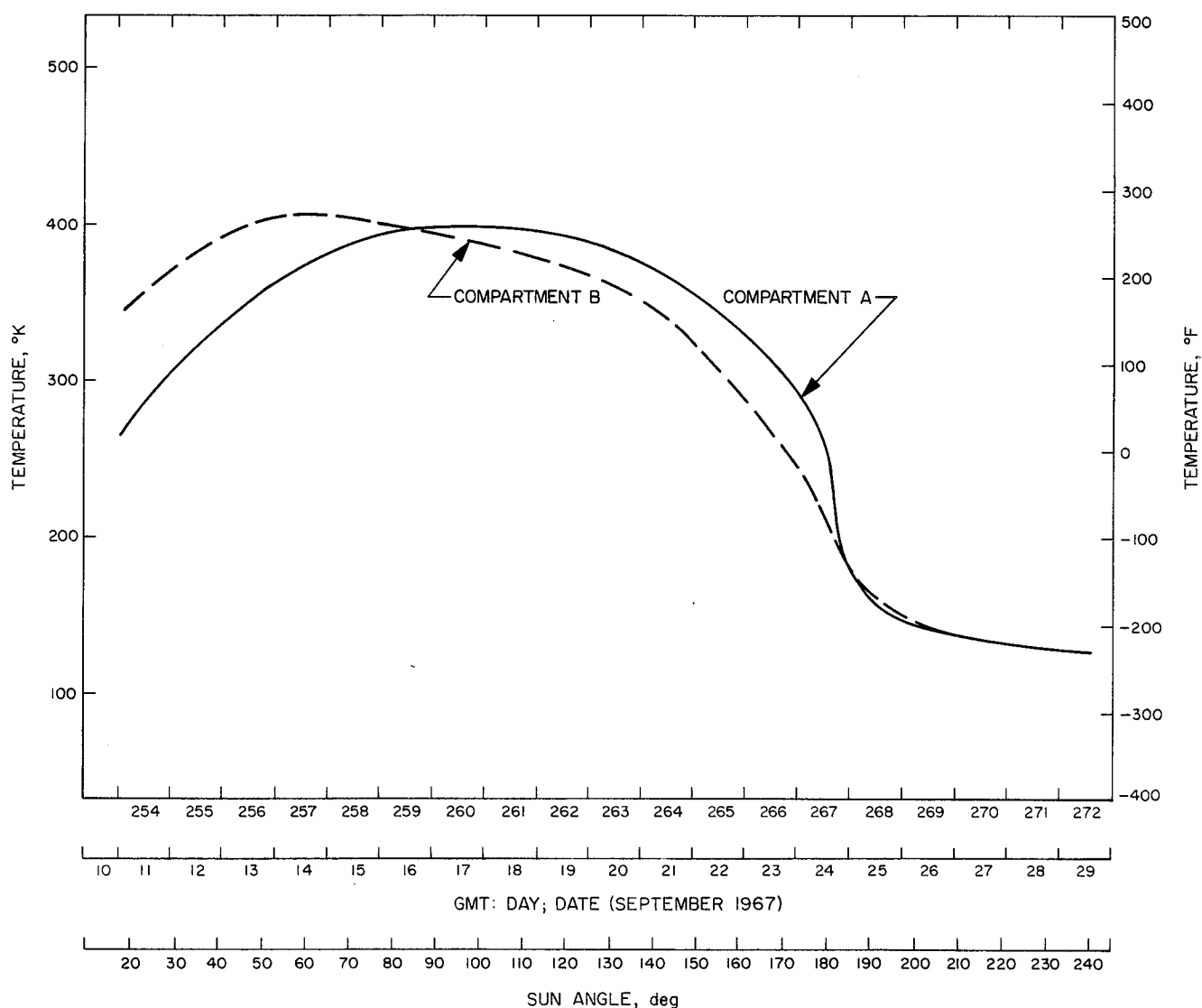
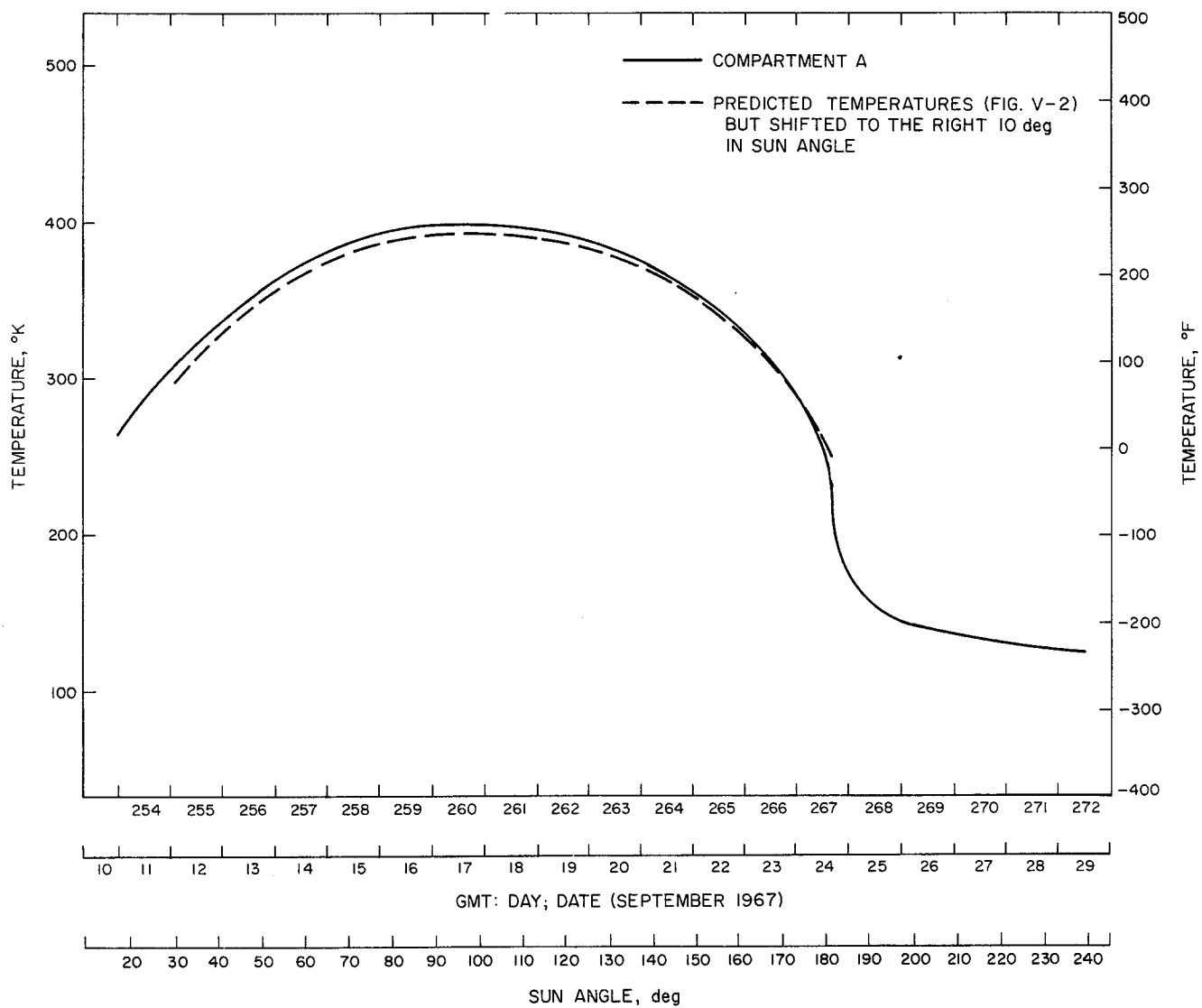
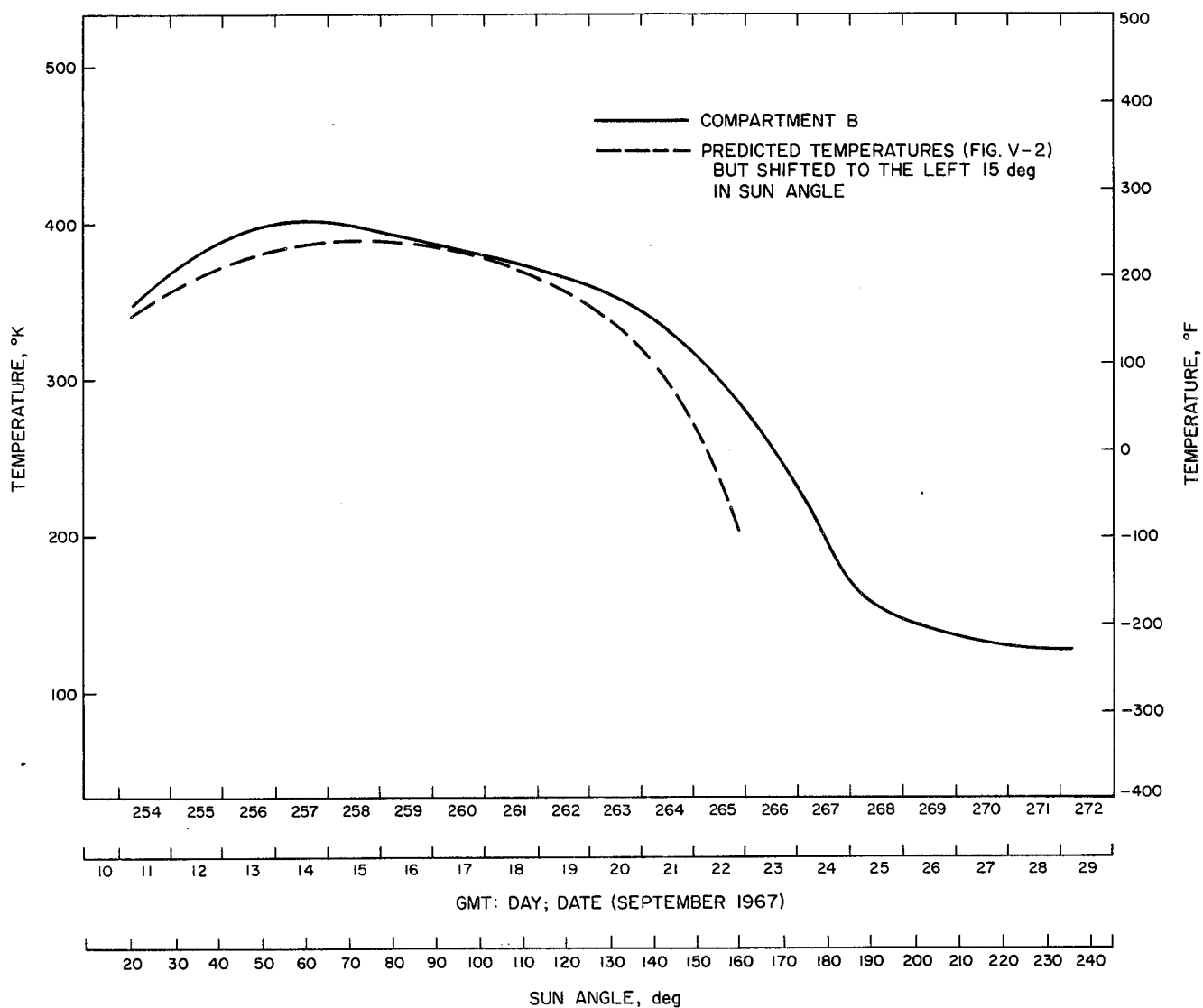


Fig. V-19. Lunar surface temperatures during first lunar day, as calculated from telemetry data for compartments A and B.



**Fig. V-20. Lunar surface brightness temperatures during first lunar day: compartment A data compared with predicted temperatures.**



**Fig. V-21. First-day brightness temperatures on lunar surface: compartment B data compared with predicted temperatures.**

to account for the approximate slope of the local lunar surface. The temperatures sensed by compartment A agree well with the predicted lambertian temperature in the afternoon; however, there is only fair agreement in the morning and at noon. There is fair agreement in the morning, good agreement at noon, and poor agreement in the afternoon for compartment B temperatures.

Lunar surface brightness temperatures derived from compartment B data for *Surveyors I* and *III* (Fig. VI-28 of Ref. V-1), and *V* (shifted 15 deg to the right) are shown in

Fig. V-22. Compared with *Surveyor I* and *III* temperatures, *Surveyor V* sensed lower temperatures in the morning, higher temperatures at noon, and lower temperatures in the afternoon. This temperature difference could be due to the difference in topography between the landing sites.

Figure V-23 shows the lunar surface temperatures, as derived from compartments A and B, after sunset; also included are *Surveyor I* data and theoretical gamma cooling curves taken from Fig. V-1. Note that both compartments sensed about the same surface temperature for the

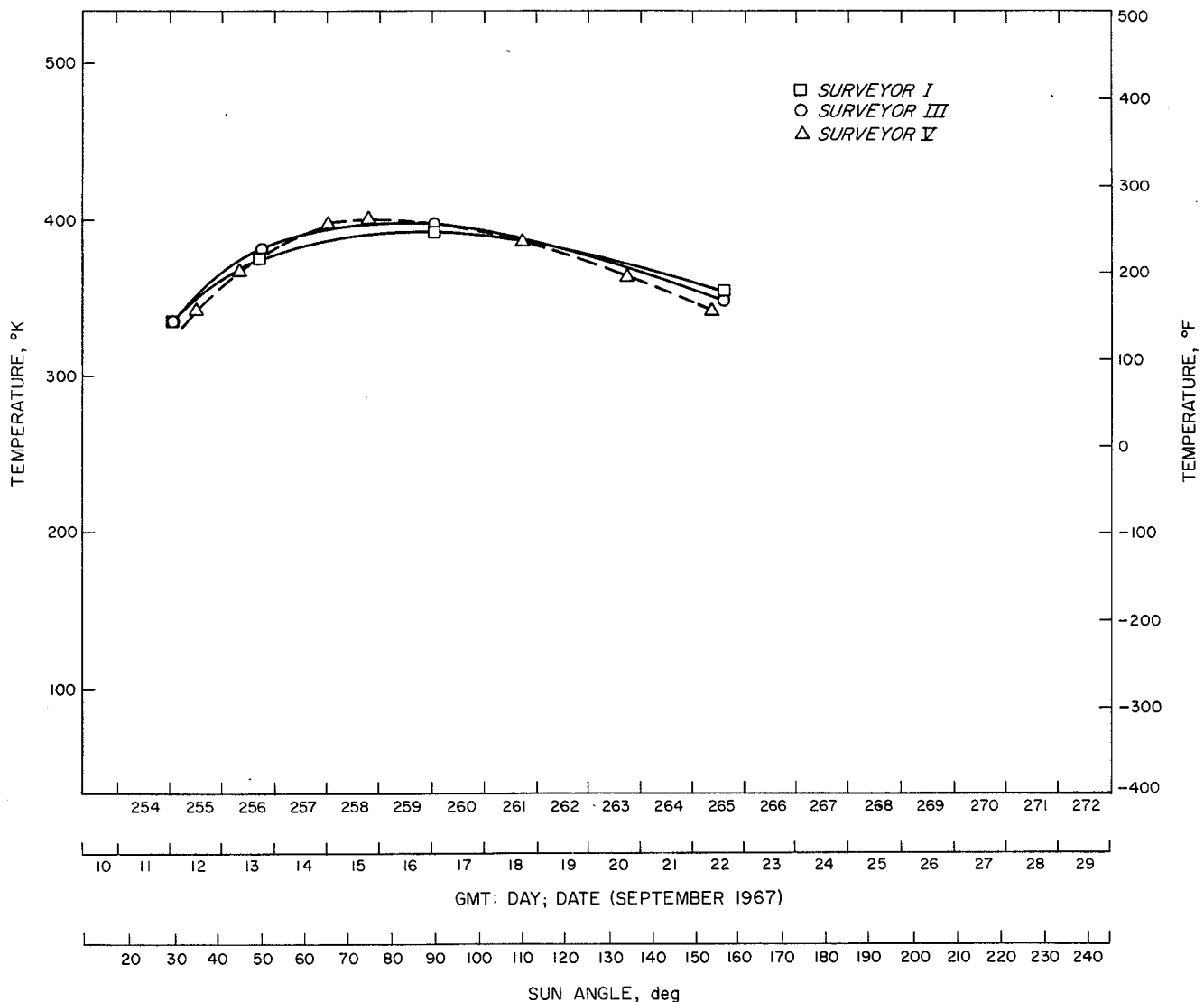
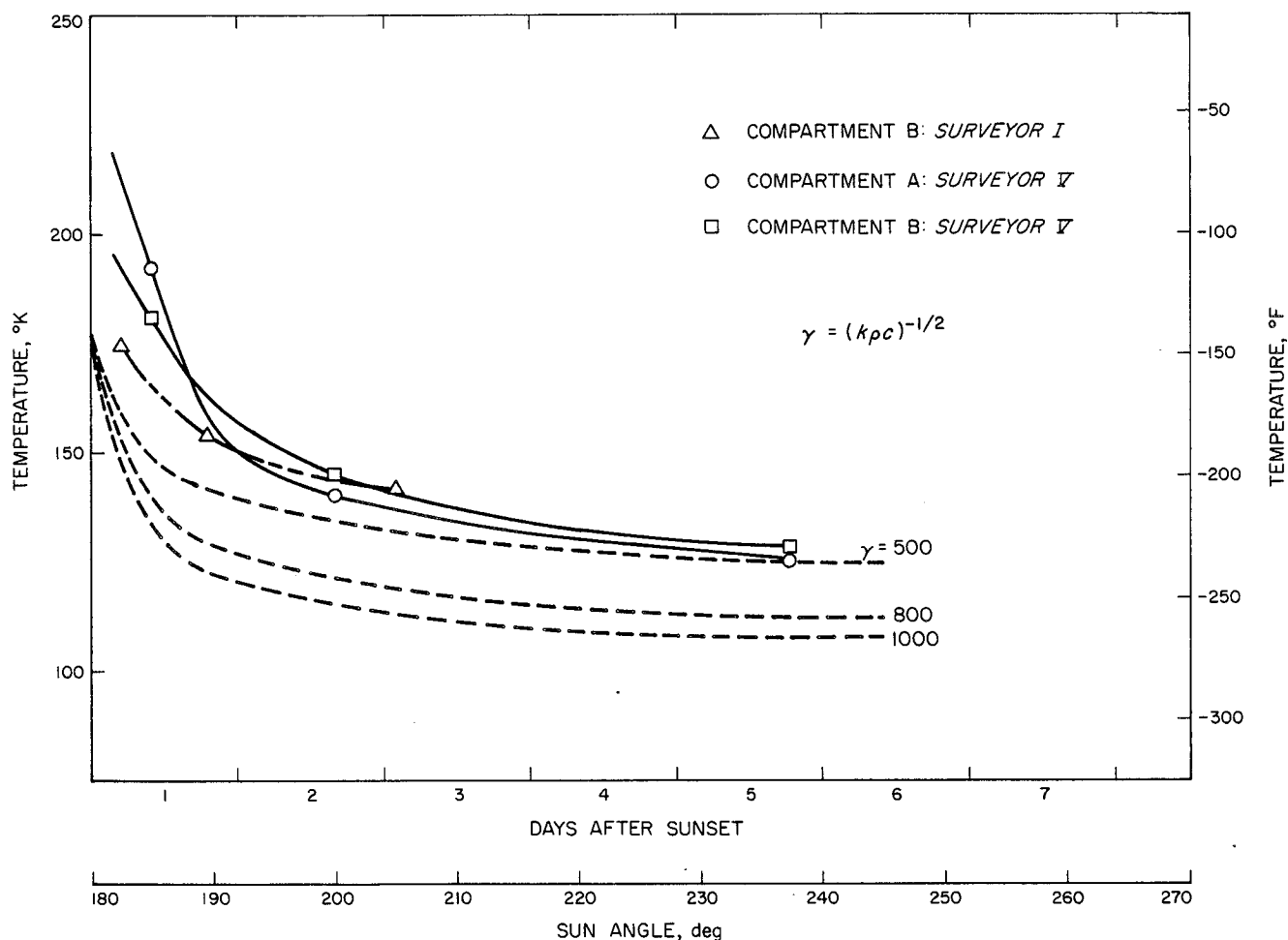


Fig. V-22. Lunar surface brightness temperatures from compartment B data on *Surveyors I*, *III*, and *V* (adjusted in time for *Surveyor V*).



**Fig. V-23. Lunar surface brightness temperatures after first-day sunset, derived from Surveyor I and V compartment data, compared with predicted temperatures for different gammas.**

Surveyor V site during the night and indicated an effective  $\gamma$  of slightly less than 500.

### 3. Eclipse

Figure V-24 shows the temperature data, as derived from compartments A and B during the eclipse. At the start of penumbra, compartment A sensed a higher temperature than compartment B; however, at the end of umbra, the reverse was true. The reason for this temperature crossover may be that the gamma of the surface material viewed by compartment A is somewhat higher than that of the material viewed by compartment B. By comparing compartment A and B eclipse data with the predicted lunar surface temperatures during the eclipse (Fig. V-4), it is observed that the temperature lagged and did not fall as low as predicted. Using the eclipse cooling curves of Jaeger (Ref. V-6), it is estimated that a lunar sur-

face with an effective  $\gamma$  of about 500 would exhibit the observed cooling. If the heat capacity of the outboard face were included in the calculations, the observed lunar surface temperature lag would be reduced, and a somewhat lower temperature would be indicated at the end of umbra.

### C. Summary

From the analysis, the following tentative conclusions may be drawn.

#### 1. Lunation Data

- (1) Differences in the lunar surface temperature, derived from compartments A and B data during morning and afternoon, may be explained by the different sun phase angles at the local lunar surface.

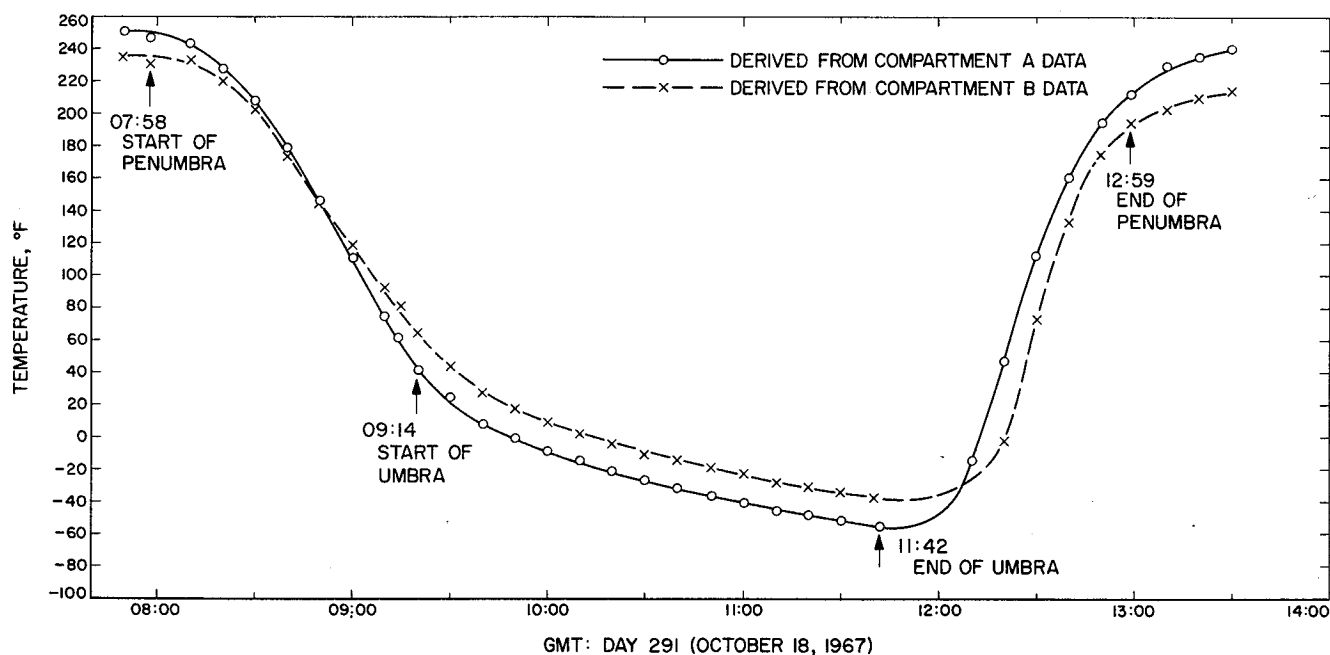


Fig. V-24. Lunar surface brightness temperatures during eclipse.

- (2) For predicted and observed surface temperatures for compartment A, there is fair agreement in the morning, fair agreement at noon, and good agreement in the afternoon. For compartment B, there is fair agreement in the morning, good agreement at noon, and poor agreement in the afternoon. Both compartments sensed higher than predicted temperatures at noon. Some of this temperature difference, however, is due to not fully considering the compartment view factor, as related to the actual landing site topography.
- (3) During the second lunar day, the compartment A and B telemetered temperatures were higher for the identical sun angles, perhaps because of the deterioration of inorganic white paint; however, further analysis is necessary to confirm this.
- (4) Compartments A and B sensed essentially the same lunar temperature after sunset. It is estimated that

a lunar surface with an effective  $\gamma$  of about 500 would exhibit the observed cooling.

## 2. Eclipse Data

- (1) At the start of penumbra phase, compartment A sensed higher surface temperatures than compartment B; at the end of the umbra phase, the reverse was true. This may indicate that the surface material viewed by compartment A has a slightly higher gamma than the surface material viewed by compartment B.
- (2) During both penumbra phases, observed lunar surface temperatures lagged those predicted from terrestrial data. Lunar surface temperatures at the end of the umbra phase were 50°K above those predicted, suggesting an effective  $\gamma$  of about 500.

## References

- V-1. Lucas, J. W., et al., "Lunar Surface Temperatures and Thermal Characteristics," *Surveyor III Mission Report. Part II: Scientific Results*, Technical Report 32-1177, Jet Propulsion Laboratory, Pasadena, Calif., June 1, 1967.
- V-2. Lucas, J. W., et al., "Lunar Surface Thermal Characteristics," *Surveyor I Mission Report. Part II: Scientific Data and Results*, Technical Report 32-1023, Jet Propulsion Laboratory, Pasadena, Calif., September 10, 1966.
- V-3. Jones, B. P., "Diurnal Lunar Temperatures," Paper 67-289, presented at AIAA Thermophysics Specialist Conference in New Orleans, La., April 17-20, 1967.
- V-4. Saari, J. M., and Shorthill, R. W., "Thermal Anomalies on the Totally Eclipsed Moon of December 19, 1964," *Nature*, Vol. 205, pp. 964-965, 1965.
- V-5. Shorthill, R. W., and Saari, J. M., "Non-uniform Cooling of the Eclipsed Moon: A Listing of Thirty Prominent Anomalies," *Science*, Vol. 150, No. 210, 1965.
- V-6. Jaeger, J. L., "Surface Temperature of the Moon," *Aust. J. Phys.*, Vol. 6, No. 10, 1953.

## Acknowledgment

Appreciation is extended to all Jet Propulsion Laboratory and Hughes Aircraft Company development and flight operation engineers who supplied raw data. Special thanks are given to L. Gamer, Hughes, for preparing shadow plots and for solar panel and planar array antenna positioning plots. Thanks are also given to C. S. Level for a computer program to calculate results, and to M. Blount for plots of results and raw data.





## VI. Astronomy

*R. H. Norton, J. E. Gunn, W. C. Livingston,  
G. A. Newkirk, and H. Zirin*

Following sunset (for the spacecraft) on the first lunar day, at 10:56 GMT on Day 267 (September 24, 1967), 37 pictures of the K- and F-corona were obtained during a 3.5-hr period while using the green filter. The focal length was 100 mm (narrow angle); the lens was focused at 4 m for each picture. Exposures obtained and the  $f$ -ratios used are listed in Table VI-1.

The resulting circle of confusion ranges from about 0.2 solar radius at  $f/22$  to 1 solar radius at  $f/4$ . For the bright K-corona (Fig. VI-1), a fairly sharp definition could be achieved by using the  $f/22$  aperture. On the longest of these exposures (10 min), streamers may be traced out to approximately 6 solar radii; the brightest streamers appear in the southern hemisphere.

**Table VI-1. Observations of solar corona at landing site**

Number of frames	Inclusive time (GMT)	Iris	Shutter	Azimuth	Elevation
6	11:02:10 to 11:03:26	$f/8$	1.2 sec	+114	+7
1	11:05:39	$f/22$	10 sec	+114	+7
2	11:07:20 to 11:08:32	$f/22$	30 sec	+114	+7
2	11:10:55 to 11:12:42	$f/22$	90 sec	+114	+7
2	11:18:19 to 11:23:35	$f/22$	5 min	+114	+7
2	11:25:21 to 11:45:55	$f/22$	10 min	+114	+7
4	12:02:49 to 12:20:25	$f/11$	5 min	+114	+7
1	12:22:44	$f/4$	40 sec	+114	+7
4	12:30:15 to 12:48:36	$f/8$	5 min	+114	+7
5	12:54:55 to 13:20:03	$f/4$	5 min	+114	+7
3	13:29:44 to 13:42:21	$f/4$	5 min	+117	+7
2	13:49:26 to 13:55:31	Shutter closed, 5-min background calibration			
1	14:04:11	$f/4$	5 min	+117	+7
4	14:10:07 to 14:28:26	$f/4$	5 min	+117	+12

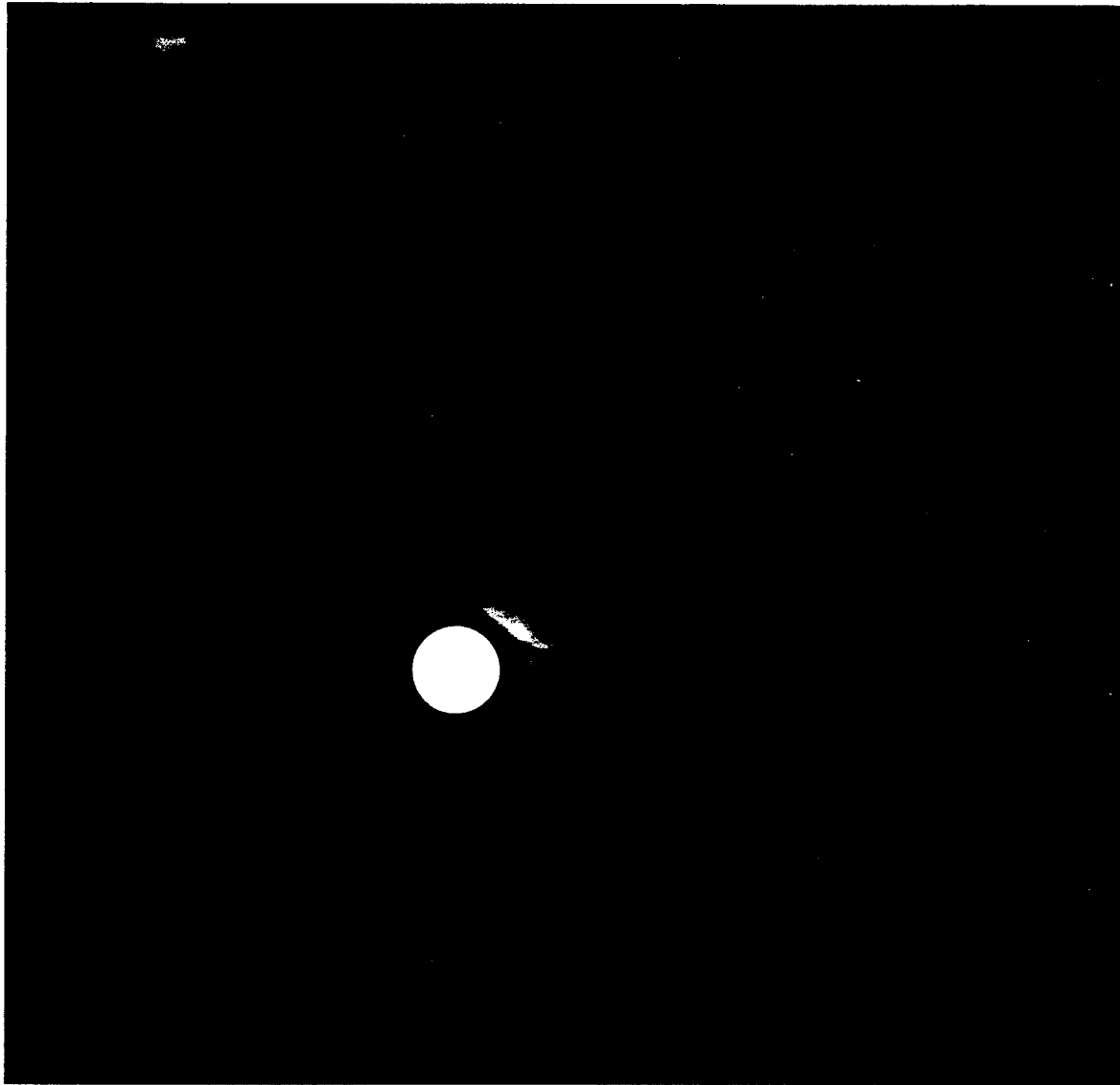


**Fig. VI-1. Picture of the K-corona; a 30-sec exposure at  $f/22$ . The upper solar limb is approximately 0.5 solar radius below the horizon. Several coronal streamers are visible. The K-corona in this picture is produced by scattering from electrons near the sun. The white circle denotes the relative size and location of the sun (Day 267, 11:08:32 GMT).**

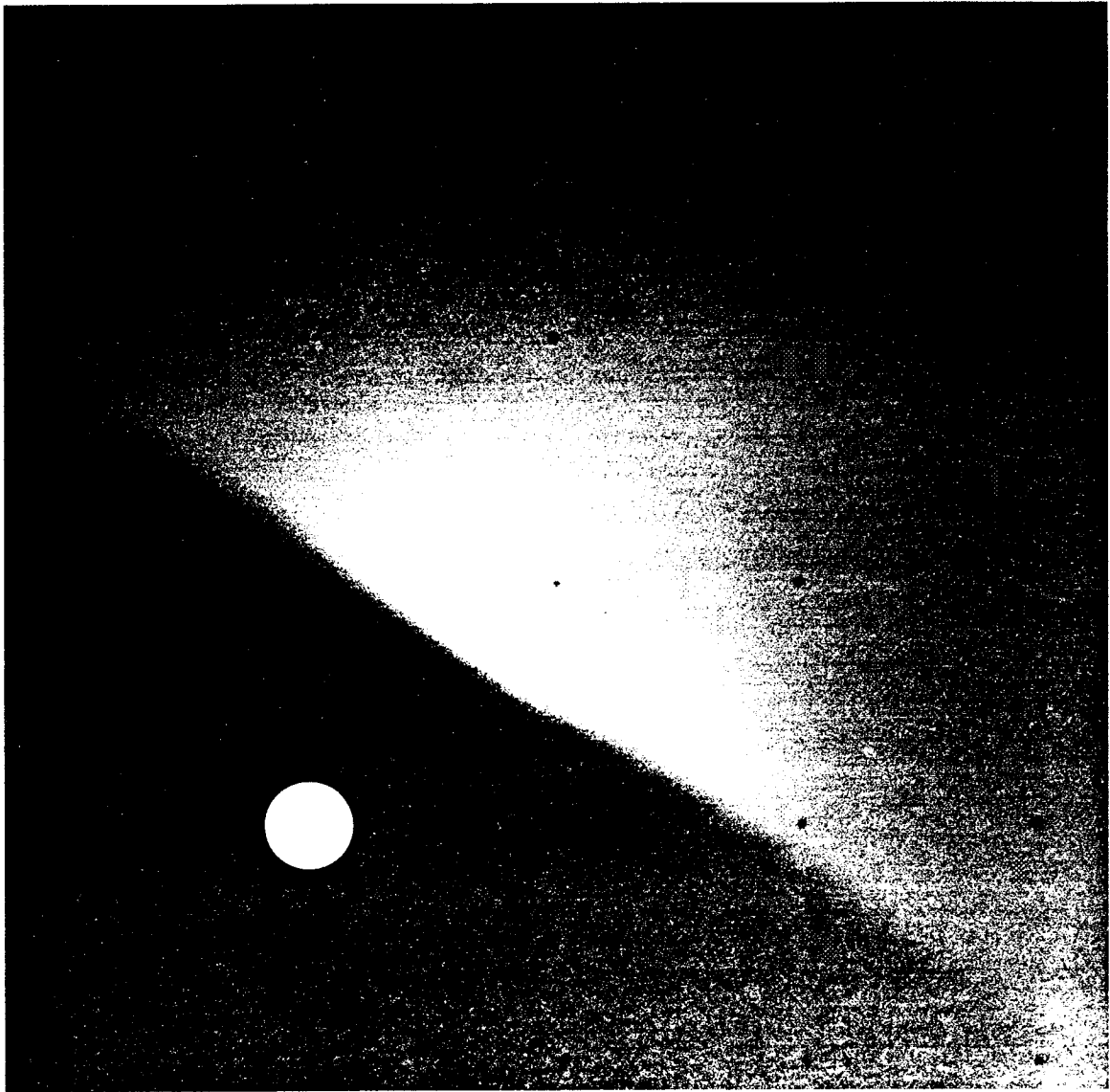


**Fig. VI-2. Picture of the F-corona: a 5-min exposure at  $f/4$ . The solar limb is 5 solar radii below the horizon. The F-corona in this picture is produced by scattering from particulate matter between the earth and the sun. The plane of the ecliptic is nearly perpendicular to the horizon. The asymmetry visible in the F-corona presumably is due to the decrease in particle density with height above the ecliptic plane. The white circle denotes the relative size and location of the sun (Day 267, 13:20:03 GMT).**

As the corona set lower on the western horizon (at the rate of 2 solar radii/hr), successively larger apertures were used to film the fainter F-corona (Fig. VI-2). Because of the increased video background level in exposures longer than 5 min, a sequence (usually four) of successive identical exposures was made at each  $f$ -ratio. (These exposures will be summed to increase the effective dynamic range and to reduce random noise.) Calibration exposures were also made with the shutter closed. During each 5-min integration, engineering interrogations of the spacecraft were performed, permitting full use of observation time and continuous records of spacecraft temperatures.

By 12:55 GMT, the bright K-corona had disappeared below the lunar horizon, and several series of full-aperture, 5-min exposures were made of the F-corona (inner zodiacal light). The camera was then shifted from the sunset position to record the F-corona at even greater distances from the sun. Data thus far indicate that infor-

mation on the F-corona has been obtained out to 30 solar radii. Plans for analysis of the data include:

- (1) Comparison with K-coronometer and other telescope data.
- (2) Addition and/or subtraction of multiple exposures in each series.
- (3) Subtraction of successive pictures to obtain the coronal brightness in the narrow strip eclipsed between frames.
- (4) Determination of the brightness distribution in the F-corona as far from the sun as possible in order to establish the distribution of particulate matter in the inner solar system.
- (5) Analysis of scattering effects by the lunar horizon, or a possible lunar atmosphere. (Note the "beaded" structure in Fig. VI-1.)

## VII. Chemical Analysis of the Moon at Surveyor V

### Landing Site: Preliminary Results

A. L. Turkevich, E. J. Franzgrote, and J. H. Patterson

A remarkable amount of information about the moon has been obtained by earth-based measurements. Together with theoretical arguments, these have provided clues as to the origin and history of this earth satellite. In the last decade, such earth-based observations have been supplemented by results from the United States and Russian space programs, which have provided high-resolution photographs, data on the physical properties of the lunar surface, and radiation measurements. Some of the basic questions about the moon, however, can best be answered by a knowledge of the chemical composition of lunar material; observations and measurements until now have provided only indirect information about this important property. The Alpha-Scattering Experiment is designed to measure directly the abundances of the major elements of the lunar surface. *Surveyor V* was the first lunar soft-landing vehicle to carry such an experiment.

The alpha-scattering method of chemical analysis, the instrument used on the *Surveyor* mission, and the nominal mission operation have been previously described

(Refs. VII-1 through VII-4). This technique is especially suitable for instrumented space missions because of characteristics such as compactness and relative simplicity of operation. It involves the measurement of the energy spectra of alpha particles scattered backward from the atomic nuclei of the sample and of protons obtained from the nuclear reactions of alpha particles with some of the lighter elements. These spectra contain quantitative information on all major elements in the sample except hydrogen, helium, and lithium. The method can readily distinguish among the lighter elements, but the atomic weight of heavier constituents can be identified only approximately.

Only part of the data from the *Surveyor V* mission have been analyzed in a preliminary manner. However, the experiment has already established the principal chemical elements present on the lunar surface at the *Surveyor V* landing site. This section summarizes the main features of the instrument and of the experiment, describes the actual mission sequence, and presents the preliminary results and some discussion of their significance.

## A. Instrument Description

The alpha-scattering instrument consists of a sensor head, which is deployed directly to the lunar surface, and a digital electronics package located in a thermal compartment on the spacecraft. Associated equipment includes an electronic auxiliary, a deployment-mechanism/standard-sample assembly, and a thermally insulated electronics compartment. Figure VII-1 is a photograph of the instrument and its auxiliary hardware.

The total weight of the alpha-scattering equipment, including mechanical and electrical spacecraft-interface substructure and cabling, is 13 kg. Power dissipation is 2 W, increasing to 17 W when heaters in the sensor head and electronics compartment are both active.

### 1. Sensor Head

The sensor head is primarily a box ( $17.1 \times 16.5 \times 13.3$  cm high), with a 30.5-cm-diameter plate on the bottom. The main purpose of the plate is to minimize the probability of the box sinking appreciably into a possibly soft lunar surface. Figure VII-2 shows a bottom view of the sensor head. In the bottom of the sensor head is a sample port, 10.8 cm in diameter. Recessed 7 cm above this circular opening is a set of six curium-242 alpha sources, collimated in such a way that the alpha particles are directed through the opening. Across the face of each collimator is a thin, aluminum-oxide film to prevent recoils from the alpha source from reaching the sample area; a second film is mounted in front of each collimator for additional protection. Close to the alpha sources are

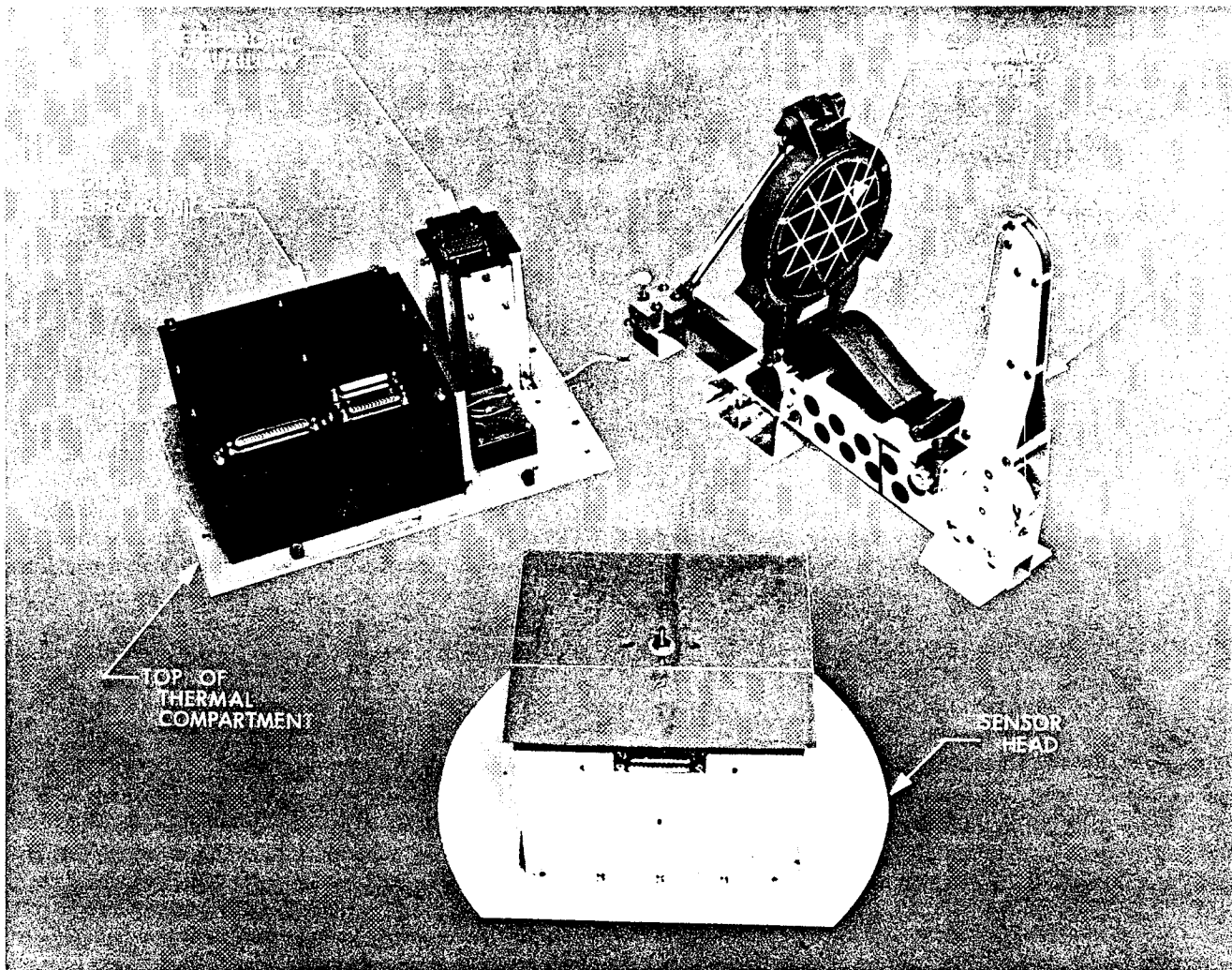


Fig. VII-1. Alpha-scattering instrument and auxiliary hardware.

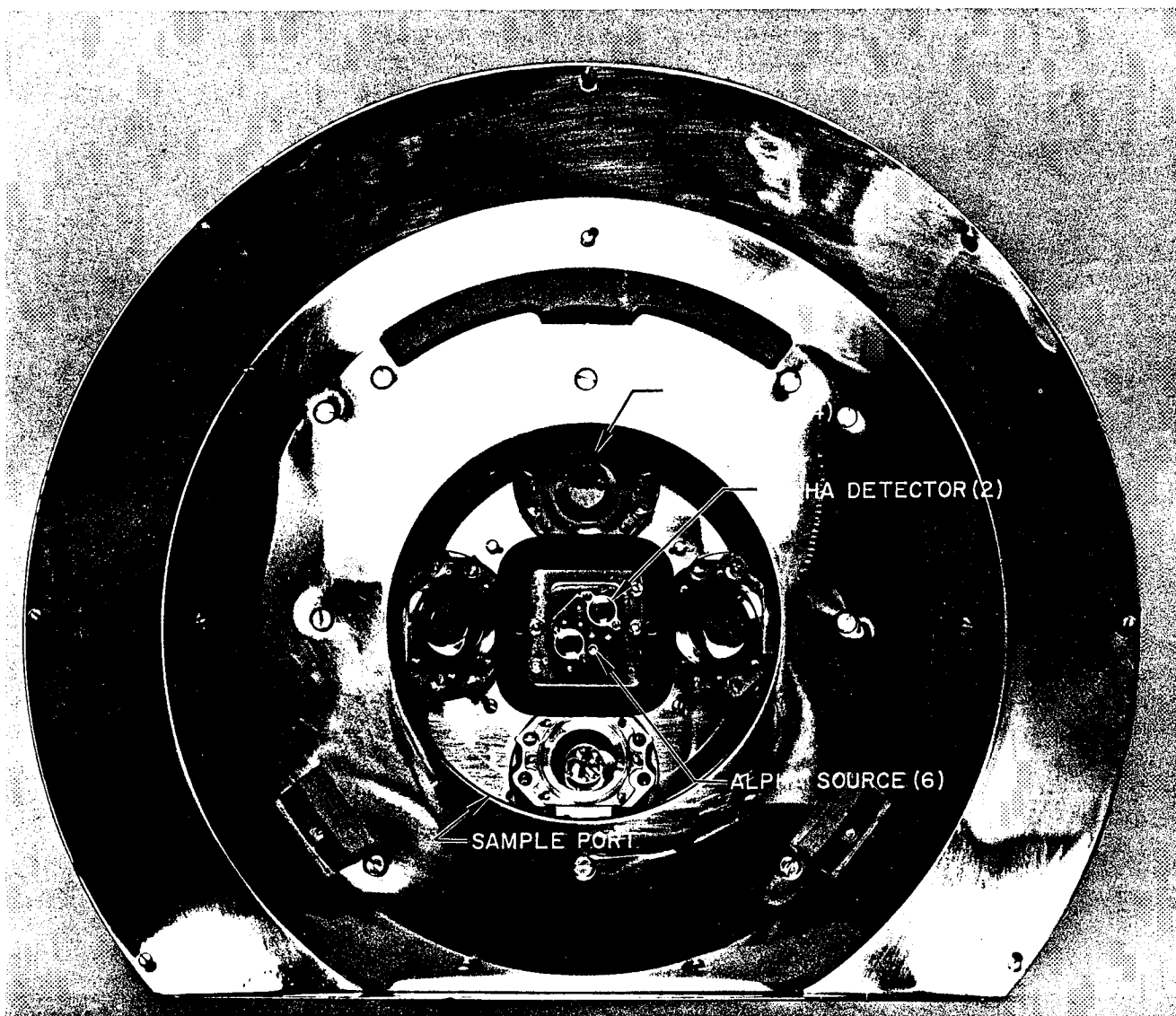


Fig. VII-2. Bottom view of the alpha-scattering sensor head.

two detectors arranged to detect alpha particles scattered back from the sample at an average angle of 174 deg from the original direction. These 0.2-cm<sup>2</sup> alpha detectors are of the silicon, surface-barrier type, with an evaporated-gold front surface.<sup>1</sup> Thin films are mounted on collimation masks to protect the detectors from alpha contamination and excessive light.

The sensor head also contains four lithium-drifted, silicon detectors (1-cm<sup>2</sup> area each) designed to detect

<sup>1</sup>A. J. Tuzzolino, J. Kristoff, and M. Perkins (to be submitted to *Nuclear Instruments and Methods*, November 1967).

protons produced in the sample by the alpha particles. Gold foils, approximately 11 $\mu$  thick, prevent scattered alpha particles from reaching these detectors. Figure VII-3 is a diagrammatic side view of the sensor head, showing the configuration of sources, sample, and detectors.

Because the expected proton rates from the sample are low, and because these detectors are more sensitive to radiation from space, the proton detectors are backed by guard detectors. Most of the charged particles from space that strike a proton detector must first pass through the

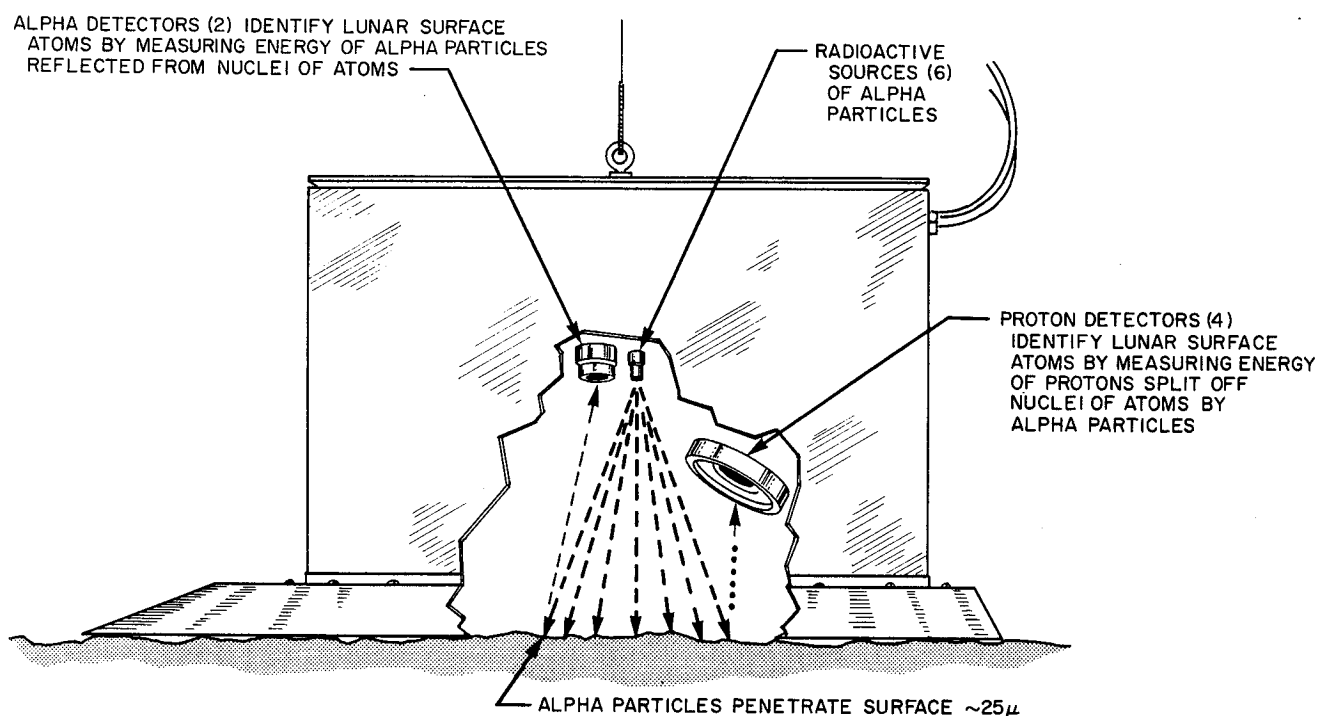


**Fig. VII-3. Diagrammatic view of alpha-scattering sensor head internal configuration.**

corresponding guard detector, whereas protons from the sample are stopped in the proton detector. The electronics associated with the guard and proton detectors are arranged so that an event registered in both will not be counted as coming from the sample. This anticoincidence arrangement reduces significantly the background in the proton mode of the instrument.

Separate 128-channel, pulse-height analyzers are used with the alpha and proton detectors. An output pulse from a detector is amplified and converted to a time-analog signal, whose duration is proportional to the energy deposited in the detector. The outputs of the two alpha detectors are combined before this conversion; a separate mixer circuit is used for the four proton-detector outputs. A ratemeter circuit is used to measure the frequency of events occurring in the guard (anti-coincidence) detectors, but provides no information on the energy of such events.

In addition to the curium-242 sources, detectors, and associated electronics, the sensor head contains a platinum-resistance thermometer, a 5-W heater, and an electronic pulser. The pulser is used to calibrate the electronics of the instrument by introducing electrical pulses of two known magnitudes at the detector stages of the alpha and

proton systems. This calibration mode is initiated by command from earth. Small amounts of alpha-radioactive einsteinium-254 are also used to calibrate the alpha and proton systems and, in addition, serve as live-time monitors. The einsteinium is located on the gold foil facing each proton detector and on the thin films mounted in front of the alpha detectors.

The external surfaces of the sensor head have been designed for passive thermal control. A second-surface mirror on top of the sensor head is used as a radiator to cool the sensitive components inside. A 5-W heater is used at low temperatures. The operating temperature range specified for the sensor head is  $-40$  to  $+50^{\circ}\text{C}$ .

## 2. Digital Electronics

The output of the sensor head is a signal (in time-analog form) that characterizes the energy of an event in either the scattered alpha or proton mode of the instrument. The signals from the sensor head are converted to nine-bit binary words by the digital electronics. Seven bits of each word identify which of the 128 channels represents the energy of the registered event. Two extra bits are added before transmission, one to identify the start of the word and one at the end of each word, as a



parity check on transmission errors. Buffer registers provide temporary storage of the energy information for readout into the spacecraft telemetry system. The transmission rates are 2200 bits/sec for the alpha mode and 550 bits/sec for the proton mode. Measured events with energy greater than the range of the analyzers are routed to channel 126 (overflow channel).

The electronics package also contains power supplies and the logical electronic interfaces between the instrument and the spacecraft. For example, the output of an individual detector, together with its associated guard detector, can be blocked by command from earth. Also via the electronics unit, the temperature of the sensor head, as well as various monitoring voltages, can be transmitted to earth.

### 3. Electronic Auxiliary

The required electrical interfaces between the sensor head, digital electronics and spacecraft circuits are provided by an electronic auxiliary that provides command decoding, signal processing, and power management. Basic spacecraft circuits interfacing directly with the sensor head and digital electronics are: (1) the central signal processor, which provides signals at 2200 bits/sec and 550 bits/sec for synchronization of instrument clocks; and (2) the engineering signal processor, which provides temperature-sensor excitation current and commutation of engineering data outputs.

The electronic auxiliary provides two data channels for the alpha-scattering instrument. The separate alpha and proton channels are implemented using two sub-carrier oscillators. Characteristics of these channels are defined as:

Characteristic	Alpha channel	Proton channel
Data input to electronic auxiliary	Digital (non-return to zero)	Digital (non-return to zero)
Input data rate	2200 bits/sec	550 bits/sec
Subcarrier oscillator center frequency	70,000 Hz	5400 Hz

The electronic auxiliary and the digital electronics are contained in electronics compartment C, which is attached to the upper part of the spaceframe. For passive control of temperatures at high sun angles, the top of this compartment is painted white and the sides and bottom are

insulated. A 10-W heater assembly, operated by means of the engineering signal processor, provides active thermal control at low temperatures. The operating temperature range specified for the electronic units in compartment C is  $-20$  to  $+55^{\circ}\text{C}$ .

### 4. Deployment Mechanism/Standard Sample

The deployment mechanism provides stowage of the sensor head, deployment to the background position, and to the lunar surface. The sensor head is mounted to the deployment mechanism by means of three support lugs on the bottom plate. The deployment mechanism clamps that engage these lugs are released during the deployment operation. Figure VII-4 illustrates the two-stage operation of the deployment mechanism. From the stowed position, the sensor head is first released on command to a position 56 cm above the nominal lunar surface by activation of an explosive-pin-puller device. From the background position, the sensor head is then lowered directly to the lunar surface by activation of another explosive-pin-puller device. The deployment velocity is controlled by an escapement.

A sample of known composition is attached to the platform on which the sensor head is mounted in the stowed

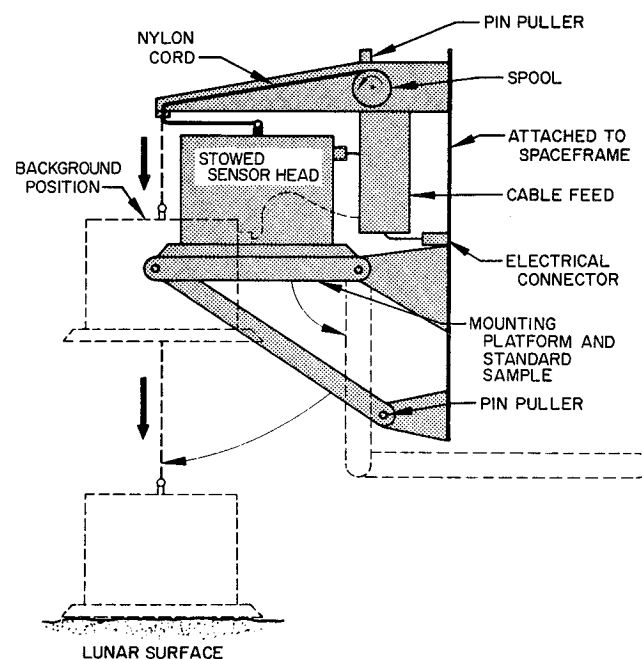


Fig. VII-4. Operation of the alpha-scattering deployment mechanism.

position. This standard-sample assembly covers the circular opening in the bottom of the sensor head during spacecraft transit and landing to minimize entrance of dust and light and to provide a means of assessing instrument performance shortly after the spacecraft lands on the moon. The standard sample and mounting platform move aside when the sensor head is deployed to the background position.

### 5. Characteristics of Alpha-Scattering Instrument Flown on Surveyor V

The general *Surveyor*-type alpha-scattering instrument has been described in the preceding paragraphs, and in

**Table VII-1. Some milestones in the history of the Surveyor V alpha-scattering instrument**

Date	Milestones
October 1, 1966	Instrument construction completed
October 29, 1966	Acceptance test completed
November 22, 1966	Science calibration completed
November 22, 1966	Cyclotron tests to measure response to solar and cosmic particles
January 18, 1967	Unit delivered to Hughes Aircraft Co.
May 13, 1967	Solar-thermal-vacuum tests on spacecraft
June 21, 1967	Combined system test
August 24, 1967	Radioactive sources installed and final tests started at Cape Kennedy
September 8, 1967	Launch (total hours of operation at time of launch: 925)

Refs. VII-3 and VII-4. The milestones in the history of the specific instrument used on *Surveyor V* are listed in Table VII-1; some of its principal, detailed nuclear characteristics are given in Table VII-2.

## B. Experiment Control

### 1. Alpha-Scattering Analysis and Command

The Alpha-Scattering Experiment is designed to be controlled from the Space Flight Operations Facility (SFOF), Pasadena, Calif., by means of commands transmitted to the spacecraft from the tracking sites. These commands are chosen on the basis of the analysis of data received from the spacecraft and relayed to the SFOF during the mission. The commands control:

- (1) Spacecraft power to the instrument.
- (2) Deployment of the sensor head.
- (3) Number of detectors used.
- (4) Electronic calibration pulser.
- (5) Heater power for thermal control.

Table VII-3 lists the command assignments for the alpha-scattering system.

Two types of information relative to the Alpha-Scattering Experiment are transmitted from the spacecraft: engineering data and science data. The engineering

**Table VII-2. Principal characteristics of the Surveyor V alpha-scattering instrument**

<b>Curium-242 Source Characteristics</b>		<b>Proton Detectors</b>	
Decompositions per minute, as of September 10, 1967 (total for six sources)	$2.75 \times 10^{11}$ d/min	Gold-foil thickness (0.420 to 0.429 mil, equivalent to 20.6 to 21.0 mg/cm <sup>2</sup> ) (energy loss for 6.1-MeV alpha particles)	5.8 MeV
Mean energy, as measured through capsule protective films	6.04 ± 0.02 MeV	(energy loss for 2.0-MeV protons)	1.17 MeV
Energy-spread range for six sources (full width at half height)	1.2 to 2.0%	<b>Guard Detector System</b>	
Thickness of secondary protective film (energy loss for 6.1-MeV alpha particles)	0.010 ± 0.003 MeV	Approximate electronic threshold	0.30 MeV
<b>Alpha Detectors</b>		Guard ratemeter response; events/sec	
Thickness of evaporated-gold surface (energy loss for 6.1-MeV alpha particles)	0.039 MeV	10	0.080 V
Thickness of alpha-mask films (energy loss for 6.1-MeV alpha particles)	0.029 MeV	30	0.300 V
		100	0.900 V
		300	1.800 V
		1000	2.500 V
		<b>Electronics Energy Scale (temperature of sensor head and of digital electronics = 25°C)</b>	
		Alpha	$N = 19.30E - 12.0$
		Proton	$N = 19.11E - 11.65$
		(N = channel number; E = energy deposited by particle in detector, MeV)	

**Table VII-3. Command assignments**

Command	Function
3501	Alpha-scattering power on
3502	Alpha-scattering power off
3503	Sensor-head heater power on
3504	Sensor-head heater power off
3505	Deploy to background position (interlocked with 3617)
3506	Deploy to lunar surface (interlocked with 3617)
3507	Alpha detector 1 on
3510	Calibration pulser on
3511	Proton detector 4 on
3512	Proton detectors 3 and 4 off
3513	Proton detector 2 on
3515	Alpha detectors 1 and 2 off
3516	Proton detectors 1 and 2 off
3517	Proton detector 1 on
3520	Calibration pulser off
3522	Proton detector 3 on
3523	Alpha detector 2 on
3617	Interlocked with deployment commands
0135	Compartment C heater power off
0136	Compartment C heater power on

measurements are used to monitor instrument voltages, temperatures, detector configuration, and background rates in the anticoincidence detectors. The seven parameters that are monitored are listed in Table VII-4.

The science data are the 9-bit digital words that characterize the energy of each of the analyzed alpha particles or protons. These data leave the instrument as separate alpha and proton bit streams and modulate separate sub-carrier oscillators; they are then combined with the engineering data and transmitted by the spacecraft to earth. The composite signal from the spacecraft is recorded on magnetic tape at the tracking sites. These FR-1400 tapes containing the raw data comprise the prime source of alpha-scattering information for use in post-mission analysis.

For purposes of monitoring the experiment in real time, the signal is separated at the tracking site by discrimina-

**Table VII-4. Engineering data**

Engineering commutator	Measurement
AS-3	Sensor head temperature
AS-4	Compartment C (digital electronics temperature)
AS-5	Guard rate monitor
AS-6 (digital)	At least one alpha detector on
AS-7 (digital)	At least one proton detector on
AS-8	7-V monitor
AS-9	24-V monitor

tors and bit synchronizers into 2200-bit/sec alpha data and 550-bit/sec proton data. These reconstituted bit streams are presented to an on-site computer; this computer establishes and maintains synchronization of the 9-bit data words and assembles, within its memory, four spectra of 128 channels each. The four spectra are: alpha parity-correct, alpha parity-incorrect, proton parity-correct, and proton parity-incorrect. In this manner, data are obtained at the tracking site in accumulations ranging in duration from 2 min during pulser calibration to a nominal 40 min during sample and background phases. The assembled spectra are transmitted via teletype to the SFOF for display and further computer processing.

Data analysis during the mission is performed so that proper control over the experiment may be exercised. The engineering data are simply displayed and compared with pre-launch measurements and predictions to assess the performance of the instrument and the functioning of commands.

The alpha and proton science data are also used to assess the performance of the instrument and are analyzed to determine the duration of the several operational phases. This science-data analysis is conducted in the SFOF using a 7094 computer program (Ref. VII-5). This computer program is designed to:

- (1) Correct for transmission errors.
- (2) Give alarm if event-rate limits are exceeded.
- (3) Normalize the spectra to a standard duration, alpha-source intensity, and number of operating detectors.
- (4) Make an approximate correction of the energy scale on the basis of temperature measurements.
- (5) Subtract theoretical or measured backgrounds.
- (6) Sum individual spectra.
- (7) Provide a statistical analysis and least-squares breakdown of the spectra into elemental components. The least-squares analysis uses a limited library of only eight elemental spectra.

This program facilitates comparison of lunar data with pre-launch spectra and gives a sensitive indication of changes in instrument performance from one accumulation of data to the next.

## 2. Alpha-Scattering Sequence of Operations

In order to interpret spectra from the lunar sample, data are obtained on the performance of the instrument

and on the background radiation in the lunar environment. These data are obtained by operating the instrument with the sensor head in each of three positions: (1) stowed, (2) background, and (3) lunar surface position.

In the stowed position, the sensor head is supported on the standard sample. Data received from this sample and from pulser calibration are compared with pre-launch measurements and give a measure of instrument characteristics in the lunar environment.

At the completion of this phase of operation, the instrument is deployed to the background position by earth command. The supporting platform and standard sample move aside, leaving the sensor head suspended about 56 cm above the lunar surface. In this position, the sensor head responds primarily to cosmic rays, solar protons, and possible surface radioactivity.

When it is determined that sufficient background data have been obtained, the sensor head is lowered directly to the lunar surface upon command from earth. The main accumulation of data is then begun, interrupted only by calibrating sequences and other spacecraft operations.

The calibration sequence is used to check the electronics of the instrument by introducing electrical pulses of two known magnitudes at the detector stages of the alpha and proton systems. The calibration pulser is operated by command from earth. The detectors and their associated amplifiers are usually calibrated individually by the proper selection of detector on/off commands.

If operations permit, the television camera is used to view the surface to which the sensor head is deployed and to monitor the deployment of the instrument. An auxiliary mirror is located on the spacecraft to give an unobstructed view of the deployment area.

Detailed alpha-scattering operations planned for *Surveyor V* were:

- (1) Television survey: stowed phase.
- (2) Alpha-scattering operations: stowed phase.
  - (a) Accumulation of data: 2 to 6 hr.
  - (b) Calibration.
- (3) Deploy sensor head to background position.
- (4) Television survey: background phase.

- (5) Alpha-scattering operations: background phase.
  - (a) Calibration.
  - (b) Accumulation of data: 2 to 6 hr.
  - (c) Calibration.
- (6) Lunar surface television survey.
- (7) Deploy sensor head to lunar surface.
- (8) Television survey of sensor head in deployed position.
- (9) Alpha-scattering operations: lunar surface phase.
  - (a) Accumulation of data: 1 hr.
  - (b) Calibration.
  - (c) Accumulation of data: at least 24 hr.
  - (d) Calibration as required.

## C. Mission Description

### 1. Pre-Launch Operations at Cape Kennedy

Approximately 2 wk before launch, the sensor head was removed from the spacecraft at Cape Kennedy and taken to a special facility for final calibration and preparation for flight. The operations performed in this facility were a shortened version of the science calibration conducted on this instrument 9 mo earlier.

A special test chamber equipped for thermal-vacuum operation and sample introduction was used for the measurements. The sensor head was calibrated at several temperatures using the electronic pulser and standard alpha sources; background measurements were taken, and a light test of the alpha-detector films was performed. The curium-242 flight sources were then installed, and spectra were obtained from a small selection of standard materials including polyethylene, magnesium, aluminum, quartz, and iron. (A spare sensor head had been calibrated by the same procedure just prior to this operation and was being stored in another vacuum chamber.)

To prevent deterioration of the flight sources, the sensor head was purged with dry nitrogen gas whenever it was exposed to the atmosphere. Nitrogen purging was continued after the sensor head was reinstalled on the spacecraft until the moment of launch.

Final checks of instrument performance on the spacecraft were made using the electronic pulser and by obtain-

ing nitrogen spectra. The last of these readiness tests was performed within 12 hr of launch.

## 2. Transit Operation

Initial operation of the alpha-scattering instrument after the launch of *Surveyor V* occurred during transit to the moon. This operation was performed several hours after the mid-course velocity correction. The command to turn alpha-scattering power on was transmitted at 10:36:47 GMT on Day 252 with the spacecraft at a distance of 221,000 km from the earth and 178,000 km from the moon. At this time, telemetry from the temperature sensor in the digital electronics indicated approximately  $-26^{\circ}\text{C}$ . The sensor head temperature was  $-1^{\circ}\text{C}$ . The spacecraft, then in view of the tracking station at Canberra, Australia, was switched to high power and transmitted alpha-scattering data via an omnidirectional antenna. Two 10-min accumulations of standard-sample data and seven 2-min pulser calibration runs were received during less than 1 hr of operation. The communications link from the spacecraft was excellent; only one parity error was observed in  $6 \times 10^6$  bits. The data agreed well with pre-launch measurements, and showed that the instrument had survived the launching and mid-course rocket firing. The spectra also showed that the radiation background rates in cislunar space at that time were low enough for useful sample measurements. This was encouraging because the background rates on the moon were expected to be even lower (due to lunar shielding), unless the surface radioactivity were unusually high.

## 3. Lunar Landing

Touchdown of *Surveyor V* occurred at 00:46:44 GMT on Day 254, after a terminal sequence in which the main retro motor was operated to within 1.6 km of the lunar surface. (The standard end-of-burning distance is about 12 km.) Since aluminum-oxide particles comprise part of the exhaust products of this solid-propellant rocket, the possibility of an effect on the Alpha-Scattering Experiment has been investigated. An analysis of the problem is included in Appendix A.

The spacecraft came to rest at a slope of about  $19.5^{\circ}$  deg on the wall of a crater, with the alpha-scattering instrument on the downhill side. The direction of slope was favorable for the deployment operations, but the high view factor to the lunar surface was at least partially responsible for the high sensor-head temperatures encountered during the mission. During spacecraft touchdown, subsurface material was scattered downslope into the area where the instrument was later deployed.

## 4. Post-Landing Operations

*a. Stowed position (Day 254).* Approximately 2 hr after landing, an engineering evaluation of the condition of the instrument was performed. The command to apply spacecraft power to the instrument was transmitted from the tracking station near Goldstone, California, at 02:49:34 GMT. The temperature of the sensor head at that time was  $16^{\circ}\text{C}$ ; the digital electronics was at  $-9^{\circ}\text{C}$ . Instrument voltages were found to be normal and the guard-detector event rate was found to be somewhat lower than that observed in transit, as expected. Because of other spacecraft operations, alpha and proton data were not obtained at that time, and power to the instrument was commanded off at 04:40:00 GMT.

After transfer of tracking operations from California to Australia, television surveys of the alpha-scattering deployment area were conducted. Television pictures of the auxiliary viewing mirror were obtained with both wide- and narrow-angle lenses. Unfortunately, however, only the lower-resolution, wide-angle frames include the reflection of the deployment area in the mirror. Figure VII-5a shows an enlargement of part of one of the wide-angle frames, with the deployment area indicated. Several rocks of about 3 to 6 cm in diameter can be seen in an original print of Fig. VII-5a. The relatively smooth appearance of the deployment area indicates that the largest particle in this area is less than about 3 cm across.

Figure VII-6 is a picture of the sensor head in the stowed position, and was obtained in Australia during these early television operations. Part of the lunar surface later covered by the edge of the sensor head may be seen at the upper right.

The instrument was again activated, and alpha-scattering operations were resumed at 07:27:02 GMT. At instrument turn-on, the only anomaly connected with alpha-scattering commands occurred; the calibration pulser started operating without being commanded on. The anomalous behavior was noted by the data analyst at the Canberra tracking site; the results were also observed in the first accumulation of alpha and proton data received at the SFOF. The pulser was turned off by command at 07:50:01 GMT.

At about this time, a decision was made to conduct a planned vernier rocket engine static firing during the next Goldstone visibility period. Since the expected effects on the Alpha-Scattering Experiment were uncertain, it was decided that the operations in the stowed and background positions should be shortened as much as possible to allow

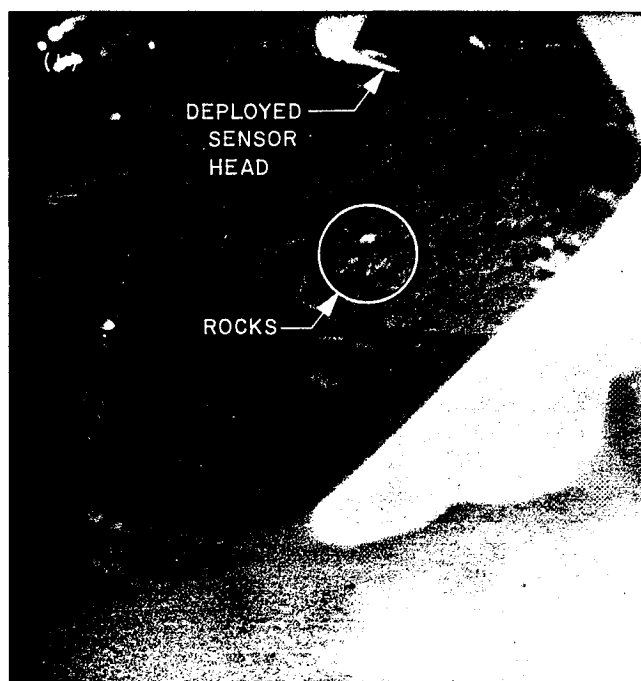
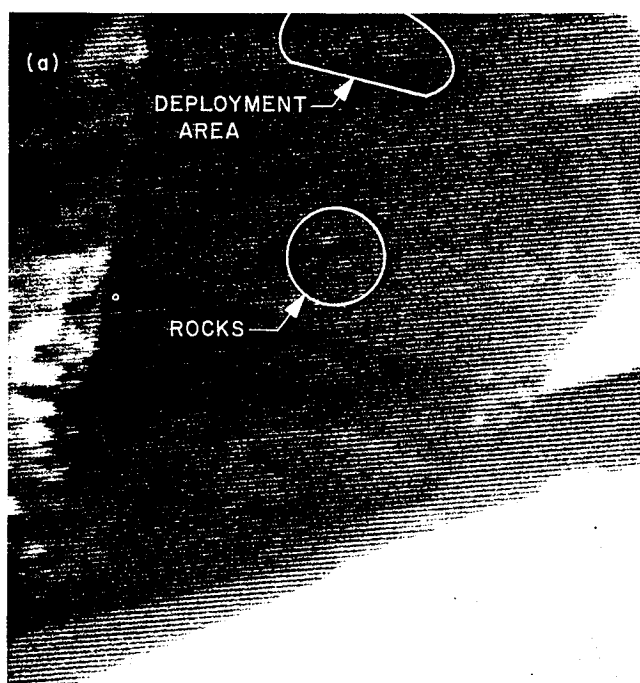


**Fig. VII-5. Surveyor V pictures of the alpha-scattering deployment area, as reflected in an auxiliary mirror. (a) Enlargement of part of a wide-angle picture showing area of lunar surface to which the sensor head was later deployed (Day 254, 08:35:17 GMT). (b) Narrow-angle view of the same area, after deployment of the sensor head (Day 255, 02:50:32 GMT).**

that lunar surface data be obtained before the rocket test. Only about 12 hr were available for the entire operation.

An abbreviated calibration sequence showed that the alpha-scattering system was performing well. Three 20-min accumulations of alpha and proton data from the standard sample were then analyzed and found to agree well, within statistics, with pre-launch results. The decision was made to deploy the sensor head to the background position.

**b. Background position (Day 254).** Because of the short time available, the planned television survey of the deployment to the background position was not conducted. Instead, the alpha data bit stream was monitored at the tracking site using an oscilloscope display of the discriminator output. If the deployment were to proceed correctly, the alpha event rate was expected to drop by more than a factor of ten as the standard sample moved away. The command was sent at 12:14:14 GMT, and after a few seconds, word of a successful deployment was received from Australia.

The planned calibration sequence was not conducted so that a maximum of background data could be obtained. Eleven accumulations of data for a total of 141 min were received from the tracking stations in Australia and Spain; one 2-min pulser calibration was run. The instrument temperatures remained relatively constant during this period.

Although more data in the background position would have been desirable, the impending vernier firing test made it advisable to end this phase of operation and proceed with the deployment to the lunar surface.

**c. Lunar surface position (Day 254).** The planned television survey of the deployed instrument was again bypassed, and the deployment was monitored by observation of the alpha data stream. The command to deploy the sensor head onto the lunar surface was transmitted from the tracking station near Robledo, Spain (DSS 61), at 15:36:03 GMT. Seconds later, the event rate had increased sharply; we knew that we were receiving data from the lunar surface.

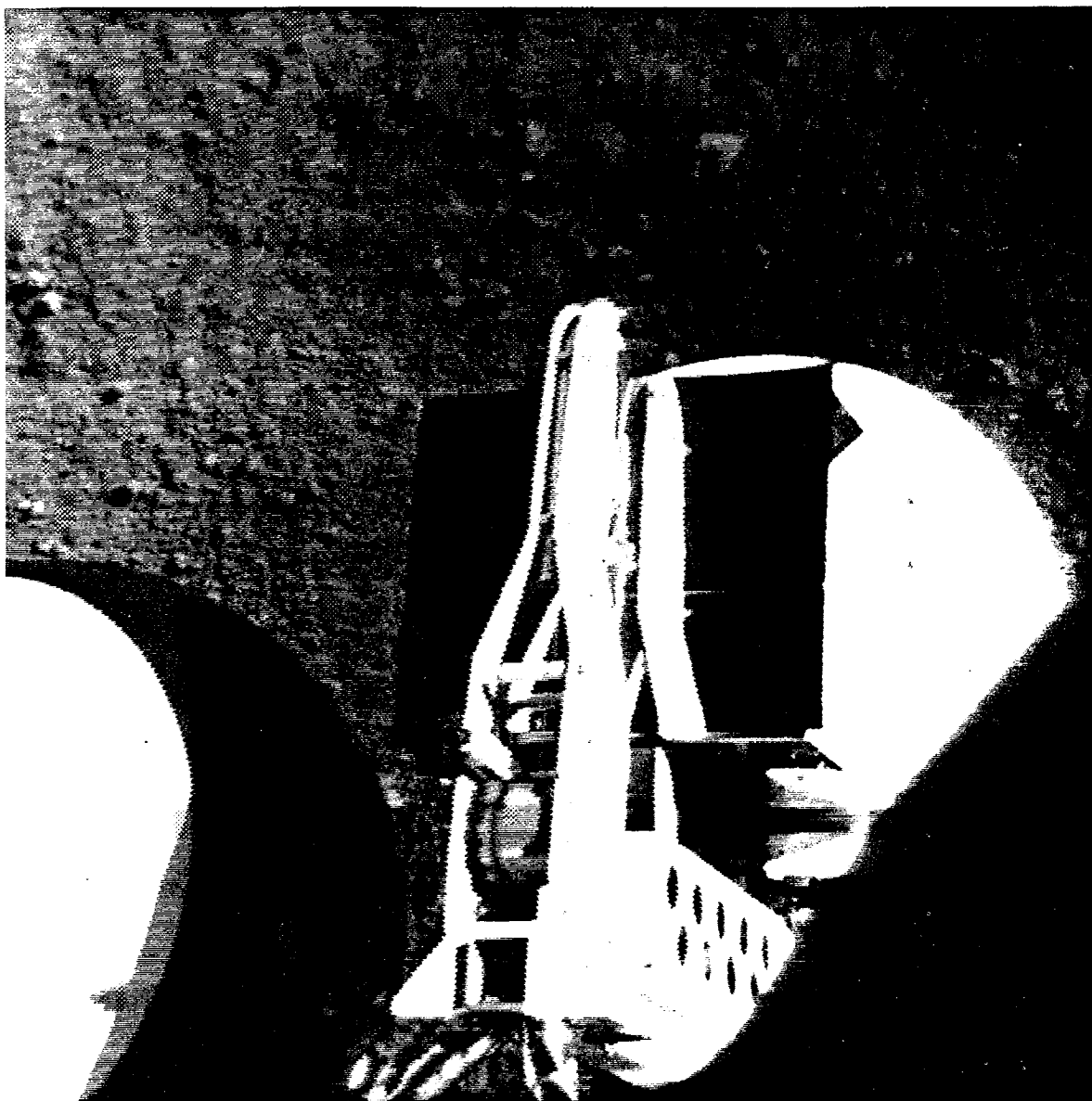
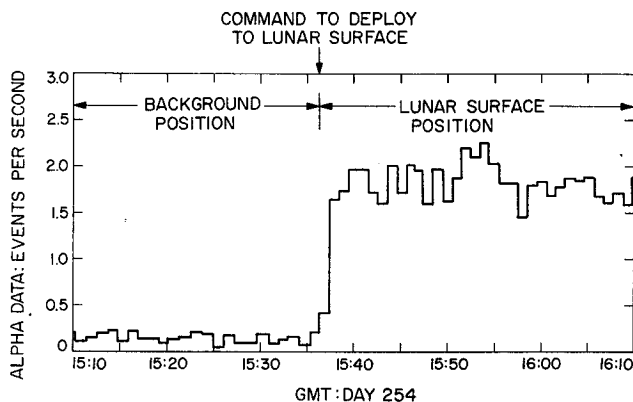


Fig. VII-6. View of the alpha-scattering instrument sensor head in the stowed position on Surveyor V (Day 254, 06:26:10 GMT).

Figure VII-7 shows the total alpha event rate during this deployment period, as derived later from a magnetic-tape recording. The rate rose from about one event in 10 sec in the background position to two events per second on the lunar surface.

The first 20-min accumulation of lunar surface data started at 15:37:00 GMT. After receiving accumulations



**Fig. VII-7.** Plot of event rate of analyzed alpha particles as a function of time, showing marked increase when sensor head was deployed from the background position to the lunar surface.

totaling 100 min, an abbreviated pulser calibration sequence was performed. Analysis of the data indicated that the operation was proceeding normally. The sensor head temperature decreased slowly during this period from about 34 to 27°C because of the larger view factor to space in the new position. The digital electronics temperature rose from 16 to 20°C during this time.

The accumulation of spectra continued until the end of the DSS 61 tracking period. A total of about 5 hr of data from the lunar sample were received; two calibration sequences were run.

Television surveys conducted over Goldstone, California (DSS 11), produced the picture shown in Fig VII-8a, in which the sensor head is seen resting in proper position on the lunar surface. (The picture has been corrected by computer processing for the sine-wave response of the camera system.) Figure VII-5b is a narrow-angle picture of the sensor head on the lunar surface taken through the auxiliary mirror at this time. It may be compared with the wide-angle picture of the deployment area (Fig. VII-5a) previously described.

*d. Lunar surface operations (Day 255).* The vernier static firing test was postponed a day, and alpha-scattering analysis of the lunar sample was resumed at 06:18:31

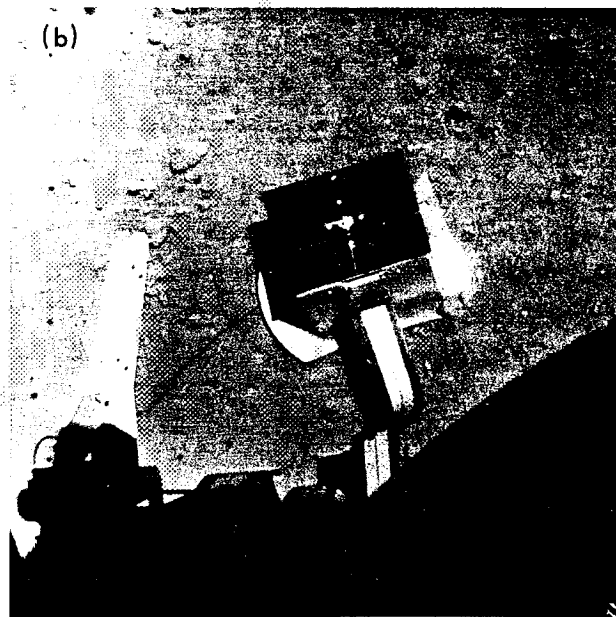
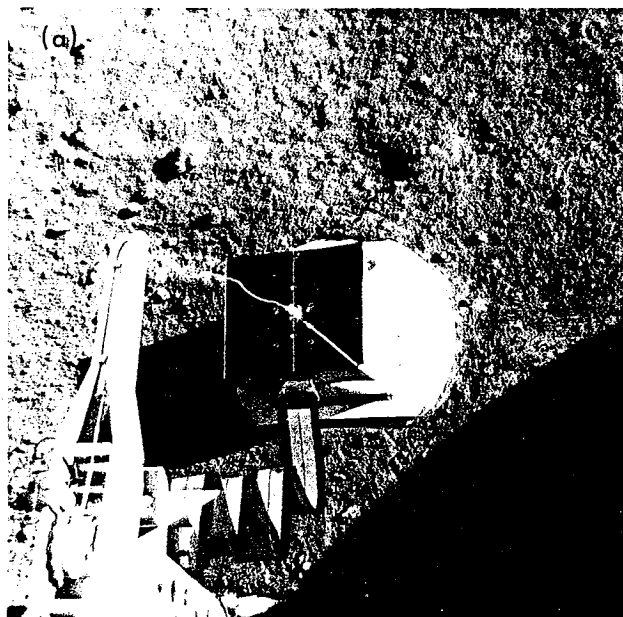


**Fig. VII-8.** Two views of the alpha-scattering sensor head on the lunar surface. (a) Initial position (first lunar sample). (b) Position after vernier rocket engine static firing.



GMT over the Canberra, Australia, Tracking Station (DSS 42). Accumulation of lunar surface data was alternated with calibration runs for the next 16 hr. By the end of this period, an additional 12 hr of lunar spectra had been secured, for a total of 17 hr. Although the sensor head had risen in temperature to about 42°C, the data appeared to be of high quality and the performance of the instrument was excellent. The instrument power was then commanded off in preparation for the vernier rocket test.

*e. Vernier static firing (Day 256).* The vernier engines were fired at 05:38 GMT. Television pictures taken shortly thereafter indicated that the sensor head and/or the spacecraft had moved. Subsequent pictures showed that the sensor head had been moved about 10 cm downslope away from the spacecraft and had been rotated slightly by the rocket blast. Figure VII-8b is a picture of the sensor head after the vernier firing taken at the same camera coordinates as Fig. VII-8a. In the second position, the downhill edge of the circular plate of the instrument has dug into the surface material, and the left-hand edge of the plate is raised slightly above the surface.

About 3 hr later, the instrument was again turned on and found to be functioning perfectly. The vernier blast had moved it about one sample diameter; data were being received from a second lunar sample.

By the end of Day 256, approximately 9 hr of alpha and proton spectra had been accumulated on the new sample. The sensor head had risen to 52°C, but all systems (including the radiation detectors) were still functioning properly.

*f. Days 257 and 258.* Because of the high temperatures of the instrument and spacecraft, only 40 min of data were obtained on Day 257; the instrument remained off for the entire Day 258.

*g. Days 259 through 266.* Starting around lunar noon, the sensor head was shadowed by the planar array (directional antenna) of the spacecraft. The sensor head temperature dropped sharply, and operations were resumed. Data were obtained on the second lunar sample for 8 consecutive days; an additional 56 hr of accumulations were received at the SFOF. These data included several hours of operation with individual detectors as a test of sample geometry.

The instrument temperatures fluctuated during this period as a result of shadowing by various parts of the

spacecraft, but never again exceeded the upper operating limits of 50°C for the sensor head and 55°C for compartment C. The final operation of the instrument occurred on Day 266 shortly before lunar sunset at a sensor head temperature of -56°C (16°C below the specified operating limit).

*h. Summary of alpha-scattering operations and performance.* Table VII-5 is a summary of the science-data accumulation time in each of the operational configurations based upon spectra assembled by the on-site computers and transmitted via teletype to the SFOF. (A total of 107 hr of data was recorded on the FR-1400 tape recorders during the 193 hr that the instrument was activated.)

The performance of the alpha-scattering equipment and operational system during the *Surveyor V* mission was excellent.

All ten of the detectors in the sensor head functioned properly. Only once, during a period of rapidly changing temperatures, was there a suggestion of noise in the proton system. Sharp breakpoints in the sample spectra showed that the high quality of the curium-242 sources had been preserved. The films covering the sources and alpha detectors had survived the launch, mid-course maneuver, and touchdown operations. The electronics, calibration pulser, and einsteinium sources performed properly as evidenced by the sharpness of calibration peaks and agreement with pre-launch data. The guard detector and anticoincidence system worked as designed; guard monitor voltage and proton background spectrum agreed well with predicted values.

The digital electronics, instrument power supply, and electronic auxiliary performed as designed. Circuits used to monitor engineering parameters provided good data. Nearly 600 commands were transmitted to the alpha-scattering system; with the exception of the one cited, all

**Table VII-5. Science-data accumulation times**

Operational configuration	Accumulation time, min
Transit	20
Stowed (standard sample)	7*
Background	170
Lunar surface sample 1	1056
Lunar surface sample 2	4005
Calibration	281
Total	5607 min (93.5 hr)

commands gave the expected response. The deployment mechanism functioned properly in spite of the 19.5-deg tilt of the spacecraft.

The communications link from the spacecraft was excellent; a bit-error-rate of less than  $10^{-6}$  was estimated from the parity-incorrect spectra. In general, deviations from this high-quality data reception occurred only when the spacecraft was being tracked near the earth's horizon. Both of the major alpha-scattering computer programs and associated equipment gave excellent processing of the science data.

Television support of the alpha-scattering operations was very useful and, except for the lack of high-resolution coverage of the deployment area, pictures were of high quality.

## D. Results

### 1. Standard Sample Measurements

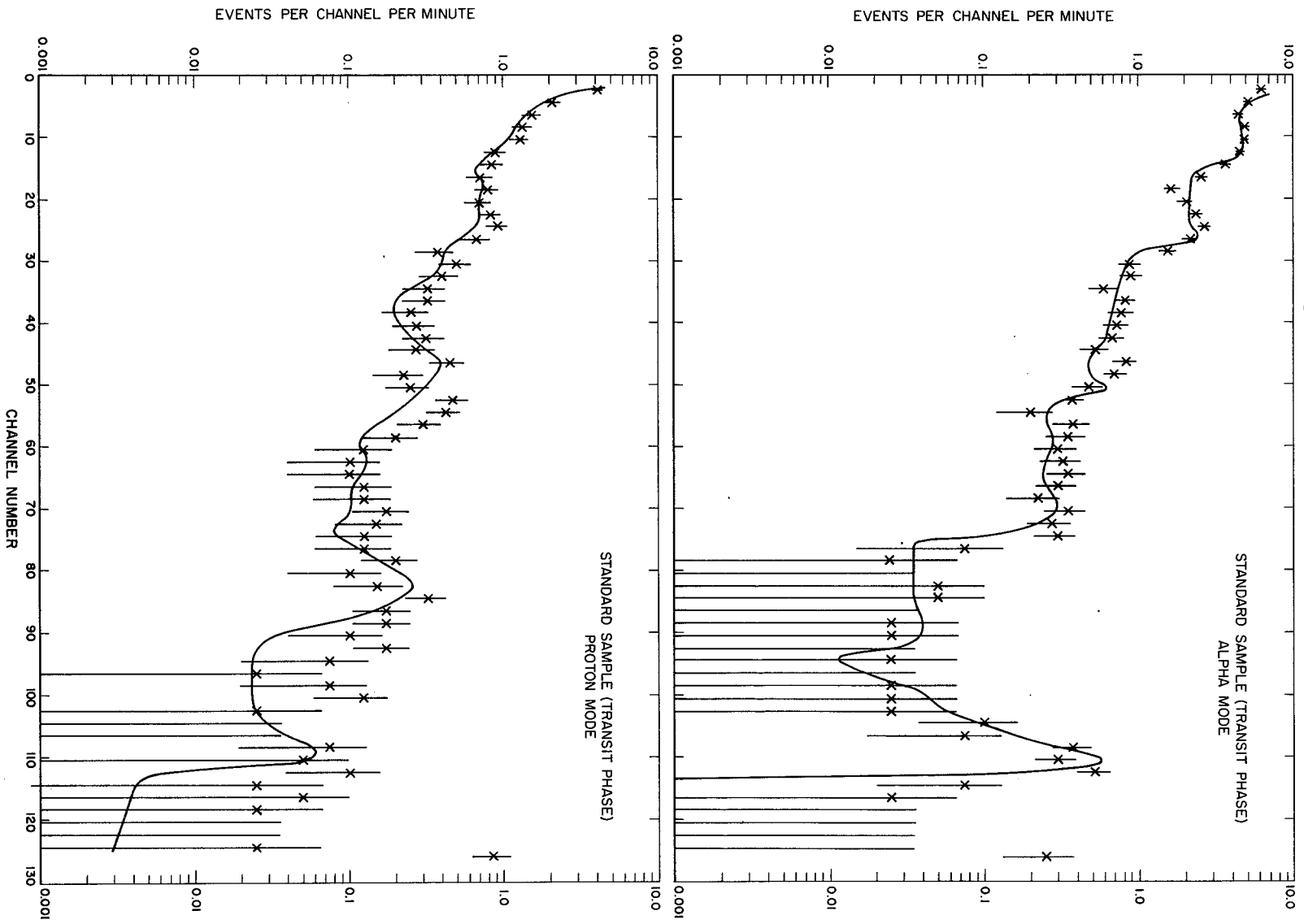
As indicated previously, there were two measurements made of the standard sample by the alpha-scattering

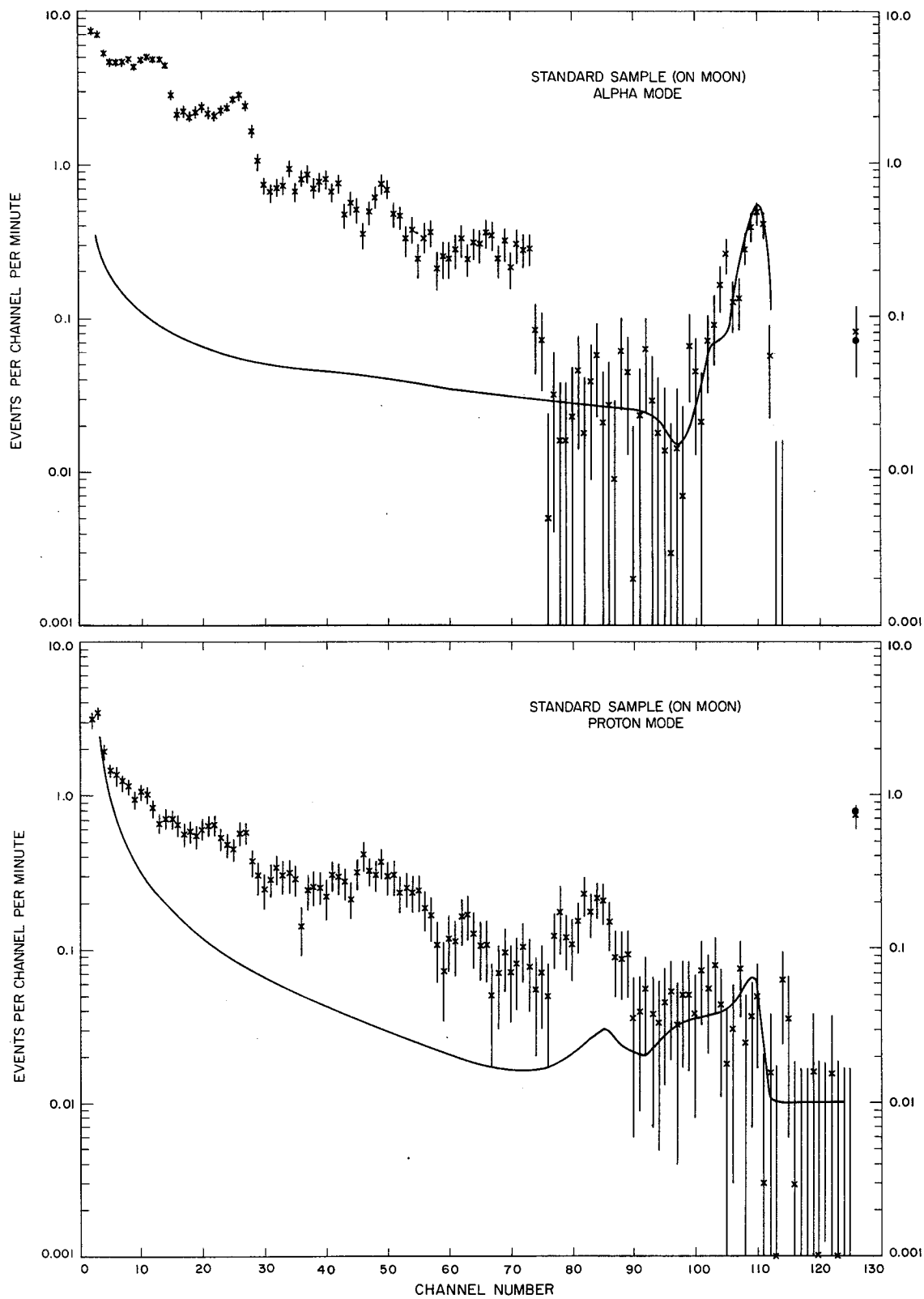
instrument during the *Surveyor V* mission. The first of these was during the transit phase, while in space between the earth and the moon; data obtained during the 20 min of measurement are shown, together with the associated statistical errors, in Fig. VII-9. In this figure, the observed events per channel of the alpha and proton modes of the instruments are plotted, on a logarithmic scale, as a function of the channel number (energy). The smooth curve in each case is derived from data obtained on a similar sample during the final calibrations of the sensor head at Cape Kennedy about 2 wk before launch. The pre-launch data have been increased by the background rates observed later on the moon.

It is seen that the data obtained during the short transit-phase operation are close to those expected from the standard sample. In particular, the agreement of observed and predicted events in the alpha mode at approximately channel 105 is evidence of little or no radioactive contamination which would have appeared had the thin protective films over the sources broken. Thus, the instrument had successfully survived the launch conditions.

**Fig. VII-9. Transit-phase data on standard sample. Data taken by the alpha-scattering instrument in the alpha and proton modes during the 20-min measurement of the standard sample during the flight to the moon. The experimental points, with statistical errors, are the averages of two channels (except in the overflow channel 126) in order to improve their statistical significance. The peaks at around channel 112 in both modes are due to the  $\text{Es}^{254}$  placed near the detectors before launch. These experimental data have not been corrected for the slightly nonstandard response of the instrument due to the low temperature at this time.**

The smooth curve in each case is derived from data obtained just before launch at Cape Kennedy. These have been corrected slightly for differences in digital electronics units (the Cape Kennedy measurements were made with the *Surveyor V* sensor head, but with a different digital electronics unit than the one flown on the mission); for the slightly different size polypropylene grid covering the standard glass sample flown on the mission as compared with that in the final calibrations; and for small differences in distance of the sample from the detectors of the instrument. The pre-launch data have also been increased by the background rates observed later on the moon.





The second measurement of the standard sample occurred after the landing of *Surveyor V* on the lunar surface. The data obtained during 60 min of measurement are shown in Fig. VII-10, together with their statistical uncertainties. In this case, the original data, as available from teletype transmission from overseas stations, have been corrected approximately to standard instrument characteristics by the SFOF computer. The background levels observed in the next stage of lunar operations are indicated by the solid curve.

The data presented in Fig. VII-10 are similar to those obtained on the standard sample before launch and during the short transit-phase operation (Fig. VII-9). A computer analysis of these data from the standard sample on the moon (after background subtraction) in terms of a library of eight elements (C, O, Na, Mg, Al, Si, Ca, and Fe) leads to a very good fit (see Fig. VII-11). The resulting chemical analysis of the standard sample glass is shown in Table VII-6. The last column in this table gives the chemical composition of the glass determined before launch by

**Table VII-6. Analysis of standard glass sample on the moon**

Element	Atomic percent	
	Surveyor V analysis <sup>a</sup>	Standard chemical analysis
Oxygen	56.4	58.6
Sodium	7.3	7.7
Magnesium	7.6	8.5
Aluminum	2.0	1.5
Silicon	20.2	17.2
Calcium	—1.5	—
Iron	8.1	6.5

<sup>a</sup>The Surveyor V results are normalized to 100% on a carbon-free basis. The glass was covered by a polypropylene grid that masked about 25% of the area.

conventional analytical techniques. Table VII-6 demonstrates that, even in as short a time as 1 hr, a chemical analysis of the glass agreeing with known values to within several percent was obtained by the alpha-scattering instrument under lunar operating conditions.

Fig. VII-10. Standard sample measurement on the moon. Data taken by the alpha-scattering instrument in the alpha and proton modes during 60 min of measurement of the standard sample after lunar landing. The experimental points (crosses) are indicated with statistical ( $1\sigma$ ) error bars. They have been corrected approximately to standard instrument response characteristics. The peaks at around channel 110 in both modes are due to  $\text{Es}^{254}$  placed near the detectors before launch. The solid curve in each case is a smoothed version of the background rates observed in the next stage of lunar operations.

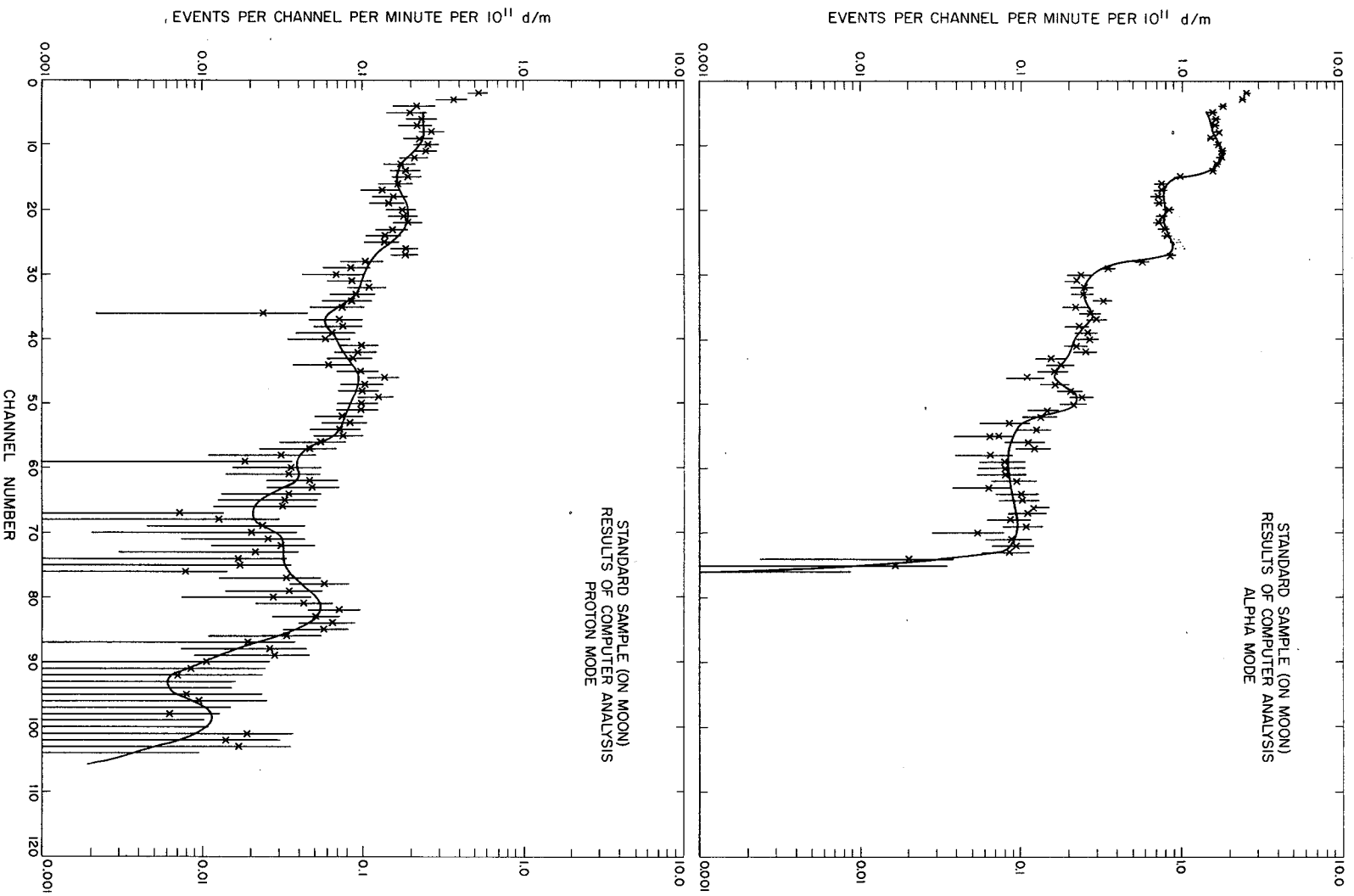
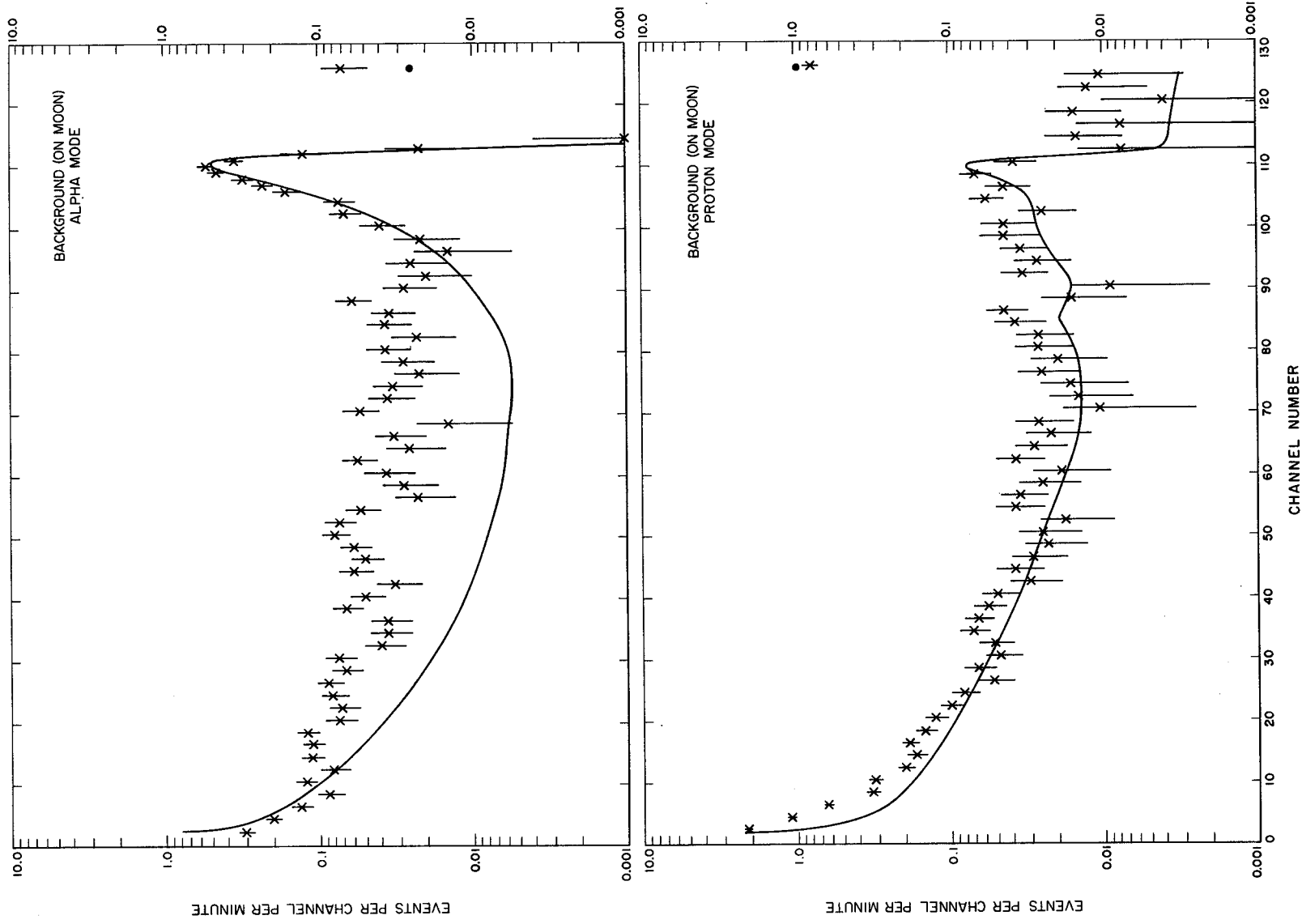


Fig. VII-11. Computer analysis of standard sample on the moon. Comparison between the calculated spectra (smooth curves), using an eight-element library, and the data obtained during 60 min on the moon (after subtraction of the background rates observed on the moon). The computer comparison has been made over channels 8-85 for the alpha mode, and over channels 8-110 in the proton mode.





## 2. Lunar Background Measurements

The second stage of the Alpha-Scattering Experiment Mission Plan is designed to measure the backgrounds in the lunar environment. In this stage of the *Surveyor V* mission, the sensor head was suspended approximately 60 cm above the lunar surface. The data obtained from 140 min of operation in this phase are shown in Fig. VII-12. Shown, also are the pre-mission predictions of the expected rates due to instrument background, and to solar and cosmic radiation.

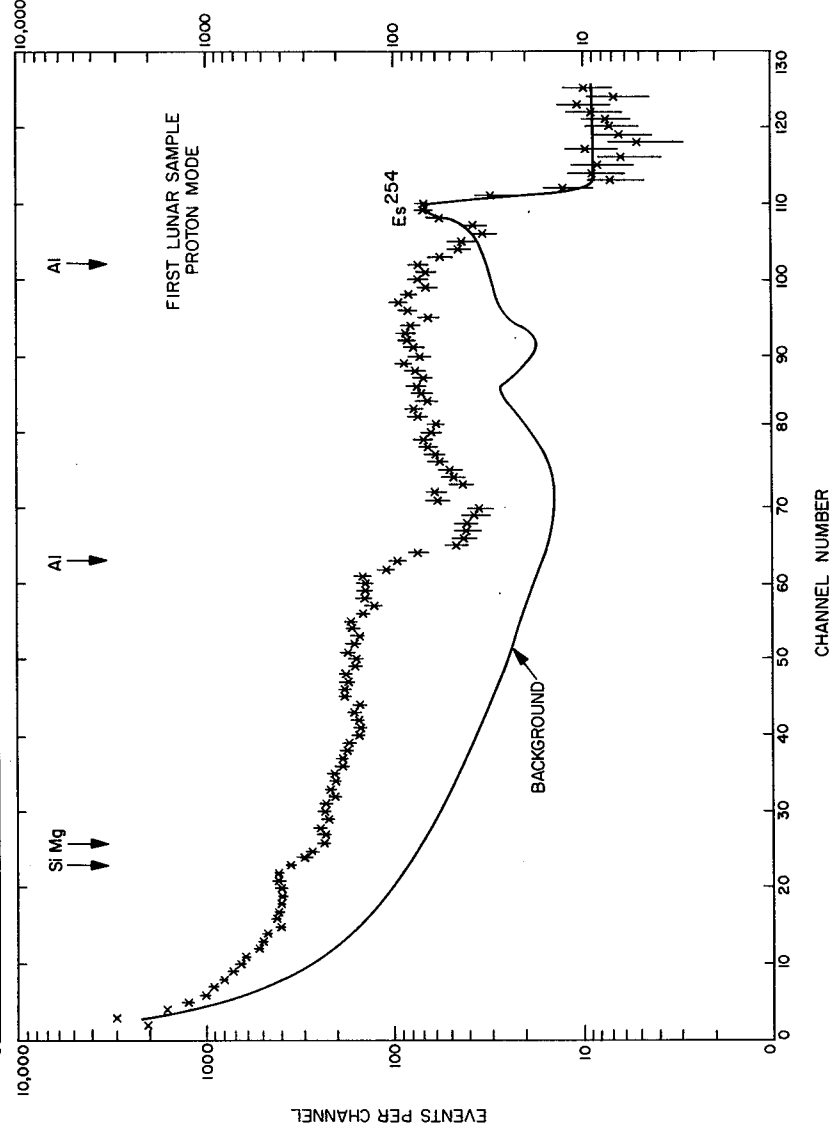
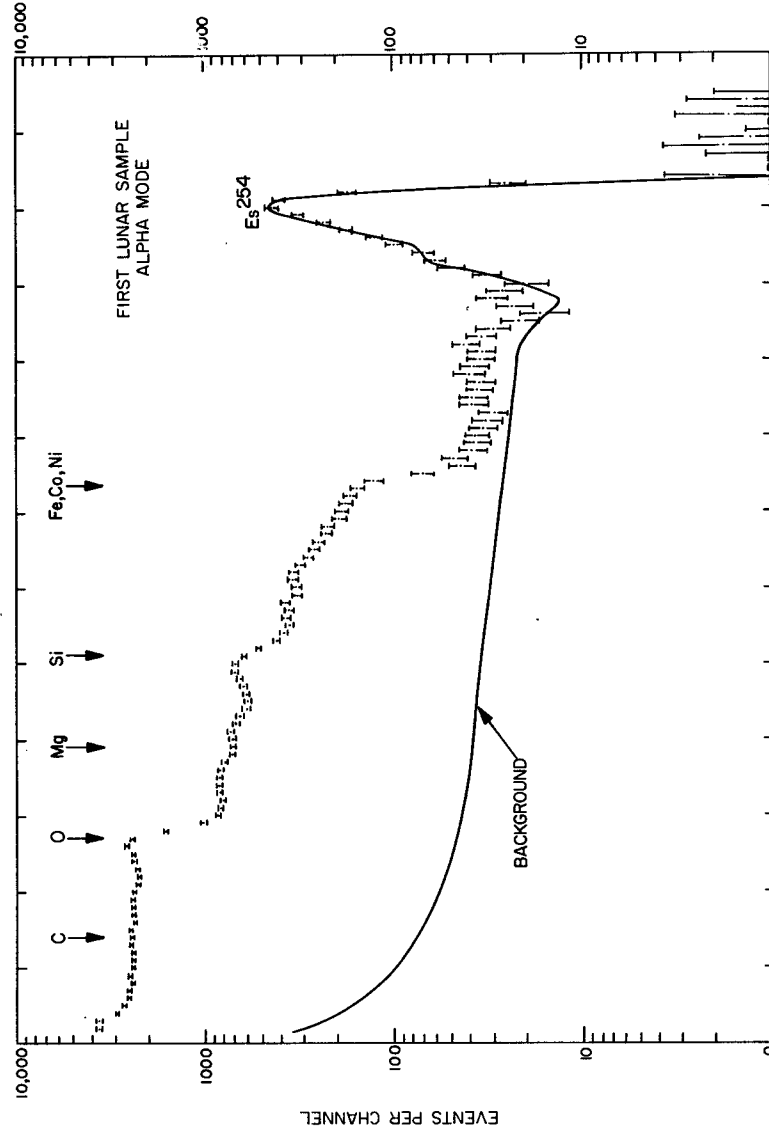
In spite of the difficulty in calculating the contributions due to solar and cosmic radiation in the complicated geometry of the instrument and detectors, the predictions for the proton mode agree quite well in spectral shape, and are only about 20% lower than the rates observed. The observed rates in the alpha mode, however, are much higher than the predicted ones, particularly in the middle-energy region. Although the reason for this is not understood with certainty, this background was still a small

fraction of the response of the instrument from a lunar sample (see below) over most of the spectrum.

The solar and cosmic radiation were the prime contributors to the background in the proton mode. Because this background was a significant fraction of the signal from the lunar sample in many parts of the proton spectrum, there was concern that variations in this contribution could affect the lunar sample data. For this reason, a check on particle radiation in space was provided by reports every 4 hr from the *Imp IV* satellite.<sup>2</sup> The alpha-scattering instrument itself had built-in monitors through the guard rate voltages and the events, primarily in the proton mode, in spectral regions above 6.5 MeV. These data indicated that the space particle rate was the same (to within 10%) during the first 900 min of lunar sample data as during background measurements. Information from the other indicators was consistent with this result.

<sup>2</sup>These data were made available on a near-real-time basis by Dr. John Simpson of the University of Chicago and the Small Satellite Tracking Center at Goddard Space Flight Center.

Fig. VII-12. Background measurements on the moon. Data taken by the alpha-scattering instrument in the alpha and proton modes in 140 min of measurement during the background phase on the moon. The experimental points, with statistical errors, are usually the averages of two channels (except near the  $\text{Es}^{254}$  peak and at the overflow channel 126) in order to improve their statistical significance. The experimental points have been corrected approximately to standard instrument response. The smooth curve, in each case, is the pre-mission prediction of the background rates based on prelaunch instrument backgrounds and calculated contribution of the solar and cosmic-ray contribution on the moon.



### 3. Lunar Sample Measurements

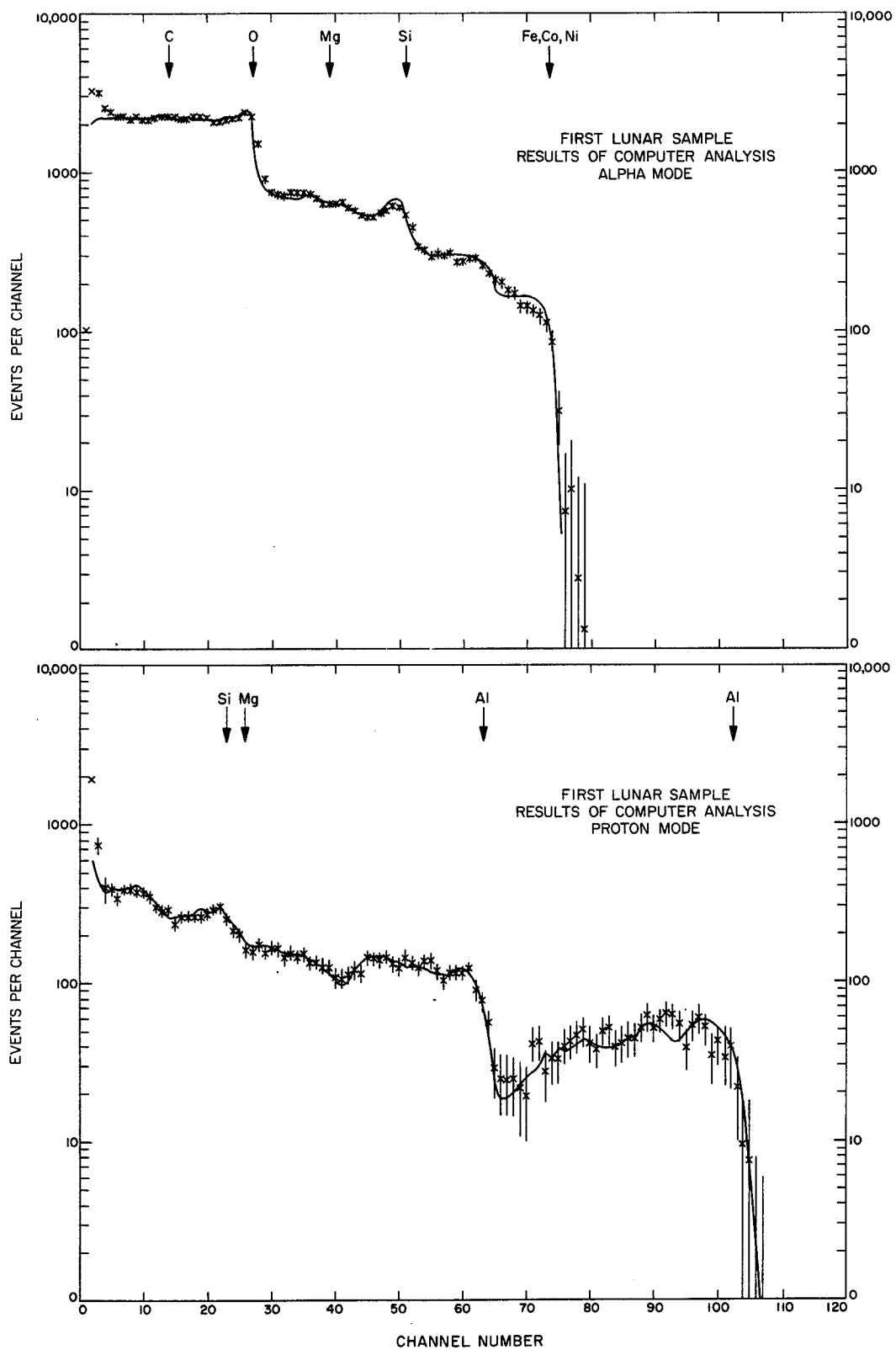
Data were obtained by the alpha-scattering instrument on two samples of the lunar surface. So far, only the data transmitted by teletype from the overseas receiving stations are available for analysis. Of these data, only those taken on the first lunar sample (before the vernier firing) have been examined. These have been subjected to only superficial certification of quality, and then processed by techniques designed primarily for monitoring instrument behavior during actual mission operations. Thus, only approximate corrections have been made to the data for the differences in temperature at which they were obtained. Similarly, the computer analysis has made use of only a small library of elemental spectra. Therefore, the present results relate to a limited number of elements and must be assigned larger errors than will be given at a later stage of analysis. Results seem to be firm and significant enough to warrant publication at this time.

The observed scattered alpha spectrum and the spectrum of protons from  $(\alpha, p)$  reactions from 900 min of measurement on the first lunar sample are presented in Fig. VII-13. The ordinate, for each spectrum, is the num-

ber of events per channel of the 128-channel analyzer, plotted on a logarithmic scale as a function of the channel number (energy). The statistical errors are indicated, together with a smoothed version of the background measured while the instrument was suspended over the lunar surface. It is seen that, for most of the alpha spectrum, the signal from the alpha particles scattered from the lunar surface is an order of magnitude higher than the background; the situation is less desirable, although adequate, in the proton mode. The peaks at around channel 110 in the two spectra are due to the 6.42-MeV alpha particles of  $\text{Es}^{254}$  placed near the detectors as energy markers.

Qualitative inspection of the alpha spectrum of Fig. VII-13 shows distinct breakpoints at energies (indicated by arrows) corresponding to maximum energy scattering from nuclei of mass 16 (oxygen), mass 28 (silicon), and approximately mass 58 (iron, cobalt, and nickel). Moreover, the low response (above background) beyond channel 73 indicates a relatively low abundance of elements of mass number heavier than 65. Similarly, the high-energy proton spectrum (above channel 60) of Fig. VII-13 is characteristic of protons from aluminum.

Fig. VII-13. First lunar sample. Data taken by the alpha-scattering instrument in the alpha and proton modes during 900 min on the lunar surface. The experimental points (crosses) are indicated with statistical ( $1\sigma$ ) errors. The data have been corrected approximately to standard instrument response. The solid curve in each case is a smoothed version of the background observed in the previous stage of lunar operations. The peaks at approximately channel 110 in both modes are due to  $\text{Es}^{254}$  placed near the detectors before launch. The positions of prominent features in some of the elemental spectra are indicated by arrows with chemical symbols.



By the methods given in Refs. VII-2 and VII-4, the observed alpha and proton spectra have been analyzed, thus far, by a computer into the spectra of only eight elements: C, O, Na, Mg, Al, Si, "Ca," and "Fe." The "Ca" stands for elements with  $28 < A \leq \sim 45$ , and "Fe" represents elements with  $\sim 45 \leq A < 65$ . Figure VII-14 shows the agreement between the observed data (after subtraction of the background and possible heavy element contribution) and the computer calculated results. It is seen that analysis into only eight elements represents the data with very few systematic deviations. One of the regions of poor fit is between alpha channels 63 and 74. For this reason, at present, there will be no attempt to identify the elements heavier than silicon; the total amount of such elements will be reported as "H.E." Figure VII-15 shows, in some detail, the contributions of the individual elements in the library to the net data observed on the moon.

Table VII-7 lists the results obtained in this way on the chemical composition of the lunar surface. The table lists the atomic percent of all atoms (heavier than lithium) represented by the element in question. The errors quoted are the present estimates of the reliability of the results; the statistical errors are much smaller.

Although the present results are preliminary, they have already been subjected to the following tests to ensure their validity:

- (1) Computer analysis of the three 300-min accumulations of data comprising the total of 900 min gives results consistent with those in Table VII-7 and shows no significant trends.

**Table VII-7. Chemical composition of lunar surface at Surveyor V site**

Element	Atomic percent <sup>a</sup>
Carbon	<3
Oxygen	$58.0 \pm 5$
Sodium	<2
Magnesium	$3.0 \pm 3$
Aluminum	$6.5 \pm 2$
Silicon	$18.5 \pm 3$
$28 < A < 65^b$	$13.0 \pm 3$
(Fe, Co, Ni)	> 3
$65 < A$	<0.5

<sup>a</sup>Excluding hydrogen, lithium, and helium. These numbers have been normalized to approximately 100%.

<sup>b</sup>This group includes, for example, S, K, Ca, Fe.

Fig. VII-14. Computer analysis of first lunar sample. Comparison between the calculated spectra (smooth curves) using an eight-element library, and the data (crosses) obtained from 900 min of measurement of the first lunar sample. The background measured in the previous stage of operations (increased in the alpha mode by 12 events per channel per 1000 min to match the data above channel 75) has been subtracted from the experimental results before presentation on the graph. The computer fit has been made over channels 8-85 for the alpha mode, and over channels 8-110 for the proton mode.

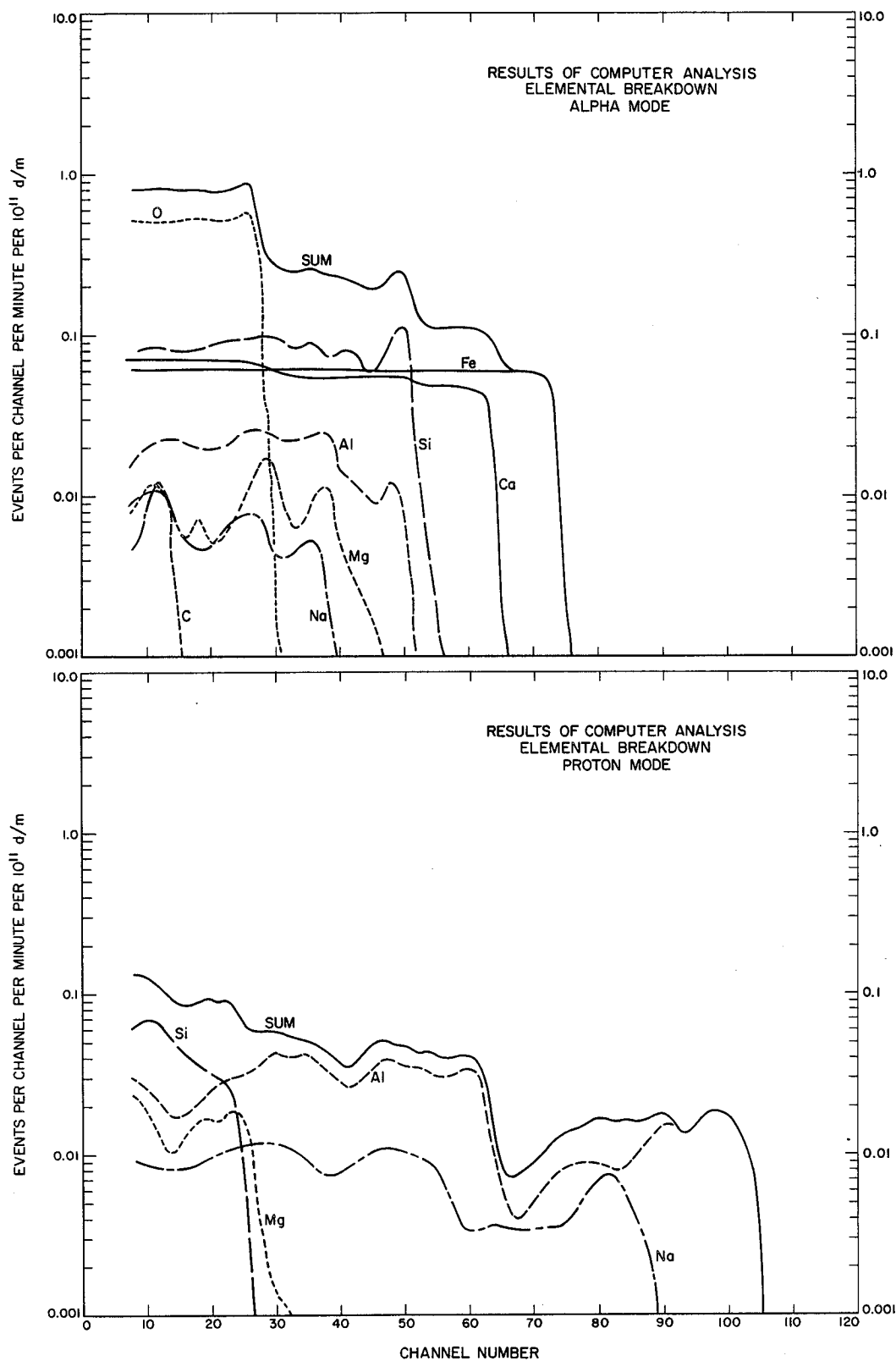
- (2) The answers are insensitive to the use of some reasonable background assumptions other than the smoothed versions shown in Fig. VII-13. Among the backgrounds tried were the actual background data rather than the smoothed version, and no background.
- (3) Although only a limited library has been used in getting the results of Table VII-7, it has been established that the analysis is insignificantly changed by inclusion in the library of spectra of nitrogen, fluorine, and potassium.
- (4) Although the data in the present state do not justify such refinements, a computer was programmed to search for changes in instrument parameters (gain or zero offset), in both alpha and proton modes, that would improve the calculated fit to the data. The result was a significant increase in goodness-of-fit as measured by a calculation of chi-squared, and as observed by a better match to such features in the spectra as the oxygen breakpoint. However, the analytical results were essentially unchanged.

These tests are not exhaustive, but provide confidence that the results presented in Table VII-7, within the errors quoted, will be unchanged by more refined treatments of the data.

From the analysis presented in the table, it is seen that the most abundant element on the lunar surface, as on the earth, is oxygen. More than half of all the atoms are of this element. Second in importance, again as on the earth's crust, is silicon. Next in abundance is aluminum (see Appendix A), and the quantity of magnesium is somewhat lower. At this stage, only upper limits can be placed on the amounts of carbon and sodium present. The data indicate surprisingly large amounts of elements heavier than silicon,  $13 \pm 3\%$ . Although a detailed breakdown of these elements cannot be made at present, it is possible to place a lower limit of 3% on the combined abundance of Fe, Co, and Ni, and an upper limit of 0.5% on that of still heavier elements. (Fig. VII-13 indicates a slight excess of events in channels 75 through 90 of the alpha mode above those expected on the basis of the background stage measurements. However, there is some evidence that the instrument background was somewhat higher during the lunar sample measurement. An upper limit is, therefore, quoted at present for the abundance of elements heavier than nickel.)

Although use of the mean values of Table VII-7 would indicate a slight deficiency of oxygen needed to oxidize all the metals, the estimated error ranges at present would include values not requiring any free iron. The overall analysis indicates that the lunar surface at the *Surveyor V* landing site is a silicate rock similar in composition to materials available on earth.

Fig. VII-15. Contribution of separate elements to least-squares computer analysis of lunar sample data. The library data for the separate elements are shown in the relative amounts needed to explain the observed lunar data. These relative amounts, when treated by the methods of Refs. VII-2 and VII-4 lead to the chemical analysis of Table VII-7. ➔



## E. Discussion

The preliminary results presented in Table VII-7 give the elemental analysis of the lunar surface material in one place on the moon. The general region is one of the relatively smooth (on a large scale) maria that represents a significant fraction of the visible lunar surface. The specific landing spot of *Surveyor V* is just inside a small crater of Mare Tranquillitatis. This crater has been interpreted as being of the "drainage" variety (see Section III). Analysis of the pictures, moreover, indicates that the alpha-scattering instrument was lowered onto a surface covered, to a significant extent, by material ejected by the footpads during the landing. It can, therefore, be concluded that the sample of the moon analyzed in this experiment is characteristic of the top layer of lunar material at a mare site, but not necessarily that of the undisturbed surface. Nevertheless, it should be remembered that this is a preliminary result, obtained on less than 100 cm<sup>2</sup> of material, by analysis of only the top few microns of the sample, in one place on the moon. The surface of the moon, even at a mare site, could well be chemically heterogeneous on the scale examined.

In spite of these obvious limitations, it is of interest to compare the results of this analysis with the chemical composition of other solar system bodies for which data is available. A comparison with the average chemical composition of the earth's crust and with some solar data is presented in Table VII-8.

Table VII-8 shows that the results obtained by *Surveyor V* are more comparable to the chemical composition of the continental crust of the earth than to that in the outer region of the sun. Both the moon and the earth have much less magnesium and more aluminum relative to silicon than does the sun. Although the comparison is closer with the earth's crust, there are significant differences: there is less sodium and more atoms of elements heavier than silicon on the moon than on the earth's crust. There is also an indication that the silicate content is lower on the moon than on the continents of the earth.

The conclusion indicated by this comparison is that, if the earth and moon were originally formed from solar-type material, the major geochemical changes to the material at the *Surveyor V* landing site must have been similar

Table VII-8. Surface chemical composition of solar system bodies

Element	Atomic percent		
	Solar atmosphere <sup>a</sup>	Earth (continental crust) <sup>b</sup>	Lunar mare ( <i>Surveyor V</i> site)
O	—	62.6	58.0 ± 5
Na	1.2	2.6	<2
Mg	16.1	1.9	3.0 ± 3
Al	1.1	6.5	6.5 ± 2
Si	(20.0)	21.2	18.5 ± 3
A > 28	18.7	5.2	13.0 ± 3

<sup>a</sup>The solar values are from H. C. Urey. The abundances of only the heavy non-volatile elements are given, normalized to a value of 20.0% for silicon.  
<sup>b</sup>The values for the crust of the earth are average values for the continents, from Howard J. Sanders, *Chem. and Eng. News*, Oct. 2, 1967.

to those that occurred to the materials comprising the terrestrial continents.

Although an elemental analysis (even one more precise than the present one) can be only a rough indicator of detailed rock type, it is of interest to compare the present results with the chemical composition of some materials that have been considered as constituents of the lunar surface. This is done in Fig. VII-16, where a comparison of the present results is made with the analysis of average (Ref. VII-6) dunites, basalts, granites, tektites, chondritic meteorites, and basaltic achondrites. It is seen from this figure that the lunar surface, at the landing site of *Surveyor V*, cannot consist entirely of material similar to chondritic meteorites or to ultrabasic rocks such as dunite. Tektitic or granitic materials are more consistent with the present estimates of errors, although they appear to be ruled out by the gamma-ray measurements of Vinogradov, et al. (Ref. VII-7). Of the comparisons made in Fig. VII-16, the closest agreement appears to be with the chemical composition of basaltic achondrites and with that of terrestrial basalts.

Figure VII-16 clearly represents only a few of all possible comparisons. Such comparisons will be even more meaningful when the data obtained on *Surveyor V* have been completely processed. However, even in the present state, the results provide experimental information on the chemical environment on the surface of the moon, the possible raw materials there, and clues as to the history of this long-time partner of the earth.



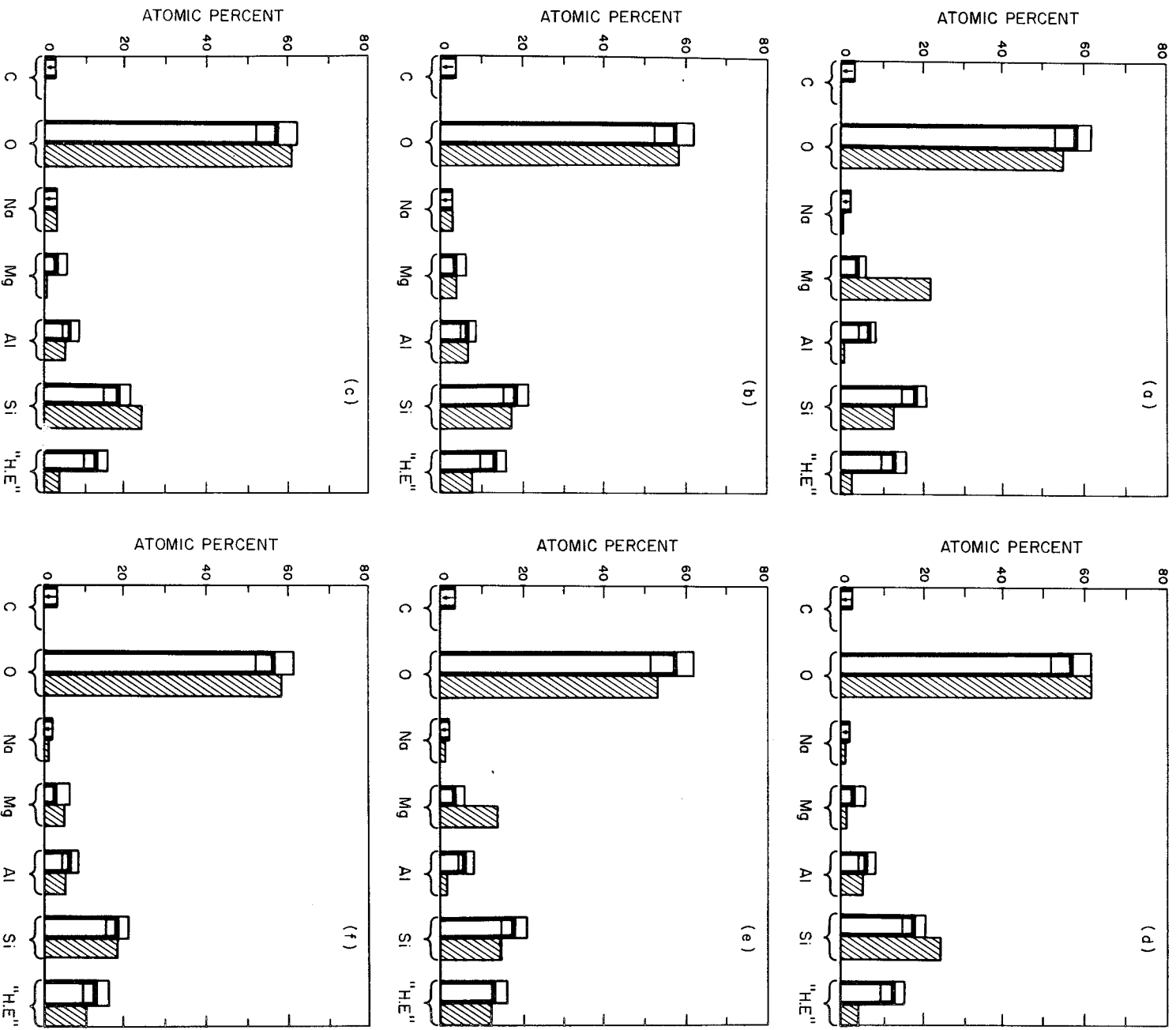


Fig. VII-16. Comparison of the observed chemical composition of the lunar sample (open bars) with the average composition (Ref. VII-6) of selected materials (cross-hatched bars). A, dunite; B, basalts; C, granites; D, tektite (Indo-Malayan body); E, low iron chondritic meteorite; F, basaltic achondritic meteorites. The "H.E." means elements heavier than silicon.

## References

- VII-1. Turkevich, A., "Chemical Analysis of Surfaces by Use of Large-Angle Scattering of Heavy Charged Particles," *Science*, Vol. 134, pp. 672-674, 1961.
- VII-2. Patterson, J. H., Turkevich, A. L., and Franzgrote, E., "Chemical Analysis of Surfaces Using Alpha Particles," *J. Geophys. Res.*, Vol. 70, No. 6, pp. 1311-1327, 1965.
- VII-3. Turkevich, A., Knolle, K., Emmert, R. A., Anderson, W. A., Patterson, J. H., and Franzgrote, E., "Instrument for Lunar Surface Chemical Analysis," *Rev. Sci. Inst.*, Vol. 37, No. 12, pp. 1681-1686, 1966.
- VII-4. Turkevich, A. L., Knolle, K., Franzgrote, E., and Patterson, J. H., "Chemical Analysis Experiment for the *Surveyor* Lunar Mission," *J. Geophys. Res.*, Vol. 72, No. 2, pp. 831-839, 1967.
- VII-5. Grotch, S. L., "Alpha Scattering Science Data Processing," presented at the ISA Aerospace Instrumentation Symposium, San Diego, 1967 (to be published).
- VII-6. Palm, A., and Strom, R. G., *Space Sciences Laboratory Research Report*, Series 3, Issue 5, University of California, Berkeley, California, 1962.
- VII-7. Vinogradov, A. P., Surkov, Yu. A., Chernov, G. M., Kirnozov, F. F., Nazarkina, G. B., *Geokhimiya*, No. 8, p. 891, Izd-vo "NAUKA," 1966. Also, a paper by the same authors presented at the Tenth Meeting of COSPAR, 1967.

## Acknowledgment

This experiment, throughout its history, has had the support of numerous organizations and people:

At the University of Chicago, many members of the Enrico Fermi Institute for Nuclear Studies, especially Mr. Ed Blume, Mr. Tom Economou, Mr. Ken Sowinski and Mr. Bernd Wendring have participated in the design, construction, and testing of the instrument.

Also at the University of Chicago, many members of the Laboratory of Astrophysics and Space Research of the Enrico Fermi Institute for Nuclear Studies, have supported the experiment. It is at this laboratory that most of the alpha-scattering instrument was designed, constructed, and tested by a team led by Mr. Wayne Anderson and including Mr. Gene Drag, Mr. Myron Weber, Mr. John Stepney, Mr. Roger Gabriel, and Mr. George Shimatori. General laboratory support and coordination have been provided by Mr. James Lamport, Mr. Leonard Ericson, and Mr. William Six. The semiconductor detectors, so vital to the technique, were developed, built, and tested at this laboratory by Dr. Anthony Tuzzolino, Mr. Julius Kristoff, and Mr. George Ho. Mechanical components were, in large measure, fabricated in the Central Development Shop of the Enrico Fermi Institute.

Members of the Argonne National Laboratory, including Mr. Harry E. Griffin, Mr. Dale Henderson, Miss Carol A. Bloomquist, Dr. E. Philip Horwitz, and Mr. Howard Harvey developed, prepared, and tested the alpha-radioactive materials used in the experiment. Mr. Dale Suddeth provided important electronic support.

At the Illinois Institute, Dr. G. Walker and Mr. Lou Wolfe contributed to the thermal design of the instrument.

The Hughes Aircraft Company, and particularly Mr. Robert Dankanyin, Mr. John N. Buterbaugh, Mr. Heaton Barker, Mr. Eugene Henderson, Mr. Paul Garrotto, and Mr. Elmer Londre were mainly responsible for the design and construction of the deployment mechanism as well as integration and testing of the instrument on the spacecraft.

Staff members at the Jet Propulsion Laboratory have also contributed throughout the history of the experiment. It received important early support from Dr. Albert Metzger. Mr. George O. Ladner, Jr., and Mr. Richard E. Parker assisted in the operation and scientific evaluation of prototype instruments. The instrument development and construction was monitored by Dr. Dennis LeCroisette, Mr. Robert Holman, Mr. C. Dan Porter, Mr. Henry C. Giunta, Mr. Charles C. Fondacaro, and Mr. C. Ed Chandler. The latter, in addition, together with Mr. William Seeger, organized the critical final calibration at Cape Kennedy. Dr. Stanley L. Grotch supervised the real-time calculational monitoring of the instrument during the mission. Important support was provided by many other JPL staff members in systems integration, environmental and system testing, control during mission operations, and other areas.

At the Headquarters of the National Aeronautics and Space Agency, Mr. Benjamin Milwitzky and Mr. Steve Dwornik have given continual support to the program.

Finally, the entire experiment would have been impossible without the dedicated efforts of countless members of the National Aeronautics and Space Agency, the Jet Propulsion Laboratory and of the Hughes Aircraft Company who designed, built, and tested *Surveyor V* and who so spectacularly placed it on the surface of the moon.



## VIII. Lunar Surface Electromagnetic Properties: Magnet Experiment

J. Negus de Wys

The morphology of the lunar surface has been a subject of considerable speculation throughout history, but only in recent years has it reached a stage of controversial climax in scientific debates. Before the flight of *Surveyor V*, there were two extreme views apparent in lunar literature: (1) only exogeneous sources could account for lunar surface material, its pulverization and lunar cratering; and (2) only endogenous sources could explain them.

Through constant pulverization and accretion by meteoritic bombardment, an addition of nickel-iron (Ni-Fe) alloys could be expected to occur in the lunar surface material. If, however, volcanism and outgassing are the more active agents, then the iron content would be more restricted to that of a given rock type.

### A. Purpose of Magnet Assembly

The magnet assembly was installed to determine the presence, and possibly the amount, of material with high magnetic permeability that might be present at the *Surveyor V* landing site. Materials that would be attracted to a 500-gauss magnet include free iron, magnetite, and Ni-Fe from meteorites. The landing site in Mare Tranquillitatis is representative of large surface expanses on

the side of the moon nearest the earth. Mare areas as a surface unit are not only widespread, but also appear, from *Lunar Orbiter* photographs and from landed spacecraft, to be homogeneous. Information obtained from mare landings probably can be extrapolated to large areas of the moon with a fair degree of confidence.

### B. Magnet Assembly Description

The magnet assembly, attached to footpad 2, consisted of a magnetic bar of Alnico V and a nonmagnetic bar of Inconel X-750; the dimensions of each bar were  $5 \times 1.27 \times 0.32$  cm (see Fig. VIII-1). The gauss readings along the pole faces range from 440 to 680 (Fig. VIII-2). The magnetic axis is horizontal with the magnetic poles extending down the left and right sides of the magnet, the magnetic-field strength down through the center dropping to zero gauss. Calibration tests of the magnetic-field strength show the dropoff (see Figs. VIII-3 and VIII-4); at a distance of 3.8 cm from the *Surveyor V* magnet, the strength was  $<0.38$  gauss. Powdered iron was collected from a distance of 1.93 cm by a 500-gauss magnet in the laboratory studies (see Fig. VIII-5). A magnet with this strength on earth supports about 20 g of the magnetic materials tested.

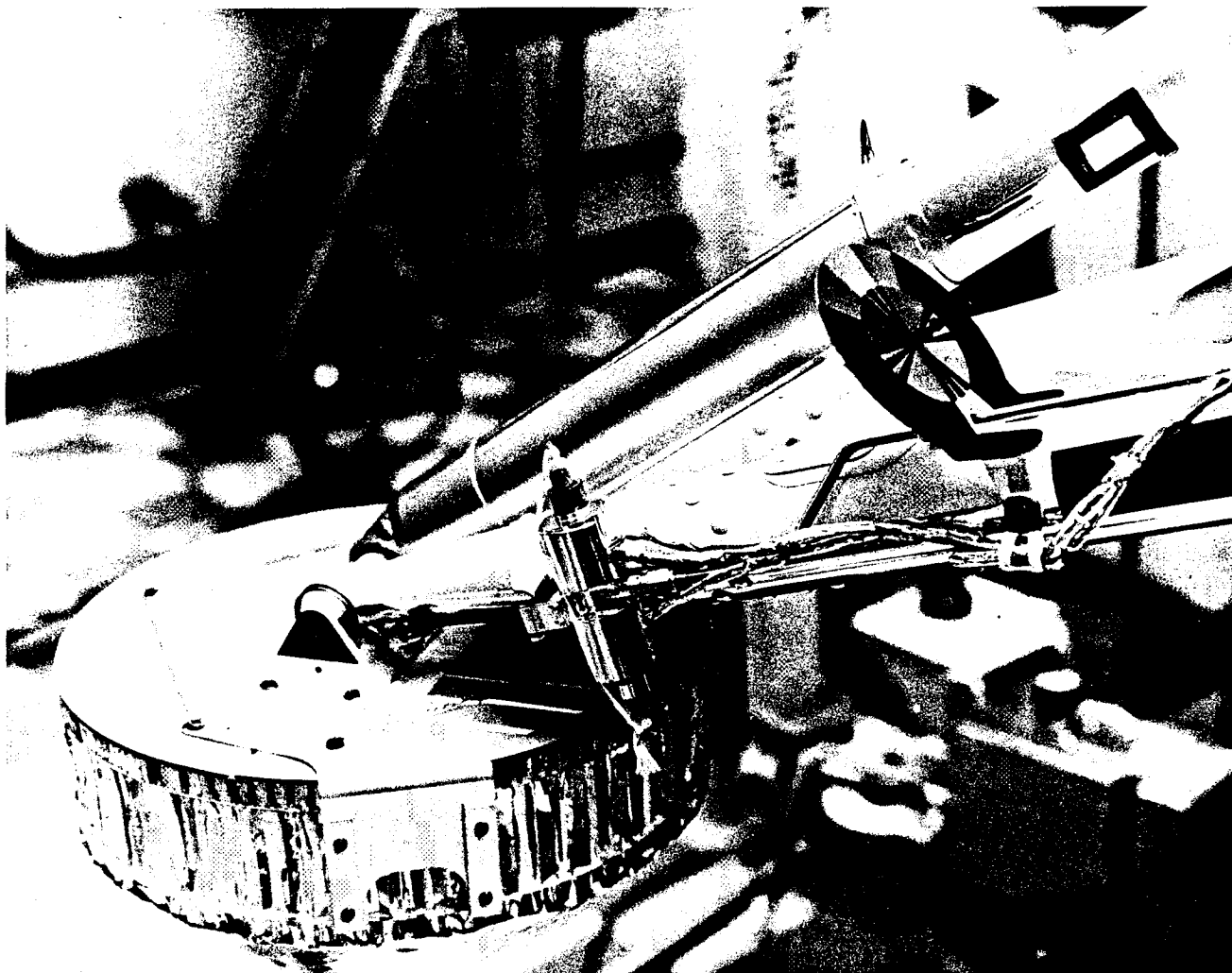


Fig. VIII-1. Magnet assembly on footpad 2 of Surveyor V prior to launch at Cape Kennedy. The pattern on bracket top is gray and white; the bracket side, magnet and nonmagnetic bar are light blue. The Alnico V magnet is on the left.

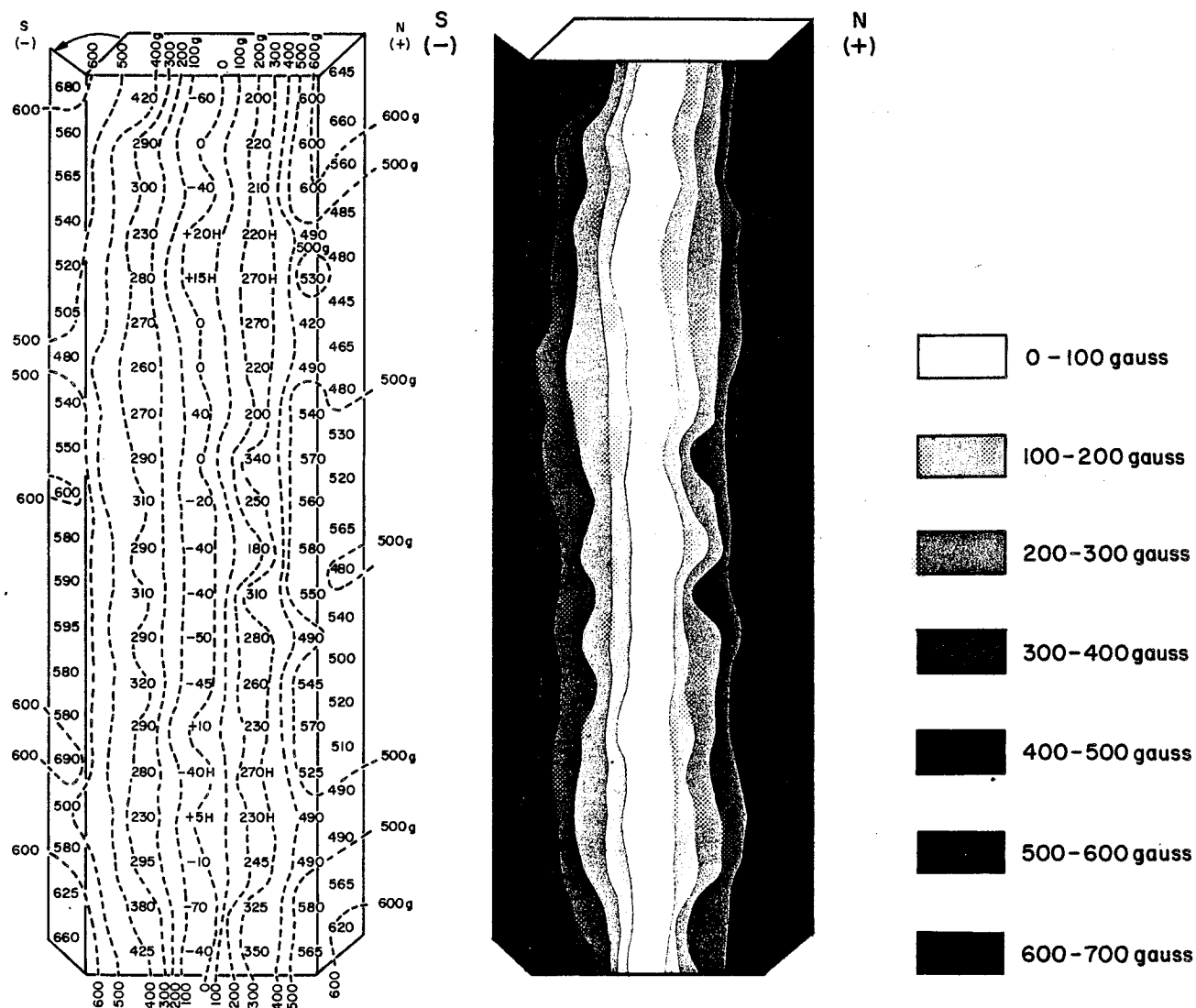


Fig. VIII-2. Detailed magnetic-strength plot of the face and magnetic poles of the magnet on Surveyor V. Readings were made at Cape Kennedy, just before the magnet was attached and bonded to the bracket. Readings were re-checked after attachment. For comparison to lunar results, note tonal plot.

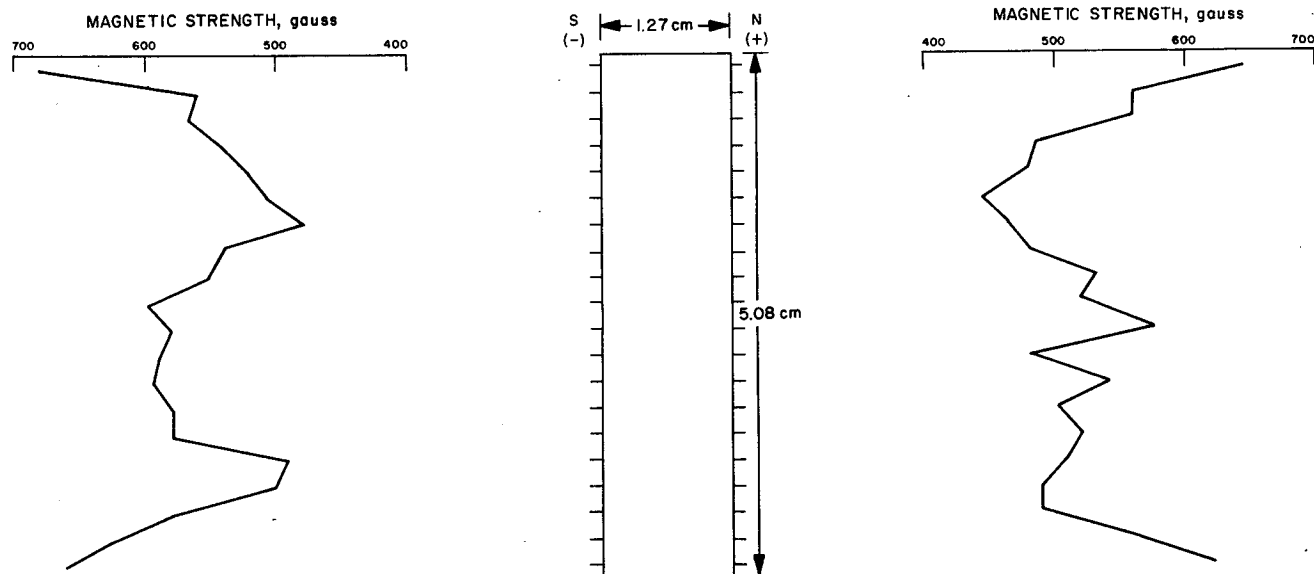


Fig. VIII-3. Plot of pole-strength dropoff along the pole faces of the magnet on Surveyor V.

Alnico V was selected because its characteristics in thermal and magnetic regimes made it suitable for lunar surface tests (see Table VIII-1 and Fig. VIII-6), and because its magnetic remanence is greater at higher temperatures than for other alloys. It is, however, a brittle material that frequently contains voids, and must therefore be handled with some care. To protect the spacecraft and

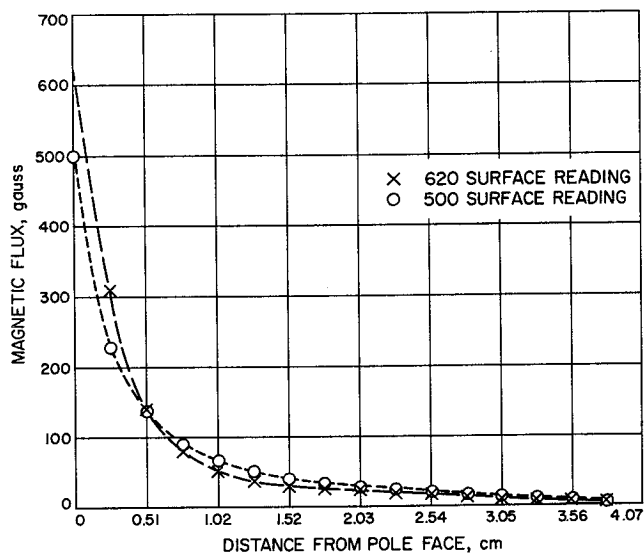


Fig. VIII-4. Plot of magnetic-strength dropoff from areas of 620 and 500 gauss at the surface. Measurements were made every 0.254 cm.

Table VIII-1. Properties and chemical composition of Alnico V

<b>Chemical Elements</b>	
Iron, %	~50.8
Titanium, %	24
Nickel, %	14
Aluminum, %	8
Copper, %	3.2
Cobalt, %	—
<b>Mechanical Properties</b>	
Tensile strength, dynes cm <sup>-2</sup>	~3.6 × 10 <sup>8</sup>
Transverse modulus of rupture, dynes cm <sup>-2</sup>	~7.2 × 10 <sup>8</sup>
Rockwell hardness	C50
<b>Electrical Properties</b>	
Resistivity temperature (25°C), microhm <sup>-1</sup> cm <sup>-2</sup>	47
<b>Magnetic Properties</b>	
Peak H, oersted	3,000
Peak induction, B, gauss	16,500
Residual induction, B <sub>r</sub> , gauss	12,600
Coercive force, H <sub>c</sub> , oersted	600
<b>Coefficient of linear expansion</b>	
20 to 120°C	11.5 × 10 <sup>-6</sup>
20 to 220°C	11.5 × 10 <sup>-6</sup>
20 to 300°C	11.6 × 10 <sup>-6</sup>
Curie point, (+10°C), °C	890
Specific heat (30 to 400°C), cal g <sup>-1</sup> /°C	0.11
<b>Additional Properties</b>	
Density, g cm <sup>-3</sup>	7.3



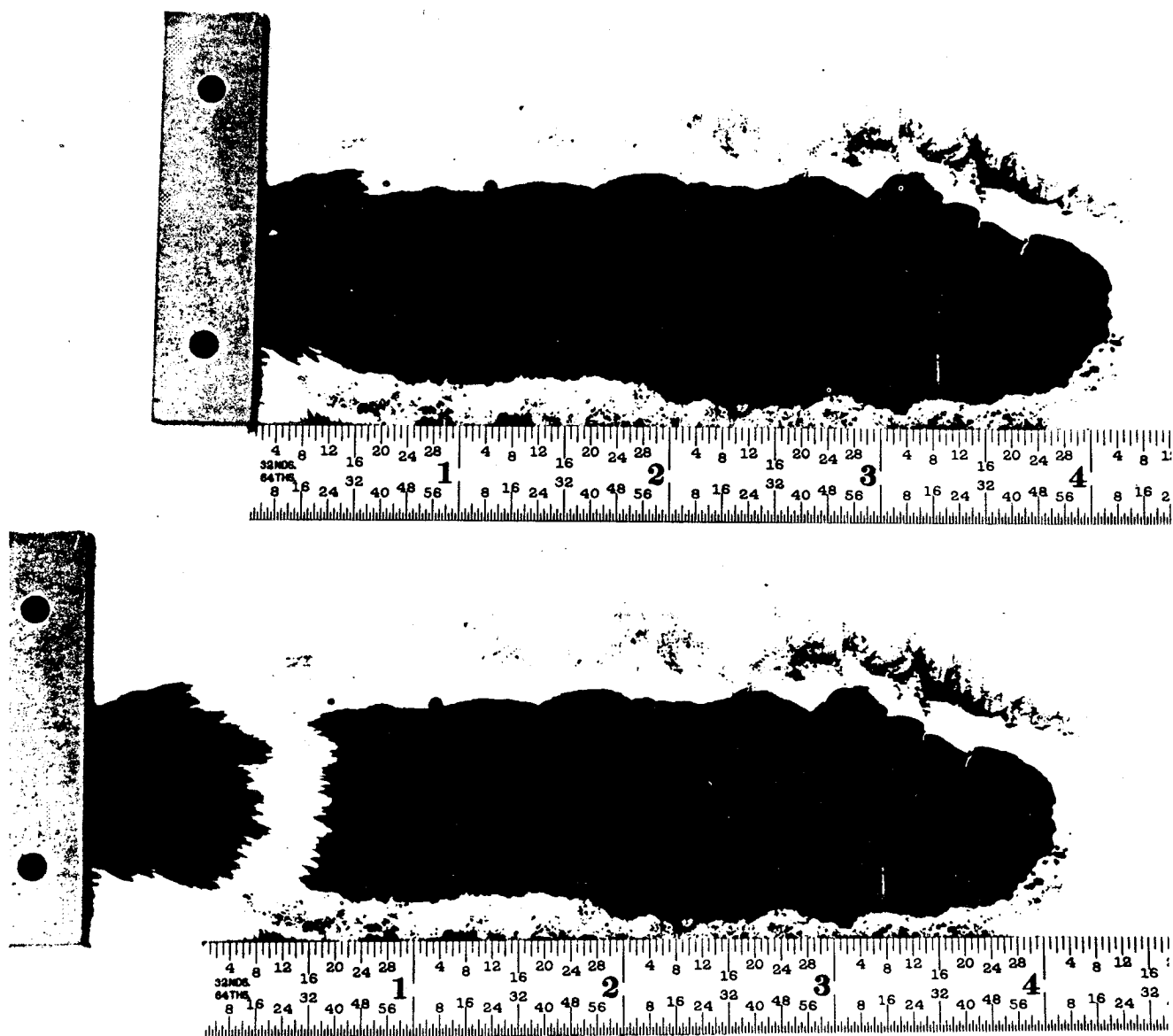
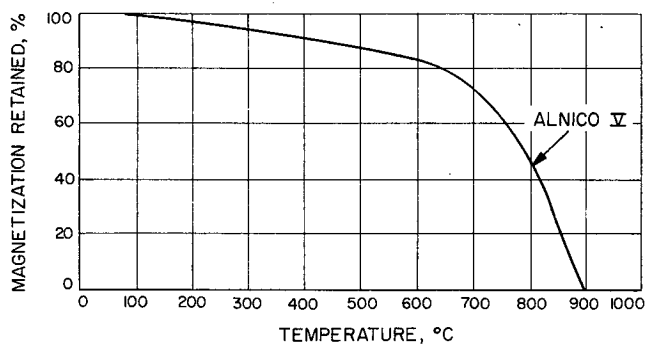
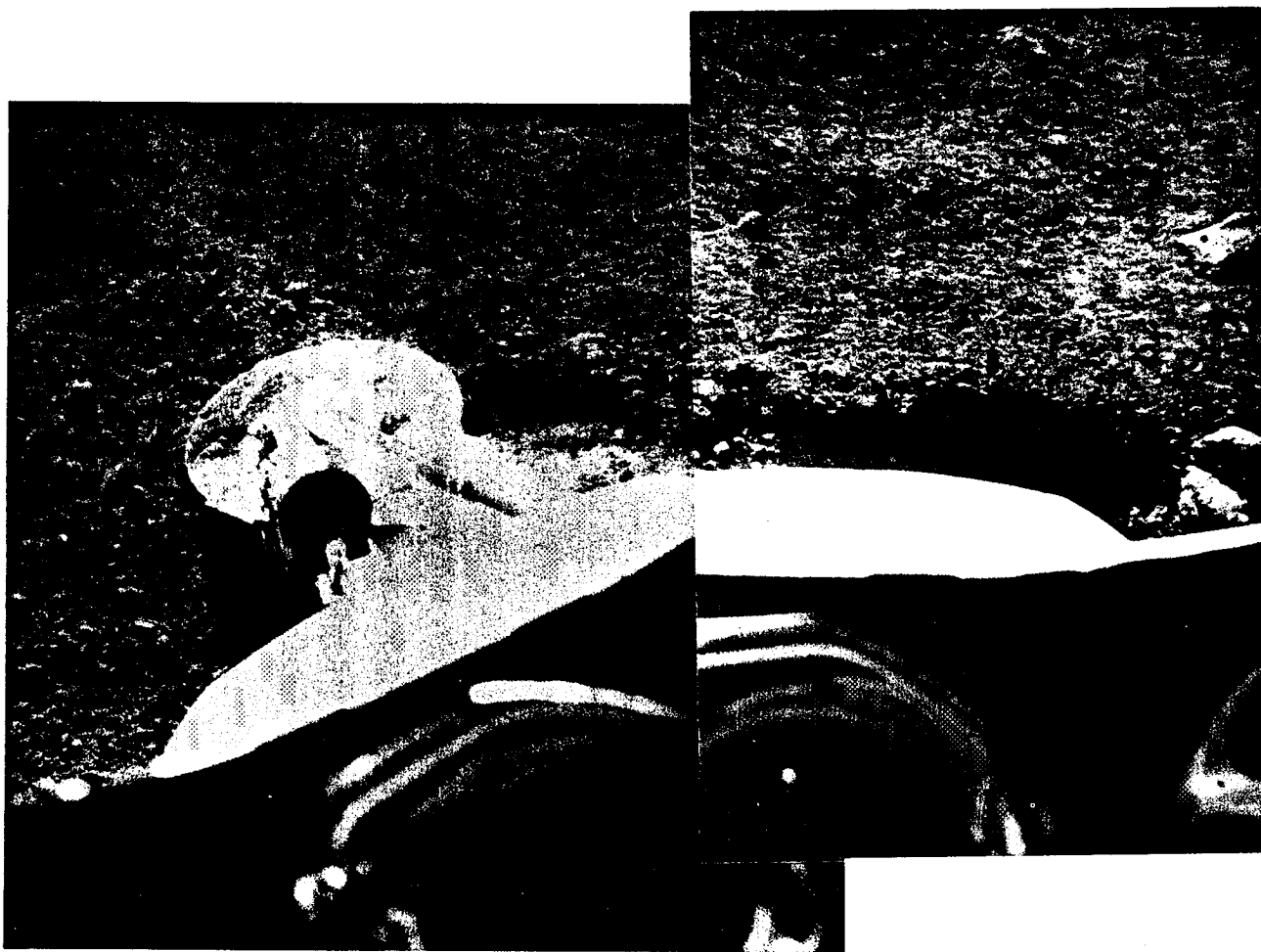


Fig. VIII-5. Distance from which magnet on Surveyor V will attract powdered iron on earth is shown by placing the magnet adjacent to powdered iron (above) and displacing the bar to the left (below). The magnet collected iron from a distance of 1.93 cm.



**Fig. VIII-6. Magnetic remanence vs temperature for Alnico V.** Internal structure and the metallurgical properties of the alloy used control the effect of high temperatures on magnetic materials. Alnico V has retraceable temperature characteristics over a wide range ( $-200$  to  $300^{\circ}\text{C}$ ). This is one of the properties that dictated its choice for the Surveyor V magnet.



**Fig. VIII-7. Landing mode of footpad 2.** The spacecraft landed on a  $19.5$ -deg, inner slope of a  $9 \times 12$ -m crater, causing footpad 2 to slide downhill a distance of about  $1$  m at a depth of  $3$  to  $10$  cm through the lunar surface material. Note material on top of the footpad; also note well-defined footpad imprint at the end of the slide and the scalloped effect in part of the trench. This is indicative of the slight bouncing of the footpad in sliding. Velocity during downhill trenching is estimated at  $1 \text{ m sec}^{-1}$  (Day 255, 00:18:35 and Day 254, 23:29:23).

experiment, both the magnetic bar and control bar were bonded with RTV-60 (bonding agent) to the bracket in addition to the screw attachment.

In no area over the surface of the control bar was the magnetic field reading  $> 0.1$  gauss; this reading was observed over the attachment screws only.

### C. Landing and Vernier Rocket Engine Firing

*Surveyor V* landed in a  $9 \times 12$ -m crater on a  $19.5^\circ$ -deg, inner north-facing slope. Footpads 2 and 3, on the downhill side, at a velocity of about  $1 \text{ m sec}^{-1}$ , performed a bouncing 1-m-long slide through the lunar surface material forming a trench before coming to a halt. The trench is 3 to 10 cm in depth (see Fig. VIII-7). From this landing mode and from the distribution of lunar material over the front of the footpad, it may be concluded that the magnet assembly contacted the lunar surface material. If the trench length is multiplied by the magnet length, then the approximate size of the lunar area to which the magnet was exposed is  $500 \text{ cm}^2$ .

Lunar material is seen in the honeycomb below the bracket, on the bracket, adhering to the lower right side of the control bar, and covering the magnetic bar. The fine coating on the control bar and bracket is probably due to vacuum cohesion. Because the magnet is on the western side of footpad 2 and the sun was low in the east, the first picture of the magnet assembly after landing (Fig. VIII-8) was in deep shadow. However, light patches of uncovered blue paint contrast brightly beside the dark lunar material, permitting the areas covered to be identified.

In landing, the magnet bracket may have been deformed, possibly cracked. In Fig. VIII-9, the light line across the bracket may be seen; the white stripe on the bracket departs from a straight line. (An approximately  $5^\circ$ -deg departure is measurable.) The magnet assembly may have hit a rock in landing, since the assembly extends from the side of the footpad. It may also be noted that the

side of the magnet assembly is no longer parallel to the honeycomb-structure pattern; before flight, the relationship was parallel.

The 0.55-sec firing of the vernier engines caused an estimated  $1 \text{ dyne cm}^{-2}$  dynamic pressure on the magnet assembly, sufficient to clean off the vacuum cohesion material on the bracket and control bar, blow material from the honeycomb structure, clean off the top outer edge of the bracket, and remove material from the zero-gauss area down the center of the magnet (see Figs. VIII-8 and VIII-10).

From laboratory jet exhaust studies in vacuum it was found that little, if any, material would be added to the magnet by the firing of the vernier engines.

Shadow progression studies conducted in the *Surveyor* Experiment Test Laboratory provided a key to the possible time of full lighting on the magnet assembly (Fig. VIII-11). Because of the combination of the crater horizon and slope angle, accurate predictions were difficult. The sun shone fully on the bracket for only 1.5 hr of the entire lunar day (approximately 14 terrestrial days). A sequence taken through the first lunar day and ending with the anticipated sunset lighting is seen in Fig. VIII-12. In sunset lighting, the coating of dark material adhering to the pole faces of the magnet and the particles forming bridges across the area of lower strength down the magnet center could be seen distinctly. The shape and size of the particles has not been determined; however, they appear to be smaller than camera resolution (1 mm). Most of the lunar material through which footpad 2 slid consists of particles less than 1 mm in diameter, similar to the material observed in *Surveyor I* and *III* pictures.

From simulation studies of the *Surveyor V* landing, it was concluded that the passage of the magnet through about a meter of lunar material would not cause a very different result from a single, solid impact in the same material.

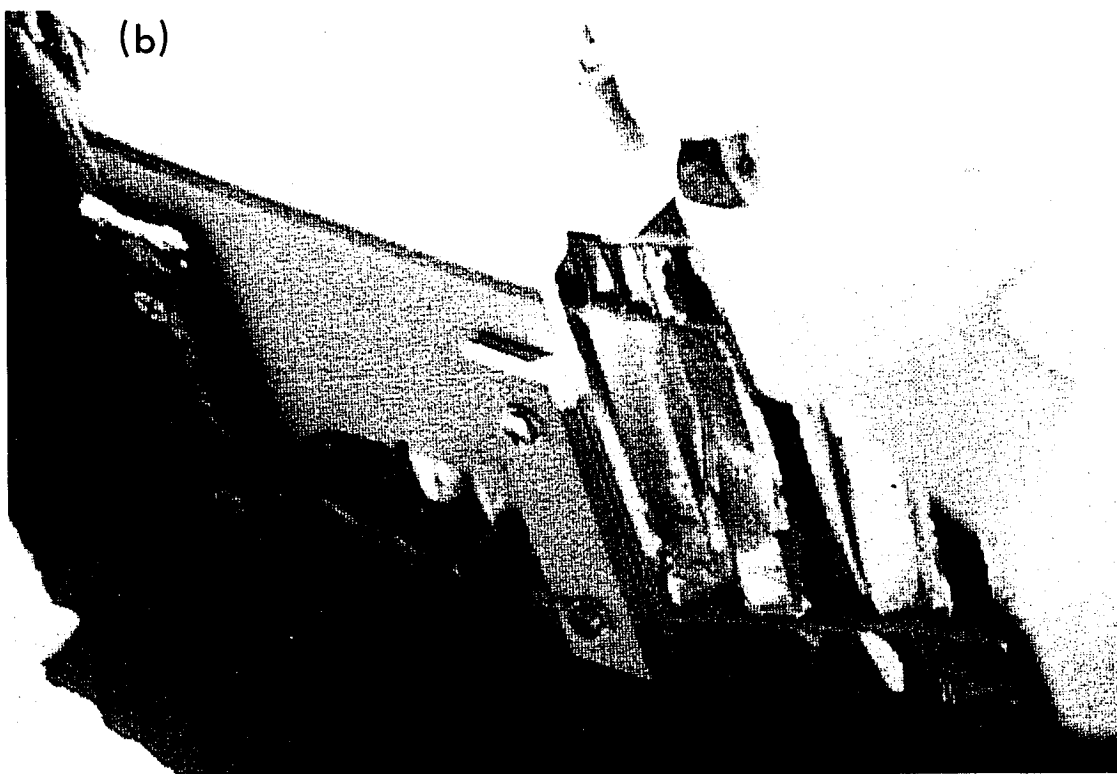


**Fig. VIII-8. Magnet assembly before and after firing of the vernier engines. (a) Right after landing. Note lunar material on bracket, control bar, and in honeycomb; also note darkly covered magnet. Light patches are blue paint showing through. Note that attachment screws on magnet are not louvered. The honeycomb to the right of the assembly has been deformed (compare with Fig. VIII-1). The material on the bracket and control bar is probably caused by vacuum cohesion (Day 255, 00:33:33; computer-enhanced picture). (b) After vernier firing. Note material has been blown out of the honeycomb, off the control bar, off the front edge of the bracket, and off the center of the magnet where the magnetic strength drops to zero gauss (Day 259, 04:48:26; computer-enhanced picture SWRF R-049).**

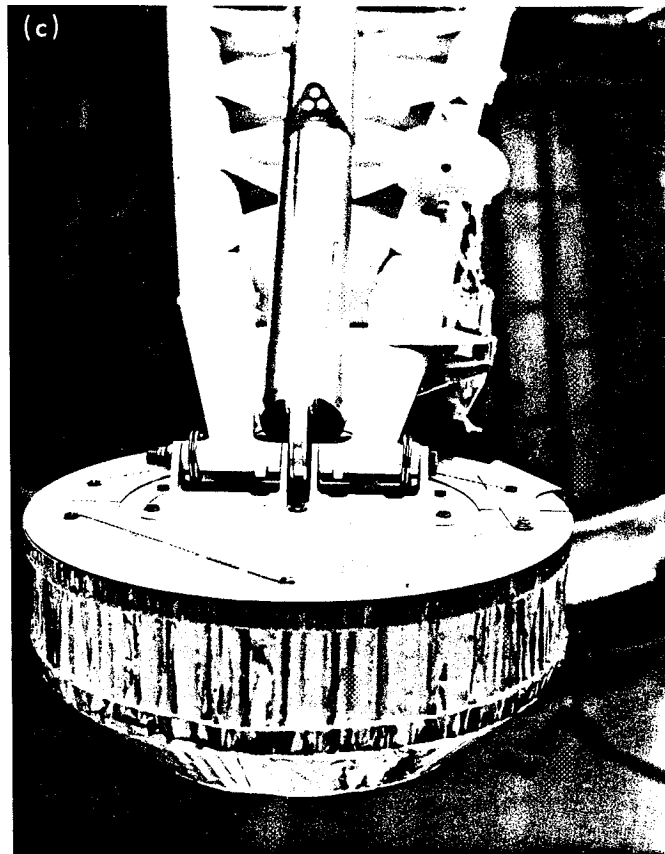
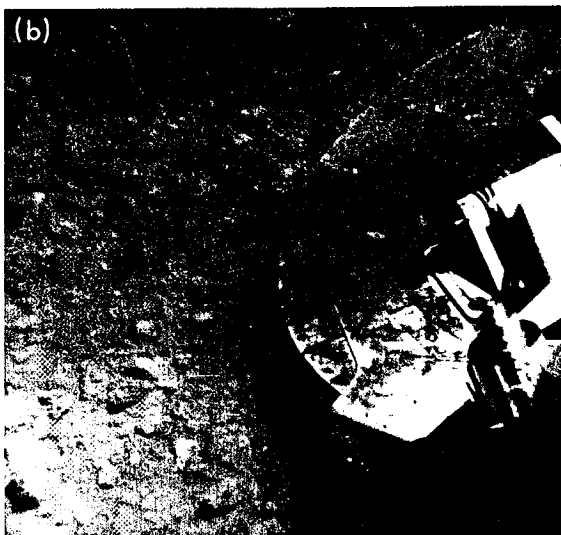
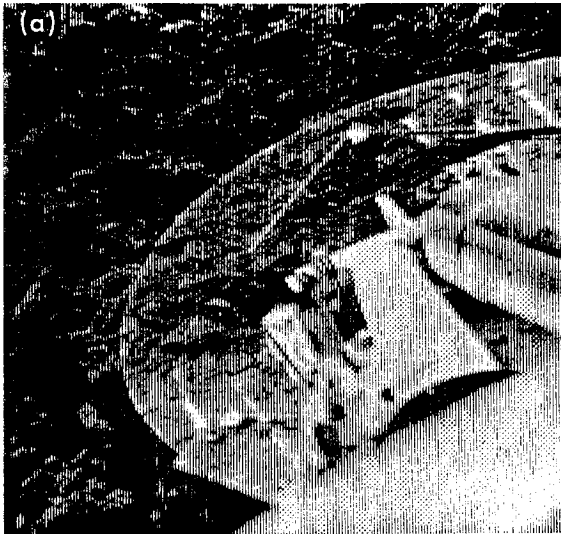
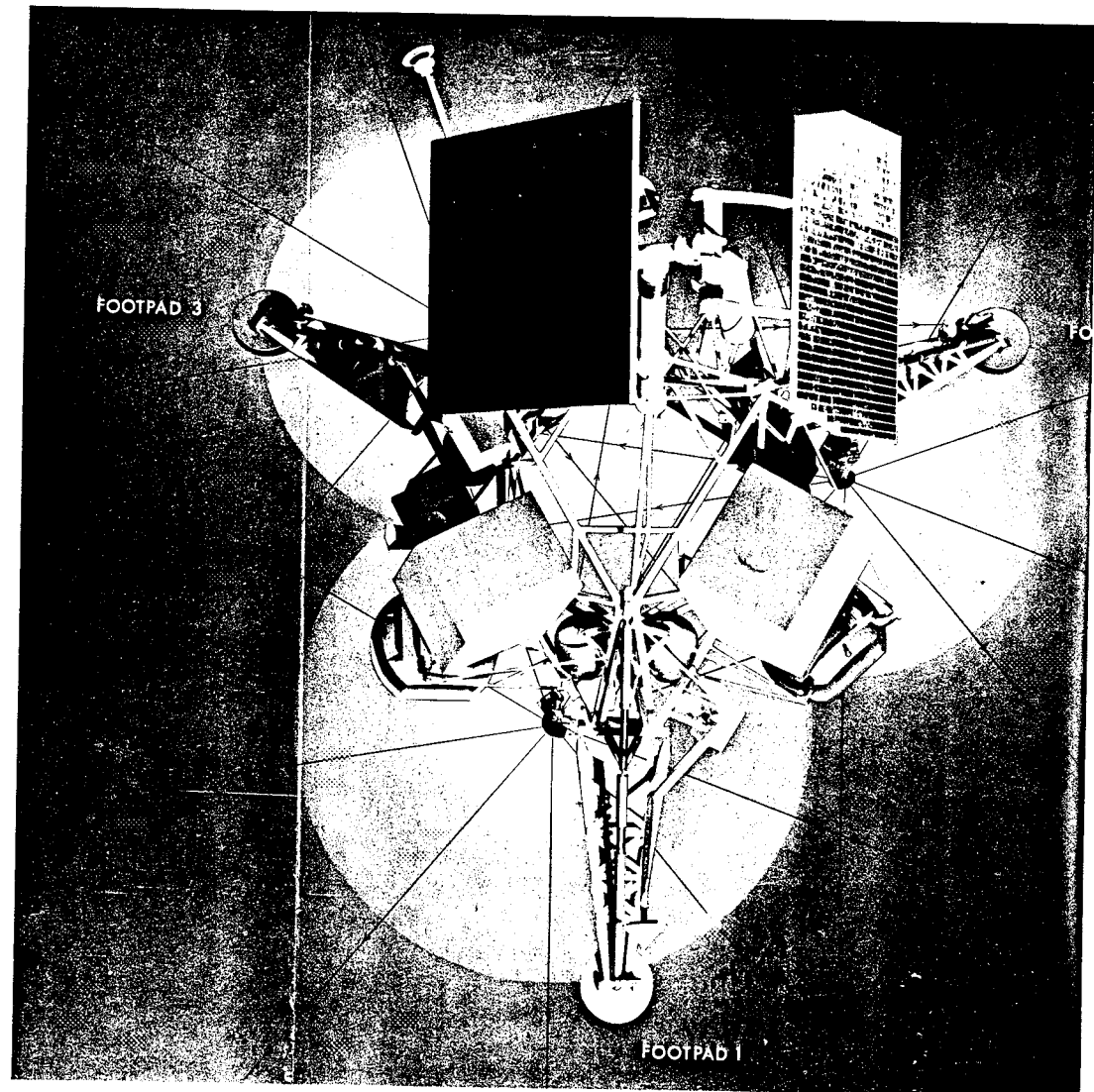


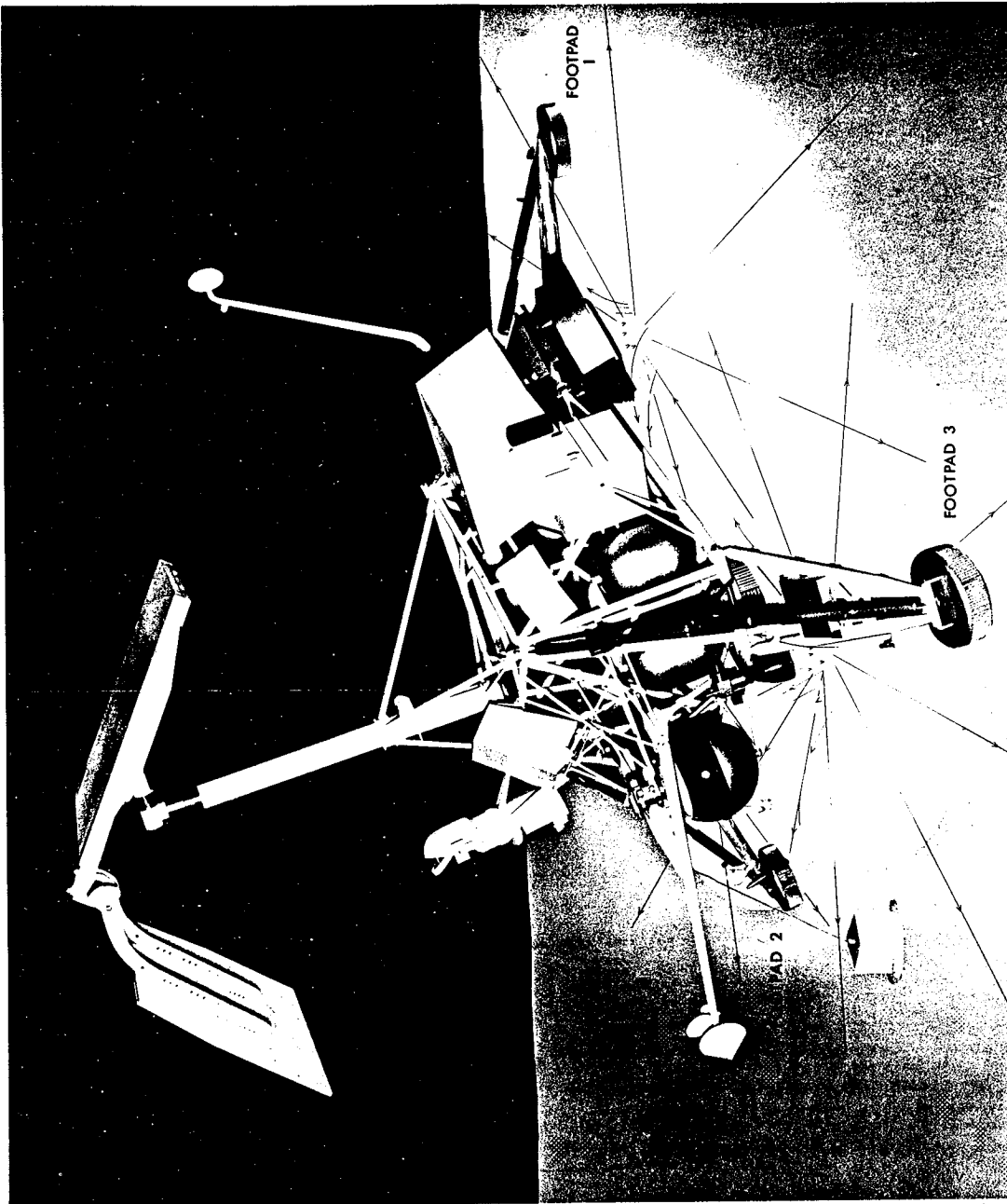
Fig. VIII-9. Sequence showing change in appearance of the footpad 2 top after vernier engine firing, and possible break in the top of the aluminum bracket holding the magnet assembly. (a) Footpad 2 right after landing. Note material on top of footpad. Dark, wavy line on bracket top is the shadow from the safety wire; the lighter line below is the site of a possible break in the bracket, probably caused by the first encounter with the lunar surface (at far right of Fig. VIII-7 showing the trench) (Day 254, 02:29:34). (b) In different lighting, seven terrestrial days later and after vernier firing. Note change in debris patterns on the footpad top. The linear break shadow is not visible, except vaguely in the center. However, by projecting a straight line along the white stripe on the bracket, it will be noted that the lower part of the stripe is offset by about 5 deg. This may explain why the light force of the vernier exhaust was more effective in cleaning off the bracket edge than farther back on the bracket. The edge may be slightly lower, which is due to the break (Day 261, 05:29:38). (c) Footpad 2 before launch, showing straight white stripe on the inner (left) side of the bracket.

Fig. VIII-10. Vernier exhaust vectors relative to the magnet assembly. The light circles represent 1.1 m from verniers at which distance the dynamic pressure was approximately 1 dyne  $\text{cm}^{-2}$ . The gas dispersion curve becomes asymptotic at about 2.44 m from the vernier engines. Left: view is looking down on the spacecraft, located on a 19.5-deg slope. North is to the top, footpad 2 is top right. Right: view looking east, showing the vernier exhaust vector relationships. The main vectors are lateral, the top of the footpads probably near the height limit for the main vectors.





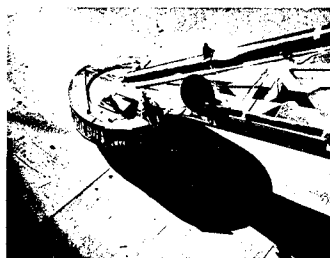




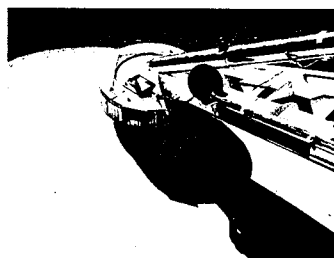
161







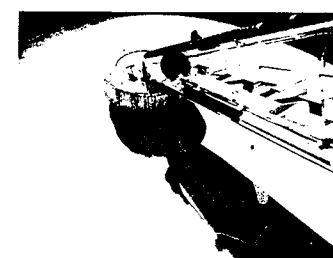
DAY 254  
SUN ELEVATION: 26.25°  
AZIMUTH: 161.27°



DAY 254  
SUN ELEVATION: 26.91°  
AZIMUTH: 163.77°



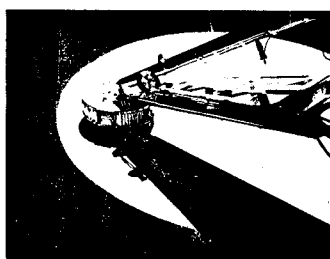
DAY 255  
SUN ELEVATION: 32.52°  
AZIMUTH: 166.53°



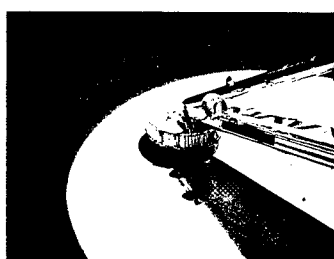
DAY 255  
SUN ELEVATION: 38.07°  
AZIMUTH: 169.64°



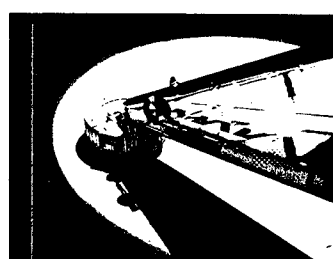
DAY 256  
SUN ELEVATION:  
AZIMUTH:



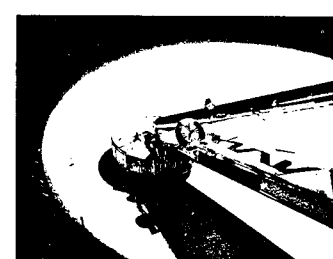
DAY 258  
SUN ELEVATION: 66.91°  
AZIMUTH: 209.76°



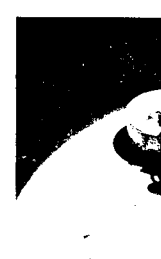
DAY 259  
SUN ELEVATION: 69.50°  
AZIMUTH: 224.65°



DAY 259  
SUN ELEVATION: 70.56°  
AZIMUTH: 242.27°



DAY 260  
SUN ELEVATION: 69.84°  
AZIMUTH: 260.18°



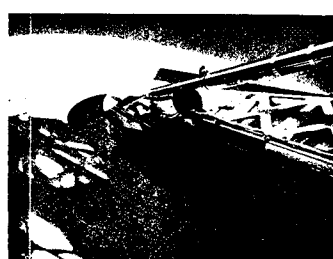
DAY 260  
SUN ELEVATION:  
AZIMUTH:



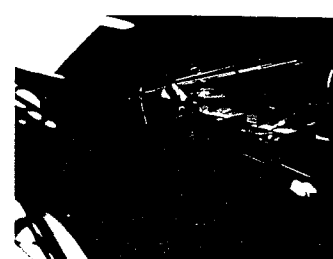
DAY 263  
SUN ELEVATION: 44.59°  
AZIMUTH: 314.06°



DAY 263  
SUN ELEVATION: 39.17°  
AZIMUTH: 42.23°



DAY 264  
SUN ELEVATION: 33.65°  
AZIMUTH: 39.05°



DAY 264  
SUN ELEVATION: 28.05°  
AZIMUTH: 36.25°



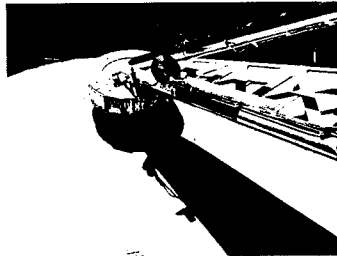
DAY 265  
SUN ELEVATION:  
AZIMUTH:

Fig. VIII-11. Shadow progression studies of footpad 2 used to determine the time of lunar day that the magnet assembly would be in full sun-light. These studies were conducted in the Surveyor Experiment Test Laboratory. The full-size spacecraft was used. The magnet assembly was in full lighting for only about 1.5 hr of the entire lunar day (14 terrestrial days).

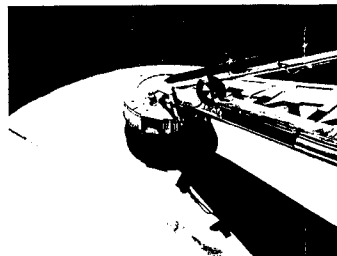




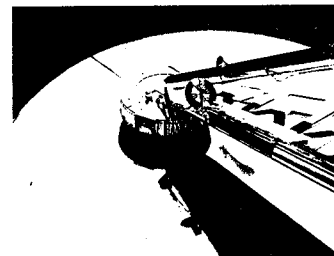
ATION: 43.52°  
t: 173.24°



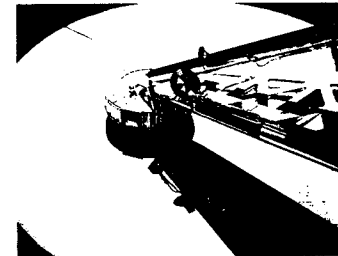
DAY 256  
SUN ELEVATION: 48.85°  
AZIMUTH: 177.53°



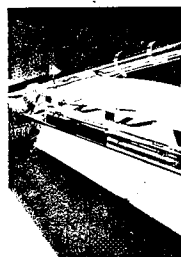
DAY 257  
SUN ELEVATION: 53.98°  
AZIMUTH: 182.80°



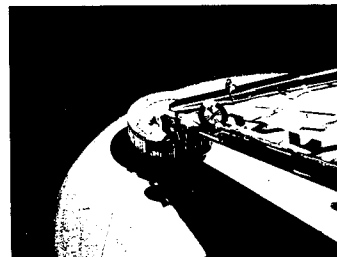
DAY 257  
SUN ELEVATION: 58.82°  
AZIMUTH: 189.50°



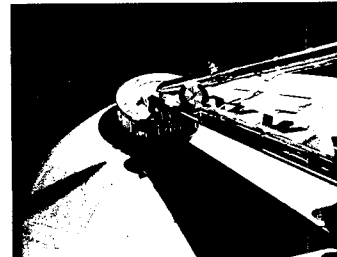
DAY 258  
SUN ELEVATION: 63.22°  
AZIMUTH: 198.23°



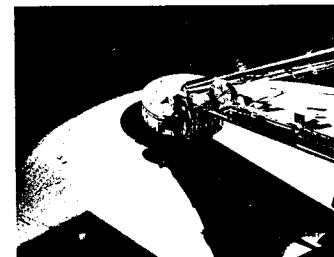
ATION: 67.51°  
t: 275.71°



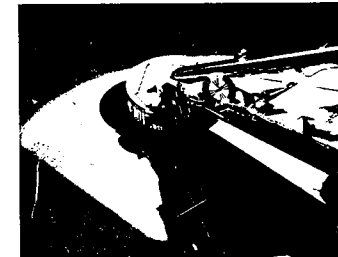
DAY 261  
SUN ELEVATION: 64.00°  
AZIMUTH: 287.87°



DAY 261  
SUN ELEVATION: 59.73°  
AZIMUTH: 287.87°



DAY 262  
SUN ELEVATION: 54.96°  
AZIMUTH: 304.10°



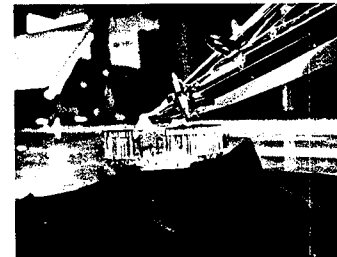
DAY 262  
SUN ELEVATION: 49.88°  
AZIMUTH: 309.61°



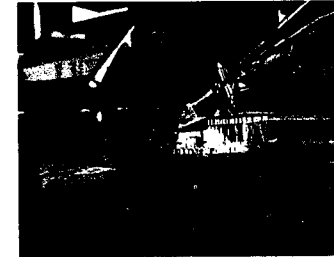
ATION: 22.42°  
t: 33.72°



DAY 265  
SUN ELEVATION: 16.74°  
AZIMUTH: 31.37°



DAY PREDICTION UNCERTAIN  
SUN ELEVATION: 9.31°  
AZIMUTH: 31.37°



DAY PREDICTION UNCERTAIN  
SUN ELEVATION: 9.00°  
AZIMUTH: 31.37°



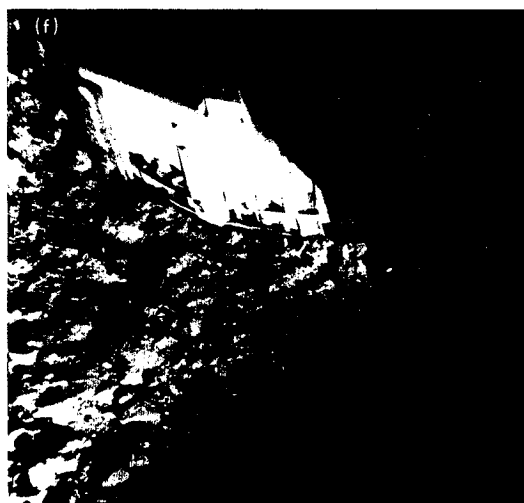
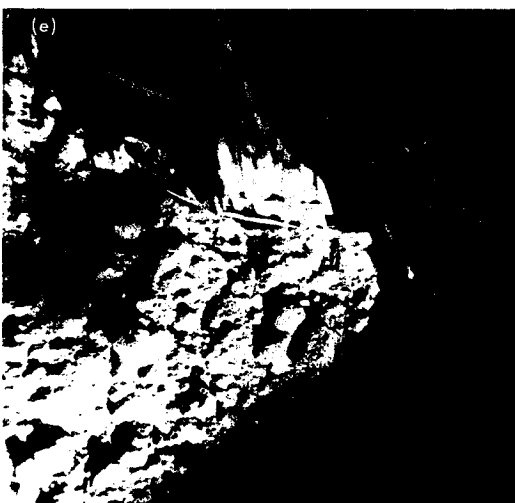
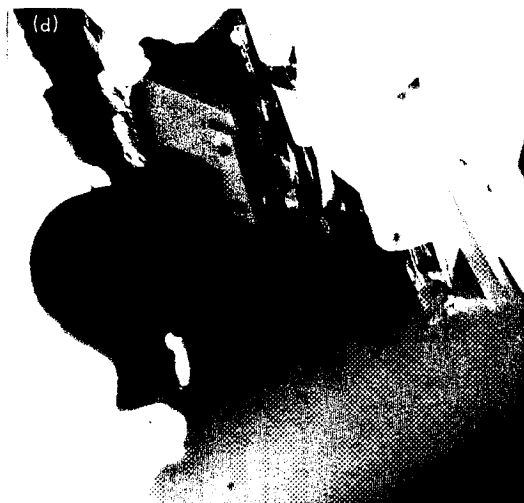
DAY PREDICTION UNCERTAIN  
SUN ELEVATION: 8.34°  
AZIMUTH: 31.37°



Fig. VIII-12. Sequence of magnet assembly through the first lunar day. (a) Before vernier firing (Day 255, 00:33:33). (b) After vernier firing (Day 258, 03:48:56). (c) Sun on top of magnet; note clumping on poles (Day 261, 06:54:02). (d) Sun on left half of magnet; note projections of material on magnet and dimple on lower left (Day 262, 05:08:04). (e) Approaching sunset; note lower tip of magnet in sunlight (Day 266, 05:54:32). (f) Sunset on magnet assembly; note patches of (blue) paint on north magnetic pole edge, and exposed area down the center (Day 266, 09:54:20).







## D. Laboratory Studies

Various studies were conducted in the laboratory to ensure better data retrieval as well as more accurate interpretation of the results of the magnet assembly on a landed spacecraft.

### 1. Shadow Progression Studies

Shadow progression studies were conducted with a full-sized spacecraft as well as with a small model; detailed studies were also conducted of footpad 2 in order to determine the periods of optimum lighting (see Fig. VIII-11). The retrieval of the final sunset picture of the magnet assembly was a direct result of these studies.

### 2. Impact Tests in Rock Types

Impact studies in the earth's atmosphere were conducted with a footpad and magnet assembly similar to the one flown on *Surveyor V*. Powders of various rock types were used, ranging from acidic (high silica content) rhyolite to ultrabasic (low silica content) peridotite (see Table VIII-2); serpentine (a hydrated basic rock) was also used. Two powder sizes were employed: 37–50 $\mu$  and 50–150 $\mu$ . The footpad with the magnet assembly was held stationary and the powder samples impacted against the side of the footpad. Other series of tests using mechanical impact or vertical plunging of the footpad into the sample showed no discrepancies in the results.

In the rock-type sequence (Table VIII-2 and Fig. VIII-13), it may be noted that only impact in basalt

**Table VIII-2. Average composition of rock types used in laboratory studies of magnet assembly impact in rock powders (from Smith, *Physical Chemistry*, pp. 372–373, 1963)**

Composition	Rhyolite, wt %	Dacite, wt %	Basalt, wt %	Peridotite, wt %
SiO <sub>2</sub>	72.80	65.68	49.06	45.07
Al <sub>2</sub> O <sub>3</sub>	13.49	16.25	15.70	5.75
Na <sub>2</sub> O	3.38	3.97	3.11	1.14
K <sub>2</sub> O	4.46	2.67	1.52	0.57
CaO	1.20	3.46	8.95	7.48
MgO	0.38	1.41	6.17	22.88
Fe <sub>2</sub> O <sub>3</sub>	1.45	2.38	5.38	3.43
FeO	0.88	1.90	6.37	4.53
TiO <sub>2</sub>	0.33	0.57	1.36	0.64
P <sub>2</sub> O <sub>5</sub>	0.08	0.15	0.45	0.15
MnO	0.08	0.06	0.031	0.26
H <sub>2</sub> O	1.47	1.50	1.62	3.10

powders resulted in much adherence of material to the magnetic bar on the left. Peridotite showed considerably less, and the more acidic rocks showed almost nothing on the magnet. Because the material adhering to the magnet in these tests is essentially magnetite, the laboratory results reflect the magnetic content of the rock types in question.

### 3. Impact Tests in Basalt With Additions of Iron

Impact studies were conducted using powdered Little Lake basalt and Pisgah scoriaceous basalt. To the 37–50 $\mu$  Little Lake basalt, 1 to 20% volumetric additions of pure powdered iron were made. A 100% iron sample was also used, as well as coarse iron shavings to determine the amount of material that the 500-gauss magnet was capable of attracting (see Figs. VIII-14 to VIII-16). A definite difference in the appearance of the magnet can be observed with each 1% increase in iron content.

### 4. Vacuum Studies

Impact and jet exhaust effects were studied in a vacuum chamber with a 10<sup>-6</sup>-torr vacuum. The impact tests in basalt with iron additions were repeated (Fig. VIII-17); an attitude control jet was fired into the sample at close range to obtain an upper limit for the possible addition of material on the magnet through the firing of the vernier engines. No appreciable amount of material adhered to the magnet with the jet tests (see Fig. VIII-18). In the vacuum impact tests, cohesion of a fine, even coating of material was observed over the side of the bracket as well as on the control bar. When the chamber was opened, very little air pressure was necessary to remove this coating. All the vacuum studies were photographed through the chamber porthole while the assembly was still in vacuum. Samples were baked at 300°F for 12 hr prior to the vacuum impact studies.

### 5. Landing Simulation Studies

Six simulations of the landing mode were conducted in a trough of 37–50 $\mu$  Little Lake basalt. A velocity of about 1 m sec<sup>-1</sup>, a distance of about 1 m, and a penetration depth of about 10 cm were used as parameters. All landings resulted in a similar appearance of the magnet (see Fig. VIII-19). A fine film of material adhered to the bracket and control bar, probably caused by moisture in the sample; this adherence afforded a comparison with vacuum cohesion on the lunar assembly. The packing in the sides of the simulated landing trough, as well as the resulting appearance of the test magnet, are similar to the lunar counterparts as observed by the *Surveyor V* camera.

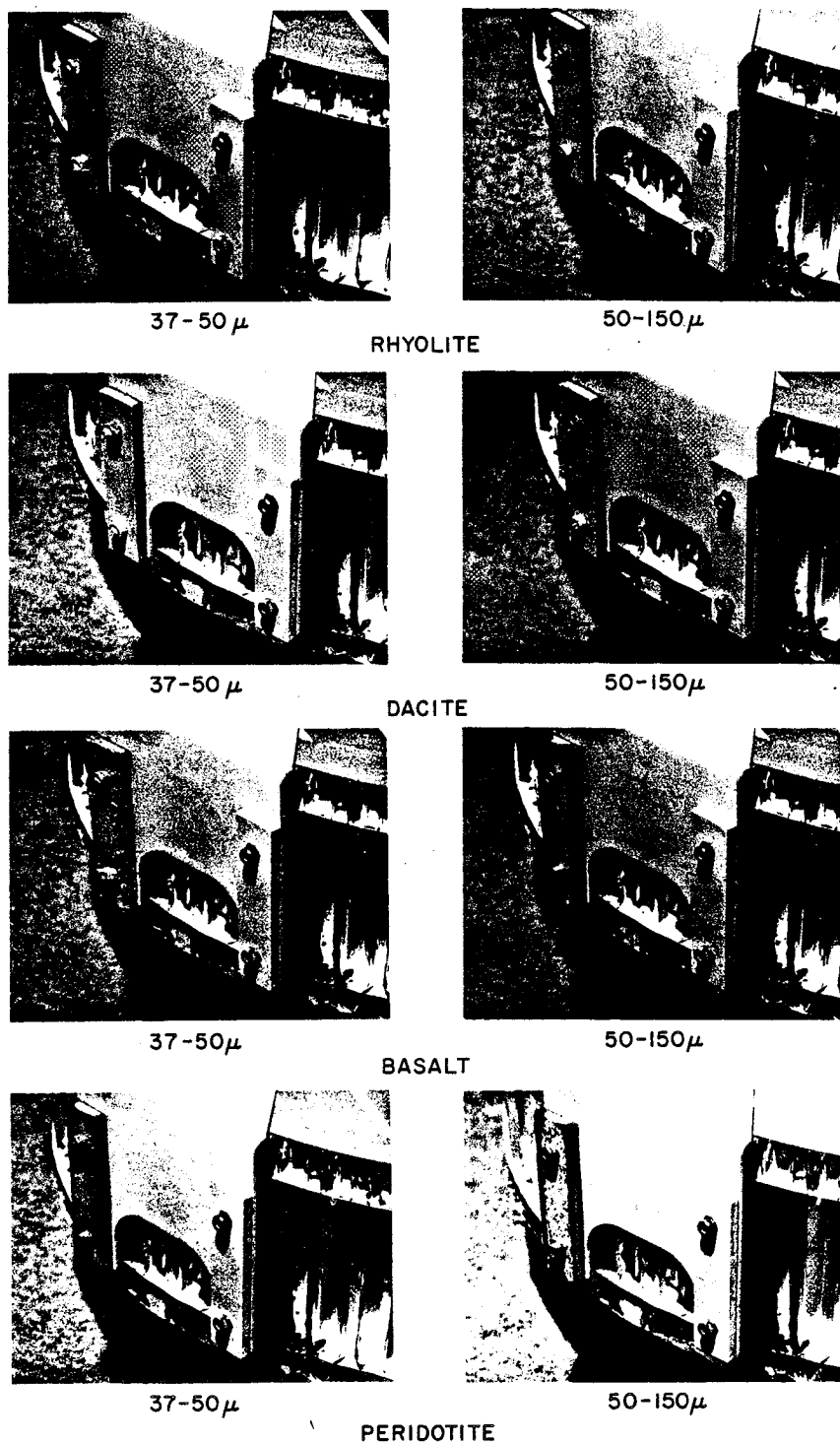


Fig. VIII-13. Results of impact in atmosphere in rock types ranging from acidic (high silica content) rhyolite to basic (low silica content) peridotite. Two powder sizes were used: 37-50 $\mu$  and 50-150 $\mu$ . Note appearance of basalt powders.

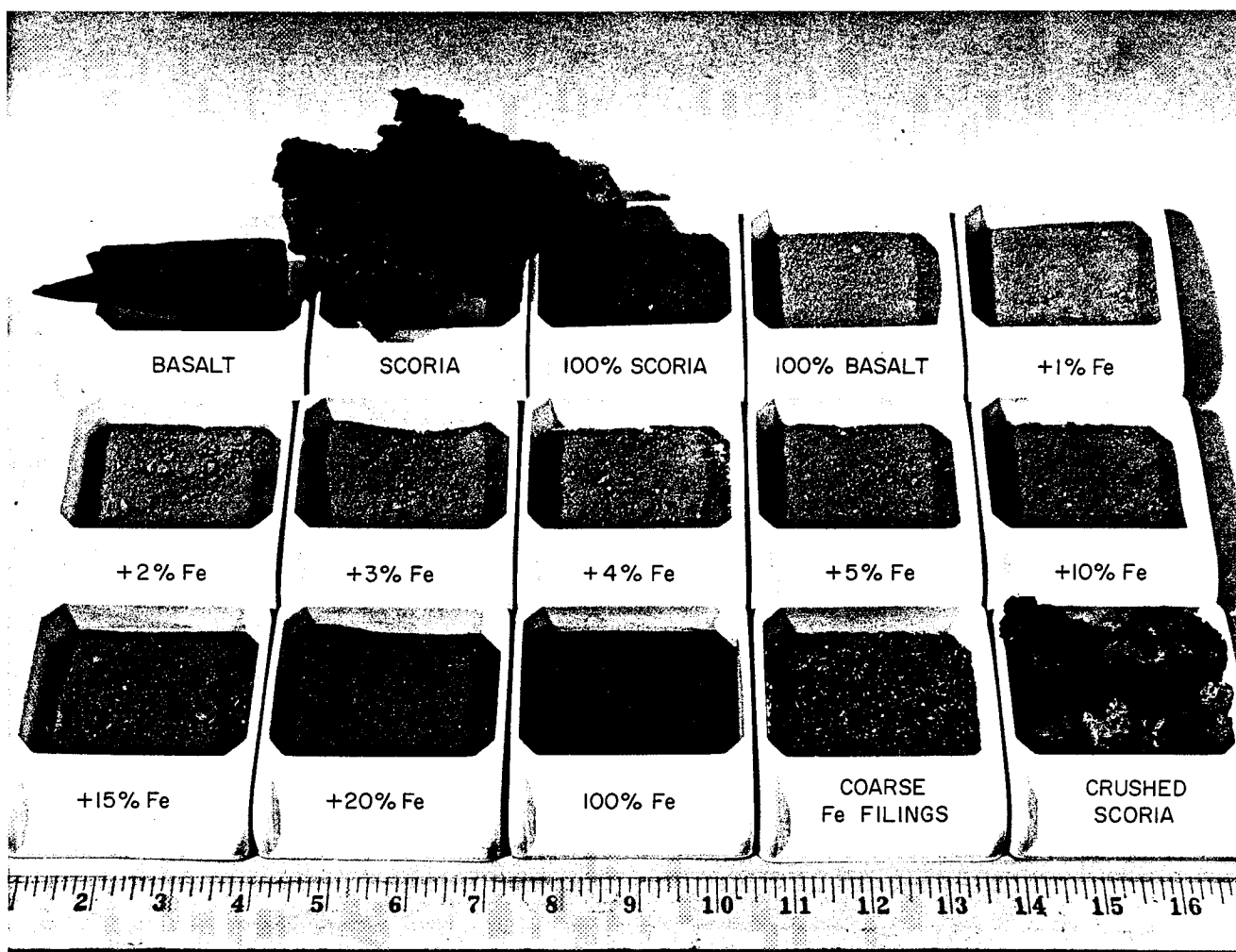


Fig. VIII-14. Materials used in powdered iron addition studies. The additions of iron are powdered iron by volume percent to powdered basalt.



SCORIACEOUS BASALT



BASALT + 2% Fe



BASALT



BASALT + 3% Fe

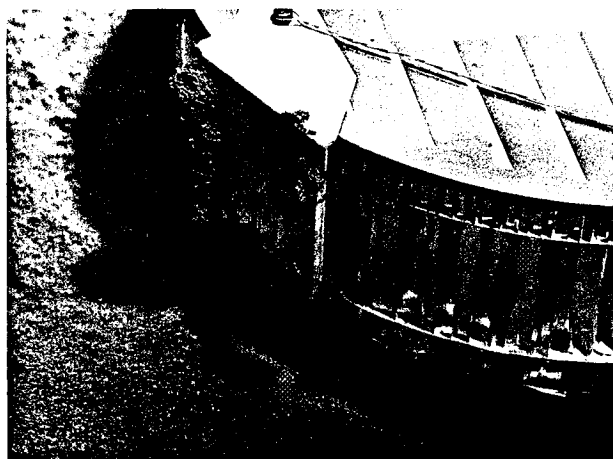


BASALT + 1% Fe

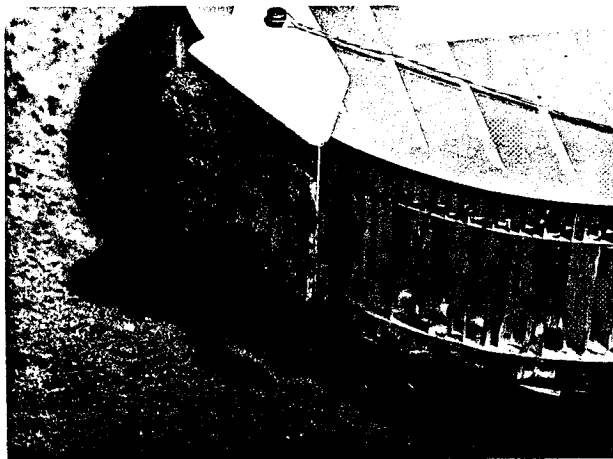


BASALT + 4% Fe

Fig. VIII-15. Impact in atmosphere into powdered basalt with additions of powdered iron by volume percent.



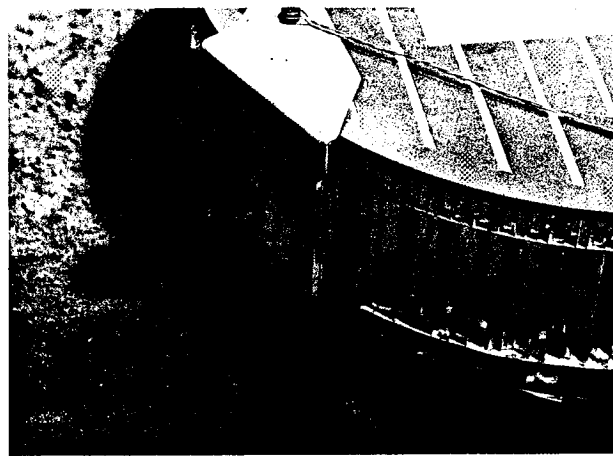
BASALT + 10% Fe



BASALT + 20% Fe

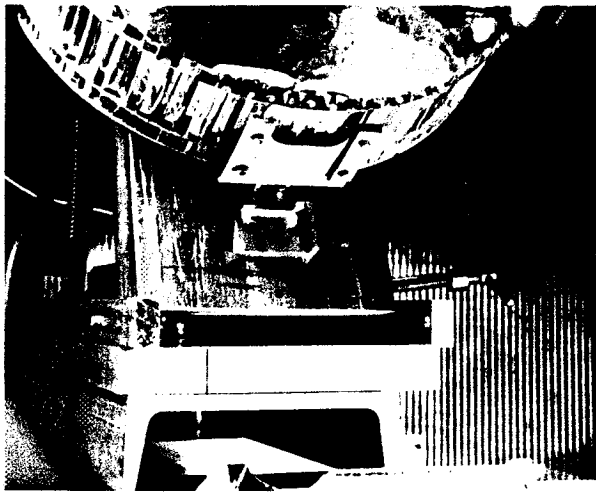


BASALT + 15% Fe

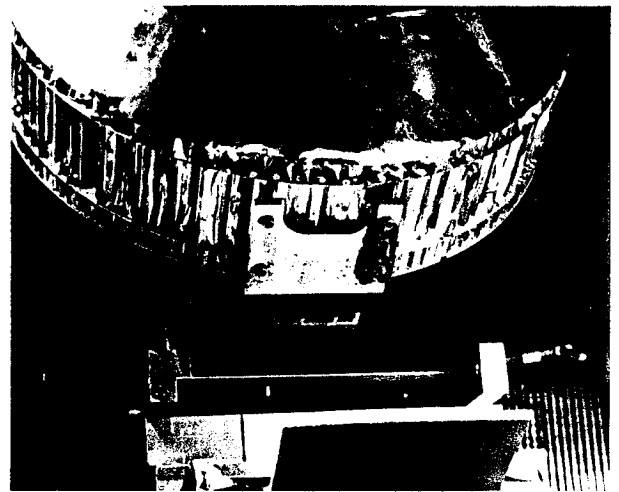


100% Fe

**Fig. VIII-16. Impact in atmosphere into powdered basalt with additions of powdered iron by volume percent. Lower right shows 100% powdered iron to indicate the amount of iron this magnet is capable of holding.**



100% BASALT



BASALT + 2% Fe



BASALT + 1% Fe



BASALT + 5% Fe

Fig. VIII-17. Impact in  $10^{-6}$ -torr vacuum into powdered basalt and basalt with volumetric additions of powdered iron as indicated. Note vacuum cohesion on bracket and control bar. Since the footpad is viewed upside down, the magnet is now on the right.

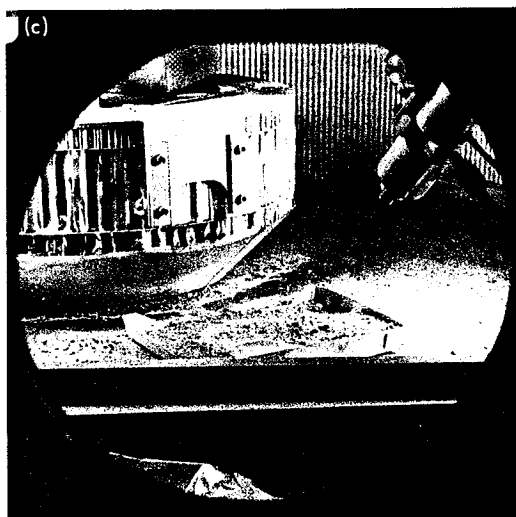
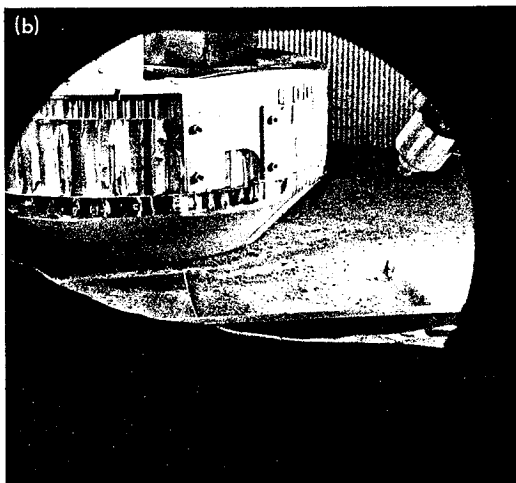
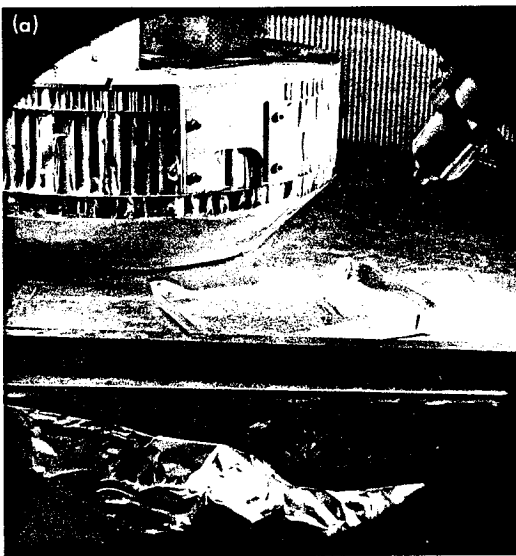


**Fig. VIII-18. Exhaust tests in  $10^{-6}$ -torr vacuum. An attitude control jet was used at close range to simulate possible forces from the vernier exhaust on the magnet assembly on the moon. (a) Prior to firing. (b) After firing into powdered basalt with 1% by volume addition of powdered iron. No material is seen to collect on the magnet. (c) After firing into powdered basalt with 4% by volume addition of powdered iron. Note small amount of material adhering to the edges of the magnet. It is concluded that very little, if any, material was added by the vernier engine firing on the moon. These pictures were taken through the viewing portal in the vacuum chamber.**



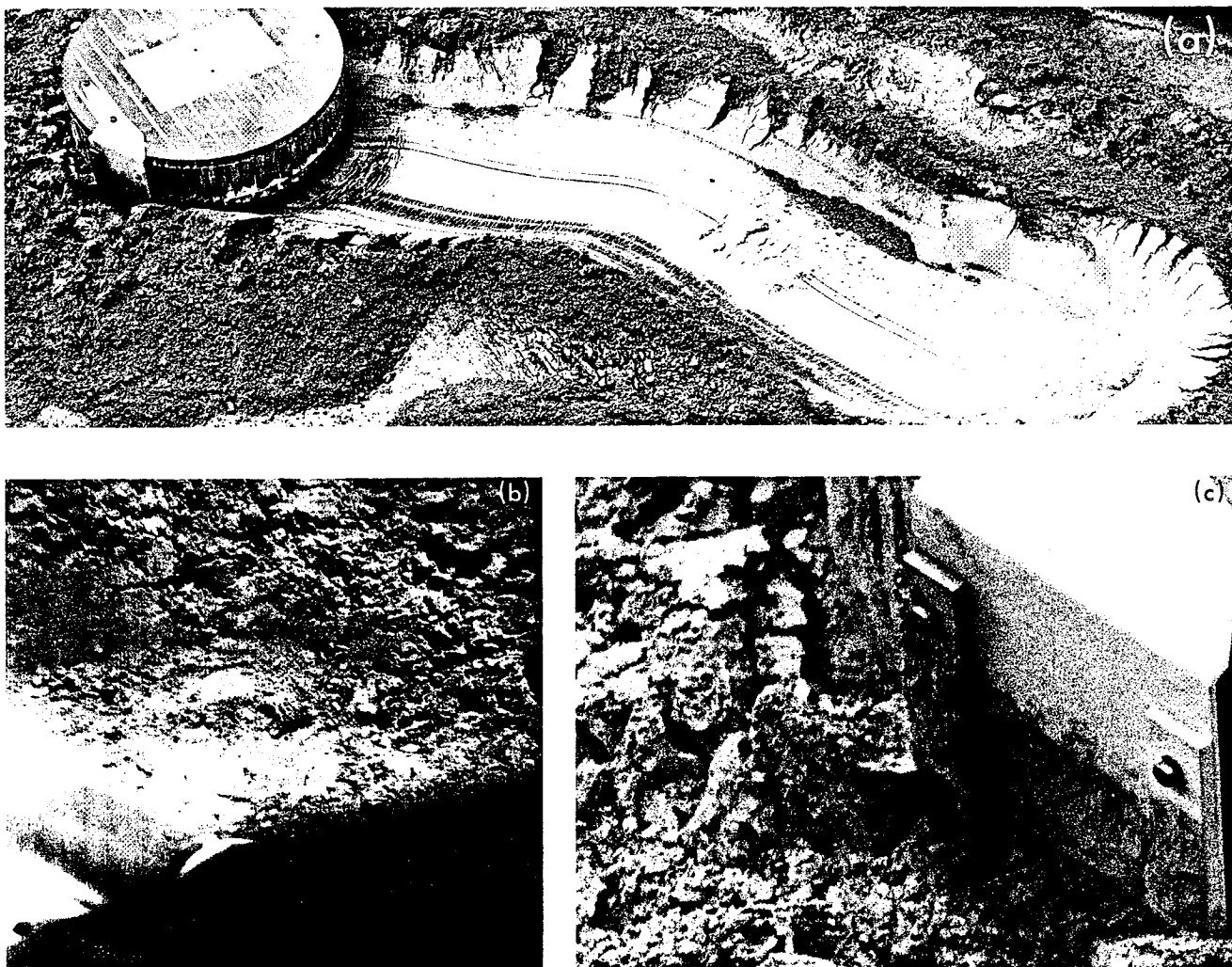


Fig. VIII-19. (a) Laboratory simulation of footpad 2 landing mode in 37–50 $\mu$  Little Lake basalt. Velocity, depth of penetration, and distance were simulated. (b) Picture taken by Surveyor V of the side of trench dug by footpad 2. Note similarity to Fig. VIII-18a and VIII-18c (Day 258, 04:02:17). (c) Closeup of footpad and magnet assembly used in laboratory simulation studies of landing (Fig. VIII-18a). Six such landings were performed; all results were similar. Note material on control bar on the right, material in the honeycomb and clumped on the magnet, covering the attachment screws. The increased humidity in the laboratory may have caused results similar to the apparent vacuum cohesion on the moon.

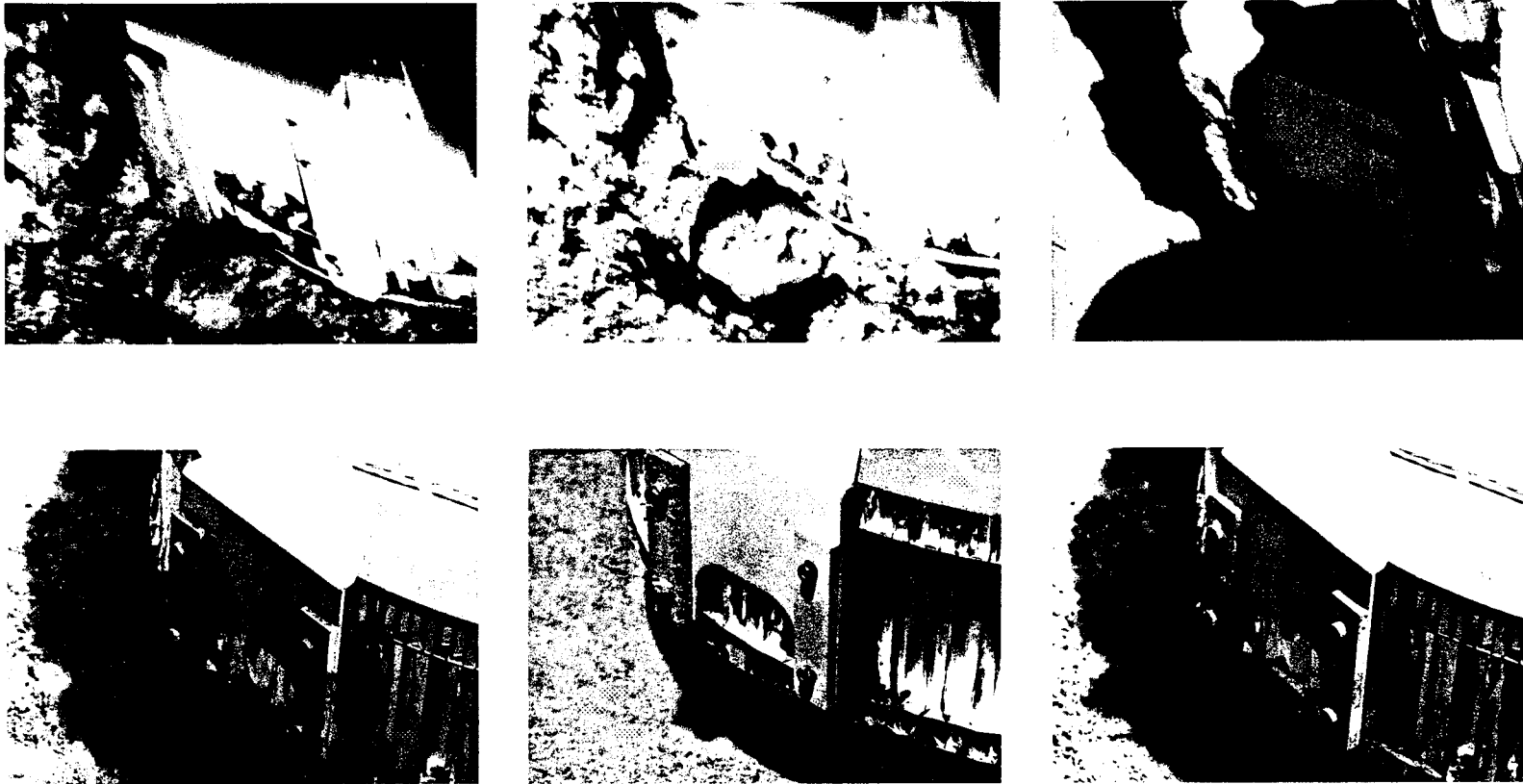


Fig. VIII-20. Comparison of lunar magnet results with laboratory material studies most closely resembling the magnet. Top row, left to right, are lunar pictures of the Surveyor V magnet (Day 266, 09:54:20; Day 266, 09:44:54; and Day 262, 05:08:04). Bottom row, left to right, are scoriaceous Pisgah basalt, Little Lake basalt 37-50 $\mu$ , Little Lake basalt with 1% by volume addition of powdered iron.

## E. Discussion

Because the success of the Magnet Experiment depended on a known solid impact with the lunar surface material, a better landing could not have been executed. From inspection of pictures of the material covering the footpad, and the trench morphology, the requirement for lunar surface material impact was met.

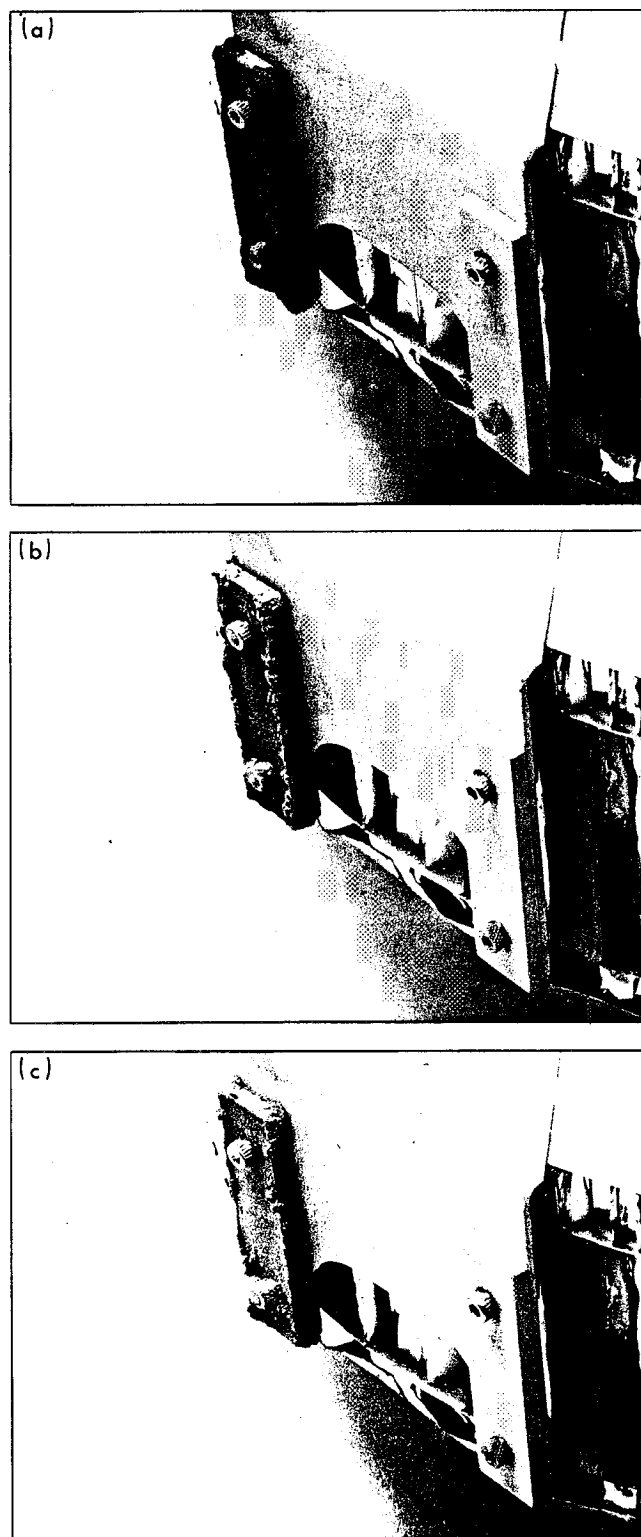
In order to impose a control on the interpretation of the cause of the adherence of material to the magnetic bar (magnetic attraction or vacuum cohesion), the non-magnetic Inconel X-750 bar was included. Prior to firing of the vernier engines, material was observed on the bracket and control bar, probably caused by vacuum cohesion; the magnet was dark. After firing the vernier engines, the bracket and control bar were perfectly clean, and the paint in the zero-gauss area of the magnet was visible. Areas of lower magnetic strength along the pole faces also showed patches of blue paint (compare Fig. VIII-12 with Fig. VIII-2). Therefore, the control for interpretation of the cause of adherence was accomplished; the material remaining on the magnet must be material with high-magnetic permeability, i.e., iron, magnetite ( $\text{Fe}_3\text{O}_4$ ), or Ni-Fe meteoritic fragments.

Interpretation of the lunar results is dependent upon visual similarity of the lunar pictures of the magnet with pictures of laboratory studies in various rock powders (with and without the addition of iron), different powder sizes, and with landing simulation studies. The results of such a comparison show some interesting similarities (Fig. VIII-20).

In comparison with the rock-type impact sequence, the only terrestrial results resembling the lunar pictures are those in fine basalt powder,  $37\text{--}50\mu$ . In a sequence of different-sized basalt powders,  $> 50\mu$  and  $< 37\mu$  caused much less material to adhere to the magnet (Fig. VIII-21).

By comparison of the lunar pictures with the iron addition sequence, the laboratory impact in 1% by volume addition of powdered iron appears to be in excess of the lunar results in terms of quantity of material adhering to the magnetic bar.

**Fig. VIII-21. Studies of impact in atmosphere, using  $< 37\mu$ ,  $37\text{--}50\mu$ , and  $50\text{--}150\mu$  Little Lake basalt with no additions of iron, showed less material adhering to the magnet bar when  $< 37\mu$  and  $> 50\mu$  basalt were used.**



The jet exhaust studies seem to preclude the possibility that any appreciable amount of material was added by the vernier firing. However, material over zero- or low-magnetic-field areas was removed.

Laboratory measurements made under vacuum conditions showed apparent vacuum cohesion of material on the bracket and control bar similar to that seen in the lunar magnet prior to vernier engine firing. Other vacuum results indicated that the studies in atmosphere were similar in terms of the amount of material adhering to the magnetic bar. Therefore, it is concluded that studies in atmosphere give valid data comparisons for interpretation for the lunar results.

From landing simulation studies, the appearance of the terrestrial magnet assembly was quite similar to that on the moon after the former had "lunar landed" in powdered basalt.

## F. Problems

In interpreting these results, several considerations warrant further study. An elemental analysis of the Little Lake basalt is shown in Table VIII-3. Most of the iron is in the form of magnetite, amounting to 10 to 12% by weight of the rock. The magnetite particles themselves

are 10 to 15 $\mu$  in size. Therefore, in the 37-50 $\mu$  powder, the size of the magnetite particles is being approached. This could be a very important point. The relationship between size of iron particle to rock powder needs further investigation in terms of magnetic attraction. This raises the question of whether iron vapor-deposited on silicate particles (following meteoritic impact) or iron coatings deposited by sputtering would be magnetic. A thickness of a few angstroms of iron on a silicate grain 50 $\mu$  in size would, from preliminary investigations, not be attracted to a 500-gauss magnet.<sup>1</sup>

A finer breakdown in size range of powders should also be used: the 37-50 $\mu$  is just beginning to approach the magnetite particle level and causes the greatest amount of material to adhere. A considerable difference is seen in the results with impact < 37 $\mu$ , 37-50 $\mu$ , and 50-150 $\mu$ . Both the <37 $\mu$  and >50 $\mu$  powders showed much less adherence. Size-range increments of 10 $\mu$  may yield fruitful results in attempting to determine the size of lunar particles from visual simulations of the magnet results. The alpha-scattering data present a control on constituents.

## G. Conclusions

The following conclusions may be made on the basis of the *Surveyor V* pictures of the magnet assembly:

- (1) Iron is present on the lunar surface at the landing site in the form of magnetite, pure iron, meteoritic Ni-Fe fragments, or some combinations of these forms of iron.
- (2) As observed from laboratory studies, an upper limit for the addition of iron to a naturally occurring rock may be represented by 1% by volume addition of powdered iron.
- (3) Lunar magnet results are not in disagreement with the laboratory results of impact in a 37-50 $\mu$  powdered basalt with no addition of iron.
- (4) The *Surveyor V* magnet results indicate considerably less magnetic material than would be expected from entirely meteoritic pulverization and cratering of the lunar surface.

These results provide support to the Alpha-Scattering Experiment, the results from which indicate that the observed lunar material has a composition similar to terrestrial basalt, by apparent agreement with the amount of magnetite to be expected in a basaltic rock.

<sup>1</sup>R. Fraser, private communication.

**Table VIII-3. Elemental analyses of the Little Lake basalt and Pisgah scoriaceous basalt used in laboratory studies**

Element	Little Lake basalt, wt %	Pisgah scoriaceous wt %
Silicon	20	24
Aluminum	10.48	6.7
Iron	5.78	7.7
Magnesium	5.03	6.4
Calcium	4.98	5.0
Titanium	2.18	1.7
Gallium	0.0055	0
Manganese	0.058	0.076
Nickel	0.0059	0.014
Vanadium	0.014	0.013
Copper	0.0032	0.0033
Sodium	2.6	1.9
Zirconium	0.018	0.016
Cobalt	0.0064	0.0098
Potassium	1.12	0.56
Strontium	0.049	0.026
Chromium	0.017	0.055
Tungsten	0.22	0
Barium	0	Trace

Since the mare surface morphology unit is a widespread homogeneous unit on the lunar surface, conclusions per-

taining to this area may be extrapolated in a wider context to the other lunar maria.

## Acknowledgment

I would like to express appreciation to D. Nash for supplying the rock powders for the impact tests in rock types. The *Surveyor* Experiment Test Laboratory, under the direction of C. Goldsmith, conducted the very useful shadow progression studies; the assistance of A. Irving in the landing simulation and impact tests in atmosphere was much appreciated.

The 6-ft vacuum chamber team is also to be commended for the assistance in vacuum chamber tests, and the planetology group under J. Adams for consultation on various aspects of the test program. Finally I would like to express appreciation to R. McFee and R. Mackin for continued support in the effort to place a controlled magnet test on the lunar surface.



## IX. Lunar Theory and Processes

*D. E. Gault, J. B. Adams, R. J. Collins, J. Green, G. P. Kuiper, H. Masursky,  
J. A. O'Keefe, R. A. Phinney, and E. M. Shoemaker*

### A. Discussion of Chemical Analysis

The chemical analysis (see Section VII) of the lunar surface at the *Surveyor V* landing site in southwestern Mare Tranquillitatis has opened a new era in the study of the origin and history of the moon and other planetary bodies. From preliminary results of the Alpha-Scattering Experiment, the elemental abundances of the major constituents are sufficiently well defined to warrant some discussion of their significance and some tentative conclusions. It is recognized that this first analysis for a single spot (10 cm in diameter) on the lunar surface may not be representative of even a small part of the mare surface. Meteoric impact or, perhaps, explosive volcanism, or both, are mechanisms for distributing and mixing lunar material so that a heterogeneous mixture of many components could have been displayed for analysis under the alpha-scattering instrument. It seems unlikely that sufficient foreign material could be mixed with the indigenous mare material to mask the composition of the parent components totally, but it must, nevertheless, be considered a possibility. The modifying effects of prolonged exposure to solar radiation must also be considered because the alpha-scattering technique permits a sam-

pling of only micron-deep layers of the exposed material. However, some subsurface material shielded from direct solar radiation was ejected by the impact of the footpads against the surface into the region where the alpha-scattering instrument was finally deployed (see Section III). Subject to such limitations and qualifications, a preliminary interpretation is presented of the results from this experiment.

The chemical analysis by Turkevich, et al. (see Section VII) is compared in Table IX-1 with six common rock types, spanning the range in silica content from ultramafic to silicic composition. Although the composition in any given classification of rocks can vary over a fairly broad range, the magnesium and aluminum abundances in the lunar sample are inconsistent with, and cannot be related to, those of ultramafic rocks such as peridotite and chondritic meteorite. Similarly, the silicic materials represented by the averages for granite and tektite are characterized by silicon and heavy elemental abundances that are also inconsistent with the alpha-scattering data. The analysis points to a basaltic composition, a conclusion that is consistent with the indications from the Magnet Experiment (see Section VIII).

**Table IX-1. Elemental abundances for some common rock types, compared with preliminary chemical analysis of the moon at the landing site**

Element	Atomic percent						
	Peridotite (Ref. IX-1)	Plateau basalt (Ref. IX-1)	Granite (Ref. IX-1)	Moon (mare) (see Section VII)	Indo-Malayan tektite (Ref. IX-2)	Basaltic achondrite (Ref. IX-2)	L-type chondrite (Ref. IX-2)
Hydrogen	2.5	4.2	1.9	—	0.4	0.9	0.7
Carbon	—	—	—	< 3	—	—	—
Oxygen	57.5	59.0	62.1	$58 \pm 5$	63.7	59.6	54.6
Sodium	0.4	1.8	2.3	< 2	1.0	0.6	0.8
Magnesium	18.7	3.6	0.5	$3 \pm 3$	1.1	5.5	14.4
Aluminum	1.9	5.8	5.9	$6.5 \pm 2$	5.4	5.1	1.2
Silicon	15.0	17.1	23.3	$18.5 \pm 3$	25.1	18.2	15.5
Phosphorous to copper	4.1	8.6	3.5	$13 \pm 3$	3.4	10.1	12.7
(Iron, cobalt, nickel)	2.4	3.9	0.9	> 3	1.5	5.3	10.0

Important genetic implications arise from a basaltic composition. Basalt is derived by chemical fractionation of an ultramafic rock. Thus, it seems highly probable that differentiation has occurred in the moon as a result of partial or fractional melting of lunar material.

The heat sources necessary to melt the lunar material probably originated within the moon rather than from an external source. Internal sources include decay of radioactive elements, gravitational compression, and dissipation of kinetic energy by mechanical processes. The possibility that the analyzed material is the fractional product from a large puddle of melt produced by a monstrous collision that formed the mare basin is inconsistent with the observations that the filling of the mare basins could not have been contemporary with their formation (Refs. IX-3 and IX-4).

Based on the ratio of silicon to sodium in relation to oxygen content (Ref. IX-5), the material analyzed by the alpha-scattering instrument approximates the chemistry of some of the most common terrestrial basalts. Even though the analysis of the data has not been refined to the point where the material can be categorized into a specific subgroup of basalt, the general trend is consistent with a widely accepted hypothesis that extensive volcanic flows have been responsible for flooding and filling of the mare basins. Extensive basalt flows are widespread on earth (Ref. IX-6). By far the greatest proportion is found as ocean-floor basalt, being derived from partial fusion of the underlying ultramafic mantle. The Columbia Pla-

teau and Deccan Traps are the best known of this genre on continents.

It is significant and gratifying that the chemical composition of the lunar material appears to be most like that of a common terrestrial rock, and this material is not composed of an unusual mixture of elements. Apparently, the geochemical processes on the earth do not differ greatly from their lunar counterparts despite environmental differences between the two bodies. Therefore, for the first time, we have some evidence for the validity of extrapolating terrestrial geochemical and geologic experience to the interpretation of the moon and of lunar processes.

If the lunar sample analyzed by the alpha-scattering instrument is fairly typical of the compositional type of material at the *Surveyor V* landing site, and this seems a reasonable assumption, then it is to be inferred that the observed composition is probably also appropriate to material in other maria because of the geologic similarities among the mare units. There is no reason to assume, however, that basaltic materials with different compositions will not be found in all maria; indeed, different compositions are to be expected as the natural consequences of normal fractionation processes. Although knowledge of such differences would be of great interest, the determination of the composition in the contrasting highland provinces now becomes of paramount importance for clarifying the extent and degree of magmatic differentiation that has occurred in the moon.



## References

- IX-1. *Handbook of Physical Constants* (S. P. Clark, Jr., editor), Geological Society of America, New York, 1966.
- IX-2. Palm, A., and Strom, R. G., *Space Sciences Laboratory Research Report*, Series 3, Issue 5, University of California, Berkeley, 1962.
- IX-3. Shoemaker, E. M., "The Geology of the Moon," *Sci. Amer.*, Vol. 211, p. 38, December 1964.
- IX-4. Kuiper, G. P., "Interpretation of *Ranger VII* Records," *Ranger VII, Part II: Experimenters' Analyses and Interpretations*, Technical Report 32-700, pp. 9-73, Jet Propulsion Laboratory, Pasadena, Calif., February 10, 1965.
- IX-5. Loomis, A. A., "Interpretation of Lunar Alpha-Scattering Data," *J. Geophys. Res.*, Vol. 70, p. 3841, 1965.
- IX-6. Parger, R. L., U. S. Geological Survey Professional Papers 440-D, DI, 1967.



# Appendix A

## Study of Contamination of Surveyor V Landing Site by Main Retro Exhaust

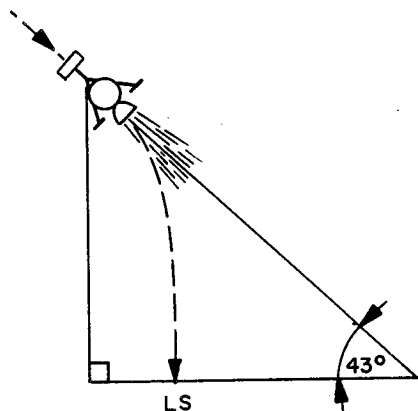
A. L. Turkevich, E. J. Franzgrote, and J. H. Patterson

Because of the nonstandard nature of the *Surveyor V* landing operation, the main retro rocket burned to within 1.6 km of the lunar surface. (The standard end-of-burning altitude is about 12 km). Since solid particles of aluminum oxide are contained in the retro exhaust, consideration has been given to the possibility that the alpha-scattering analysis has been affected by the retro operation.

A calculation of the mass per unit area of aluminum oxide deposited at the landing site has been made, based on:

- (1) Trajectory of the spacecraft.
- (2) Pointing angle of the retro motor relative to the landing site.
- (3) Cone angle of the exhaust products.
- (4) Mass of aluminum oxide exhausted as a function of burning time.

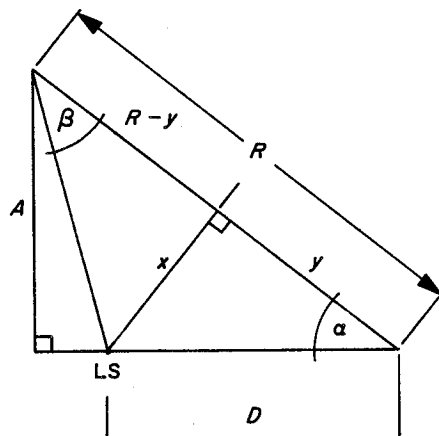
The following sketch shows the attitude of the spacecraft and its location relative to the landing site (LS) near the end of retro burning:



Because of the large off-vertical angle of approach, the retro operation during the final few seconds of burning did not deposit aluminum oxide at the landing site. This

served to materially reduce the contamination relative to that expected for a vertical landing (at comparable distances from the surface).

The geometrical relationships used in the calculation are shown in the following sketch:



where

$A$  = altitude of spacecraft

$R$  = range to lunar surface along the trajectory

$D$  = distance from the retro aiming point to the landing site

The values  $A$ ,  $R$ , and  $D$  as a function of time are known from *Surveyor V* trajectory data:

Time (after vernier ignition), sec	$A$ , km	$R$ , km	$D$ , km
0	46	64	1.0
10	28	40	1.3
20	15	21	1.6
30	5.2	7.6	1.7
40	1.6	2.3	1.7

Since the retro aiming direction and the line of the trajectory were within a degree of each other, they are assumed to be the same for these calculations. The ratio of  $R$  to  $A$  remained fairly constant throughout retro operation, and the angle  $\alpha$  is assumed to be constant at 43 deg.

Beta is the half-angle of the retro exhaust cone. The sketch illustrates the special case where the exhaust cone just intersects the landing site at a distance,  $R - y$ . By using a value of  $\beta$ , which is appropriate for the main retro motor,  $R - y$  may be found to satisfy this special condition. Then, at all greater ranges, the landing site will be included in the exhaust cone. (The particles can be assumed to travel in straight lines.)

Two values of  $\beta$  were chosen. For case I, the angle was defined by the geometry of the rocket nozzle; 100% of the solid particles are contained within that angle ( $\cot \beta = 4.0$ ). For case II, since studies of the distribution of solid particles in rocket exhausts indicate that the particles are more concentrated along the central axis of the nozzle, an angle half that of case I was assumed ( $\cot \beta = 8.0$ ).

Using these two cone angles, the values of  $R - y$  for the critical condition were found to be 4.3 km for case I and 9.1 km for case II. At various values of  $R - y$  greater than these critical values, the area of the circular cross-section of the exhaust cone (where this cross-section includes the landing site) may be calculated. The mass of aluminum oxide per unit area can then be calculated for a given interval of burning, assuming an even distribution of particles across the cross-section of the cone. The mass flow-rate of aluminum oxide from the retro engine can be

taken to be constant at  $4.3 \times 10^3$  g/sec for the period 1 to 40 sec after vernier ignition.

Calculations of the mass of aluminum oxide per unit area were made for both cases, integrating stepwise for several time intervals back to the start of the retro rocket firing. The total amount of contamination at the landing site was found to be  $3.0 \times 10^{-7}$  g/cm<sup>2</sup> for case I and  $3.2 \times 10^{-7}$  g/cm<sup>2</sup> for case II.

The results are fairly insensitive to changes in the exhaust cone angle for the following reason. At narrow angles, the exhaust cone includes the landing site only at the greater ranges; however, the solid particles are more concentrated because of the narrow angle.

The average particle size (on a mass basis) for a motor of the *Surveyor* characteristics is about  $3.5\mu$ . A sample of material with a density of 2.0 g/cm<sup>3</sup> and  $3.5\mu$  thick has a mass per unit area of  $7 \times 10^{-4}$  g/cm<sup>2</sup>. The percentage of area covered by the particles deposited by *Surveyor V*, is, therefore

$$\approx \frac{3 \times 10^{-7} \text{ g/cm}^2}{7 \times 10^{-4} \text{ g/cm}^2} (100) = 0.04\% \text{ aluminum oxide}$$

or, approximately 0.02% aluminum.

Even if the contamination level were an order of magnitude higher than that estimated, it would be negligible in comparison with the  $6.5 \pm 2\%$  aluminum found in the preliminary analysis of the lunar sample. Moreover, because of the high velocity of impingement (varying between one and two times the lunar escape velocity), it is unlikely that the aluminum-oxide particles come to rest on the very surface of the moon at the point of impact.

## Appendix B

### Surveyor Science Teams

Analysis of the scientific data, for the *Surveyor V* mission, was conducted by the *Surveyor* Scientific Evaluation Advisory Team, Investigator Teams, and Working Groups. Membership for *Surveyor V* was:

#### A. Surveyor Scientific Evaluation Advisory Team

L. D. Jaffe, Chairman	Jet Propulsion Laboratory
S. A. Batterson	Langley Research Center
W. E. Brown, Jr.	Jet Propulsion Laboratory
E. M. Christensen	Jet Propulsion Laboratory
S. E. Dwornik	NASA Headquarters
D. E. Gault	Ames Research Center
J. W. Lucas	Jet Propulsion Laboratory
R. H. Norton	Jet Propulsion Laboratory
R. F. Scott	California Institute of Technology
E. M. Shoemaker	U. S. Geological Survey
G. H. Sutton	University of Hawaii
A. L. Turkevich	University of Chicago

#### B. Investigator Teams

##### 1. Television

E. M. Shoemaker, Principal Investigator	U. S. Geological Survey
R. A. Altenhofen	U. S. Geological Survey
R. M. Batson	U. S. Geological Survey
H. E. Holt	U. S. Geological Survey
G. P. Kuiper	University of Arizona
E. C. Morris	U. S. Geological Survey
J. J. Rennilson	Jet Propulsion Laboratory
E. A. Whitaker	University of Arizona

##### 2. Alpha-Scattering

A. L. Turkevich, Principal Investigator	University of Chicago
E. J. Franzgrote	Jet Propulsion Laboratory
J. H. Patterson	Argonne National Laboratory

#### C. Working Groups

##### 1. Lunar Surface Thermal Properties

J. W. Lucas, Chairman	Jet Propulsion Laboratory
-----------------------	---------------------------

J. E. Conel  
R. R. Garipay  
D. Greenshield  
W. A. Hagemeyer  
H. C. Ingrao  
B. P. Jones  
J. M. Saari

Jet Propulsion Laboratory  
Hughes Aircraft Company  
Manned Spacecraft Center  
Jet Propulsion Laboratory  
Harvard College Observatory  
Marshall Space Flight Center  
The Boeing Company

## **2. Lunar Surface Electromagnetic Properties**

W. E. Brown, Jr., Chairman  
R. A. Dibos  
G. B. Gibson  
D. O. Muhleman

W. H. Peake  
V. J. Poehls  
J. Negus de Wys

Jet Propulsion Laboratory  
Hughes Aircraft Company  
Manned Spacecraft Center  
California Institute of  
Technology  
Ohio State University  
Ryan Aeronautical Company  
Jet Propulsion Laboratory

## **3. Lunar Surface Mechanical Properties**

E. M. Christensen, Chairman  
S. A. Batterson  
H. E. Benson  
R. Choate  
L. D. Jaffe  
R. H. Jones  
H. Y. Ko  
F. N. Schmidt  
R. F. Scott

R. L. Spencer  
F. B. Sperling  
G. H. Sutton

Jet Propulsion Laboratory  
Langley Research Center  
Manned Spacecraft Center  
Jet Propulsion Laboratory  
Jet Propulsion Laboratory  
Hughes Aircraft Company  
University of Colorado  
Bellcomm, Inc.  
California Institute of  
Technology  
Jet Propulsion Laboratory  
Jet Propulsion Laboratory  
University of Hawaii

## **4. Astronomy**

R. H. Norton, Chairman  
J. E. Gunn  
W. C. Livingston

G. A. Newkirk  
H. Zirin

Jet Propulsion Laboratory  
Jet Propulsion Laboratory  
Kitt Peak National  
Observatory  
High Altitude Observatory  
Mt. Wilson and  
Palomar Observatories

## **5. Lunar Theory and Processes**

D. E. Gault, Chairman  
J. B. Adams

Ames Research Center  
Jet Propulsion Laboratory

R. J. Collins  
T. Gold  
J. Green  
G. P. Kuiper  
H. Masursky  
J. A. O'Keefe  
R. A. Phinney  
E. M. Shoemaker  
H. E. Urey

University of Minnesota  
Cornell University  
McDonnell-Douglas Corp.  
University of Arizona  
U. S. Geological Survey  
Goddard Space Flight Center  
Princeton University  
U. S. Geological Survey  
University of California, San Diego







